COLLECTED PAPERS

ON

NANO/ATOM PHOTONICS

Volume 18

August 2002–July 2003

Professor

Motoichi OHTSU

TOKYO INSTITUTE OF TECHNOLOGY

Interdisciplinary Graduate School of Science and Engineering

4259 Nagatsuta-cho, Midori-ku, Yokohama, Kanagawa 226-8502, JAPAN

TEL : +81–45–924–5455

FAX : +81–45–924–5599

E-mail : ohtsu @ ae. titech. ac. jp

PREFACE

In order to realize the ultimate status of light and matter, M. Ohtsu tries to control the spatial properties of light. The approach he has used is through the research of near-field optics and its application to nano-structure fabrication and atom manipulation(Fig.1). This will open up a new era of nano/atom photonics. It should be pointed out that the nano/atom photonics is closely related to quantum optics, atom optics, high density optical storage, nano-structure fabrication technology, and so on. And for this relationship of near-field optics with a variety of fields, nano/atom photonics exhibits rapid progress. Further researches are done to realize novel nanometric materials ,devices, and their integration(Fig.2).

Ohtsu-Saiki group, which is executed in Kanagawa Academy of Science and Technology(KAST) and directed by Ohtsu and Saiki, has started from April, 2001 in order to transfer the results of the research of the previous “PHOTON CONTROL” project to industry so as to produce commercial near field optical spectrometers, optical memories, fiber probes, and so on(*). The “LOCALIZED PHOTON” project, which is supported as ERATO (Exploratory Research for Advanced Technology) by Japan Science and Technology Corporation and directed by Ohtsu, studies a novel theory of optical near-field, nano-photonics, and atom-photonics.(+) Further, a national project on “Ultrahigh capacity optical storage”, which is supported by METI(Ministry of Economy, Trade and Industry) and directed by Ohtsu, has started from the fiscal year 2002 to develop a prototype of an optical storage system of 1Tb/in^2 storage density. Results of the recent research carried out by Ohtsu are reviewed in this issue of the COLLECTED PAPERS.

August 2003

Motoichi OHTSU
大津　元一

(*) Address: Ohtsu-Saiki group,
Kanagawa Academy of Science and Technology
KSP East, Rm. 408, 3-2-1 Sakado, Takatsu-ku,

Kawasaki-shi, Kanagawa 213-0012, JAPAN
Phone: +81-44-819-2075
Fax: +81-44-819-2072
〒213-0012　神奈川県川崎市高津区坂戸３－２－１
ＫＳＰ東棟４０８号室
（財）神奈川科学技術アカデミー，光科学重点研究室
大津・斎木グループ

(+) Address: Localized photon project,
Japan Science and Technology
4th-floor, Tenko Building #17
687-1 Tsuruma, Machida-shi, Tokyo 194-0004
Phone: +81-42-788-6030
Fax: +81-42-788-6031
〒194-0004　東京都町田市鶴間 687-1
第１７天幸ビル４階
科学技術振興事業団　「局在フォトン」プロジェクト

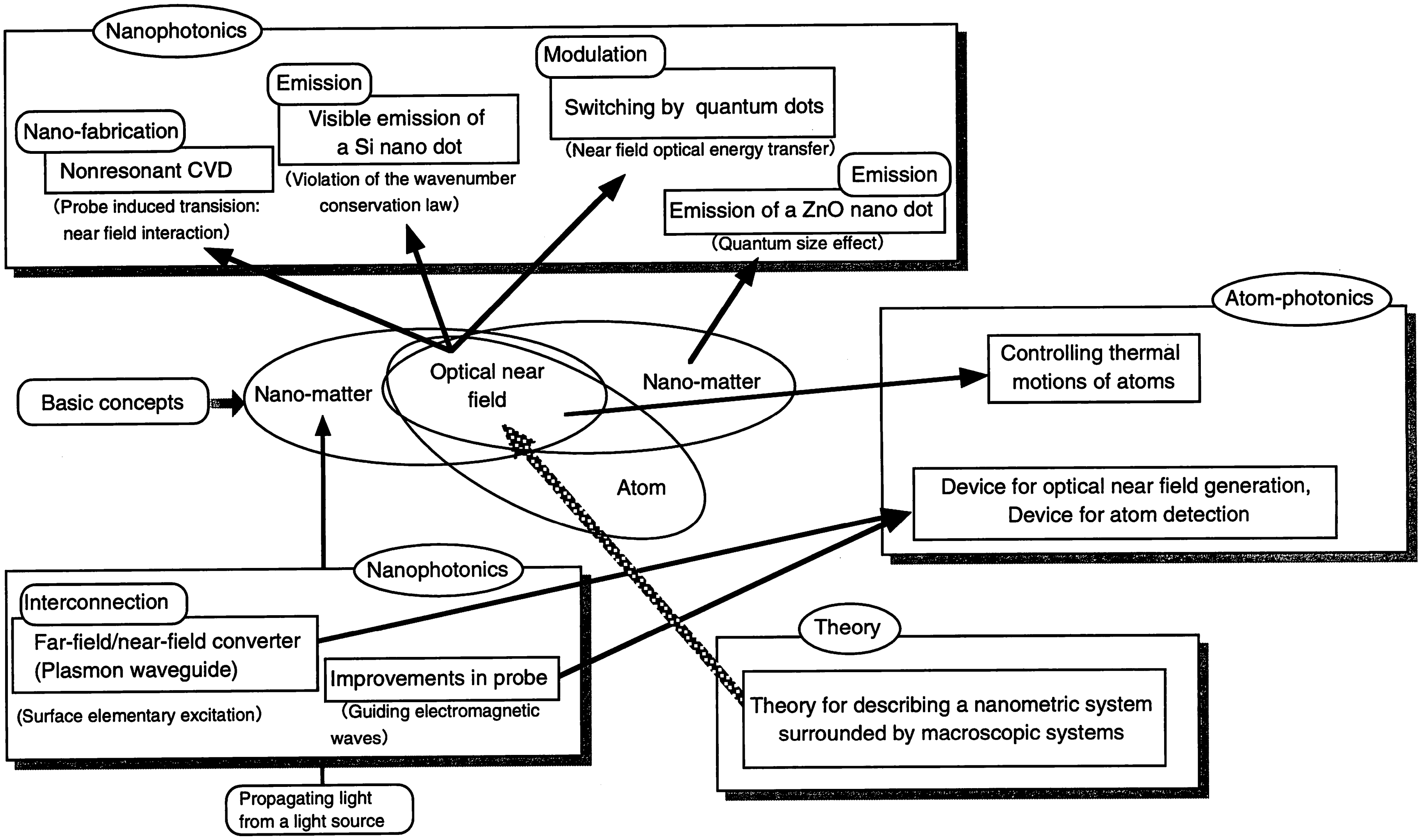

Fig.1 Concepts of nanophotonics, atom-photonics, and theory of optical near field.

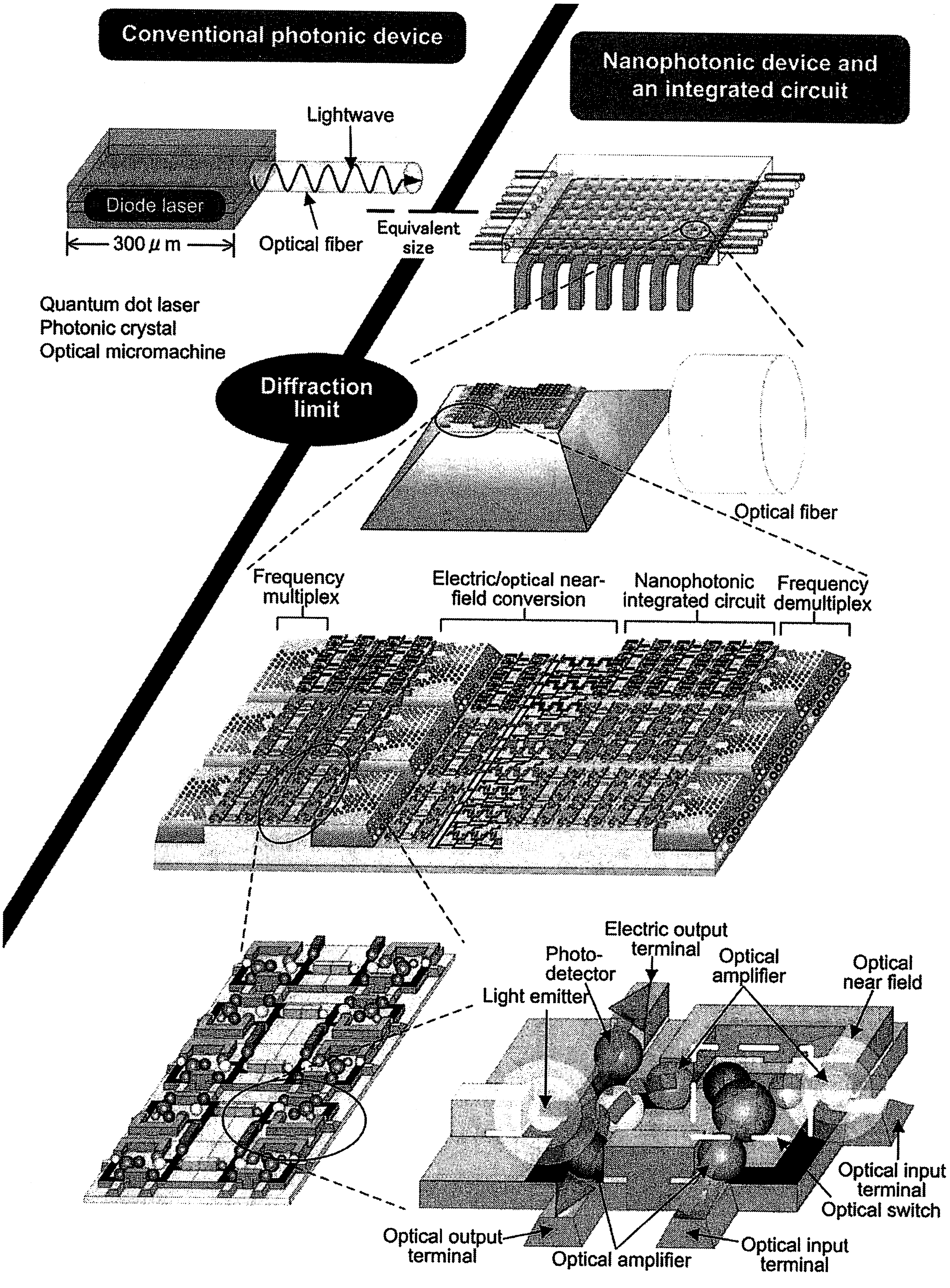

Fig.2 Concepts and structures of nanophotonic devices and their integration.

MEMBERS

(From April 1, 2003)

[I] TOKYO INSTITUTE OF TECHNOLOGY

Professor

Motoichi OHTSU(a-c) (Dr. Eng.)

Associate Professor

Haruhiko ITO(d) (Dr. Sci.)

Graduate Students (Doctor Candidates)

Yoshinobu NAKAYAMA
Yun-Jin CHOI
Jungshik LIM
Shungo YAMADA
Kazuhiro YAMAMOTO

Graduate Students (Master Course)

Wataru NOMURA
Shinya MARUYAMA
Shunsuke YAMAZAKI
Kiichi SUZUKI
Yoshihiko MATSUURA
Kazunori KOBAYASHI
Takashi NAGIRA
Hiroyuki KASHIWAGI
Kazutaka HARA
Keiichi MURAISHI

Undergraduate Students

Ryoichi HAGA
Shin TOMINAGA

Visiting Scientists

Motonobu KOUROGI(e) (Dr. Eng.)

Kazuhiro IMAI[e]	(Dr. Eng.)
Takashi YATSUI[f]	(Dr. Eng.)

Secretaries

Chikako ISHIDA
Kaoru OGURA

a) Also with Kanagawa Academy of Science and Technology (Director, Ohtsu-Saiki group)
b) Also with ERATO, Japan Science and Technology Corporation (Director, "Localized photon" project)
c) Also a director, "Ultrahigh capacity optical storage", Ministry of Economy, Trade and Industry
d) Also with "Localized photon" project, ERATO, Japan Science and Technology Corporation
e) Permanent affiliation: Optical Comb Laboratories, Inc.
f) Permanent affiliation: "Localized photon" project, ERATO, Japan Science and Technology Corporation

[II] "LOCALIZED PHOTON" PROJECT, ERATO, JAPAN SCIENCE AND TECHNOLOGY CORPORATION

Researchers

Theory Group

Kiyoshi KOBAYASHI(g)	(Dr. Sci.)	(Group Leader)
Suguru SANGU	(Dr. Eng.)	
Akira SHOJIGUCHI	(Dr. Sci.)	

Nano-photonics Group

Tadashi KAWAZOE	(Dr. Sci.)
Takashi YATSUI	(Dr. Eng.)
T.-W. KIM	(Dr. Eng.)

Atom-photonics Group

Kouki TOTSUKA	(Dr. Sci.)
Akifumi TAKAMIZAWA	(Dr. Eng.)

Managers

Akiyoshi ORIDE(h)
Takaaki MORIYAMA

Secretaries

Tomoko TOTAKE

g) Permanent affiliation: Japan IBM Co. Ltd.
h) Permanent affiliation: RICOH Co.Ltd.

[III] KANAGAWA ACADEMY OF SCIENCE AND TECHNOLOGY

Full-Time Researchers

Shuji MONONOBE	(Dr. Eng.)

Part-Time Researchers

Motonobu KOUROGI(i)	(Dr. Eng.)

Secretary

Kazumi NAKAHARA

i) Permanent affiliation: Optical Comb Laboratories, Inc.

LIST OF PAPERS

[(pp.XX-XX); pages in this issue of the COLLECTED PAPERS]

[I] PAPERS IN NANO/ATOM PHOTONICS

[I-1] PAPERS IN ATOM PHOTONICS

(a) Journal Papers

[1] A. Takamizawa, H. Ito, S. Yamada, and M. Ohtsu, "Accumulative Atom Detection by Magneto-Optical Trap for Near-Field Optical Funnel", Jpn. J. Appl. Phys., Vol.42, Part 1, No.6A, June 2003, pp.3658-3661

(pp.1-4)

[2] K. Totsuka, H. Ito, K. Suzuki, K. Yamada, M. Ohtsu, and T. Yatsui, "A slit-type atom deflector with near-field light", Appl. Phys. Lett., Vol.82, No.10, March 2003, pp.1616-1618

(pp.5-7)

[3] K. Totsuka, H. Ito, and M. Ohtsu, "Fluorescence Spectroscopy of Rb Atoms with Two-Color Optical Near Fields for a High-Resolution Slit-Type Detector", IEICE Trans. Electron., Vol.E85-C, No.12, December 2002, pp.2093-2096

(pp.8-11)

[4] A. Takamizawa, H. Ito, and M. Ohtsu, "Multireflection of Cold Atoms in a Near-Field Optical Funnel", Jpn. J. Appl. Phys., Vol.41, Part 1, No.10, October 2002, pp.6215-6218

(pp.12-15)

(b) International Conferences

[1] K. Totsuka, H. Ito, A. Takamizawa, K. Yamamoto, and M. Ohtsu, "Deflecting, detecting and funneling atoms using near-field light", Proceedings of European Quantum Electronics Conference, Munich, Germany June23-27, (paper number EG2-4-MON)

(p.16)

[2] A. Takamizawa, H. Ito, S. Yamada, and M. Ohtsu, "Cold-atom funnel using near-field light", Technical Digest of Quantum Electronics and Laser Science Conference, June 2-6, 2003, Baltimore, MD, (paper number QThJ10)

(pp.17-18)

[3] H. Ito, "Atom manipulation using near-field light", The first German-Japanese Symposium on Spatially resolved spectroscopy and fabrication of nano-structures for nano-atom photonics, March 17-19, 2003, Berlin, Germany (paper number, TuPM)
[Invited presentation]

(p.19)

[I-2] PAPERS IN NANOPHOTONICS

(a) Journal Papers

[1] T.-W. Kim, T. Kawazoe, S. Yamazaki, J. Lim, T. Yatsui, and M. Ohtsu, "Room temperature ultraviolet emission from ZnO nanocrystallites fabricated by the low temperature oxidation of metallic Zn precursors", Solid State Commun., vol.127, 2003, pp.21-24

(pp.21-24)

[2] K. Kobayashi, S. Sangu, T. Kawazoe, A. Shojiguchi, K. Kitahara, and M. Ohtsu, "Excitation dynamics in a three-quantum dot system driven by optical near field interaction: towards a nanometric photonic device", J. Microscopy, Vol.210, Pt 3, June 2003, pp.247-251

(pp.25-29)

[3] A. Shojiguchi, K. Kitahara, K. Kobayashi, and M. Ohtsu, "A method for controlling the spins of atoms using optical near-fields", J. Microscopy, Vol.210, Pt 3, June 2003, pp.301-306

(pp.30-35)

[4] T. Kawazoe, K. Kobayashi, S. Sangu, and M. Ohtsu, "Demonstration of a nanophotonic switching operation by optical near-field energy transfer", Appl. Phys. Lett., Vol.82, No.18, May 2003, pp.2957-2959

(pp.36-38)

[5] S. Sangu, K. Kobayashi, A. Shojiguchi, T. Kawazoe, and M. Ohtsu, "Excitation energy transfer and population dynamics in a quantum dot system induced by optical near-field interaction", J. Appl. Phys., Vol.93, No.5, March 2003, pp.2937-2945

(pp.39-47)

[6] T. Kawazoe, K. Kobayashi, S. Sangu, and M. Ohtsu, "Demonstrating nanophotonic switching using near-field pump-probe photoluminescence spectroscopy of CuCl quantum cubes", J. Microscopy, Vol.209, Pt 3, March 2003, pp.261-266

(pp.48-53)

[7] J. Lim, T. Kawazoe, T. Yatsui, and M. Ohtsu, "Fabrication of a Ferromagnetic-Coated Fiber Probe with a Double-Layer Structure", IEICE Trans. Electron., Vol.E85-C, No.12, December 2002, pp.2077-2080

(pp.54-57)

[8] Y. Yamamoto, M. Kourogi, M. Ohtsu, G.-H. Lee, and T. Kawazoe, "Lateral Integration of Zn and Al Dots with Nanometer-Scale Precision by Near Field Optical Chemical Vapor Deposition Using a Sharpened Optical Fiber Probe", IEICE Trans. Electron., Vol.E85-C, No.12, December 2002, pp.2081-2085

(pp.58-62)

[9] A. Shojiguchi, K. Kobayashi, S. Sangu, K. Kitahara, and M. Ohtsu, "Coherent dipole oscillation induced by localized photons", Nonlinear Optics, Vol.29 (10-12), 2002, pp.563-569

(pp.63-69)

[10] T. Yatsui, T. Kawazoe, M. Ueda, Y. Yamamoto, M. Kourogi, and M. Ohtsu, "Fabrication of nanometric single zinc and zinc oxide dots by the selective photodissociation of adsorption-phase diethylzinc using a nonresonant optical near field", Appl. Phys. Lett., Vol.81, No.19, November 2002, pp.3651-3653

(pp.70-72)

[11] M. Ohtsu, K. Kobayashi, T. Kawazoe, S. Sangu, and T. Yatsui, "Nanophotonics: Design, Fabrication, and Operation of Nanometric Devices Using Optical Near Fields", IEEE J. of Selected Topics in Quantum Electron., Vol.8, No.4, July/August 2002, pp.839-862 **[Invited paper]**

(pp.73-96)

(b) International Conferences

[1] M. Ohtsu, "What is nanophotonics?", The International Nanophotonics Symposium Handai, July 24-26, 2003, Osaka, (paper number IL-19)
[Invited presentation]

(p.97)

[2] T. Kawazoe, K. Kobayashi, S. Sangu, and M. Ohtsu, "Nanophotonic Switching using CuCl Quantum Cubes", Technical Digest of Quantum Electronics and Laser Science Conference, June 2-6, 2003, Baltimore, MD, (paper number QMD3)

(pp.98-100)

[3] T.-W. Kim, T. Kawazoe, S. Yamazaki, J. Lim, T. Yatsui, and M. Ohtsu, "Ultraviolet-emission and lasing from ZnO nanostructures fabricated by a simple method involving the low-temperature oxidation of metallic Zn", Technical Digest of Conference on Lasers and Electro-Optics, June 2-6, 2003, Baltimore, MD, (paper number CTuF5)

(pp.101-102)

[4] S. Sangu, K. Kobayashi, T. Kawazoe, A. Shojiguchi, and M. Ohtsu, "A nanophotonic switch: transient dynamics and switching operation", Technical Digest of Quantum Electronics and Laser Science Conference, June 2-6, 2003, Baltimore, MD, (paper number QTuK6)

(pp.103-105)

[5] T. Kawazoe, K. Kobayashi, S. Takubo, and M. Ohtsu, "Non-Adiabatic Nanometric Near-Field Optical Chemical Vapor Deposition using Visible Light for Ultraviolet Metal-Organic Gas Source", Technical Digest of Quantum Electronics and Laser Science Conference, June 2-6, 2003, Baltimore, MD, (paper number QWA12)

(pp.106-108)

[6] T. Yatsui, W. Nomura, M. Kourogi, and M. Ohtsu, "Plasmon condenser for optical far/near-field conversion", Technical Digest of Conference on Lasers and Electro-Optics, June 2-6, 2003, Baltimore, MD, (paper number CWP3)

(pp.109-110)

[7] T. Yatsui, S. Takubo, J. Lim, T. Kawazoe, M. Kourogi, and M. Ohtsu, "Controlling the growth of Zn nanoparticles in a nonresonant optical near fields using size-dependent resonance", Technical Digest of Conference on Lasers and Electro-Optics, June 2-6, 2003, Baltimore, MD, (paper number CFL2)

(pp.111-112)

[8] M. Ohtsu, ""Physics and Applications of Nanophotonics", International Symposium on New Frontiers for Ubiquitous IT Services, May 26-27, 2003, Atsugi, Kanagawa, (paper number7)
[Invited presentation]

(p.113)

[9] M. Ohtsu, "Operation and Fabrication of Nanophotonic Devices", The First International Congress on Bio-Nanointerface, May 19-24, 2003, Tokyo, (paper number 23D-15-KL2) **[Invited presentation]**

(p.114)

[10] M. Ohtsu, "Optical near-field phenomena and their applications I: Nanophotonics", The first German-Japanese Symposium on Spatially resolved spectroscopy and fabrication of nano-structures for nano-atom photonics, March 17-19, 2003, Berlin, Germany (paper number, MoAM)
[Invited presentation]

(p.115)

[11] T. Yatsui, "Optical near-field phenomena and their applications II: Near-field chemical vapor deposition and an optical far/near-field conversion device", The first German-Japanese Symposium on Spatially resolved spectroscopy and fabrication of nano-structures for nano-atom photonics, March 17-19, 2003, Berlin, Germany (paper number,MoAM)

(p.116)

[12] T. Kawazoe, "Optical near-field phenomena and their applications III: Non-resonant photo-dissociation and dipole forbidden energy transfer by optical near field", The first German-Japanese Symposium on Spatially resolved spectroscopy and fabrication of nano-structures for nano-atom photonics, March 17-19, 2003, Berlin, Germany (paper number, MoAM)

(p.117)

[13] K. Kobayashi, S. Sangu, A. Shojiguchi, T. Kawazoe, and M. Ohtsu, "Characteristic dynamics inherent in a near-field coupled quantum dot system", The first German-Japanese Symposium on Spatially resolved spectroscopy and fabrication of nano-structures for nano-atom photonics, March 17-19, 2003, Berlin, Germany (paper number, WeAM)

(p.118)

[14] K. Kobayashi, A. Shojiguchi, S. Sangu, K. Kitahara, and M. Ohtsu, "Dipole-ordered state controlled by localized photons and superradiant multiple pulse generation", The first German-Japanese Symposium on Spatially resolved spectroscopy and fabrication of nano-structures for nano-atom photonics, March 17-19, 2003, Berlin, Germany (paper number, WePM)

(p.119)

[15] M. Ohtsu, "Nanophotonic Devices: Their Functions and Fabrications", Proceedings of the Taiwan-Japan Symposium on Nanophotonics Technology, Osaka, November 5-6. 2002, pp.21-22 **[Invited presentation]**

(pp.120-121)

[16] M. Ohtsu, "Nanophotonics: Design, Fabrication, And Operation of Nanophotonic Devices", Workshop on Optical Storage and Communication, Taipei, Taiwan, October 19-20, 2002, (paper number P-3)
[Plenary presentation]

(p.122)

[17] T. Yatsui and M. Ohtsu, "Development of nano-photonic devices and their integration by optical near field", 2002 IEEE/LEOS International Conference on Optical MEMs, August 20-23, 2002, Lugano, Switzerlend, (paper number FB1) **[Invited presentation]**

(pp.123-124)

[18] T. Yatsui, M. Ueda, Y. Yamamoto, T. Kawazoe, M. Kourogi, and M. Ohtsu, "Fabrication of 25-nm Zn Dot with Selective Photodissociation of Adsorption-phase Diethylzinc by Optical Near field", Abstract of the 7th International Conference on Near-field Optics and Related Techniques, August 11-15, 2002, Rochester, USA, (p.117)

(p.125)

[19] T.-W. Kim, T. Yatsui, M. Kourogi, and M. Ohtsu, "Fabrication of a temperature-controllable B-doped Si probe for optical near-field photochemical vapor deposition", Abstract of the 7th International Conference on Near-field Optics and Related Techniques, August 11-15, 2002, Rochester, USA, (p.127)

(p.126)

[20] A. Shojiguchi, K. Kobayashi, K. Kitahara, S. Sangu, and M. Ohtsu, "Manifestation of an electric dipole order induced by optical near fields", Abstract of the 7th International Conference on Near-field Optics and Related Techniques, August 11-15, 2002, Rochester, USA, (p.137)

(p.127)

[21] T. Yatsui, T. Abe, M. Kourogi, and M. Ohtsu, "Plasmon Condenser with a Microscatter for Optical Far/Near field Conversion", Abstract of the 7th International Conference on Near-field Optics and Related Techniques, August 11-15, 2002, Rochester, USA, (p.148)

(p.128)

[22] T. Kawazoe, K. Kobayashi, S. Sangu, and M. Ohtsu, "Near-field Pump-probe Luminescence Spectroscopy of CuCl quantum cubes in ultraviolet region", Abstract of the 7th International Conference on Near-field Optics and Related Techniques, August 11-15, 2002, Rochester, USA, (p.193)

(p.129)

[23] K. Kobayashi, S. Sangu, T. Kawazoe, A. Shojiguchi, K. Kitahara, and M. Ohtsu, "Localized Photon Picture vs. Effective Interaction Picture: Towards a Nanometric Photonic Device", Abstract of the 7th International Conference on Near-field Optics and Related Techniques, August 11-15, 2002, Rochester, USA, (p.218)

(p.130)

[I-3] REVIEW PAPERS

[1] K. Kobayashi and M. Ohtsu, "Progress in Optics 2002: 7. Near-Field Optics", J. Optical Society of Japan, Vol.32, No.4, April 2003, pp.211-212
【小林潔、大津元一、「２００２年光学界の進展　７．近接場光学」、光学、第３２巻、第４号、２００３年４月、pp.211-212】

(pp.131-133)

[2] M. Ohtsu, "Frontier of Nanophotonics", Expected Materials for the Future, Vol.3., No. 3, March 2003, pp.78-81
【大津元一、「ナノフォトニクス事始め」、未来材料、第３巻、第３号、２００３年３月、pp.78-81】

(pp.134-137)

[3] M. Ohtsu, "Nanophotonics", J. IEICE, Vol.85, No.11, November, 2002, pp.834-838
【大津元一、「ナノフォトニクス」、電子情報通信学会誌、第８５巻、第１１号、２００２年１１月、pp.834-838】

(pp.138-142)

[4] M. Ohtsu, "An Introduction: What is nanophotonics?", Optronics, No.11, November 2022, pp.128-131
【大津元一、「総論：ナノフォトニクスとは何か？その目指す方向は？」、オプトロニクス、２００２年１１号、pp.128-131】

(pp.143-146)

[5] T. Kawazoe, "Nanophotonic devices and their integration", Optronics, No.11, November 2002, pp.132-137
【川添忠、「ナノフォトニックデバイスとその集積化」、オプトロニクス、２００２年１１号、pp.132-137】

(pp.147-152)

[6] M. Ohtsu, T. Yatsui, "Nano-deoptision by optical near fields", Optronics, No.11, November 2002, pp.162-165
【八井崇、「近接場光によるナノ構造堆積」、総論：ナノフォトニクスとは何か？その目指す方向は？】、オプトロニクス、２００２年１１号、pp.128-131】

(pp.153-156)

[7] H. Ito, K. Totsuka, and M. Ohtsu, "Atom Deflection and Detection with

Optical Near Fields", J. Optical Society of Japan, Vol.31, No.10, October 2002, pp.755-757
【伊藤治彦、戸塚弘毅、大津元一、「光近接場による原子の偏向と検出」、光学、第３１巻、第１０号、２００２年１０月、pp.755-757】

(pp.157-159)

[8] M. Ohtsu, "Nanophotonics", Japanese Scientific Monthly, Vol.55, No.8, August 2002, pp.764-768
【大津元一、「ナノフォトニクス」、学術月報、第５５巻、第８号、２００２年８月、pp.764-768】

(pp.160-164)

[III] PUBLISHED BOOKS

[1] M. Ohtsu and K. Kobayashi, "Fundamentals of Optical Near-Fields", Ohm-sha, Tokyo, January 2003 (252 pages)

【大津元一、小林潔、「近接場光の基礎」、オーム社、東京、2003 年 1 月 (252 頁）】

[2] M. Ohtsu, "Depositing Atoms by Light", Optics and Nanotechnology, pp. 26-33, ed. by S. Kawata, Kuba-pro., Tokyo, September 2002
【大津元一、「光で原子を積む」、光とナノテクノロジー、河田聡編、クバプロ、東京、2002 年 9 月、pp.26-34】

[3] M. Ohtsu, "Near-Field Optical Microscopy and Application to Nanophotonics", in *Optical Imaging and Microscopy*, Ed. by P. Torok and F.-J. Kao, Springer-Verlag, Berlin, 2003, pp.339-356

[4] M. Ohtsu, "Nano- and Atom Photonics", in International Trends in Applief Optics, Ed. by A.H. Guenther, SPIE Press, Bellingham, 2002 pp.389-409

[5] M. Kourogi, B. Widiyatmoko, and M. Ohtsu, "The cavity-enhanced optical-frequency comb generator and its applications", in *Cavity-Enhanced Spectroscopies*, Ed. by R.D. van Zee, Academic Amsterdam, 2002, pp.297-319

[IV] PRESENTED PH.D THESIS

[1] T. Ouchi, “Study on thin film pringing of optical devices and optical fiber connections for optical interconnecting modules”, December 2002
【尾内敏彦、「光配線モジュールのための光デバイス薄膜転写および光ファイバ結合に関する研究」、2002 年 12 月】

[V] AWARDS

[1] S. Sangu, The 13rd Young Scientists Award, Japan Society of Applied Phyiscs, March 2003
【三宮俊、第 13 回応用物理学会講演奨励賞: “光近接場による量子ドット間エネルギー移動の過渡応答特性,” 第 63回応用物理学会秋期講演会、2002 年 9 月、発表番号 25p-D-7,】

[I] PAPERS IN NANO/ATOM PHOTONICS

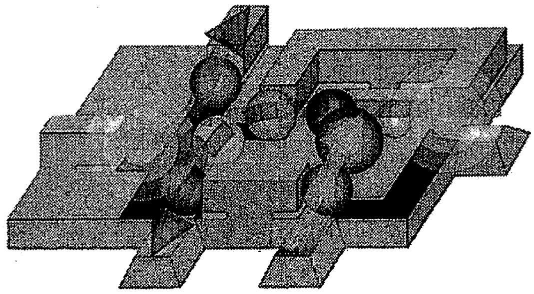

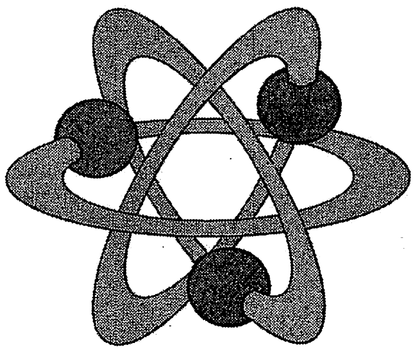

[I-1] PAPERS IN ATOM PHOTONICS

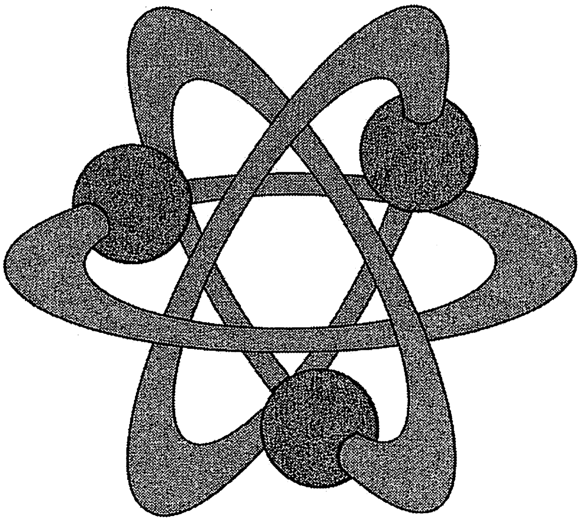

Jpn. J. Appl. Phys. Vol. 42 (2003) pp. 3658–3661
Part 1, No. 6A, June 2003

Accumulative Atom Detection by Magneto-Optical Trap for Near-Field Optical Funnel

Akifumi TAKAMIZAWA[1], Haruhiko ITO[1], Shungo YAMADA[1] and Motoichi OHTSU[1,2]

[1] *Interdisciplinary Graduate School of Science and Engineering, Tokyo Institute of Technology, 4259, Nagatsuta-cho, Midori-ku, Yokohama 226-8502, Japan*
[2] *ERATO, Japan Science and Technology Corporation, 687-1 Tsuruma, Machida 194-0004, Japan*

(Received September 30, 2002; accepted for publication February 17, 2003)

We use a magneto-optical trap as an integrating counter for descending cold atoms. In the case of cold ^{87}Rb atoms with an initial mean temperature of 9 μK, 60% of the total number of 2.6×10^7 are captured after a 26-cm free-fall and trapped for a long time of 270 s. From the capture efficiency and the decay time, the minimum detectable flux intensity of a cold ^{87}Rb atomic beam is estimated to be 2×10^5 atom/cm^2·s. The atom-counting system is used for detection and evaluation of a cold atomic beam produced out of a near-field optical funnel. [DOI: 10.1143/JJAP.42.3658]

KEYWORDS: accumulative atom detection, magneto-optical trap, cold atomic beam, near-field optical funnel

1. Introduction

The thermal motion of gaseous atoms had been a barrier to high-resolution laser spectroscopy for a long time. However, owing to the recent development of atom cooling,[1)] it has been possible to greatly control the thermal motion. Since an ultracold atomic ensemble was generated,[2)] its application to physics and technology has attracted considerable interest. Consequently, atom optics making full use of resonant and near-resonant interactions between light and atoms has been established, and reflection,[3)] diffraction,[4)] and channeling[5)] of atomic beams have been demonstrated. Moreover, the atom laser[6)] has been produced from the Bose-Einstein condensate of alkali-metal atoms,[7)] and applied to technologies such as atom interferometry[8)] and atom holography.[9)]

Control of thermal atomic beams by means of atom-optical methods is also applied to nanoscale patterning.[10,11)] If a cold atomic beam is used instead of the thermal atomic beam, it will be possible to fabricate nano-structures with higher spatial accuracy. However, in the case of the conventional schemes using far-field light, it is difficult to obtain spatial-control accuracy beyond a half wavelength due to the diffraction effects, so that it is not easy to form dot-shaped structures. Indeed, fabrication of a nanostructure with an arbitrary shape has not been reported so far, although line-shaped patterns have been formed. To overcome the diffraction limit, we are developing new atom-optical methods with nanometric optical near fields, including atom deflection and single-atom trapping which control each individual atom species- and state-selectively.[12)] The atom-control techniques are necessary for realization of optical atomic-scale deposition.

A cold atomic beam with high flux intensity is required for interaction with nanometric optical near fields. To this end, we are planning to produce the cold atomic beam using a funnel-shaped optical near field.[13)] In this scheme, cold atoms fall from a magneto-optical trap (MOT)[14)] into a hollow funnel-prism where the orifice is directed upward. Under a blue-detuning condition, the atoms approaching the inner-wall surface are reflected by the repulsive dipole force from the optical near field generated on the inner wall. Moreover, if a weak pumping light beam is added, the so-called Λ-type three-level atoms such as alkali-metal atoms lose their kinetic energy at each reflection through the Sisyphus cooling mechanism.[15,16)] As a result, the atoms are collected at the bottom and go out of a small exit hole. In our previous work,[17)] we observed multireflection of cold Rb atoms in the near-field optical funnel, and estimated the optimum frequency detuning and diameter of the light beam that excited the optical near field from measurements of the reflection efficiency.

A CW cold atomic beam can be generated by multi-loading of cold atoms from the MOT into the funnel. Under our experimental conditions, the flux intensity of the atomic beam is estimated to be 8.3×10^{12} atom/cm^2·s from the Monte Carlo simulations.[18)] This value is sufficient for the interaction with the optical near field stimulated on a nanometric aperture, but not for evaluation of the cold atomic beam from observation of resonance fluorescence or absorption change of a probe light beam. Indeed, although the number of descending atoms from an MOT is often estimated by a probe light beam, the number of atoms passing through the detection region per unit time in the case of the cold atomic beam coming out of the funnel is smaller than that of the simplex release from the MOT by three orders of magnitude, so that it is difficult to detect the cold atomic beam. In addition, if we take the flight distance from the exit to the detection region to be sufficiently long to accurately measure the mean longitudinal temperature of the cold atomic beam, it expands in the lateral direction even if it is well-collimated, so that the number density of atoms is reduced. Therefore, the system that efficiently detects a small number of atoms is required for evaluation of the cold atomic beam.

In this paper, we present a detection scheme of accumulating atoms with an MOT. In particular, under the ultrahigh vacuum pressure of 10^{-9} Pa, the capture time reaches over 3 min and many atoms can be gathered. Consequently, the number of captured atoms is easily estimated from the measurement of the intensity of resonance fluorescence, which is induced by absorption of the light beams used for the MOT, with a popular charge-coupled device (CCD) camera.

In §2, we describe an experiment of detecting cold ^{87}Rb atoms in the double MOT configuration.[19)] The capture efficiency is obtained from the number of atoms trapped in the second MOT for detection increasing with the number of loading times from the first MOT for cold-atom generation. The capture time in the detection MOT is also obtained from the number of trapped atoms decreasing with time after the stop of loading. Next, in §3, we discuss the detection sensitivity in the case where the atom-detection scheme is used for a cold atomic beam generated by the near-field optical funnel. Finally, we give the conclusion in §4.

2. Experiment

Figure 1 shows the double MOT setup in which we detect cold ^{87}Rb atoms falling for a long distance, where the MOT for detection is made 26 cm below the MOT for cold-atom generation. The two MOTs are connected by a 8.1-cm-long stainless-steel tube of which the inner diameter increases stepwise from 4 mm to 12 mm from top to bottom. The upper MOT consists of a pair of anti-Helmholtz coils that produces a quadrupole magnetic field with a gradient of 10 G/cm and three orthogonal pairs of two counterpropagating $\sigma^+ - \sigma^-$ circularly-polarized light beams with the diameter of 1 cm and the intensity of 4 mW/cm^2 under a background pressure of 10^{-7} Pa. The six light beams are red-detuned by 10 MHz with respect to the $5S_{1/2}$, $F = 2 \leftrightarrow 5P_{3/2}$, $F = 3$ transition of ^{87}Rb. Repumping light beams with the diameter of 1 cm and the intensity of 5 mW/cm^2 tuned to the $5S_{1/2}$, $F = 1 \leftrightarrow 5P_{3/2}$, $F = 2$ transition are superimposed over the cooling light beams.

A ^{87}Rb ensemble of 2.6×10^7 atoms with a diameter of 2 mm is first generated 5 mm above the entrance of the connecting tube. Then, after turning off the quadrupole magnetic field, we conduct the polarization gradient cooling[20)] for 10 ms by changing the red detuning to 80 MHz and cool the ^{87}Rb atoms to a mean temperature of 9 μK. Next, when all light beams are turned off, the cold ^{87}Rb atoms are released from the upper MOT and divergently fall into the lower MOT under a background pressure of 10^{-9} Pa. The cooling light beams of the lower MOT are red-detuned by 17 MHz with respect to the $5S_{1/2}$, $F = 2 \leftrightarrow 5P_{3/2}$, $F = 3$ transition. Both of the cooling and repumping light beams have the same intensity of 1 mW/cm^2. The diameter of all light beams is 2 cm and all atoms coming through the connecting tube enter the capture region of the lower MOT. The other conditions of the lower MOT are the same as those of the upper MOT. The cold ^{87}Rb atoms captured in the lower MOT make a cloud with a diameter of 4 mm and emit resonance fluorescence with a wavelength of 780 nm. The number of trapped atoms is estimated from the fluorescence intensity measured using a photo-transistor.

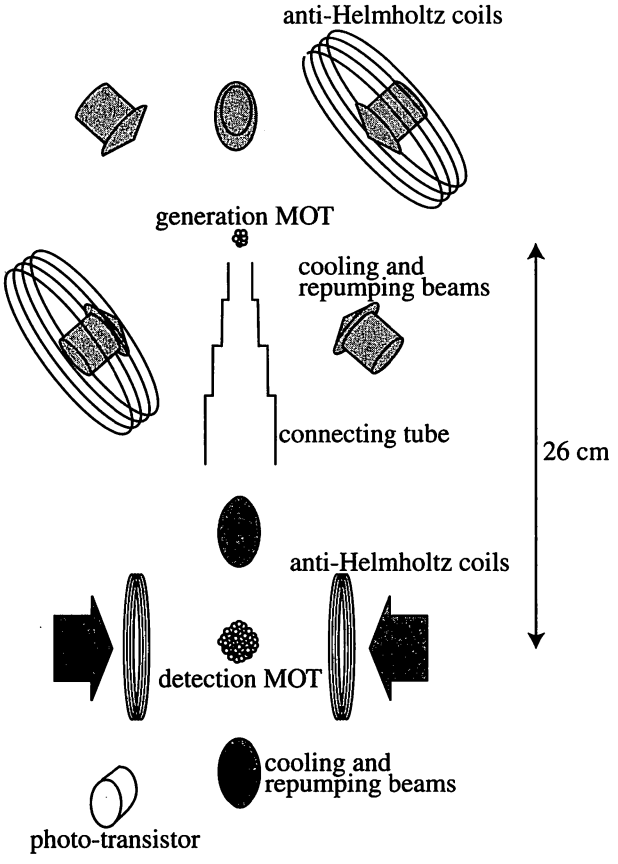

Fig. 1. Experimental setup with double MOTs. Both of the MOTs are composed of circularly-polarized cooling light beams, repumping light beams, and a pair of anti-Helmholtz coils. The MOT for detection is made 26 cm below the MOT for cold-atom generation, and a stainless-steel tube connects the two MOTs. The background pressures of the upper and lower MOTs are 10^{-7} Pa and 10^{-9} Pa, respectively. The cold atoms of 2.6×10^7 with a mean temperature of 9 μK are released from the upper MOT and 40% of them fall into the lower MOT through the connecting tube. Resonance fluorescence radiating from the ^{87}Rb atoms captured in the lower MOT is observed using a photo-transistor.

Cold ^{87}Rb atoms are multiloaded from the upper MOT into the lower MOT. Figure 2 shows the number of atoms captured in the lower MOT plotted as a function of the number of loading times. The cold atoms are stored for 2 s in the upper MOT and then released. The next cold-atom generation begins at 0.5 s after release. As shown in Fig. 2, the number of captured atoms linearly increases until the number of loading times is about 20, and then it reaches saturation: after 100 loading times, it becomes 3×10^8. The ratio β of the capture number in the lower MOT to the supply number from the upper MOT is 0.23 in the linear-increase region. As discussed below, since some atoms are lost in the connecting tube by collision with the wall, the effective capture number is larger. In the next section, we will estimate the net capture efficiency α of the detection MOT by taking the lost atoms into consideration.

Figure 3 shows the capture number of cold ^{87}Rb atoms plotted as a function of time t after the completion of loading. Here, filled circles and a solid curve indicate the experimental values and the fitting with the function

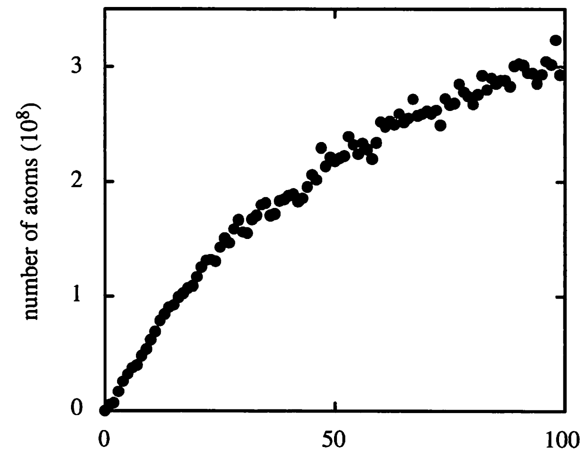

Fig. 2. The number of ^{87}Rb atoms stored in the detection MOT plotted as a function of the number of loading times. The capture number linearly increases until the number of loading times is about 20, and then reaches saturation.

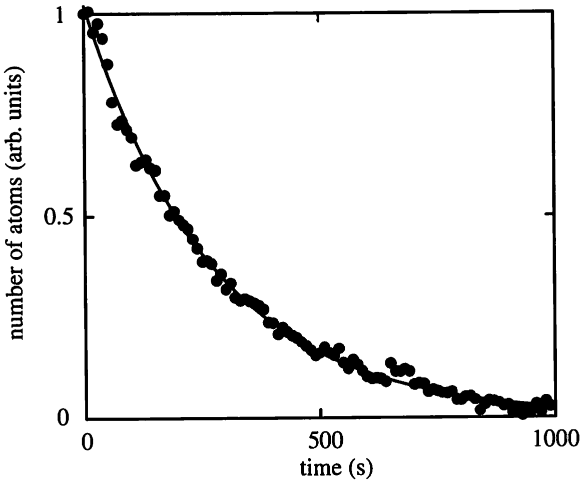

Fig. 3. Time change of the number of ^{87}Rb atoms stored in the detection MOT after the completion of loading. Here, the experimental values are indicated by dots, while the solid curve shows the fitting by the function $\exp(-\gamma t)$ with $\gamma^{-1} = 270$ s.

$\exp(-\gamma t)$, respectively. From Fig. 3, the time γ^{-1} at which the number of atoms stored in the lower MOT decays to e^{-1} times is estimated to be 270 s.

3. Discussion

We are planning to use the accumulative-counting scheme for evaluation of a cold atomic beam produced by the near-field optical funnel mentioned in the introduction. From the numerical simulations, about 10^7 atoms per second are estimated to be outputted from the funnel.[13] It corresponds to the linear region of the MOT detector. In the experiment described in the previous section, ^{87}Rb atoms are always pumped into the $5S_{1/2}$, $F = 2$ upper ground state of the hyperfine structure by the repumping light beams of the two MOTs. On the other hand, in the near-field optical funnel, ^{87}Rb atoms are pumped into the $5S_{1/2}$, $F = 1$ lower ground state at every reflection for the Sisyphus cooling. In the funnel case, when the MOT detector operates, the ^{87}Rb atoms in the lower ground state are first transferred into the upper ground state and then trapped.

In order to examine the influence of the pumping on the capture efficiency, we conducted a similar experiment in the case of ^{87}Rb atoms in the lower ground state. Here, we pumped the cold ^{87}Rb atoms to the lower ground state just after release from the upper MOT by illuminating them with a weak pumping light beam tuned to the $5S_{1/2}$, $F = 2 \leftrightarrow 5P_{3/2}$ $F = 2$ transition. The result shows that the capture efficiency with the additional pumping light beam reduces by 3% compared to that without it. From this, we find that the capture efficiency is hardly affected by the ground states which atoms occupy.

Let us estimate the detection sensitivity in the case where the near-field optical funnel is used in the place of the upper MOT. First, we calculate the net capture efficiency α of the MOT detection system based on the results of the double-MOT experiment, where some atoms hit the inner wall of the connecting tube and adhere to the surface. The tube radius increases from 2 mm to 6 mm from top to bottom at each step of about 2 cm-length. Note that the loss of incident atoms occurs in the first tube part with the smallest radius. We assume that ^{87}Rb atoms with a distribution radius σ_0 and a mean temperature T divergently fall through the connecting tube. The probability η that an atom with a mass m falling from the upper MOT under the gravitational acceleration g passes through the first tube part with a radius R and a length l is approximately given by[21]

$$\eta = 1 - \exp\left\{ -\frac{R^2}{\sigma_0^2 + \dfrac{4k_B T(l+h)}{mg}} \right\}, \qquad (1)$$

where k_B and h are the Boltzmann constant and the height of the upper MOT from the entrance of the connecting tube, respectively. Substituting the experimental values of $\sigma_0 = 1$ mm and $T = 9\,\mu$K together with $R = 2$ mm, $l = 1.5$ cm and $h = 0.5$ cm into eq. (1), we obtain $\eta = 0.4$. Consequently, it follows that $\alpha = \beta/\eta = 0.6$. Since a collimated cold atomic beam passes through the connecting tube without hitting the inner wall, the quantity α is the capture efficiency in the atom-funnel case.

Then, assuming that a CW cold atomic beam with a constant flux intensity F is outputted from the exit hole of the funnel with a radius r, we consider the case of observing resonance fluorescence radiating from the ^{87}Rb atoms trapped in the detection MOT by a CCD camera. If the capture number N_{cap} is much larger than 1 and successively changes, the increase rate of N_{cap} is approximately given by

$$\frac{dN_{\text{cap}}}{dt} = \pi r^2 \alpha F - \gamma N_{\text{cap}} \qquad (2)$$

where the first term on the right-hand side is the number of atoms captured per unit time and the second term is the number of atoms escaping from the detection MOT per unit time. Putting $dN_{\text{cap}}/dt = 0$, we obtain the steady-state value

$$N_{\text{cap}}^{\text{st}} = \frac{\pi r^2 \alpha F}{\gamma} \qquad (3)$$

In our near-field optical funnel technique for generating a cold atomic beam, we use intense laser light with a power exceeding 1 W. To avoid a detector breakdown by the scattered intense light, we use a CCD camera for detection although a photomultiplier tube has a high sensitivity. Let us take an example of observation with a commercial CCD camera (SONY XC-ST50, imaging lens VLC-50Y-M), which is placed 44 cm away from the center point of the MOT. When the CCD chip receives the intensity $I_{\min} = 8 \times 10^{-6}$ mW/cm^2 of the 780 nm-fluorescence, a pixel of the CCD chip takes 1 count. Considering that fluorescence with the intensity $I_{\text{atom}} = 8 \times 10^{-10}$ mW/cm^2 comes from an atom to the CCD chip, we obtain the minimum detectable number $N_{\min} = I_{\min}/I_{\text{atom}} = 1 \times 10^4$. The condition that the ^{87}Rb atoms can be detected by the CCD camera is $N_{\text{cap}}^{\text{st}} \geq N_{\min}$. From eq. (3) with $r = 0.1$ mm, we obtain the minimum detectable flux intensity $F_{\min} = 2 \times 10^5$ atom/cm^2·s. This value is much smaller than the expected one of $F = 4 \times 10^{11}$ atom/cm^2·s obtained from the numerical simulations.[17] Taking the ratio of the cold-atom flux intensity to the minimum detectable one, we find that the detection sensitivity is 63 dB. Thus, even if we use a commonplace CCD camera, the accumulative method gives a high detection sensitivity.

The most popular method for detecting an atomic beam is to use a hot wire. If the work function of the wire metal is larger than the atomic ionization energy, the hot-wire detector using surface ionization has a high detection sensitivity for neutral atoms. However, since the surface ionization is not selective, the background noise is large even in ultrahigh vacuum, so that the signal-to-noise ratio is low compared to resonant detection methods. Although a micro-channel plate is also used for detection of an atomic beam, it is efficient for metastable atoms but inefficient for ground-state atoms used in the near-field optical manipulation we are developing. Two-step photoionization is one of the most elegant methods for resonant detection of ground-state atoms. However, it generally requires high-power laser light, for example, Ar-ion laser light with a power exceeding 1 W for ionization of Rb atoms. By contrast, the accumulative method using MOT allows a background-free resonant detection of ground-state cold atoms with low-power lasers such as diode lasers.

It takes about 1 ms for the detection MOT to capture atoms under our experimental conditions. On the other hand, as discussed above, the minimum detectable number is 1×10^4 for the CCD-camera observation. Consequently, the time resolution of this accumulative detection method is determined by the MOT time and the minimum detectable number. If the atomic flux intensity is sufficiently high, the atoms are detectable to the time resolution of 1 ms. As an example of time-resolution experiments using the accumulative detection method, let us consider measurement of the longitudinal velocity distribution of cold atoms by means of the time-of-flight method. From the Monte Carlo simulations, the mean longitudinal temperature of a cold Rb atomic beam generated through the near-field optical funnel is estimated to be 60 μK at the exit hole.[18] In the case where we take a long distance of 26 cm from the cold-atom source to the detection MOT, an atom with the initial velocity of 0 reaches down to the detection MOT after 230 ms, while an atom with the initial velocity equal to the root-mean-square velocity reaches down to the detection MOT faster by 10 ms. The time difference is sufficiently large for measuring the longitudinal velocity distribution of the cold atomic beam.

Incidentally, under the conditions given in §2, the ^{87}Rb atom with a velocity of 10 m/s can be trapped by the detection MOT. The velocity is obtained as the result of 5 m-free-fall. This corresponds to the flight time of 1 s. This indicates that the accumulative method allows the long-distance detection of cold atoms.

4. Summary

The MOT method enhances the detection sensitivity by accumulating atoms. Compared to the other ionization methods for detection of neutral atoms, it has a great advantage of efficiently detecting cold atoms in the ground state without a high-power laser. It is also effective when one requires a long distance from the atomic source to the detection region.

1) H. J. Metcalf and P. van der Straten: *Laser Cooling and Trapping* (Springer, New York, 1999).
2) S. Chu, L. Hollberg, J. E. Bjorkholm, A. Cable and A. Ashkin: Phys. Rev. Lett. **55** (1985) 48.
3) V. I. Balykin, V. S. Letokhov, Yu. B. Ovchinnikov and A. I. Sidorov: Phys. Rev. Lett. **60** (1988) 2137.
4) P. E. Moskowitz, P. L. Gould, S. R. Atlas and D. E. Pritchard: Phys. Rev. Lett. **51** (1983) 370.
5) C. Salomon, J. Dalibard, A. Aspect, H. Metcalf and C. Cohen-Tannoudji: Phys. Rev. Lett. **59** (1987) 1659.
6) M.-O. Mewes, M. R. Andrews, D. M. Kurn, D. S. Durfee, C. G. Townsend and W. Ketterle: Phys. Rev. Lett. **78** (1997) 582.
7) M. H. Anderson, J. R. Ensher, M. R. Matthews, C. E. Wieman and E. A. Cornell: Science **269** (1995) 198.
8) P. R. Berman: *Atom Interferometry* (Academic Press, New York, 1997).
9) M. Morinaga, M. Yasuda, T. Kishimoto, F. Shimizu, J. Fujita and S. Matsui: Phys. Rev. Lett. **77** (1996) 802.
10) G. Timp, R. E. Behringer, D. M. Tennant, J. E. Cunningham, M. Prentiss and K. K. Berggren: Phys. Rev. Lett. **69** (1992) 1636.
11) R. W. McGowan, D. M. Giltner and S. A. Lee: Opt. Lett. **20** (1995) 2535.
12) H. Ito and M. Ohtsu: *Near-Field Nano/Atom Optics and Technology*, ed. M. Ohtsu (Springer, Tokyo, 1998) Chap. 11.
13) H. Ito, K. Sakaki, W. Jhe and M. Ohtsu: Phys. Rev. A **56** (1997) 712.
14) E. L. Raab, M. Prentiss, A. Cable, S. Chu and D. E. Pritchard: Phys. Rev. Lett. **59** (1987) 2631.
15) J. Söding, R. Grimm and Yu. B. Ovchinnikov: Opt. Commun. **119** (1995) 652.
16) Yu. B. Ovchinnikov, I. Manek and R. Grimm: Phys. Rev. Lett. **79** (1997) 2225.
17) A. Takamizawa, H. Ito and M. Ohtsu: Jpn. J. Appl. Phys. **41** (2002) 6215.
18) A. Takamizawa, H. Ito and M. Ohtsu: Tech. Dig. I-512, 4th Pacific Rim Conference on Lasers and Electro-Optics, 2001, TuH2-1.
19) A. Steane, P. Szriftgiser, P. Desbiolles and J. Dalibard: Phys. Rev. Lett. **74** (1995) 4972.
20) J. Dalibard and C. Cohen-Tannoudji: J. Opt. Soc. Am. B **6** (1989) 2023.
21) D. S. Weiss, E. Riis, Y. Shevy, P. J. Ungar and S. Chu: J. Opt. Soc. Am. B **6** (1989) 2072.

APPLIED PHYSICS LETTERS VOLUME 82, NUMBER 10 10 MARCH 2003

A slit-type atom deflector with near-field light

Kouki Totsuka[a]
Japan Science and Technology Corporation, 684-1 Tsuruma, Machida, Tokyo 194-0004, Japan

Haruhiko Ito, Kiichi Suzuki, Kazuhiro Yamamoto, and Motoichi Ohtsu[b]
Interdisciplinary Graduate School of Science and Engineering, Tokyo Institute of Technology, 4259 Nagatsuta-cho, Midori-ku, Yokohama, Kanagawa 226-8502, Japan

Takashi Yatsui
Japan Science and Technology Corporation, 684-1 Tsuruma, Machida, Tokyo 194-0004, Japan

(Received 23 October 2002; accepted 16 January 2003)

We developed a near-field optical deflector for precise direction control of atomic motion using a dipole force. The blue-detuned, near-field light used to deflect atoms was generated near the edge of a 100-nm-wide slit and had a spatial distribution of 126 nm at a distance of 10 nm from the top edge. The deflection angle for a Rb atom was a function of light intensity, frequency detuning, and atomic velocity. © *2003 American Institute of Physics.* [DOI: 10.1063/1.1558222]

Atom optics deals with resonant interactions between light and atoms.[1] By focusing an atomic beam using atom-optical methods,[2] one can selectively deposit atom species on a substrate to make small structures.[3] However, the conventional methods using far-field light have limited spatial accuracy of atom control due to the diffraction limit, which is about half the wavelength of the light used. Consequently, it is difficult to move atoms to the exact position they are aimed at. It is also difficult to make arbitrary shapes using far-field light methods. Although lines and arrays have been produced,[4–11] dots have not been made using pure atom-optical methods. For optical nanofabrication, one can use near-field light, which is not affected by the diffraction limit. Such near-field light is generated at the nanometric aperture of a sharpened fiber probe.[12] Since near-field light decays as a Yukawa-type function,[13,14] it exerts a strong dipole force on atoms that is proportional to the spatial gradient of the light intensity.[15] Using the dipole force from nanometric near-field light, one can precisely control atomic motion beyond the diffraction limit.

We proposed atom manipulation using a fiber probe to produce so-called atomic quantum dots.[12] The feasibility of deflecting and trapping atoms with a fiber probe has been examined theoretically.[16,17] These atom manipulation techniques can be applied to atom-by-atom deposition. In this letter, we describe a scheme for deflecting atoms using blue-detuned, near-field light generated at a long, narrow slit. Like the fiber-probe method, a slit-type deflector also allows highly accurate atomic spatial control. In addition, it has the advantage of being able to deflect many atoms at once, so that it is easier to detect the deflected atoms than with a fiber probe. Consequently, it is useful for a demonstration of precise atom control with near-field light.

For high-density, high-speed recording/reading with near-field light, Yatsui *et al.* made a pyramidal silicon probe with a small aperture at the peak, which efficiently generated nanometric near-field light.[18] Considering this advantage, we fabricated a slit-type deflector from a pyramidal probe. Figure 1 illustrates the deflection of atoms using the slit-type deflector. A triangular-pillar structure is made on one side of the slit in order to introduce a light beam. Near-field light is generated at an edge of the slit by irradiating the back-side surface with a light beam. Atoms passing through the slit are deflected by the repulsive dipole force under blue-detuning conditions; the dipole force becomes repulsive when the light frequency exceeds the atomic resonance frequency (blue detuning), while it becomes attractive in the opposite case (red detuning). Atoms not entering the near-field light are blocked by the V-shaped groove in front of the slit, so that only deflected atoms leave the deflector.

We made a slit-type deflector with a slit 100 nm wide and 100 μm long by photolithography and anisotropic chemical etching of a (100)-oriented silicon-on-insulator substrate. A V-shaped groove on the (111) face was formed by anisotropic etching with 34-wt % KOH at a temperature of 80 °C. The groove was 10-μm deep, with a slope length of 14 μm, and an edge angle of 54.8°. Part of the Si and

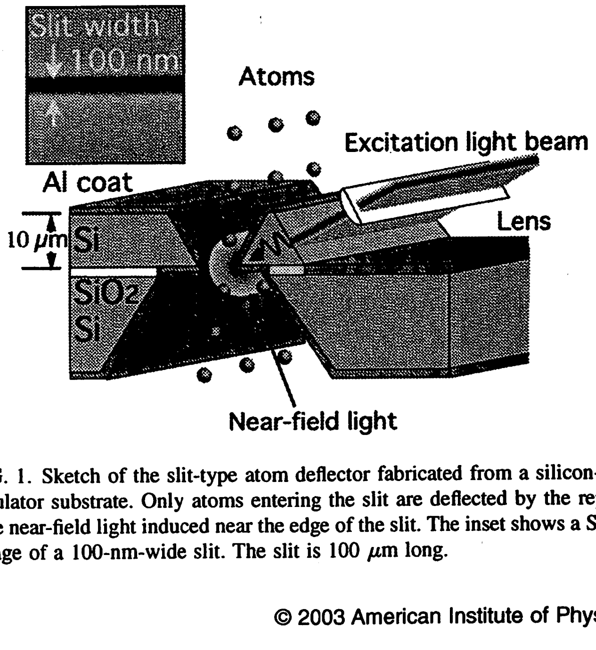

FIG. 1. Sketch of the slit-type atom deflector fabricated from a silicon-on-insulator substrate. Only atoms entering the slit are deflected by the repulsive near-field light induced near the edge of the slit. The inset shows a SEM image of a 100-nm-wide slit. The slit is 100 μm long.

---

[a] Electronic mail: ktotsu@ohtsu.jst.go.jp

[b] Also with: Japan Science and Technology Corporation, 684-1 Tsuruma, Machida, Tokyo 194-0004, Japan.

0003-6951/2003/82(10)/1616/3/$20.00

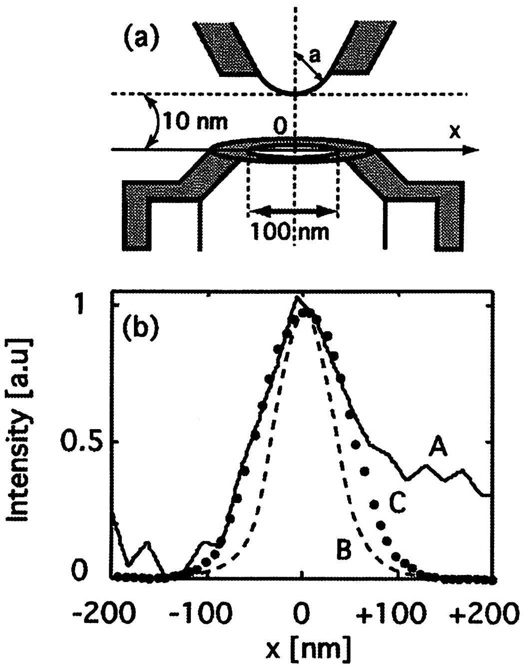

FIG. 2. (a) Measurement configuration of the light-intensity distribution near the slit edge with a 100-nm-aperture fiber probe. The scanning is performed along the x-axis 10 nm below the edge with radius a. (b) The solid curve (A) shows the experimental result, where a light beam with a wavelength of 780 nm is used for Rb-atom deflection. The broken (B) and dotted (C) curves show the numerical profiles when the aperture size is not convoluted and is convoluted, respectively. In the experimental case, a far-field component arises in the region exceeding +90 nm.

SiO_2 layers behind the slit on the output side was removed using KOH and buffered-hydrofluoric-solution etching. The residual Si layer supported the slit structure. An aluminum coating formed by vacuum deposition of aluminum metal on both sides of the slit edge perpendicular to the surface was used to suppress far-field light. The directional deposition leaves the incident surface for the excitation light beam and the top edge uncoated. In order to induce near-field light with a localization length equal to the slit width, we adjusted the radius of curvature of the top edge to 50 nm with a coat thickness of 40 nm.

Since the slit width and length are easily determined by controlling the etching time and the mask length used for photolithography, we can make smaller, shorter slits as needed. In this case, the slit width and length were determined so that the slit-type deflector could be combined with a slit-type atom detector that we developed.[19] The inset in Fig. 1 shows a scanning electron microscope (SEM) image of the slit in the deflector. Its 100-nm width equals the spatial resolution of the detector. The deviation of a Rb atom from the incident axis is estimated to exceed 10 μm under realistic conditions.[19] This indicates that the deflected atoms can be detected with a spatial uncertainty of less than 1%. By contrast, the detection efficiency depends on the slit length. When the slit length of the detector is the same as that of the deflector, the detection efficiency is estimated to exceed 10%,[19] if laser-cooled atoms are used.[20]

In order to examine the spatial distribution of the near-field light, we scanned the edge with a 100-nm-aperture fiber probe. As shown in Fig. 2(a), the origin of the x-axis denoting the scanning direction was taken as 10 nm from the top edge. For simplicity, we assume that the uncoated slit edge is approximately hemicylindrical with radius a.

The solid curve A in Fig. 2(b) shows the light-intensity profile produced by a light beam with a wavelength of 780 nm (for Rb-atom deflection), a power of 1 mW, and a spot diameter of 10 μm. Here, the light beam is polarized perpendicular to the slit-length direction, since there is no cutoff and near-field light is generated efficiently.[21] In this measurement, we remove the opposite part of the slit where the near-field light is not induced to facilitate probe scanning. The distribution length of the near-field light component was 180 nm, as estimated subsequently. However, note that this convolutes the size of the aperture. Incidentally, propagating far-field light appears in the outer region at a distance exceeding +90 nm. This is due to the imperfect metal coating of the bottom surface.

In order to evaluate the effective distribution length of the near-field light, we calculated the intensity profile using the phenomenological formula $I_{nf}(\mathbf{R})=I_{nf}(0)H(\mathbf{R})/H(\mathbf{0})$, where $H(\mathbf{R})=|\nabla\Psi(\mathbf{R})|^2+|\Psi(\mathbf{R})|^2/\Lambda^2$ with a Yukawa-type function $\Psi(\mathbf{R})=\int\exp(-|\mathbf{R}-\mathbf{R}'|/\Lambda)/|\mathbf{R}-\mathbf{R}'|dS$.[13] The coordinate vectors $\mathbf{R}$ and $\mathbf{R}'$ indicate the measurement point on the aperture of the probe and the source point on the slit edge, respectively, and the origin is at the top edge. The surface integral is made over the area $\pi a\times L$, where L is the excitation length equal to the spot diameter of the excitation light beam. For decay length $\Lambda=a=50$ nm, when we calculate $I_{nf}(\mathbf{R})$, we get curve B in Fig. 2(b). From the numerical result, the effective distribution length is estimated to be 126 nm, which is defined as the full width at the e^{-2} maximum. Moreover, integrating $I_{nf}=\int I_{nf}(\mathbf{R})dS$ over the aperture area $\pi\times 50^2$ nm^2, we get curve C in Fig. 2(b). This curve closely matches the experimental profile and the full width at the e^{-2} maximum is 180 nm.

Let us estimate the deflection angle for a Rb atom. The deflection angle θ of a ballistic atom is given by[22]

$$\theta=\pi-2b\int_{r_t}^{\infty}\frac{dr}{r^2}\left[1-\frac{b^2}{r^2}-\frac{U_{tot}(r)}{K_a}\right]^{-1/2}, \qquad (1)$$

where b, r_t, and K_a, are the impact parameter, turning point, and atomic kinetic energy, respectively. The distance r is measured from the center of the hemicylindrical slit edge. The total potential $U_{tot}(r)$ consists of the repulsive dipole-force potential $U_{dip}(r)$ given by[15]

$$U_{dip}(r)=\frac{1}{2}\hbar\delta\ln\left[1+\frac{I(r)}{I_s}\frac{\gamma^2}{4\delta^2+\gamma^2}\right], \qquad (2)$$

and the attractive van der Waals potential $U_{vdw}(r)$ given by[13]

$$U_{vdw}(r)=-\frac{1}{16(r-a)^3}\sum_j\frac{\hbar\gamma_j}{k_j^3}\frac{n_j^2-1}{n_j^2+1}, \qquad (3)$$

where δ is the detuning of the light frequency from the atomic resonance frequency. The natural linewidth γ and the saturation intensity I_s are $2\pi\times 6$ MHz and 1.6 mW/cm^2 for the Rb D_2 line, respectively. The van der Waals potential is summed over the allowed dipole transitions using the natural linewidth γ_j and the wave number k_j. The refractive index n_j of the slit edge is 3.7 for the 780-nm wavelength of the Rb D_2 line.

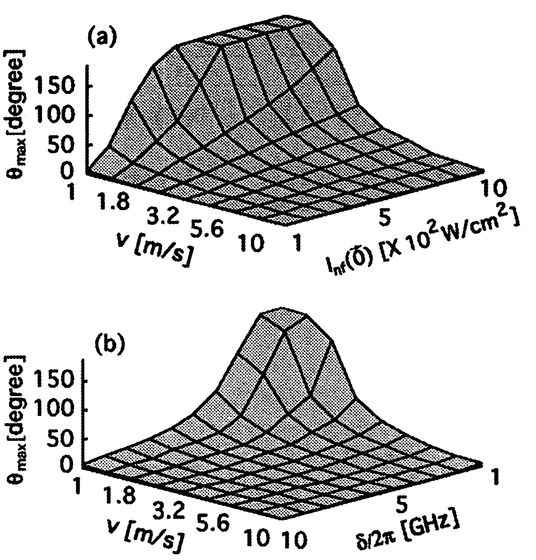

FIG. 3. The maximum deflection angle θ_{max} of a Rb atom (a) plotted as a function of the atomic velocity v and near-field-light intensity $I_{nf}(\mathbf{0})$ under the frequency detuning $\delta/2\pi=+1$ GHz and (b) plotted as a function of v and $\delta/2\pi$ for $I_{nf}(\mathbf{0})=10^3$ W/cm^2. The atomic velocity is log-plotted.

Figure 3(a) shows the maximum deflection angle θ_{max} plotted as a function of the atomic velocity v (log plot) and the near-field-light intensity $I_{nf}(\mathbf{0})$. For simplicity, instead of the exact Yukawa-type function, we use the approximation $I_{nf}(r)=I_{nf}(\mathbf{0})\exp[-(r-a)/1.6\times10^{-8}]$ with $\delta=+2\pi\times 1$ GHz. Since the throughput, which is defined as the ratio of the intensities of the output near-field light to the input far-field light, at the triangular pillar is about 1%, as the excitation-light power changes from 1 to 10 mW, the near-field light intensity changes from 10^2 to 10^3 W/cm^2. By contrast, slow atoms with a velocity of less than 10 m/s are easily generated with a magneto-optical trap. Such cold atoms are required for efficient interaction with nanometric near-field light. The maximum deflection angle θ_{max} increases as the intensity $I_{nf}(\mathbf{0})$ increases and also as the atomic velocity v decreases. When $I_{nf}(\mathbf{0})=5\times10^2$ W/cm^2, a Rb atom with $v=1$ m/s is retroreflected.

Figure 3(b) shows the maximum deflection angle θ_{max} plotted as a function of the atomic velocity v (log plot) and the frequency detuning $\delta/2\pi$ for $I_{nf}(\mathbf{0})=10^3$ W/cm^2. When the frequency detuning $\delta/2\pi$ changes from $+10$ to $+1$ GHz, the maximum deflection angle θ_{max} changes from 5.3° to 180° when $v=1$ m/s.

In summary, a slit-type deflector is useful for controlling the direction in which atoms are flying. The deflection direction can be changed with light intensity and frequency detuning over a wide range. The atom deflection technique will be used for optical deposition of neutral atoms and for detailed study of the interaction between atoms and near-field light.

[1] P. Meystre, *Atom Optics* (Springer, New York, 2001).
[2] V. I. Balykin and V. S. Letokhov, *Atom Optics with Laser Light* (Harwood Academic, Chur, Switzerland, 1995), chap. 4.
[3] H. Ito, K. Sakaki, M. Ohtsu, and W. Jhe, Appl. Phys. Lett. **70**, 2496 (1997).
[4] G. Timp, R. E. Behringer, D. M. Tnnant, J. E. Cunningham, M. Prentiss, and K. K. Berggren, Phys. Rev. Lett. **69**, 1636 (1992).
[5] M. Prentiss, G. Timp, N. Bigelow, R. E. Behringer, and J. E. Cunningham, Appl. Phys. Lett. **60**, 1027 (1992).
[6] J. J. McClelland, R. E. Scholten, E. C. Palm, and R. J. Celotta, Science **262**, 877 (1993).
[7] R. Gupta, J. J. McClelland, Z. J. Jabbour, and R. J. Celotta, Appl. Phys. Lett. **67**, 1378 (1995).
[8] R. W. McGowan, D. M. Giltner, and S. A. Lee, Opt. Lett. **20**, 2535 (1995).
[9] W. R. Anderson, C. C. Bradley, J. J. McClelland, and R. J. Celotta, Phys. Rev. A **59**, 2476 (1999).
[10] Th. Schulze, T. Müther, D. Jürgens, B. Brezger, M. K. Oberthaler, T. Pfau, and J. Mlynek, Appl. Phys. Lett. **78**, 1781 (2001).
[11] E. Jurdik, J. Hohlfeld, H. van Kempen, Th. Rasing, and J. J. McClelland, Appl. Phys. Lett. **80**, 4443 (2002).
[12] *Near-Field Nano/Atom Optics and Technology*, edited by M. Ohtsu (Springer, Tokyo, 1998).
[13] M. Ohtsu and H. Hori, *Near-Field Nano-Optics* (Kluwer/Plenum, New York, 1999), chap. 8.
[14] K. Kobayashi and M. Ohtsu, J. Microsc. **194**, 249 (1999).
[15] J. P. Dowling and J. Gee-Banacloche, Adv. At., Mol., Opt. Phys. **37**, 1 (1996).
[16] K. Kobayashi, S. Sangu, H. Ito, and M. Ohtsu, in *Near-Field Optics: Principles and Applications*, edited by X. Zhu and M. Ohtsu (World Scientific, Singapore, 2000), p. 82.
[17] K. Kobayashi, S. Sangu, H. Ito, and M. Ohtsu, Phys. Rev. A **63**, 013806 (2001).
[18] T. Yatsui, M. Kourogi, K. Tsutsui, M. Ohtsu, and J. Takahashi, Opt. Lett. **25**, 1279 (2000).
[19] K. Totsuka, H. Ito, T. Kawamura, and M. Ohtsu, Jpn. J. Appl. Phys. **41**, 1566 (2002).
[20] H. J. Metcalf and P. van der Straten, *Laser Cooling and Trapping* (Springer, New York, 1999).
[21] H. U. Danzebrink, Th. Dziomba, T. Sulzbach, O. Ohlsson, C. Lehrer, and L. Frey, J. Microsc. **194**, 335 (1999).
[22] R. G. Newton, *Scattering Theory of Waves and Particles*, 2nd ed. (Springer, New York, 1982).

PAPER *Special Issue on Near-Field Optics and Its Applications*

Fluorescence Spectroscopy of Rb Atoms with Two-Color Optical Near Fields for a High-Resolution Slit-Type Detector

Kouki TOTSUKA†a), **Haruhiko ITO**††, *and* **Motoichi OHTSU**†,††, ***Regular Members***

SUMMARY We introduce stepwise resonant excitation by two-color optical near fields in order to detect Rb atoms with a slit-type detector. Blue fluorescence of the second D_2 line is monitored for background-free detection. Feasibility of the method is shown from an experiment with a Rb vapor cell, where a sub-Doppler spectrum with the FWHM of 80 MHz is obtained. The detection efficiency is estimated at about 3% for cold Rb atoms.

key words: *optical near field, evanescent wave, atom detection, Rb atom spatial resolution*

1. Introduction

We are developing near-field optical methods of controlling gaseous atoms with high spatial accuracy far beyond the diffraction limit of light waves. The techniques, including atom deflection and atom trap by means of a fiber probe with a nanometric aperture for precise control of atomic motion and position [1], are expected to be applied to nanofabrication and atom-by-atom deposition. Note that it is difficult to make a nanometric structure of an arbitrary shape by using conventional atom-optical methods with propagation light [2], [3], because they suffer from the diffraction limit.

In our previous work [4], we have reported a new atom detector with a small slit. It utilizes the interaction between atoms and optical near fields generated on the slit, so that the spatial resolution is basically determined by the slit width. Now we are planning to detect Rb atoms deflected by the fiber probe. Since the interaction occurs in a nanometer region, cold atoms with very low speed are required for the sufficient interaction time. Such cold atoms are generated by well-known laser-cooling techniques [5]. In a typical case, a cold Rb atomic ensemble has a velocity distribution where the tail reaches 10 m/s. When the atom has a velocity of 10 m/s, the deflection angle is estimated to be about 0.1° under feasible experimental conditions. It leads to the displacement of 10 μm from the incident axis [4]. In order to resolve the atomic position with a spatial accuracy of 1%, we fabricate a slit width of 100 nm. Although there are a couple of popular methods with a microchannel plate or a secondary-electron multiplier for atom detection, the spatial resolution is only 1 μm at most [6]. In addition, they are effective for metastable atoms, while inefficient for ground-state atoms we manipulate.

We discussed a detection scheme using photoionization by two-color optical near fields in our previous paper [4]. In the scheme, the slit-type detector works as an atom ionizer and the ionized atoms are counted with a channel electron multiplier. The detection efficiency is estimated to be more than 10% for ground-state atoms. Moreover, thanks to the resonant character, we can detect atoms species- and state-selectively. However, a high power laser with several watts is used for efficient ionization of the ground-state atoms. Use of the intense laser beam may thermally damage the near-field optical device and also use of the additional ion detector complicates the vacuum chamber system.

In this paper, we describe an alternative spectroscopic method without intense laser beams for detecting Rb atoms with high spatial resolution. In this case, the Rb atoms are excited to the $5D_{5/2}$ state by two-color optical near fields, which are generated by two diode lasers with low intensities. The excited Rb atoms emit fluorescence with a wavelength of 420 nm and decay to the ground state. By monitoring the blue fluorescence different from the infrared excitation laser light, we can detect the Rb atoms without being disturbed by scattering light.

2. Method

Optical near fields generated on a planar surface, i.e. evanescent waves, have been employed for fluorescence and reflection-absorption spectroscopy of atoms near a surface [7]–[9]. They are also used for monitor of optically-thick atomic gas that totally absorbs resonant light and does not transmit it [10]. Recently, two-photon spectroscopy with evanescent waves has been studied both theoretically and experimentally [11]. Moreover, saturation-absorption spectroscopy has

---

Manuscript received May 7, 2002.
Manuscript revised July 31, 2002.

†The authors are with ERATO Localized Photon Project, Japan Science and Technology Corporation, Machida-shi, 194-8502 Japan.

††The authors are with Interdisciplinary Graduate School of Science and Engineering, Tokyo Institute of Technology, Yokohama-shi, 226-8502 Japan.

a) E-mail: ktotsu@ohtsu.jst.go.jp

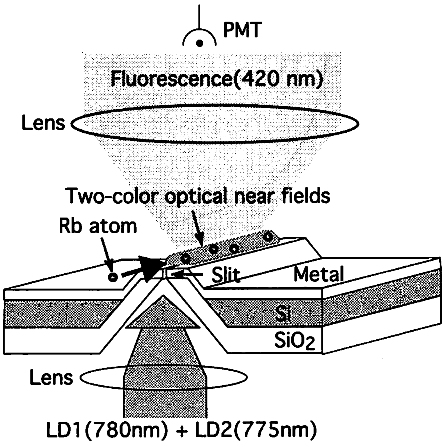

Fig. 1 Sketch of a slit-type atom detector fabricated from a silicon-on-insulator wafer with Si and SiO_2 layers. Two-color optical near fields are generated on a small-width slit by illuminating the V-groove with two diode-laser beams LD1 (780 nm) and LD2 (775 nm). Rb atoms are excited by the two-color optical near fields and detected by observing blue fluorescence with a wavelength of 420 nm.

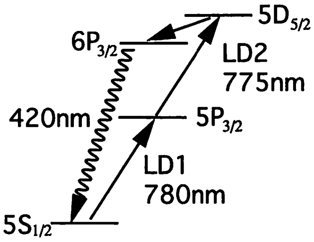

Fig. 2 Relevant energy levels of Rb. The first diode laser (LD1) with a wavelength of 780 nm excites Rb atoms from the $5S_{1/2}$ ground state to the $5P_{3/2}$ state and then the second diode laser (LD2) with a wavelength of 775 nm excites them to the $5D_{5/2}$ state. Part of the excited Rb atoms spontaneously fall into the $5S_{1/2}$ state by way of the $6P_{3/2}$ state, emitting fluorescence with a wavelength of 420 nm.

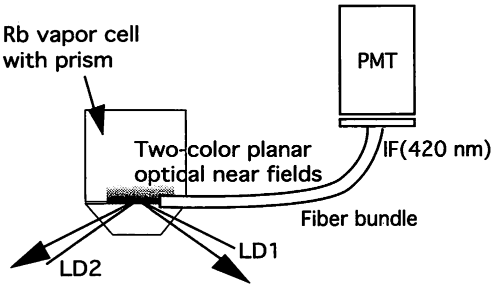

Fig. 3 Experimental setup with a Rb vapor cell. Total-internal reflection of two counterpropagating diode-laser beams LD1 and LD2 are made through a prism attached to a glass window, so that two-color planar optical near fields (evanescent waves) are generated in the vicinity of the inner wall surface. The incident angles of LD1 and LD2 are 43° and 53°, respectively. Fluorescence with a wavelength of 420 nm is collected by a fiber bundle and sent into a photomultiplier tube (PMT) with an interference filter (IF).

been applied to measurement of the pseudomomentum of evanescent waves [12], [13].

Here, we introduce a new method of two-step atomic excitation with two-color optical near fields generated on a small slit. Differently from the planar evanescent waves that the penetration depth is determined by the wavelength used, the localization length of the optical near field is comparable to the slit width. We apply this scheme to observation of Rb atoms with a slit-type detector.

Figure 1 is a sketch of the slit-type detector consisting of Si and SiO_2 layers. Two kinds of layer are required for fabrication of the small slit. The metal coating is made for suppression of far-field light. As reported already, we have fabricated a slit with a width of 70 nm and a length of 100 μm [4]. In order to increase the interaction chance, we make the length of the slit. Two-color optical near fields detecting atoms are generated on the slit by illuminating a V-groove from the back with two diode-laser beams LD1 and LD2: their wavelengths are 780 nm and 775 nm, respectively. The V-groove structure enables us to generate the optical near fields with high throughput, if we choose the polarization of the excitation light such that the direction is perpendicular to the slit [4].

The Rb atoms entering the near-field region are excited from the $5S_{1/2}$ ground state to the $5D_{5/2}$ state via the $5P_{3/2}$ state by the two diode-laser beams as shown in Fig. 2. The excited Rb atoms spontaneously decay to the $6P_{3/2}$ state or the $5P_{3/2}$ state in the branching ratio of 3 to 5 in a lifetime of 1.56 μs. Then, the Rb atoms in the $6P_{3/2}$ state spontaneously decay to one of the $5S_{1/2}$, $6S_{1/2}$, $4D_{5/2}$ and $4D_{3/2}$ states in a lifetime of 3.45 μs: the ratio of the $5S_{1/2}$ decay channel to the other channels is 1 to 4. When the Rb atoms transfer to the $5S_{1/2}$ state, they emit fluorescence with a wavelength of 420 nm. Considering the lifetimes and the branching ratios, we find that the blue-fluorescence emission takes place at a rate of $2.9 \times 10^5\,s^{-1}$. By observing the fluorescence, one can detect the small number of atoms avoiding the scattering light from the excitation LD beams.

3. Experiment with a Rb Vapor Cell

In order to show the feasibility of the atomic excitation with two-color optical near fields, we perform the fluorescence spectroscopy with a Rb vapor cell. Figure 3 shows the experimental setup. The Rb oven is heated up to 140°C. As shown in Fig. 3, the two-color optical near fields (evanescent waves) are generated through a prism attached to a cell window, where the two counterpropagating diode-laser beams LD1 and LD2 are coupled to the prism at incident angles of 43° and 53°, respectively. The blue-fluorescence photons are collected by a fiber bundle with an efficiency of 0.02. The collected signal is guided through the fiber bundle and a 420-nm interference filter (IF) with a bandwidth of

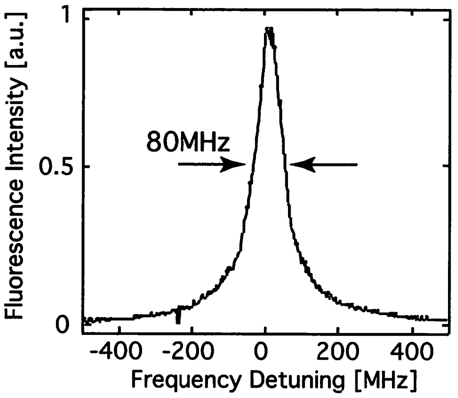

Fig. 4 Sub-Doppler spectrum of fluorescence with a wavelength of 420 nm. The intensity is plotted as a function of the frequency detuning of LD2, where LD1 is locked to the $5S_{1/2}$, $F = 3 \rightarrow 5P_{3/2}$, $F = 4$ hyperfine transition. The FWHM of the spectrum is 80 MHz.

7 nm to a photomultiplier tube (PMT).

Figure 4 shows the fluorescence spectrum plotted as a function of the frequency detuning of LD2, where the frequency of LD1 is locked to the $5S_{1/2}$, $F = 3 \rightarrow 5P_{3/2}$, $F = 4$ hyperfine transition. The linewidth of the diode-laser beams is below 1 MHz and the beam diameter is 2 mm. The intensities of LD1 and LD2 are 2.9 mW/cm^2 and 112 mW/cm^2, respectively. As seen in Fig. 4, the FWHM of the spectrum is 80 MHz. Note that it is narrower than the Doppler width of about 500 MHz. This comes from the experimental configuration where the two diode-laser beams counterpropagate. The sub-Doppler profile is determined by the natural linewidths of the relevant transitions and the time-of-flight broadening originating from that atoms traverse the near-field region.

4. Discussion

Our goal is the application of the fluorescence method to our slit-type detector. Let us estimate the detection rate of the slit-type detector for the Rb atom in the $5S_{1/2}$ ground state. If both Rabi frequencies of the $5S_{1/2} \rightarrow 5P_{3/2}$ and $5P_{3/2} \rightarrow 5D_{5/2}$ transitions are the same and much larger than the both natural linewidths, the atomic decay from the $5P_{3/2}$ state does not take place, so that the occupation probability of the $5D_{5/2}$ state becomes maximum, i.e. 0.5. Note that the $5P_{3/2}$ state is so-called dark state: since the density matrix elements with respect to the transitions from the $5S_{1/2}$ state and the $5D_{5/2}$ state are out of phase each other, the $5P_{3/2}$ state is not occupied due to the destructive interference [14]. In this case, the blue-fluorescence emission occurs most frequently. From the fact that the $5D_{5/2} \rightarrow 6P_{3/2} \rightarrow 5S_{1/2}$ decay takes place at a rate of $2.9 \times 10^5\,\mathrm{s}^{-1}$, it follows that the blue fluorescence occurs at a rate of $1.5 \times 10^5\,\mathrm{s}^{-1}$. Then, assuming that the collection efficiency of the fluorescence photons is 0.01 in the case of using a lens with an NA of more than 0.2, we find that the detection rate of the PMT with a quantum efficiency of 0.2 for 420 nm is $3 \times 10^2\,\mathrm{s}^{-1}$.

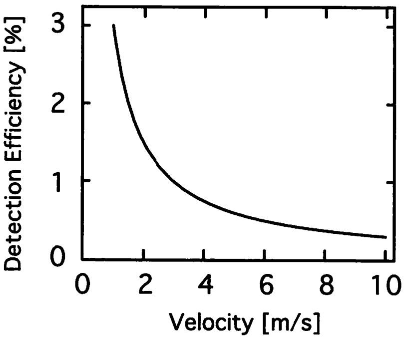

Fig. 5 Detection efficiency of Rb atoms plotted as a function of the atomic velocity in the case where the slit length is 100 μm.

We are planning to deflect a cold Rb atomic beam. In fact, we are making it with a near-field optical funnel [15]. Let us consider the case where the collimated atomic beam flies along the slit length of 100 μm. In this case, a Rb atom with a velocity of 10 m/s interacts with the optical near fields for 1×10^{-5} s. Therefore, the detection efficiency for the atom with the highest speed of the cold atomic beam is estimated to be 0.3%. Figure 5 shows the detection efficiency in the low-velocity region of Rb. The detection efficiency increases in proportion to interaction time with the optical near fields: it reaches about 3% for a velocity of 1 m/s.

5. Conclusion

We consider resonant excitation of Rb atoms with two-color optical near fields and application to a slit-type atom detector. From a demonstration experiment with a Rb vapor cell, we show the feasibility of the detection scheme with blue-fluorescence observation. Using this method, one can species- and state-selectively detect atoms with high spatial resolution. Although the detection efficiency is not necessarily high, it is sufficient for detection of cold atoms we are planning to manipulate.

References

[1] M. Ohtsu, ed., Near-Field Nano/Atom Optics and Technology, Chap. 11, Springer-Verlag, Tokyo, 1998.

[2] G. Timp, R.E. Behringer, D.M. Tennant, J.E. Cunningham, M. Prentiss, and K.K. Berggren, "Using light as a lens for submicron, neutral-atom lithography," Phy. Rev. Lett., vol.69, p.1636, 1992.

[3] J.J. McClelland, R.E. Scholten, E.C. Palm, and R.J. Celotta, "Laser-focused atomic deposition," Science, vol.262, p.877, 1993.

[4] K. Totsuka, H. Ito, T. Kawamura, and M. Ohtsu, "High spatial resolution atom detector with two-color optical near fields," Jpn. J. Appl. Phys., vol.41, p.1566, 2002.

[5] H.J. Metcalf and P. van der Straten, Laser Cooling and Trapping, Springer, New York, 1999.

[6] C. Kurtsiefer and J. Mlynek, "A 2-dimensional detector with high spatial and temporal resolution for metastable rare gas atoms," Appl. Phys. B, vol.64, p.85, 1997.
[7] A.L.J. Burgmans, M.F.H. Schuurmans, and B. Bölger, "Transient behavior of optically excited vapor atoms near a solid interface as observed in evanescent wave emission," Phys. Rev. A, vol.16, p.2002, 1977.
[8] P. Simoneau, S. Le Boiteaux, C.B. De Araujo, D. Bloch, J.R.R. Leite, and M. Ducloy, "Doppler-free evanescent wave spectroscopy," Opt. Commun., vol.59, p.103, 1986.
[9] D. Suter and J. Äbersold, "Evanescent wave spectroscopy of sublevel resonances near a glass/vapor interface," Opt. Commun., vol.84, p.269, 1991.
[10] P. Boissel and F. Kerherve, "Absorption de lumiere par des atomes dans une onde evanescente," Opt. Commun., vol.37, p.397, 1981.
[11] V.G. Bordo and H.G. Rubahn, "Two-photon evanescent-wave spectroscopy of alkali-metal atoms," Phys. Rev. A, vol.60, p.1538, 1999.
[12] T. Matsudo, H. Hori, T. Inoue, H. Iwata, Y. Inoue, and T. Sakurai, "Direct detection of evanescent electromagnetic waves at a planar dielectric surface by laser atomic spectroscopy," Phys. Rev. A, vol.55, p.2406, 1997.
[13] T. Matsudo, Y. Takahara, H. Hori, and T. Sakurai, "Pseudomomentum transfer from evanescent waves to atoms measured by saturated absorption spectroscopy," Opt. Commun., vol.145, p.64, 1998.
[14] M.O. Scully and M.S. Zubairy, Quantum Optics, Chap. 7, Cambridge University Press, U.K., 1997.
[15] H. Ito, K. Sakaki, W. Jhe, and M. Ohtsu, "Atomic funnel with evanescent light," Phys. Rev. A, vol.56, p.712, 1997.

Kouki Totsuka received the D.S. degree in physics from Shizuoka University, Shizuoka, Japan, in 1999. He has been a researcher of the "Localized Photon" project of ERATO (Exploratory Research for Advanced Technology), JST (Japan Science and Technology Corporation), Japan. He is engaged in atom manipulation with optical near fields and its application to atom photonics. He is a member of the Physical Society of Japan, the Japan Society of Applied Physics.

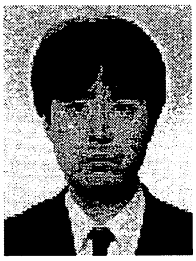

Haruhiko Ito was born in Yokkaichi, Japan, in 1961. He received the D.S. degree in physics from Kyoto University, Kyoto, Japan, in 1994. He joined the Kanagawa Academy of Science and Technology, Japan, in 1994. Since 1999, he has been an Associate Professor at the Interdisciplinary Graduate School of Science and Engineering, Tokyo Institute of Technology, Yokohama, Japan. His current research interests include atom manipulation with optical near fields and its application to atom photonics. Dr. Ito is a member of the Physical Society of Japan, the Japan Society of Applied Physics, and the American Physical Society. He has been received the Paper Award of JPS in 1997 and the Marubun Academic Award in 2000.

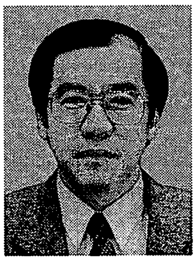

Motoichi Ohtsu received the B.E., M.E., and Dr.E. degrees in electronics engineering from the Tokyo Institute of Technology, Tokyo, Japan, in 1973, 1975, and 1978, respectively. In 1978, he was appointed a Research Associate, and in 1982, he became an Associate professor at the Tokyo Institute of Technology. From 1986 to 1987, while on leave from the Tokyo Institute of Technology, he joined the Crawford Hill Laboratory, AT&T Bell Laboratories, Holmdel, NJ. In 1991, he became a Professor at the Tokyo Institute of Technology. Since 1993, he has been concurrently the Leader of the "Photon Control" project of the Kanagawa Academy of Science and Technology, Kanagawa, Japan. Since 1998, he has been concurrently the Leader of the "Localized Photon" project of ERATO (Exploratory Research for Advanced Technology), JST (Japan Science and Technology Corporation), Japan. He has written over 320 papers and received 87 patents. He is the author and co-author of 39 books, including seven in English, entitled Highly Coherent Semiconductor Lasers (Artech House, Boston, 1991), Coherent Quantum Optics and Technology (Kluwer, Dordrecht, 1993), Frequency Control of Semiconductor Lasers (Wiley Interscience, New York, 1996), Near-Field Nano/Atom Optics and Technology (Springer Verlag, Berlin, 1998), Near-Field Nano-Optics (Kluwer Academic/Plenum Publishers, New York, 1999), Optical and Electronic Properties of Nano-matters (Kluwer Academic/KTK Scientific Publishers, Dordrecht/Tokyo, 2001), and Progress in Nano Electro-Optics (Springer Verlag, Berlin, 2002). In 1999, he was the Vice-President of the IEEE/LEOS Japan Chapter, and in 2000, he was appointed as the President. From 2000, he is an executive director of the Japan Society of Applied Physics. He served as a Technical Program Co-chair for the 4th Pacific Rim Conference on Lasers and Electro-Optics (CLEO/PR01), 2001. He has been a tutorial lecturer of the SPIE and the OSA. His main fields of interests are the nano-photonics and atom-photonics. Dr. Ohtsu is a member of the Japan Society of Applied Physics, the Institute of Electrical Engineering of Japan, the Optical Society of America, and American Physical Society. He has been awarded ten prizes from academic institutions, including the Issac Koga Gold Medal of URSI (International Union of Radio Science) in 1984, the Japan IBM Science Award in 1988, two awards from the Japan Society of Applied Physics in 1982 and 1990, and the Inoue Science Foundation Award in 1999.

Jpn. J. Appl. Phys. Vol. 41 (2002) pp. 6215–6218
Part 1, No. 10, October 2002

Multireflection of Cold Atoms in a Near-Field Optical Funnel

Akifumi TAKAMIZAWA[1], Haruhiko ITO[1] and Motoichi OHTSU[1,2]

[1]*Interdisciplinary Graduate School of Science and Engineering, Tokyo Institute of Technology, 4259, Nagatsuta, Midori-ku, Yokohama 226-8502, Japan*
[2]*ERATO, Japan Science and Technology Corporation, 687-1 Tsuruma, Machida 194-0004, Japan*

(Received May 29, 2002; accepted for publication July 10, 2002)

Multireflection of cold Rb atoms occurs inside a reversed triangular hollow prism with a blue-detuned optical near field. We examine it with a probe light beam, using the frequency detuning and the diameter of an excitation light beam as parameters. In the first bounce, the number density of the reflected atoms reaches a maximum of 10^6 atom/cm^3 at a blue detuning of 0.7 GHz when the beam diameter is 4 mm. The Rb atoms repeat reflection with a period of about 15 ms and an efficiency of 83% per bounce. A cold Rb atomic beam with a high flux of 4×10^{11} atom/(cm^2·s) can be generated through a near-field optical funnel composed of the prism. [DOI: 10.1143/JJAP.41.6215]

KEYWORDS: optical near field, atom reflection, atom funnel, cold atomic beam, dipole force

1. Introduction

An optical near field generated on a prism surface, so-called evanescent light, exerts a repulsive dipole force on atoms when the frequency is slightly higher than an atomic resonant one, which is called blue detuning, and can reflect them approaching the surface. The atom mirror has been used for isotope separation[1)] and detection of van der Waals force on a ground-state atom.[2)] Multireflection of cold Cs atoms falling out of a magneto-optical trap (MOT) has also been observed.[3)] A gravitational cavity with an atom mirror[4)] and an atom resonator made up of two atom mirrors for an atom laser[5)] have been proposed. In addition to the planar atom mirror, a cylindrical optical near field generated in a hollow fiber can be used as a tunnel mirror for guiding atoms.[6,7)] In fact, Rb atoms have been successfully guided through a small hollow glass fiber supported by a blue-detuned optical near field.[8,9)]

We are planning to generate a cold atomic beam with a funnel-shaped optical near field.[10)] Figure 1 schematically shows the atom funnel. Cold atoms are produced using an MOT[11)] in a reversed conical or triangular hollow prism with a small exit hole at the bottom, and then released from the trap. When an optical near field is excited on the inner-wall surface by a blue-detuned doughnut light beam[12)] shone upward, the falling atoms are reflected in the vicinity of the inner wall due to the repulsive dipole force. Moreover, regarding an alkali-metal atom such as Rb, which forms the Λ-type three-level system between two hyperfine ground states and an excited state, if the excitation doughnut light beam is blue-detuned with respect to both ground states and a weak pump beam that compels the atom to be in the lower ground state at the beginning of reflection is shone downward, the atom loses its kinetic energy at every reflection (Sisyphus cooling).[13,14)] As a result of repetition of reflection and cooling, many atoms are collected at the bottom and go out of the hole. Multiloading of cold atoms from the MOT to the funnel results in the generation of a cold atomic beam with high flux. Such a cold atomic beam is necessary for atom manipulation with high spatial accuracy using nanometric optical near fields.[15)]

The highest atom flux is obtained under a maximum reflection efficiency of the cold atoms. The strength of the dipole force and the height of the potential that dominate reflection depend on the frequency detuning and the intensity of the excitation light beam.[16)] If the blue detuning is too small or too large, the repulsive potential decreases, so that it cannot reflect atoms. Also, heating of atoms due to spontaneous emission of photons can take place in the case of small detuning. On the other hand, as the beam diameter becomes larger, the near-field area that can be excited becomes wider, so that more atoms can be collected. However, since the light power is limited, it reduces the light intensity and then the repulsive potential.

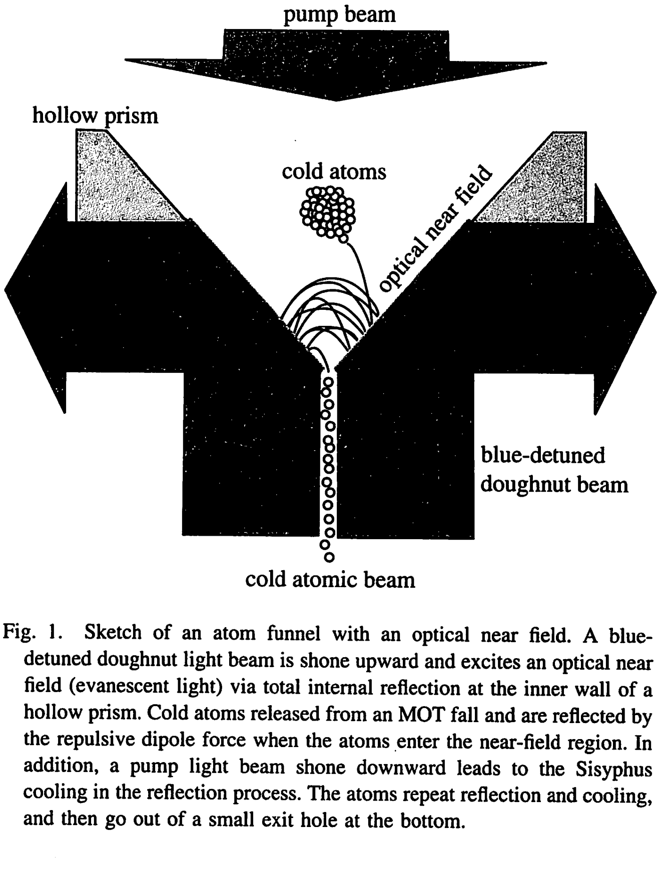

Fig. 1. Sketch of an atom funnel with an optical near field. A blue-detuned doughnut light beam is shone upward and excites an optical near field (evanescent light) via total internal reflection at the inner wall of a hollow prism. Cold atoms released from an MOT fall and are reflected by the repulsive dipole force when the atoms enter the near-field region. In addition, a pump light beam shone downward leads to the Sisyphus cooling in the reflection process. The atoms repeat reflection and cooling, and then go out of a small exit hole at the bottom.

In this paper, we examine the dependence of the atom-reflection efficiency on the frequency detuning and the diameter of the excitation light beam, and determine the optimum blue detuning and beam diameter for the atom funnel. In §2, we describe an experiment of the observation of multireflection of cold Rb atoms by monitoring the absorption of a probe light beam introduced along the thalweg of a reversed triangular prism. Number density of

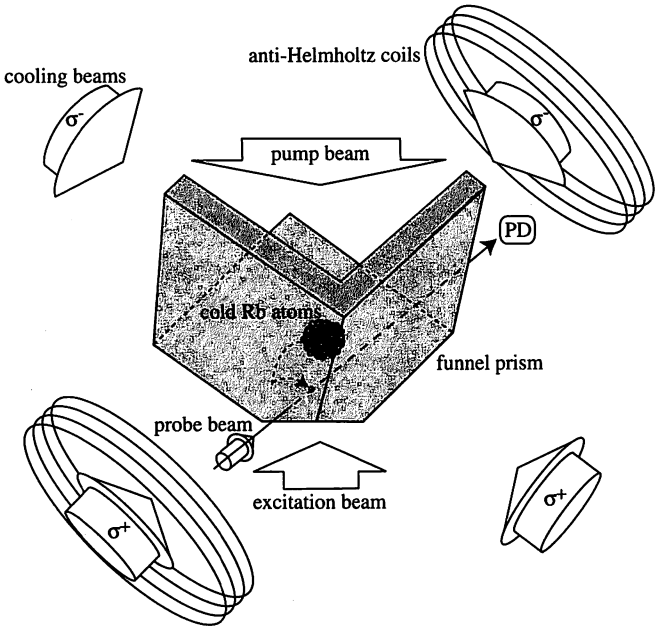

Fig. 2. Experimental configuration for absorption measurement with a probe light beam. The funnel prism with an exit hole of 200 μm is made by combining three square glass plates, and is illuminated with a blue-detuned Gaussian light beam with a power of 590 mW so that the repulsive optical near field that reflects atoms is generated on the inner-wall surface. The probe light beam with a power of 1.4 μW and a diameter of 1 mm is incident along the thalweg of the funnel prism at a height of 2.5 mm above the exit hole, and the absorption change due to ^{85}Rb atoms is monitored with a photodiode (PD). The spherical cold ^{85}Rb atom ensemble produced by the MOT is centered at a height of 5 mm above the exit hole and is cooled to 13 μK by means of the polarization gradient cooling. A pump light beam with an intensity of 5 mW/cm^2 is shone downward for pumping of the ^{85}Rb atoms to the $5S_{1/2}$, $F = 3$ upper ground state. The bottom plane of the funnel prism is an equilateral triangle with a side of 12.8 mm.

the reflected atoms is plotted as a function of the blue detuning for three excitation-beam diameters. After a discussion in §3, we remark a conclusion in §4.

2. Experiment

In order to detect cold ^{85}Rb atoms reflected inside the near-field optical funnel, we observe the absorption change of a probe light beam tuned to the resonant wavelength of 780 nm. Figure 2 shows the experimental configuration. The funnel optics, hereafter called funnel prism, consists of three square quartz glass plates combined at right angles each other: the refractive index $n = 1.45$, and the side and the thickness of the plate are 25 mm and 3 mm, respectively. It is placed in a vacuum chamber under a pressure of 5×10^{-8} Torr, in which the orifice is directed upward. Three circularly-polarized light beams are incident through each glass plate and an MOT is formed within the upper part, while the bottom corner is ground flat and a small hole with a diameter of 200 μm is made in the center. The lower part works as a triangular funnel, illuminated with a Gaussian light beam from a Ti:Al$_2$O$_3$ laser with wavelength $\lambda = 780$ nm and a power of 590 mW. The frequency is blue-detuned between 0.4 GHz and 2 GHz with respect to the transition frequency between the $5S_{1/2}$, $F = 3$ and $5P_{3/2}$, $F = 4$ states. Note that the excitation light beam propagates in the glass plates upward by repeating total internal reflection, and the optical near field is generated on the inner-wall surface. From the incident angle $\theta = 55°$, the decay length of the optical near field[17)]

$$\eta = \frac{\lambda}{2\pi\sqrt{n^2 \sin^2\theta - 1}} \tag{1}$$

is estimated to be 190 nm. Incidentally, the upper edge of the funnel prism is opaque so that the excitation light beam is blocked.

A diode-laser beam with a power of 10 mW and a diameter of 10 mm is divided into the three circularly-polarized light beams. The three light beams and their retroreflection beams are used as cooling light for the MOT, where the frequency is red-detuned by 10 MHz with respect to the transition frequency between the $5S_{1/2}$, $F = 3$ upper ground state and the $5P_{3/2}$, $F = 4$ excited state of the ^{85}Rb hyperfine structure. Repumping light beams tuned to the transition between the $5S_{1/2}$, $F = 2$ lower ground state and the $5P_{3/2}$, $F = 3$ excited state are superimposed over the cooling light beams. By applying a quadrupole magnetic field with a gradient of 10 G/cm using a pair of anti-Helmholtz coils, a cold ^{85}Rb atom ensemble composed of 10^6 atoms, whose diameter is 1.5 mm, is produced at a height of 5 mm above the exit hole. Next, decreasing the power of the cooling light to 30% as well as changing the red detuning to 90 MHz after turning off the quadrupole magnetic field, we perform the polarization gradient cooling[18)] and cool the ^{85}Rb atoms to a temperature of 13 μK. Then, the cooling and repumping light beams are turned off, and the cold atoms fall into the funnel prism.

As shown in Fig. 2, a probe light beam with a diameter of 1 mm and a power of 1.4 μW is incident along the thalweg of the funnel prism at a height of 2.5 mm above the exit hole. The frequency modulation of 30 kHz with an amplitude of three times larger than the natural linewidth $\gamma/2\pi = 6.1$ MHz of the $5P_{3/2}$ state is applied to the probe light beam at the transition frequency between the $5S_{1/2}$, $F = 3$ and $5P_{3/2}$, $F = 4$ states. The modulated absorption signal of the probe light beam is detected with a lock-in-amplifier. Moreover, an additional light beam with an intensity of 5 mW/cm^2, which is tuned to the $5S_{1/2}$, $F = 2 \rightarrow 5P_{3/2}$, $F = 3$ transition, illuminates the whole funnel prism, and pumps the ^{85}Rb atoms in the lower ground state to the upper ground state. Note that, since the Sisyphus cooling does not take place in this case, we can observe the pure reflection process.

The repulsive dipole-force potential for reflection is approximately given by

$$U = \frac{1}{8}\frac{I}{I_s}\frac{\hbar\gamma^2}{\delta}, \tag{2}$$

where δ, I, and $I_s = 1.6$ mW/cm^2 are the frequency detuning, the light intensity, and the saturation intensity, respectively. Considering the attractive van der Waals force from the glass plates, we calculate the reflection potential to be 1 mK in terms of temperature in the case of $\delta/2\pi = +1$ GHz.[10)]

Figure 3 shows the number density of the reflected atoms plotted as a function of the time t after release from the MOT, where the blue detuning and the beam diameter of the excitation light beam are 0.7 GHz and 4 mm, respectively. The latter is given as fullwidth at e^{-2} maximum in the

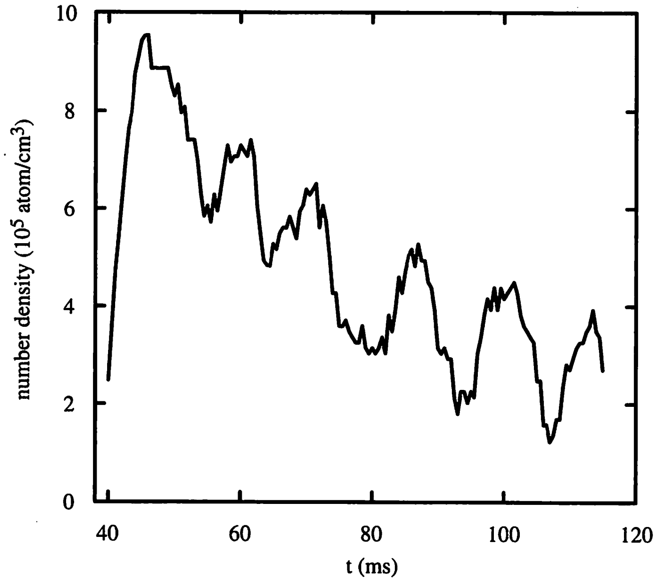

Fig. 3. Multireflection of ^{85}Rb atoms inside the funnel prism. The number density of the reflected atoms is plotted as a function of the time t after release from the MOT, where the blue detuning and the beam diameter of the excitation light beam are 0.7 GHz and 4 mm, respectively. The number density is derived by subtracting the value in the case where the optical near field is not excited from that in the case where the optical near field is excited. The first reflection occurs after $t = 40$ ms.

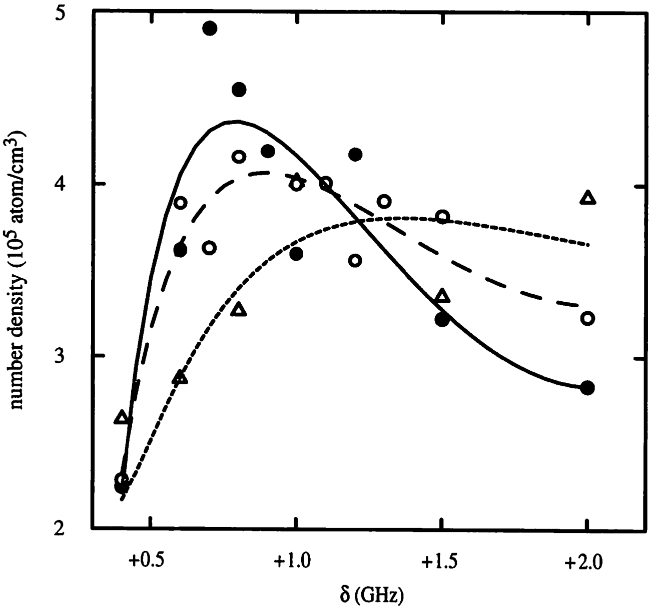

Fig. 4. Number density of the reflected atoms plotted as a function of the frequency detuning δ, where the time average is taken over 40 ms $< t <$ 115 ms. The open circles (broken curve), the filled circles (solid curve), and the open triangles (dotted curve) show the number densities for beam diameters of 3 mm, 4 mm, and 5 mm, respectively.

intensity profile. Note that the Rb atoms arrive on the funnel-prism wall at about $t = 30$ ms. Here, the number density of the reflected atoms is determined as follows. First, the total atom number is estimated from the absorption quantity of the probe light beam. Then, since the observed atoms are contained in a volume given by multiplying the probe-beam cross section of $\pi(0.5)^2$ mm^2 by the probe-beam propagation length of 5 mm, the total number density is derived by dividing the total atom number by the volume. Finally, the reflected-atom number density is obtained by subtracting the value for the case without the excitation light beam from the total number density. In Fig. 3, we find that the Rb atoms bounce many times with a period of about 15 ms. The reflected-atom number density has a maximum of 10^6 atom/cm^3 in the first bounce, and then decreases with a constant rate every bounce. From the ratio of two successive peak values, we obtain the reflection efficiency of 83% per bounce.

Figure 4 shows the number density of the reflected atoms plotted as a function of the frequency detuning δ in three cases where the beam diameter is 3 mm (open circles), 4 mm (filled circles), and 5 mm (open triangles). Here, the number density is time-averaged over 40 ms $< t <$ 115 ms. The broken, solid, and dotted curves are fitted for the beam diameters of 3 mm, 4 mm, and 5 mm, respectively. From Fig. 4, we find that the most efficient reflection of the ^{85}Rb atoms occurs when the blue detuning is 0.7 GHz and the beam diameter is 4 mm.

3. Discussion

There is an optimum blue detuning at which the reflection efficiency is maximum. The dipole-force potential has a dispersion characteristic with respect to the atomic resonant frequency and is maximum at a blue detuning, which shifts to the higher side as the light intensity becomes stronger. Although the reflected atom moves in the direction of the velocity vector, the probability that it flies to the area with no optical near field increases as the excitation-beam diameter decreases. On the other hand, the intensity of the optical near field decreases as the excitation-beam diameter becomes larger, so that the repulsive potential becomes lower and it reduces the upper limit of the atomic kinetic energy possible to reflect. The atoms that bounce to the outside of the area with the repulsive optical near field and those that hit the glass surface without reflection and are adsorbed there contribute to the reflection loss. The decrease in the atom number at every reflection in Fig. 3 is due to such reflection loss. Note that, because there is no cooling process in this experiment, there is little probability that the reflected atom falls into the minute exit hole at the bottom of the funnel prism, so that the loss due to escape from the hole is negligible. In addition to the atoms reflected on the two glass plates on both sides of the probe light beam, the atoms reflected on the third glass plate can contribute to the atom number shown in Fig. 3. The peaks appearing with a period of 15 ms originate from the complex motion of those atoms.

On the other hand, the optimum beam diameter depends on the light power, the size and the mean temperature of the cold atom ensemble, and the height at which the cold atom ensemble is made. Note that the height is an important factor because the atoms are accelerated by gravity. In general, a larger beam diameter can be used for a higher light power. The optimum beam diameter is chosen according to the spatial and velocity distributions of the incident atoms. If the light intensity is too strong, the probability that undesirable spontaneous emission occurs increases, so that the atoms are heated or transferred to the level at which the reflection potential is low. These result in a decrease of the reflection efficiency. If a higher excitation light power is used and then a larger beam diameter is used, the reflection efficiency can be higher under a suitable blue detuning.

When the Sisyphus cooling is carried out, the atoms falling from MOT are collected at the bottom of the funnel prism and then exit through the small hole. In contrast to the other methods, for example, boosting atoms from an MOT with a laser beam[19] or a two-dimensional MOT funnel,[20,21] the near-field optical funnel can generate a CW cold atomic beam by multiloading of cold atoms from the MOT to the funnel. From the Monte Carlo simulation in the case where the blue detuning is 0.7 GHz and the beam diameter is 4 mm, following the procedure described in ref. 10, we estimate the ^{85}Rb atom flux coming out of the reversed triangular funnel with an exit hole of 200 μm to be 4×10^{11} atom/(cm^2·s). It is a sufficient value for the atom-manipulation experiments with nanometric optical near fields.[15]

4. Conclusion

In the near-field optical funnel, multireflection of cold atoms arises and funneling efficiency depends on reflection efficiency. For a given excitation light power and MOT conditions, there are a blue detuning and an excitation-beam diameter that maximize the reflection efficiency. By choosing optimum blue detuning and beam diameter suitable for an experimental situation, one can produce a high-flux cold atomic beam. Such a cold atomic beam will be applied to the near-field optical manipulation with a nanometric fiber probe, including precise atom deflection and single-atom trapping.

1) V. I. Balykin, V. S. Letokhov, Yu. B. Ovchinnikov and A. I. Sidorov: Phys. Rev. Lett. **60** (1988) 2137.
2) A. Landragin, J.-Y. Courtois, G. Labeyrie, N. Vansteenkiste, C. I. Westbrook and A. Aspect: Phys. Rev. Lett. **77** (1996) 1464.
3) C. G. Aminoff, A. M. Steane, P. Bouyer, P. Desbiolles, J. Dalibard and C. Cohen-Tannoudji: Phys. Rev. Lett. **71** (1993) 3083.
4) H. Wallis, J. Dalibard and C. Cohen-Tannoudji: Appl. Phys. B **54** (1992) 407.
5) G. Lenz, P. Meystre and E. M. Wright: Phys. Rev. A **50** (1994) 1681.
6) H. Ito, K. Sakaki, T. Nakata, W. Jhe and M. Ohtsu: Opt. Commun. **115** (1995) 57.
7) H. Ito, K. Sakaki, T. Nakata, W. Jhe and M. Ohtsu: Ultramicroscopy **61** (1995) 91.
8) M. J. Renn, E. A. Donley, E. A. Cornell, C. E. Wieman and D. Z. Anderson: Phys. Rev. A **53** (1996) R648.
9) H. Ito, T. Nakata, K. Sakaki, M. Ohtsu, K. I. Lee and W. Jhe: Phys. Rev. Lett. **76** (1996) 4500.
10) H. Ito, K. Sakaki, W. Jhe and M. Ohtsu: Phys. Rev. A **56** (1997) 712.
11) E. L. Raab, M. Prentiss, A. Cable, S. Chu and D. E. Pritchard: Phys. Rev. Lett. **59** (1987) 2631.
12) A. Takamizawa, H. Ito and M. Ohtsu: Jpn. J. Appl. Phys. **39** (2000) 6737.
13) J. Söding, R. Grimm and Yu. B. Ovchinnikov: Opt. Commun. **119** (1995) 652.
14) Yu. B. Ovchinnikov, I. Manek and R. Grimm: Phys. Rev. Lett. **79** (1997) 2225.
15) H. Ito and M. Ohtsu: *Near-Field Nano/Atom Optics and Technology*, ed. M. Ohtsu (Springer, Tokyo, 1998) Chap. 11.
16) J. P. Dowling and J. Gea-Banacloche: *Advances in Atomic, Molecular, and Optical Physics*, eds. B. Bederson and H. Walther (Academic Press, San Diego, 1996) Vol. 37, p. 1.
17) S. Feron, J. Reinhardt, M. Ducloy, O. Gorceix, S. Nic Chormaic, Ch. Miniatura, J. Robert, J. Baudon, V. Lorent and H. Haberland: Phys. Rev. A **49** (1994) 4733.
18) J. Dalibard and C. Cohen-Tannoudji: J. Opt. Soc. Am. B **6** (1989) 2023.
19) Z. T. Lu, K. L. Corwin, M. J. Renn, M. H. Anderson, E. A. Cornell and C. E. Wieman: Phys. Rev. Lett. **77** (1996) 3331.
20) K. Dieckmann, R. J. C. Spreeuw, M. Weidemüller and J. T. M. Walraven: Phys. Rev. A **58** (1998) 3891.
21) S. Weyers, E. Aucouturier, C. Valentin and N. Dimarcq: Opt. Commun. **143** (1997) 30.

Deflecting, detecting, and funneling atoms using near-field light

Kouki Totsuka*, Haruhiko Ito*, **, Akifumi Takamizawa, Kazuhiro Yamamoto**, Motoichi Ohtsu*,****
** ERATO Localized Photon Project, Japan Science and Technology Corporation, 684-1 Tsuruma, Machida, Tokyo 194-0004, Japan*
ktotsu@ohtsu.jst.go.jp
*** Interdisciplinary Graduate School of Science and Engineering, Tokyo Institute of Technology, 4259 Nagatsuta-cho, Midori-ku, Yokohama, Kanagawa 226-8502, Japan*

Atom optics using nanometric near field light allows us control of atoms with high spatial accuracy beyond the diffraction limit. It can be applied to new optical nanofabrication like atom-by-atom deposition. To this end, we developed a slit-type atom deflector that sends atoms at the aimed point on a substrate. In addition, we made a multi-slit atom detector with high spatial resolution. For the atom deflection by near-field light, a cold atomic beam is required. We generated it with an atom funnel composed of evanescent-light mirrors.

Figure 1 shows the configuration of atom deflection. A slit-type deflector is fabricated from a silicon-on-insulator wafer by photolithography and anisotropic etching [1]. Repulsive near-field light deflecting atoms is generated at the top of triangular-pillar part of the 100-nm-wide slit (see the upper inset) by irradiating the backside with a blue-detuned light beam. Atoms not entering the near-field region are blocked by the V groove of the input side. The deflected atoms are observed with a multi-slit detector (see the lower inset) using two-step photoionization induced by two-color near-field light. For Rb atoms, two-color near-field light is generated by a 780-nm diode-laser beam tuned to the $5S_{1/2}$ - $5P_{3/2}$ transition and a 476.5-nm Ar-ion laser beam. The ionized atoms are counted by a channel electron multiplier (CEM) applied a negative bias. We are planning to make the multi-slit such that the individual width is 100 nm. In this case, a Rb atom deviated by 10 μm at the deflection angle of 0.1 degree can be detected with a spatial accuracy of 1 %. The slit length is taken to be 100 μm, which is the same as that of the deflector, so that the detection efficiency is estimated to be about 10 % for laser-cooled atoms [2].

For efficient interaction with nanometric near-field light, atomic source should be dense and cold. For this purpose, we made a cold atomic beam by a near-field optical funnel [3]. Figure 2 shows the cross-section, where repulsive evanescent light reflecting Rb atoms falling from a magneto-optical trap (MOT) is generated via total-internal reflection of a blue-detuned hollow light beam (see the inset) in the inner wall. The cold Rb atoms are collected at the bottom after the Sisyphus cooling induced by a pumping light to the lower ground state, and come out of the small exit hole. The generated cold atomic beam is confined and guided by the hollow light beam. To show the feasibility, we performed the hollow-beam guiding of Rb atoms with a mean temperature of 10 μK from a MOT over a long distance of 26 cm. The guiding efficiency was 21% when the Sisyphus cooling is also made inside the guiding beam. The atom flux obtained by the funnel is estimated to be about 10^{13} cm^{-2}s^{1}.

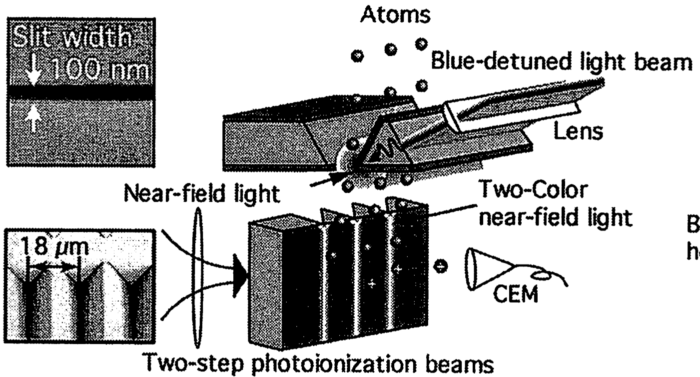

Fig. 1 Slit-type atom deflector and multi-slit atom detector. The upper and lower insets are SEM pictures of deflector slit and detector slits, respectively.

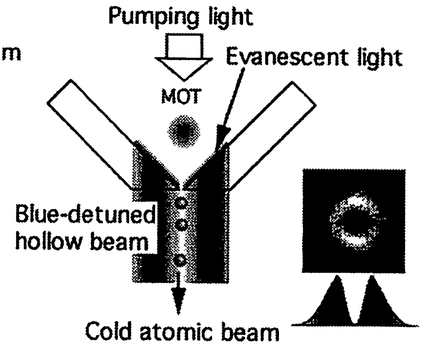

Fig. 2 Generation of a cold atomic beam by a near-field optical funnel. The inset shows a CCD camera image of a hollow-beam cross-section.

[1] K. Totsuka *et al.*, "Atom deflector with optical near fields", Technical Digest of QELS 2002, 66(Long Beach, CA, USA).
[2] K. Totsuka et al., "High spatial resolution atom detector with two-color optical near fields", Jpn. J. Appl. Phys. **41**, 1566(2002).
[3] H. Ito et al., "Atomic funnel with evanescent light," Phys. Rev. A **56**, 712 (1997).

Cold-atom funnel using near-field light

Akifumi Takamizawa[1], Haruhiko Ito[1], Shungo Yamada[1], and Motoichi Ohtsu[1,2]
[1] *Interdisciplinary Graduate School of Science and Engineering, Tokyo Institute of Technology, 4259 Nagatsuta-cho, Midori-ku, Yokohama 226-8502, Japan*
[2] *ERATO, Japan Science and Technology Corporation, 687-1 Tsuruma, Machida 194-0004, Japan*
Tel: +81 42-788-6041, Fax: + 81 42-788-6031, e-mail: takami@ae.titech.ac.jp

Abstract: We observed the output of Rb atoms from a near-field optical funnel. A beam flux of 10^5 atoms/cm^{2}s is obtained by performing Sisyphus cooling under blue detuning of +1 GHz.

OCIS codes: (140.3320) Laser cooling; (020.7010) Trapping; (999.9999) Nano-optics

We are planning to control atoms with high spatial accuracy beyond the diffraction limit using optical near-fields. The futuristic manipulation techniques, including fine atom deflection [1] and single-atom trapping [1,2], allow atom-by-atom deposition for nanofabrication, which is difficult for conventional atom-optical methods using propagating light. This scheme requires high-density cold atoms for the interaction between the atoms and the nanometric optical near-fields to occur efficiently. To generate a high-flux cold atomic beam suitable for near-field optical manipulation, we have proposed an atom funnel that uses blue-detuned evanescent light [3,4]. Here, we report a recent experiment in which funneled atoms were observed with a magneto-optical trap (MOT).

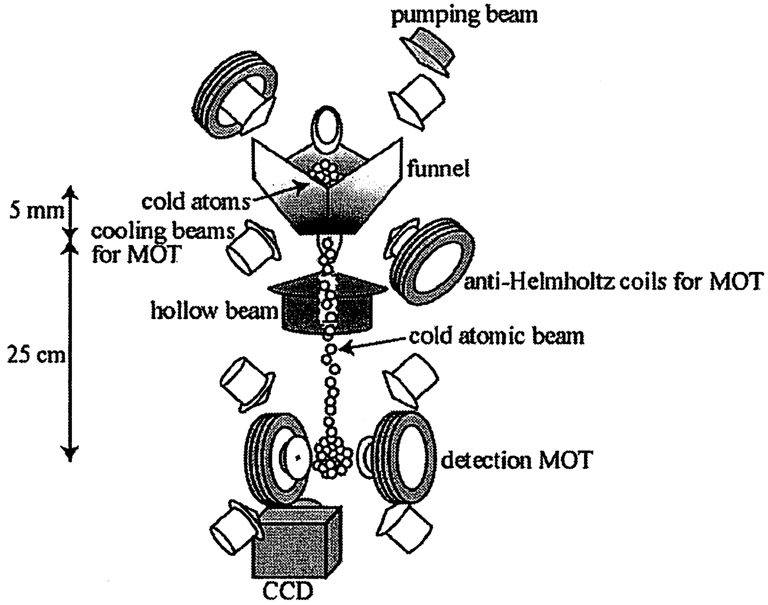

Fig. 1. Experimental configuration.

Figure 1 shows the experimental configuration for funneling and detection. Repulsive evanescent light is induced on the inner wall of an optical funnel composed of three glass plates by the total-internal reflection of a blue-detuned hollow light beam shone in the upward direction. A cold ^{87}Rb atom cloud is produced inside the optical funnel, 5 mm above the bottom, by the upper MOT, followed by polarization gradient cooling. The top view is shown in Fig. 2. Then 10^8 atoms with a mean temperature of 7 μK are released and transferred to the $5S_{1/2}$, $F = 1$ lower ground state by a pumping light beam. The free-fall atoms are reflected repeatedly inside the funnel [5] while losing kinetic energy due to Sisyphus cooling [6]; they collect at the bottom and pass through a 200-μm exit-hole. The output ^{87}Rb atoms are stored by the lower MOT, located 25 cm below, under a background pressure of 10^{-11} torr. The accumulated atoms are counted by observing the resonance fluorescence with a CCD camera.

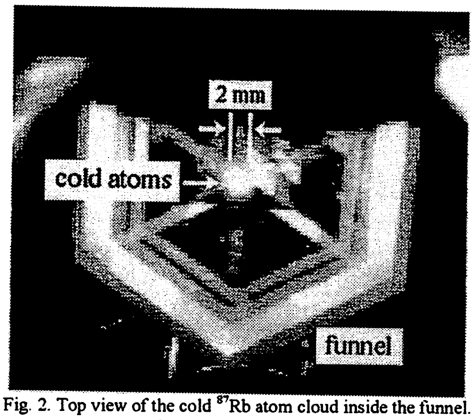

Fig. 2. Top view of the cold ^{87}Rb atom cloud inside the funnel.

The lower MOT also captures atoms escaping the funnel without interaction, that is, atoms falling straight from the upper MOT. In order to estimate the net funneled atoms, we subtract the number obtained without the pumping light beam from that obtained with Sisyphus cooling. Figure 3 shows the number of funneled atoms plotted as a function of the blue detuning measured with respect to the $5S_{1/2}$, F = 1 - $5P_{3/2}$, F = 2 transition. Here, instead of a hollow light beam, we use a 110-mW Gaussian light beam with a waist of 4 mm. For Sisyphus cooling, we also apply a 7-μW/cm^2 pumping light beam, red-detuned by 10 MHz with respect to the $5S_{1/2}$, F = 2 - $5P_{3/2}$, F = 2 transition. As shown in Fig. 3, the maximum number of ^{87}Rb atoms passes through the funnel at a blue detuning of 1 GHz. A cold atomic beam is generated by multi-loading from the upper MOT. The flux of the output ^{87}Rb beam is estimated to be 10^5 atoms/cm^{2}s at the exit hole. In blue detuning below 1 GHz, atoms are lost because of the heating caused by scattering spontaneous photons. On the other hand, in blue detuning above 1 GHz, atoms are lost because the dipole-force potential that reflects the atoms becomes low. We are trying to increase the number of output atoms by using a hollow light beam.

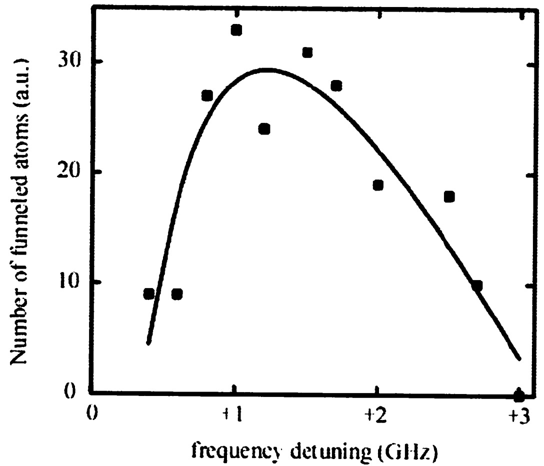

Fig. 3. Number of funneled ^{87}Rb atoms plotted as a function of blue detuning.

[1] M. Ohtsu (ed.), Near-Field Nano/Atom Optics and Technology (Springer, Tokyo, 1998), Chap. 11.

[2] K. Kobayashi, S. Sangu, H. Ito and M. Ohtsu, "Near-field optical potential for a neutral atom," Phys. Rev. A **63**, 013806 (2001).

[3] H. Ito, K. Sakaki, W. Jhe and M. Ohtsu, "Atomic funnel with evanescent light," Phys. Rev. A **56**, 712-718 (1997).

[4] A. Takamizawa H. Ito and M. Ohtsu, "Generation of a cold atomic beam with a near-field optical funnel," CLEO/Pacific Rim 2001, Technical Digest I, 512-513.

[5] A. Takamizawa, H. Ito and M. Ohtsu, "Multireflection of Cold Atoms in a Near-Field Optical Funnel," Jpn. J. Appl. Phys. **41**, 6215-6218 (2002).

[6] J. Söding, R. Grimm and Yu. B. Ovchinnikov, "Gravitational laser trap for atoms with evanescent-wave cooling," Opt. Commun. **119**, 652-662 (1995).

Atom manipulation using near-field light

Haruhiko Ito

Interdisciplinary Graduate School of Science and Engineering
Tokyo Institute of Technology

We are developing several atom-manipulation techniques based on resonant interaction between atoms and near-field light. Since near-field light decays as Yukawa-function, it exerts a strong dipole force on atoms. The dipole force is attractive when the light frequency is lower than the atomic resonant frequency (red detuning), while repulsive in the opposite case (blue detuning).

We first made an atom fiber composed of a hollow optical fiber. When a blue-detuned light beam is coupled to the core, repulsive near-field light is induced around the inner-wall surface. Atoms entering the hollow region are reflected whenever they approach the inner wall and guided through the hollow region. We conduced guiding of Rb atoms with a micron-sized hollow fiber and detected the guided Rb atoms by two-step photoionization.

We also proposed atom deflection with a slit-type deflector. The near-field light induced in the slit deflects atoms entering the slit. A 100-nm-wide slit was fabricated in an SOI substrate using photolithography and anisotropic etching. The spatial distribution of near-field light was measured using a fiber probe with a nanometric aperture. From the result, the optical potential and the deflection angle for Rb atoms were estimated. The deflected atoms can be detected by a slit-type detector similar to the deflector. For high-efficient detection of ground-state neutral atoms, two-step photoionization with two-color near-field light is used. In order to increase the detection efficiency, we made a multi-slit detector.

A cold atomic beam with high flux intensity is required for the near-field optical manipulation. To this end, we demonstrated an atom funnel using near-field light. In the funnel, cold Rb atoms produced by a magneto-optical trap (MOT) are collected at the bottom through reflection and Sisyphus cooling, and go out of a small exit hole as a collimated beam. The output atoms are detected by an accumulative detector using MOT.

Finally, feasibility of a single-atom trap using near-field light is discussed. These atom-manipulation techniques will be useful for atom-by-atom deposition.

[I-2] PAPRES IN NANO PHOTONICS

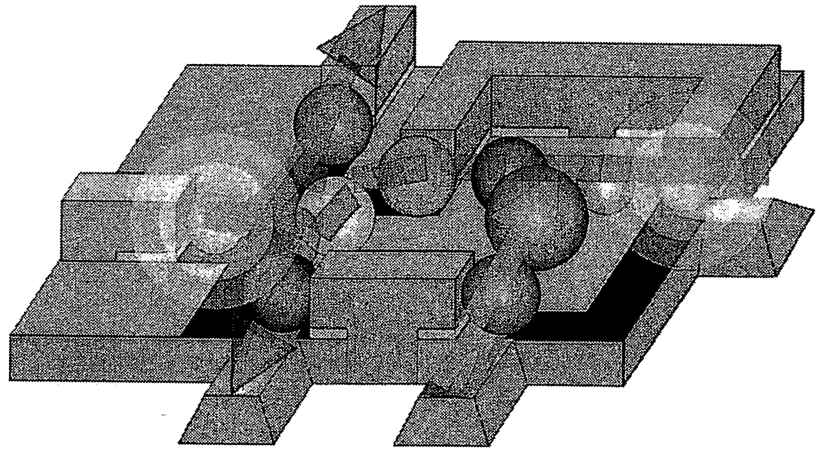

PERGAMON

Available online at www.sciencedirect.com
SCIENCE DIRECT•

Solid State Communications 127 (2003) 21–24

solid
state
communications

www.elsevier.com/locate/ssc

Room temperature ultraviolet emission from ZnO nanocrystallites fabricated by the low temperature oxidation of metallic Zn precursors

Tae-Won Kim[a,*], Tadashi Kawazoe[a], Shunsuke Yamazaki[b], Jungsik Lim[b], Takashi Yatsui[a], Motoichi Ohtsu[a,b]

[a]*Japan Science and Technology Corporation, Ohtsu Project, 687-1 tenko Bld. 4F, Tsuruma, Machida, Tokyo 194-0004, Japan*
[b]*Interdisciplinary Graduate School of Science and Engineering, Tokyo Institute of Technology, Yokohama, Kanagawa 226-8502, Japan*

Received 21 February 2003; received in revised form 21 April 2003; accepted 22 April 2003 by H. Akai

Abstract

We have successfully fabricated ZnO nanocrystallites emitting strong ultraviolet radiation at room temperature via the simple thermal oxidation of metallic Zn precursors at 380 °C. X-ray diffraction measurements showed only the diffraction peak from ZnO, revealing that metallic Zn precursors were successfully oxidized even at the low temperature of 380 °C. The mean size of the ZnO nanocrystallites determined using Scherrer's formula was ca. 30 nm. Room temperature photoluminescence measurements using a cw He–Cd laser ($\lambda = 325$ nm) showed a strong emission peak at 3.27 eV, which was ascribed to free exciton recombination. These results suggest that sufficient oxygen can diffuse into the metallic Zn precursors, even at temperatures as low as 380 °C, to allow the fabrication of pure ZnO nanocrystallites.

PACS: 61.46; 78.55; 78.66; 81.65.M

Keywords: A. Nanostructures; D. Optical properties

The low-dimensional structure of semiconductors has been of great interest in novel nanotechnology applications as well as in fundamental physics, due to its unique physical phenomena [1,2]. Recently, the nanostructure of wide-band gap semiconductors, such as GaN [3,4] and ZnO [5–7], has attracted much attention for application to nanophotonic devices in the ultraviolet (UV) region [8]. ZnO, with its wide bandgap (3.37 eV at 300 K) and large exciton binding energy (60 meV), is a promising material for UV region optoelectronic devices. So far, many attempts have been made to synthesize ZnO nanostructures using various techniques such as physical vapor deposition [9], thermal evaporation [10], and catalysis-assisted vapor–liquid solution growth method [11]. Although ZnO nanostructures are formed, most of these processes require temperatures above 1000 °C. A high process temperature is disadvantageous in the fabrication of a nanophotonic integrated circuit (IC). At low temperature, the direct oxidation of metallic Zn to fabricate ZnO may be feasible for realizing a nanophotonic IC, since ZnO nanodots can be used as a nanometric light emitter in the device [8].

Recently, we reported the fabrication of a single ZnO nanodot via the oxidation of a metallic Zn nanodot fabricated by optical near-field chemical vapor deposition (NFO-CVD) [12]. In that report, we demonstrated that by combining an adequate oxidation method, i.e. laser annealing in an oxygen atmosphere at room temperature, NFO-CVD is a feasible method for fabricating ZnO nanodots with high controllability of size and position, which are indispensable for function in a nanophotonic IC.

In this study, we report the successful fabrication of ZnO

---

[*] Corresponding author. Tel.: +81-427-788-6042; fax: +81-427-788-6031.
E-mail address: twkim90@ohtsu.jst.go.jp (T.W. Kim).

0038-1098/03/$ - see front matter © 2003 Elsevier Science Ltd. All rights reserved.
doi:10.1016/S0038-1098(03)00346-6

nanocrystallites with strong UV emission at RT using the thermal oxidation of metallic Zn precursors at a temperature of 380 °C. We used a simple method to fabricate ZnO nanocrystallites; metallic Zn precursors with a nominal thickness of 50 nm were first deposited on sapphire (001) substrate by thermal evaporation of pure metallic Zn powder (99.999%) and then the sample was placed in a thermal furnace under a constant flow of high-purity oxygen gas. The metallic Zn precursors were transformed into ZnO nanocrystallites by thermal oxidation at 380 °C. The crystal structure and morphology of the samples were characterized using X-ray diffraction (XRD) and scanning electron microscopy (SEM), respectively. The elemental composition of the oxidized Zn was examined by energy-dispersive X-ray spectrometry (EDX). Photoluminescence (PL) was measured with a cw He–Cd laser ($\lambda = 325$ nm) at room temperature.

Fig. 1 shows the XRD patterns of ZnO and as-deposited metallic Zn precursors. For the as-deposited metallic Zn, two significant peaks were observed at $2\theta = 36.30°$ and 43.26°, which correspond to the (002) and (101) diffraction of hexagonal phase Zn. After oxidation at 380 °C for 6 h, no diffraction peak of metallic Zn was observed. Instead, diffraction peaks corresponding to (100), (002), and (101) planes of ZnO with a hexagonal wurtzite structure were clearly observed. Indeed, no peak of metallic Zn was detected by XRD for the sample oxidized at 380 °C for 1 h. This indicates that the metallic Zn precursors are completely transformed into crystalline ZnO at temperature as low as 380 °C. Increasing the annealing time to 14 h, the reflections from ZnO become sharp and strong, indicating the growth and high crystallinity of the ZnO. From the position of the reflection peaks, the lattice parameter of ZnO was determined to be $a = 3.252$ and $c = 5.208$ Å. These values are in good agreement with the reported values for ZnO [9]. The mean size of the ZnO nanocrystallites determined using Scherrer's formula [13] was ca. 30 nm for annealing at 380 °C for 14 h.

Fig. 2 shows typical SEM images of as-deposited Zn precursors (a) and ZnO nanocrystallites (b) after thermal oxidation at 380 °C for 14 h. Many characteristic hexagonal Zn nanoplates are seen in Fig. 2(a). The diameters of the nanoplates ranged from 50 to 200 nm with thicknesses from 20 to 50 nm. This morphology was only observed when the growth rate was as slow as 2 nm/min. We believe that this hexagonal shape implies the formation of single-crystal pure metal Zn precursors. After oxidation, the hexagonal plates swelled as they incorporated oxygen, which increased the cell volume. In Fig. 2(b) a hexagonal plate composed of several nanocrystallites is indicated with a white arrow. The mean diameter, 30 nm, is consistent with the value determined by XRD.

In order to examine the elemental composition of the ZnO produced, EDX measurement was carried out. To

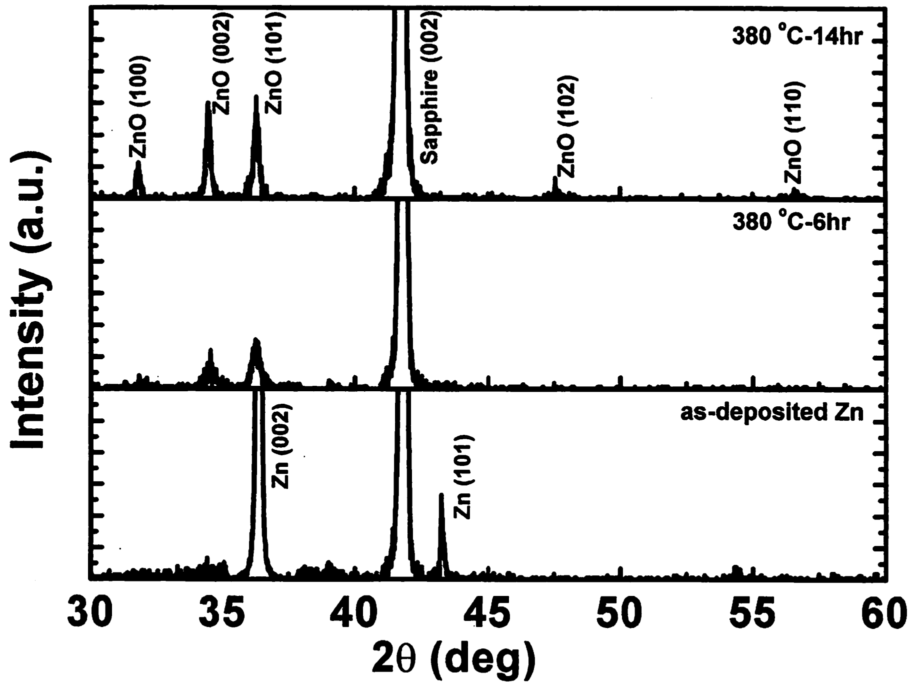

Fig. 1. XRD patterns of the ZnO and as-deposited metallic Zn precursors. For the as-deposited metallic Zn, two significant peaks were observed at $2\theta = 36.30°$ and 43.26°, which correspond to the (002) and (101) diffractions of hexagonal phase Zn. After oxidation at 380 °C, no diffraction peak of metallic Zn was observed. Instead, diffraction peaks corresponding to the (100), (002), and (101) planes of ZnO with a hexagonal wurtzite structure were clearly observed.

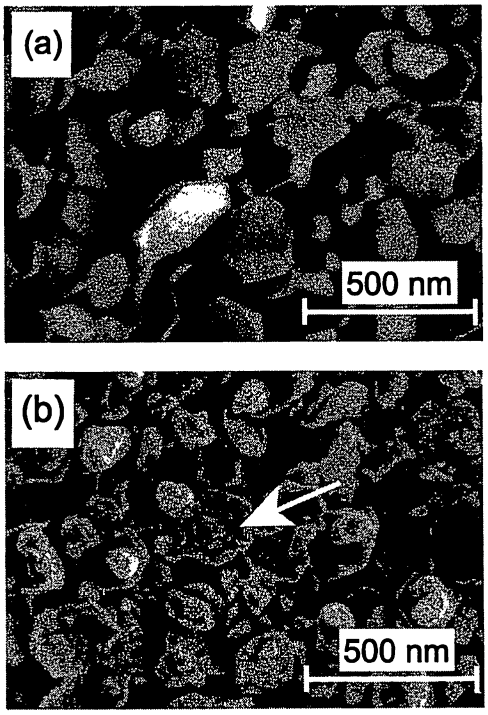

Fig. 2. Typical SEM images of as-deposited Zn precursors (a) and ZnO nanocrystallites (b) after thermal oxidation at 380 °C for 14 h. Hexagonal Zn nanoplates are observed in Fig. 2(a). After oxidation, the swelled hexagonal plate composed of several nanocrystallites is indicated with a white arrow.

avoid detecting the oxygen signal originating from the sapphire substrate, CaF_2 (111) was used as the substrate. Under the same fabrication conditions, ZnO was formed on CaF_2 (111) substrate. Fig. 3 shows the EDX spectrum, in which only five characteristic X-ray peaks originating from Zn, O, Ca, and F are observed; each peak is indexed in the figure. The EDX measurements showed that there was no contamination or impurities in the ZnO and the atomic ratio of Zn/O was approximately 1:1 within the accuracy of the equipment. The XRD and EDX measurements suggest that our approach is useful for fabricating pure polycrystalline ZnO nanomaterials at temperatures as low as 380 °C.

PL was used to examine the luminescence properties of the sample. Fig. 4 shows PL spectra of ZnO fabricated at 380 °C measured at 10, 60, and 297 K. At 10 K, two dominant peaks were observed at 3.362 and 3.320 eV, which were assigned to bound-exciton-emission at neutral-donor site, (D°, X) and two-electron transitions at the neutral donor site [14–16]. The (D°, X) line had a linewidth of 13 meV. This value is comparable with that of epitaxial ZnO [16]. As the temperature increased to 60 K, the intensity of the (D°, X) emission decreased significantly and the peak positions of the (D°, X) and the two-electron transitions shifted to 3.356 and 3.317 eV, respectively, keeping separation of about 40 meV. With a further increase in temperature, the intensities of (D°, X) and two-electron transitions decreased drastically, and the peaks disappeared at above 90 K. Above 90 K, the intensity of the free exciton peak $X_{A,B}$ became dominant. At room temperature PL measurement, a single strong peak was observed at 3.27 eV,

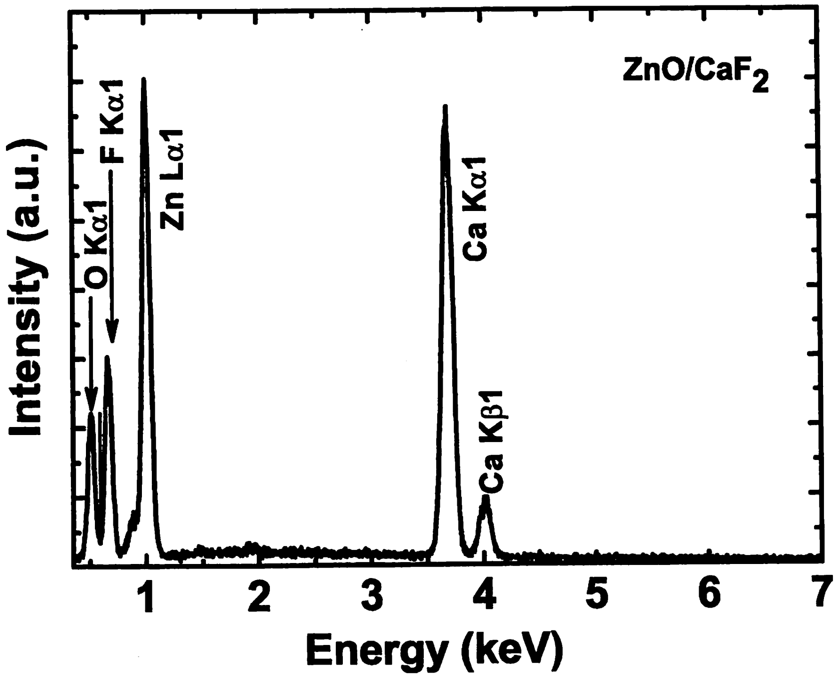

Fig. 3. EDX spectrum of ZnO fabricated on CaF_2 (111) substrate. Only five characteristic X-ray peaks originating from Zn, O, Ca, and F are observed; each peak is indexed in the figure.

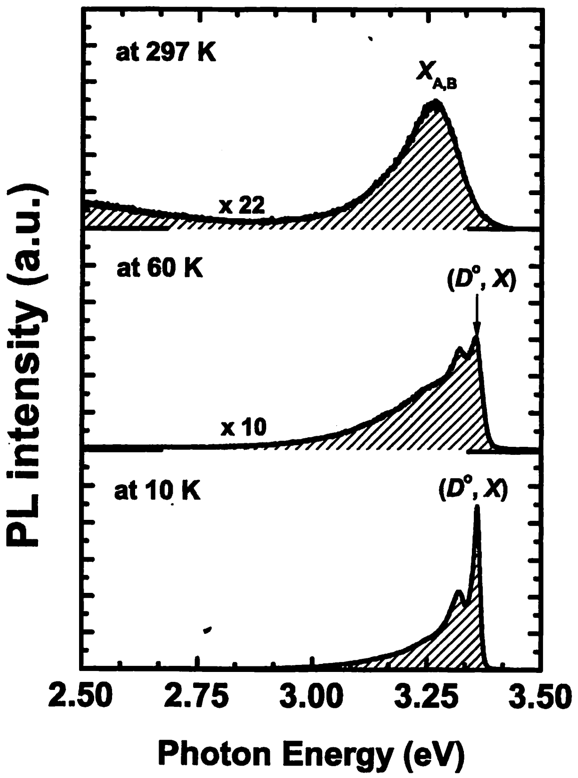

Fig. 4. PL spectra of ZnO nanocrystallites fabricated at 380 °C measured at 10, 60, and 297 K. In the figure, $X_{A,B}$ and (D°, X) denote free excitonic emission and bound-exciton-emission at neutral donors, respectively. Numbers in the figure indicate magnification value of the y-axis.

which was ascribed to free exciton recombination. Note that comparable intensity of the UV emissions was maintained up to room temperature and the intensity dominated the green emission around 2.5 eV. Moreover, the linewidth of 130 meV was comparable to the reported value, while the value of 3.27 eV was slightly lower than that of epitaxial ZnO films reported previously [16]. This can be explained by considering the strain-induced energy shift with exciton transitions of ZnO [17,18]. Ong et al. reported that the exciton transition energies varied in the presence of a strain field [18]. XRD, which can determine the lattice parameter, is one of the methods most commonly used to estimate the strain induced in a sample. In our case, the XRD results revealed that the ZnO nanocrystallites had lattice constants of $a = 3.252$ and $c = 5.208$ Å, which are close to those of bulk ZnO. This reflects the absence of residual strain in our sample, unlike an epitaxial ZnO thin film, in which residual strain induced by a lattice mismatch is generally observed. When biaxial strain exists in a sample, then the c-axis is lengthened, and the transition energies of the exciton increase. This shifts the PL peak to a slightly high-energy region compared with a sample without strain [18,19]. The PL peak observed at 3.27 eV was in good agreement with that of strain-free samples [5,9,19]. In addition, our ZnO sample exhibited optically pumped UV lasing at room temperature.

In conclusion, we successfully fabricated ZnO nanocrystallites emitting strong UV at room temperature via the simple thermal oxidation of metallic Zn precursors at 380 °C. XRD and room temperature PL measurements showed that the metallic Zn precursors were successfully oxidized at temperatures as low as 380 °C and the sample possessed sufficient luminescent properties. These results suggest that sufficient oxygen can diffuse into the metallic Zn precursors, even at temperatures as low as 380 °C, to allow the fabrication of pure ZnO nanocrystallites. We believe that the thin hexagonal plate of metallic Zn used as a starting material play an important role in the low temperature oxidation process, because sufficient oxygen can diffuse into such thin metallic Zn, even at low temperature.

References

[1] X. Duan, Y. Huang, Y. Chi, J. Wang, C.M. Lieber, Nature 409 (2001) 66.

[2] C.M. Lieber, Solid State Commun. 107 (1998) 607.

[3] S. Nakamura, Science 281 (1998) 956.

[4] H.M. Kim, D.S. Kim, Y.S. Park, D.Y. Kim, T.W. Kang, K.S. Chung, Adv. Mater. 14 (2002) 991.

[5] M.H. Huang, S. Mao, H. Feick, H. Yan, Y. Wu, H. Kind, E. Weber, R. Russo, P. Yang, Science 292 (2001) 1897.

[6] Y.B. Li, Y. Bando, T. Sato, K. Kurashima, Appl. Phys. Lett. 81 (2002) 144.

[7] B.D. Yao, Y.F. Chan, N. Wang, Appl. Phys. Lett. 81 (2002) 757.

[8] M. Ohtsu, K. Kobayashi, T. Kawazoe, S. Sangu, T. Yatsui, IEEE J. Selected Topics Quantum Electron. 8 (2002) 839.

[9] Y.C. Kong, D.P. Yu, B. Zhang, W. Fang, S.Q. Feng, Appl. Phys. Lett. 78 (2001) 407.

[10] B.D. Yao, Y.F. Chan, N. Wang, Appl. Phys. Lett. 81 (2002) 757.

[11] M.H. Huang, Y. Wu, H. Feick, N. Tran, E. Weber, P. Yang, Adv. Mater. 13 (2001) 113.

[12] T. Yatsui, T. Kawazoe, M. Ueda, Y. Yamamoto, M. Kourogi, M. Ohtsu, Appl. Phys. Lett. 81 (2002) 3651.

[13] B.D. Cullity, Elements of X-Ray Diffractions, Addison-Wesley, Reading, MA, 1978, p. 102.

[14] P.J. Dean, J.D. Cuthbert, D.G. Thomas, R.T. Lynch, Phys. Rev. Lett. 18 (1967) 122.

[15] D.C. Reynolds, D.C. Look, B. Jogai, C.W. Litton, T.C. Collins, W. Harsch, G. Cantwell, Phys. Rev. B. 57 (1998) 12151.

[16] H.J. Ko, Y.F. Chen, Z. Zhu, T. Yao, I. Kobayashi, H. Uchiki, Appl. Phys. Lett. 76 (2000) 1905.

[17] T. Makino, T. Yasuda, Y. Segawa, A. Ohtomo, K. Tamura, M. Kawasaki, H. Koinuma, Appl. Phys. Lett. 79 (2001) 1282.

[18] H.C. Ong, A.X.E. Zhu, G.T. Du, Appl. Phys. Lett. 80 (2002) 941.

[19] W.I. Park, G.C. Yi, J. Electron. Mater. 30 (2001) 1.

Journal of Microscopy, Vol. 210, Pt 3 June 2003, pp. 247–251
Received 10 August 2002; accepted 25 October 2002

Excitation dynamics in a three-quantum dot system driven by optical near-field interaction: towards a nanometric photonic device

K. KOBAYASHI*, S. SANGU*, A. SHOJIGUCHI*,
T. KAWAZOE*, K. KITAHARA† & M. OHTSU*,‡
**ERATO Localized Photon Project, Japan Science and Technology, 687-1 Tsuruma, Machida-shi, Tokyo 194-0004, Japan*
†Division of Natural Sciences, International Christian University, Tokyo, Japan
‡Interdisciplinary Graduate School of Science and Engineering, Tokyo Institute of Technology, Kanagawa, Japan

Key words. Coherent dynamics, nanometric photonic device, optical near-field interaction, phonon relaxation, Yukawa function, effective finite-range interaction.

Summary

Using density operator formalism, we discuss interdot excitation energy transfer dynamics driven by the optical near-field and phonon bath reservoir, as well as coherent excitation dynamics of a quantum dot system. As an effective interaction between quantum dots induced by the optical near-field, the projection operator method gives a renormalized dipole interaction, which is expressed as a sum of the Yukawa functions and is used as the optical near-field coupling of quantum dots. We examine one- and two-exciton dynamics of a three-quantum dot system suggesting a nanometric photonic switch, and numerically obtain a transfer time comparable with the recent experimental results for CuCl quantum dots.

1. Introduction

In near-field optical microscopy and spectroscopy, localization and tunneling of photons have played essential roles in spatial resolution beyond the diffraction limit. They are now recognized as key issues for nano and atom photonics (Ohtsu *et al.*, 2002), and it is very important to experimentally achieve local manipulation and control of the quantum states of an atom, molecule or quantum dot (QD) (Shojiguchi *et al.*, 2003). In this respect, coherent dynamics with dephasing of such a system driven by the optical near-field should be thoroughly investigated from the theoretical viewpoint. At the same time, we need to explore an intuitive understanding of the coherent excitation dynamics of QD systems and of their clear differences driven by either the far- or near-field.

The purpose of this study is to theoretically address the above issues, in particular, the interdot excitation energy transfer via the optical near-field and the coherent excitation dynamics of a QD system. We follow an effective interaction picture to provide a systematic, consistent and quantitative method. Using an example of a three-QD system, we examine the one- and two-exciton dynamics driven by the optical near-field that competes with the exciton–phonon interaction, and compare the time scale required for the transfer with recent experimental work (Kawazoe *et al.*, 2002, 2003). On the basis of this analysis, an optical near-field nano-switch is proposed as a fundamental building block of nano photonics.

The paper is organized as follows. Section 2 discusses the optical near-field interaction between QDs, which is responsible for the interdot excitation energy transfer, from an effective interaction viewpoint. We then examine the excitation dynamics of a three-QD-system driven by the optical near-field interaction as well as the phonon interaction in Section 3. Section 4 gives some numerical results obtained from the equation of motion, followed by a proposal of a nano-switch based on the interdot excitation energy transfer in Section 5. Finally, concluding remarks are presented in Section 6.

2. Optical near-field interaction between quantum dots as an effective interaction and the interdot excitation energy transfer

According to the theoretical framework developed in our previous studies (Kobayashi & Ohtsu, 1999; Kobayashi *et al.*, 2001; Sangu *et al.*, 2001; Ohtsu *et al.*, 2002), let us consider an interdot interaction due to the optical near-field. The total Hamiltonian $\hat{H}$ for the system consists of $\hat{H}_{\text{photon}}$ for incident photons, $\hat{H}_{\text{matter}}$ for a surrounding macroscopic matter system,

Correspondence: K. Kobayashi. Tel.: +81 42 788 6036; fax: +81 42 788 6031; e-mail: kkoba@ohtsu.jst.go.jp

$\hat{H}_{\mathrm{QD}}$ for a nanometric QD system, and their interactions $\hat{V}$ as given by the multipolar QED Hamiltonian (Cohen-Tannoudji *et al.*, 1989; Craig & Thirunamachandran, 1998; Andrews & Demidov, 1999).

$$\begin{aligned} \hat{H} &= \hat{H}_{\mathrm{photon}} + \hat{H}_{\mathrm{matter}} + \hat{H}_{\mathrm{QD}} + \hat{V}, \\ \hat{V} &= -\sum_i \hat{\vec{\mu}}_i \cdot \hat{\vec{D}}(\vec{r}_i), \end{aligned} \tag{1}$$

where $\hat{\vec{\mu}}_i$ denotes the dipole operator of either constituents of the macroscopic matter system or each QD, and $\hat{\vec{D}}(\vec{r}_i)$ represents the electric displacement vector at position $\vec{r}_i$. It is convenient to treat this kind of problem in two stages. First, the photons and macroscopic matter system are described on an equal basis in terms of a so-called polariton basis. The interaction between the QD system and the macroscopic system is then expressed using the polariton basis as

$$\begin{aligned} \hat{H} &= \hat{H}_0 + \hat{V}' = \sum_{\vec{k}} E(k)\hat{\xi}_{\vec{k}}^{\dagger}\hat{\xi}_{\vec{k}} + \sum_{\alpha} E_{\alpha}\hat{B}_{\alpha}^{\dagger}\hat{B}_{\alpha} - \sum_{\alpha} \hat{\vec{\mu}}_{\alpha} \cdot \hat{\vec{D}}(\vec{r}_{\alpha}), \\ \hat{\vec{D}}(\vec{r}_{\alpha}) &= i\sqrt{\frac{2\pi\hbar}{V}} \sum_{\vec{k}\lambda} \vec{e}_{\vec{k}\lambda} f(k)[\hat{\xi}_{\vec{k}} e^{i\vec{k}\cdot\vec{r}_{\alpha}} - \hat{\xi}_{\vec{k}}^{\dagger} e^{-i\vec{k}\cdot\vec{r}_{\alpha}}]. \end{aligned} \tag{2}$$

Here the creation and annihilation operators of the polariton with wave vector $\vec{k}$ and eigenenergy $E(k)$ are denoted as $\hat{\xi}_{\vec{k}}^{\dagger}$ and $\hat{\xi}_{\vec{k}}$, whereas those of excitons in QD α are designated as $\hat{B}_{\alpha}^{\dagger}$ and $\hat{B}_{\alpha}$, with E_{α} being the exciton energy. The electric displacement vector is expanded in terms of the polariton basis and the coupling coefficient $f(k)$ between the macroscopic matter system and photons with polarization vector $\vec{e}_{\vec{k}\lambda}$. The Planck constant divided by 2π and the normalization volume are $\hbar$ and V, respectively. The coupling coefficient $f(k)$ can be written as

$$f(k) = \frac{\hbar c k}{\sqrt{\hbar E(k)}} \sqrt{\frac{E(k)^2 - E_m^2}{2E(k)^2 - E_m^2 - (\hbar c k)^2}}, \tag{3}$$

where c and E_m are the velocity of light in a vacuum and the excitation energy of the macroscopic matter system, respectively.

Although the Hamiltonian of Eq. (2) provides a variety of information about both static and dynamic properties of the system, here we restrict ourselves to exploring the interaction between QDs. Then it is more practical to use some of eigenstates $|\Psi_{\lambda}^{P}\rangle$ of $\hat{H}_0$, instead of exact eigenstates $|\Psi_{\lambda}\rangle$ of $\hat{H}$, and an effective interaction operator $\hat{V}_{\mathrm{eff}}$ that satisfies the following relation

$$\langle \Psi_f^P | \hat{V}_{\mathrm{eff}} | \Psi_i^P \rangle = \langle \Psi_f | \hat{V} | \Psi_i \rangle. \tag{4}$$

These procedures are carried out on the basis of the projection operator method, as discussed previously in detail. When we set the relevant initial and final states in P-space to $|\Psi_i^P\rangle = |A^*\rangle|B\rangle|0\rangle$ and $|\Psi_f^P\rangle = |A\rangle|B^*\rangle|0\rangle$, with $|\alpha\rangle$, $|\alpha^*\rangle$ ($\alpha = A, B$) and $|0\rangle$ being the ground, excited states of QDs and the vacuum state of the polaritons, the effects of both the photons and the macroscopic matter system, i.e. the polaritons, are renormalized into an effective two-body interaction between QDs. We call this effective interaction the optical near-field interaction or coupling which is explicitly given as

$$\begin{aligned} \hbar U(r) &\equiv \langle \Psi_f^P | \hat{V}_{\mathrm{eff}} | \Psi_i^P \rangle \\ &= -\frac{\mu_A \mu_B}{6\pi^2} \int d^3k\, f^2(k) \left\{ \left[\frac{1}{E(k) + E_A} + \frac{1}{E(k) + E_B} \right] e^{i\vec{k}\cdot\vec{r}} \right. \\ &\quad \left. + \left[\frac{1}{E(k) - E_A} + \frac{1}{E(k) - E_B} \right] e^{-i\vec{k}\cdot\vec{r}} \right\} \\ &= \frac{\mu_A \mu_B}{3(\hbar c)^2} \sum_{\alpha=A}^{B} \left[W_{\alpha+} Y(\Delta_{\alpha+} r) + W_{\alpha-} Y(\Delta_{\alpha-} r) \right], \end{aligned} \tag{5}$$

where the transition dipole moments of the relevant QDs A and B are denoted as μ_A and μ_B, respectively. In addition, $W_{\alpha\pm}$ denotes the weight factor of each Yukawa function defined as

$$\begin{aligned} Y(\Delta_{\alpha\pm} r) &= \frac{\exp[-\Delta_{\alpha\pm} r]}{r}, \\ \Delta_{\alpha\pm} &= \frac{1}{\hbar c}\sqrt{2E_p(E_m \pm E_{\alpha})}, \end{aligned} \tag{6}$$

with the interdot distance $r = |\vec{r}_A - \vec{r}_B|$, the polariton effective mass rewritten as $E_p = m_p c^2$. The factor $\Delta_{\alpha-}$ becomes either real or pure imaginary depending on the magnitude of E_m and E_{α}, which means that this component behaves as either a localized or propagation mode. We are primarily interested in the localized mode, and also neglected two additional terms in Eq. (5) that are independent of the QD parameters as a far-field contribution. Here it should be noted that the optical near-field coupling $U(r)$ could induce the interdot energy transfer process when the neighbouring QDs have resonant levels, i.e. $E_A = E_B$.

3. Excitation dynamics driven by both optical near-field and phonon interactions

In the preceding section, we focused on the optical near-field interaction between QDs. However, phonon effects on the coherent excitation dynamics of a QD system cannot be excluded. Using an example of a three-QD system shown schematically in Fig. 1, we discuss how the interdot excitation energy and quantum coherence are transferred under the optical near-field and the phonon interactions with the QDs. The model Hamiltonian of such a system can be written as

$$\begin{aligned} &\hat{H} = \hat{H}_0 + \hat{V}_{\mathrm{NF}} + \hat{V}_{\mathrm{vib}},\ \hat{H}_0 = \hat{H}_{\mathrm{QD}} + \hat{H}_{\mathrm{ph}}, \\ &\hat{H}_{\mathrm{QD}} = E_2\hat{D}^{\dagger}\hat{D} + E_1\hat{A}_1^{\dagger}\hat{A}_1 + (E_2 - E_1)\hat{C}^{\dagger}\hat{C} + E_1\hat{A}_2^{\dagger}\hat{A}_2, \\ &\hat{H}_{\mathrm{ph}} = \sum_n \varepsilon_n \hat{b}_n^{\dagger}\hat{b}_n, \\ &\hat{V}_{\mathrm{NF}} = \hbar U(r_{12})(\hat{D}^{\dagger}\hat{A}_1\hat{C} + \hat{D}\hat{C}^{\dagger}\hat{A}_1^{\dagger}) + \hbar U(r_{23})(\hat{A}_1^{\dagger}\hat{A}_2 + \hat{A}_1\hat{A}_2^{\dagger})\hat{C}\hat{C}^{\dagger}, \\ &\hat{V}_{\mathrm{vib}} = \sum_n \hbar(g_n\hat{b}_n^{\dagger}\hat{C} + g_n^{*}\hat{b}_n\hat{C}^{\dagger}), \end{aligned} \tag{7}$$

where $\hat{H}_{\mathrm{QD}}$, $\hat{H}_{\mathrm{ph}}$, $\hat{V}_{\mathrm{NF}}$, and $\hat{V}_{\mathrm{vib}}$ describe the isolated QD excitons, the phonon bath reservoir, optical near-field interaction and exciton–phonon interaction, respectively. The eigenenergies

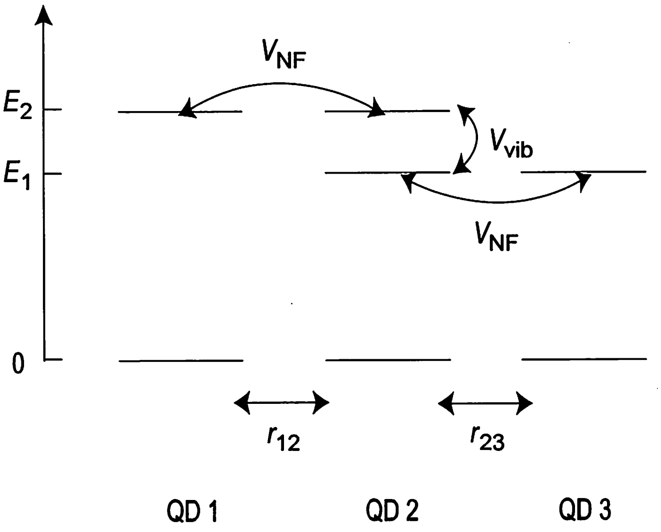

Fig. 1. Three-QD system coupled via optical near-field (V_{NF}) and phonon (V_{vib}) interactions. The horizontal lines represent energy levels of each QD, and the distance between two neighbouring QDs is denoted as $r_{12}(r_{23})$.

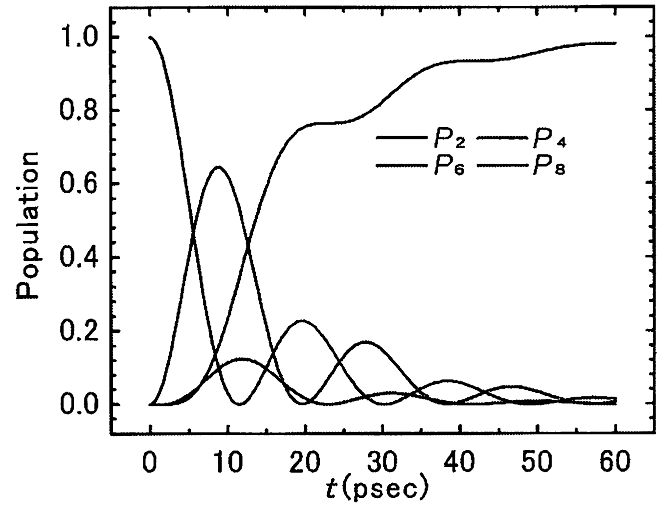

Fig. 2. One-exciton dynamics. The population probabilities of P_1, P_3, P_5, and P_7, corresponding to the operators $\hat{O}(1), \hat{O}(3), \hat{O}(5)$, and $\hat{O}(7)$ are plotted as a function of time. The operator $\hat{O}(1)$ represents a one-exciton state in QD 1, $\hat{O}(3)$ and $\hat{O}(5)$ describe one-exciton in the E_2 and E_1 level in QD 2, respectively, and $\hat{O}(7)$ describes one in QD 3.

of each QD and the phonon levels are denoted as E_1, E_2, and ε_n, whereas g_n denotes the QD–phonon bath coupling constant. The operators $(\hat{D}^\dagger, \hat{D})$, $(\hat{A}_2^\dagger, \hat{A}_2)$, and $(\hat{A}_1^\dagger, \hat{A}_1)$ are fermionic operators for the creation and annihilation of an exciton in QD 1, QD 3 and the lower energy level of QD 2, respectively, while the fermionic operators $(\hat{C}^\dagger, \hat{C})$ and the bosonic operators $(\hat{b}_n^\dagger, \hat{b}_n)$ are for the $(E_2 - E_1)$ level of QD 2 and for the phonon bath reservoir, respectively. The equation of motion describing the dynamics of the system can be obtained using Born–Markov approximation (Carmichael, 1999) as

$$\frac{\partial\hat{\rho}(t)}{\partial t} = \frac{1}{i\hbar}[\hat{V}_{NF}, \hat{\rho}(t)] - \frac{\gamma}{2}(\{\hat{C}^\dagger\hat{C}, \hat{\rho}(t)\} - 2\hat{C}\hat{\rho}(t)\hat{C}^\dagger), \qquad (8)$$

where we trace out the degrees of freedom of the phonon bath reservoir, and define the density operator of the QD system in the interaction representation as $\hat{\rho}(t)$, representing the relaxation constant as γ. In order to solve Eq. (8), we use the following expansion for the density operator, instead of the usual density matrix form:

$$\hat{\rho}(t) = \sum_\ell P_\ell(t)\hat{O}(\ell), \qquad (9)$$

where $P_\ell(t)$ refers to the occurrence probability of the state defined by the operator $\hat{O}(\ell)$. As shown in Table 1, the operator $\hat{O}(\ell)$ is related to either the number of excitons occupied in the system or the quantum coherence of the system, and it is suitable for examining one-exciton dynamics, two-exciton dynamics and so forth.

4. Numerical results

We show some numerical results obtained from Eqs (8) and (9) in order to discuss the exciton dynamics of the system illustrated in Fig. 1. In the following we assume cubic CuCl QDs embedded in NaCl matrix whose physical quantities are cited from the references (Hanamura, 1988; Kataoka *et al.*, 1993; Sakakura & Masumoto, 1997). Figure 2 presents an example of one-exciton dynamics that illustrates how fast an exciton located in QD 1 at time $t = 0$ is transferred to QD 3. It follows from the figure that it takes about 10–20 ps under the condition of $\hbar\gamma = 160\,\mu\text{eV}$, $\hbar U(r_{12}) = \hbar U(r_{23}) = 40\,\mu\text{eV}$. This condition was estimated from Eq. (5) for CuCl QDs with a size of 5 nm arranged equidistantly at 10 nm, and with transition

Table 1. Explicit expressions for the operator $\hat{O}(\ell)$.

One-exciton part	Two-exciton part	Quantum coherence part
$\hat{O}(1) = \hat{D}^\dagger\hat{D}\hat{A}_1\hat{C}\hat{A}_1^\dagger\hat{C}^\dagger\hat{A}_2\hat{A}_2^\dagger$,	$\hat{O}(2) = \hat{D}^\dagger\hat{D}\hat{A}_1\hat{C}\hat{A}_1^\dagger\hat{C}^\dagger\hat{A}_2^\dagger\hat{A}_2$	$\hat{O}(c1) = \frac{i}{\sqrt{2}}(\hat{D}^\dagger\hat{A}_1\hat{C} - \hat{D}\hat{A}_1^\dagger\hat{C}^\dagger)\hat{A}_2\hat{A}_2^\dagger, \hat{O}(c2) = \frac{i}{\sqrt{2}}(\hat{D}^\dagger\hat{A}_1\hat{C} - \hat{D}\hat{A}_1^\dagger\hat{C}^\dagger)\hat{A}_2^\dagger\hat{A}_2$
$\hat{O}(3) = \hat{D}\hat{D}^\dagger\hat{A}_1^\dagger\hat{C}^\dagger\hat{A}_1\hat{C}\hat{A}_2\hat{A}_2^\dagger$,	$\hat{O}(4) = \hat{D}\hat{D}^\dagger\hat{A}_1^\dagger\hat{C}^\dagger\hat{A}_1\hat{C}\hat{A}_2^\dagger\hat{A}_2$	
$\hat{O}(5) = \hat{D}\hat{D}^\dagger\hat{A}_1^\dagger\hat{C}\hat{A}_1\hat{C}^\dagger\hat{A}_2\hat{A}_2^\dagger$,	$\hat{O}(6) = \hat{D}^\dagger\hat{D}\hat{A}_1^\dagger\hat{C}\hat{A}_1\hat{C}^\dagger\hat{A}_2\hat{A}_2^\dagger$	$\hat{O}(c3) = \hat{D}^\dagger\hat{D}\frac{i(\hat{A}_1^\dagger\hat{A}_2 - \hat{A}_1\hat{A}_2^\dagger)}{\sqrt{2}}\hat{C}\hat{C}^\dagger, \hat{O}(c4) = \hat{D}\hat{D}^\dagger\frac{i(\hat{A}_1^\dagger\hat{A}_2 - \hat{A}_1\hat{A}_2^\dagger)}{\sqrt{2}}\hat{C}\hat{C}^\dagger$
$\hat{O}(7) = \hat{D}\hat{D}^\dagger\hat{A}_1\hat{C}\hat{A}_1^\dagger\hat{C}^\dagger\hat{A}_2^\dagger\hat{A}_2$,	$\hat{O}(8) = \hat{D}\hat{D}^\dagger\hat{A}_1^\dagger\hat{C}\hat{A}_1\hat{C}^\dagger\hat{A}_2^\dagger\hat{A}_2$	
$\hat{O}(9) = \hat{D}\hat{D}^\dagger\hat{A}_1\hat{C}\hat{A}_1^\dagger\hat{C}^\dagger\hat{A}_2\hat{A}_2^\dagger$		$\hat{O}(c5) = \frac{i}{\sqrt{2}}(\hat{D}^\dagger\hat{C}\hat{A}_2 + \hat{D}\hat{C}^\dagger\hat{A}_2^\dagger)\hat{A}_1^\dagger\hat{A}_1$

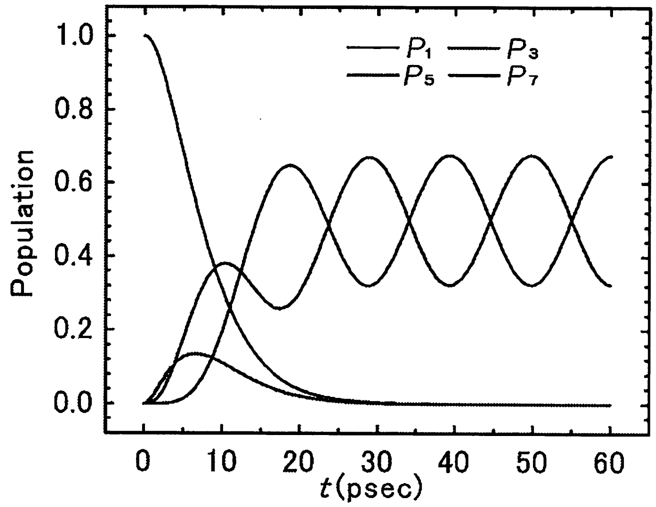

Fig. 3. Two-exciton dynamics. The time evolution of the population probabilities of P_2, P_4, P_6, and P_8 are plotted, similar to Fig. 2. Initially, one exciton exists in QD 1 and another in QD 2, denoted as $P_6(0) = 1$. The probability P_8 shows exciton transfer from QD 1 to QD 3 when an exciton exists in QD 2.

dipole moments of $\mu_A = \mu_B = 0.29\ (\mathrm{eV}\cdot\mathrm{nm}^3)^{1/2}$. The theoretically estimated time scale is found to be consistent with the recent experimental results (Kawazoe *et al.*, 2002a,b). Moreover, nutation can be seen in $P_5(t)$ and $P_7(t)$, owing to the quantum coherence between QDs 2 and 3.

Figure 3 depicts an example of two-exciton dynamics under the initial condition that one exciton exists in QD 1 and another in QD 2 at time $t = 0$, i.e. $P_6(0) = 1$. The other conditions are the same as used in Fig. 2. The probability $P_8(t)$ in Fig. 3 shows that exciton transfer from QD 1 to QD 3 takes place in less than 60 ps when an exciton exists in QD 2. The exciton, or excitation energy, is transferred via the quantum coherences $\hat{O}(c3)$, $\hat{O}(c7)$, and $\hat{O}(c2)$ driven by the optical near-field interaction. This coincides with the oscillations with a period of about 20 ps in $P_2(t)$, $P_4(t)$, and $P_8(t)$, as well as $P_6(t)$, although they are damped due to the phonon relaxation. It should be noted that the first peak shift between $P_2(t)$ and $P_4(t)$ originated from the fermionic nature of the exciton in QD 2. In addition, the decay rate of the quantum coherence of the three-QD system is half that of the two-QD system, and this fact suggests a possibility of controlling the relaxation time and the excitation transfer time via quantum coherence.

5. Three-QD system as a building block of a nanometric photonic switch based on interdot excitation energy transfer

Applying the above considerations to a nanometric photonic device, one may have a building block for a photonic switch as illustrated in Fig. 4. It consists of three QDs (QD-I, QD-O, QD-C), and each of the two neighbouring QD pairs has a resonant energy level coupled by the optical near-field. The signal transmission relies on the excitation energy transfer from QD-I to QD-O via the optical near-field interaction. The control field applied to QD-C governs the optical near-field interaction between QD-I and QD-C, as well as QD-O and QD-C, and provides the switching mechanism. In the ON state of the switch (Fig. 4a), the signal transmission to QD-C is blocked by the state filling effect of (1,1,1) level in QD-C, and the input energy from QD-I is directed to QD-O resulting in the output signal that can be detected either by near-field coupling to the detector or by far-field light emitted with electron-hole recombination. By contrast, the input signal in the OFF state is collected at QD-C as a result of the optical near-field and exciton–phonon coupling, which leads to no output signal in QD-O. The switching speed of the device is estimated as a few to a

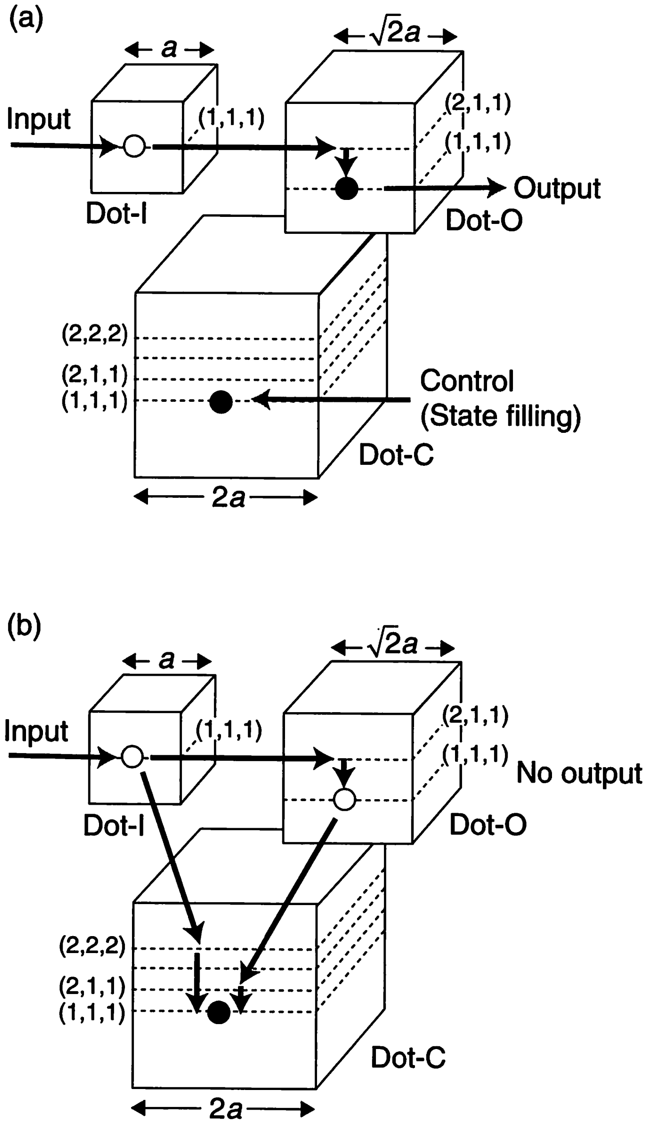

Fig. 4. Building block composed of three QDs for a photonic switch showing (a) ON, (b) OFF states. As indicated by arrows, input population in QD-I is transferred to QD-O, whose signal is detected either by near-field coupling to the detector or by far-field light.

hundred picoseconds similar to the time scale obtained in Fig. 3, although it depends on the material, size, and spacing of the QDs.

6. Concluding remarks

Towards the realization of nanometric photonic devices, we investigated the dynamics of a nanometric QD system under the competition of the optical near-field and phonon interactions, from the effective interaction picture to provide a systematic and consistent method of analysing the optical near-field interaction quantitatively. Using the example of a three-QD system, we examined one- and two-exciton dynamics, both of which show that excitation energy transfer from QD 1 to QD 3 occurs in a few tens of picoseconds. This time scale is consistent with the experimental results obtained with CuCl QDs. By utilizing the theoretical results obtained, a photonic switch as a new scheme of nano-photonic device based on interdot excitation energy transfer via optical near-fields has been suggested. Owing to the page limit, a detail analysis on the device will be published elsewhere (see, for example, Sangu *et al.*, 2003).

References

Andrews, D.L. & Demidov, A.A. (1999) *Resonance Energy Transfer*. Wiley, Chichester.

Carmichael, H.J. (1999) *Statistical Methods in Quantum Optics 1*. Springer, Berlin.

Cohen-Tannoudji, C., Dupont-Roc, J. & Grynberg, G. (1989) *Photons and Atoms*. Wiley, New York.

Craig, D.P. & Thirunamachandran, T. (1998) *Molecular Quantum Electrodynamics*. Dover Publications, New York.

Hanamura, E. (1988) Very large optical nonlinearity of semiconductor micro-crystallites. *Phys. Rev. B*, 37, 1273–1279.

Kataoka, T., Tokizaki, T. & Nakamura, A. (1993) Mesoscopic enhancement of optical nonlinearity in CuCl quantum dots: giant-oscillation strength effect on confined excitons. *Phys. Rev. B*, 48, 2815–2818.

Kawazoe, T., Kobayashi, K., Lim, J., Narita, Y. & Ohtsu, M. (2002) Direct observation of optically forbidden energy transfer between CuCl quantum cubes via near-field optical spectroscopy. *Phys. Rev. Lett.* 88, 067404–067401-4.

Kawazoe, T., Kobayashi, K., Sangu, S. & Ohtsu, M. (2003) Demonstrating nanophotonic switching operation by near-field pump-probe photoluminescence spectroscopy of CuCl quantum cubes. *J. Microsc.*

Kobayashi, K. & Ohtsu, M. (1999) Quantum theoretical approach to a near-field optical system. *J. Microsc.* 194, 249–254, and references therein.

Kobayashi, K., Sangu, S., Ito, H. & Ohtsu, M. (2001) Near-field optical potential for a neutral atom. *Phys. Rev. A*, 63, 013806–1–9.

Ohtsu, M., Kobayashi, K., Kawazoe, T., Sangu, S. & Yatsui, T. (2002) Nanophotonics: design, fabrication, and operation of nanometric devices using optical near fields. *IEEE J. Selected Topics Quantum Electron.* 8, 839–862.

Sakakura, N. & Masumoto, Y. (1997) Persistent spectral-hole-burning spectroscopy of CuCl quantum cubes. *Phys. Rev. B*, 56, 4051–4055.

Sangu, S., Kobayashi, K. & Ohtsu, M. (2001) Optical near fields as photon-matter interacting systems. *J. Microsc.* 202, 279–285.

Sangu, S., Kobayashi, K., Shojiguchi, A., Kawazoe, T. & Ohtsu, M. (2003) Excitation energy transfer and population dynamics in a quantum dot system induced by optical near-field interaction. *J. Appl. Phys.* 93, 2937–2945.

Shojiguchi, A., Kobayashi, K., Sangu, S., Kitahara, K. & Ohtsu, M. (2003) Coherent dipole oscillation induced by localized photons. *Nonlinear Optics*, and references therein.

Journal of Microscopy, Vol. 210, Pt 3 June 2003, pp. 301–306
Received 10 August 2002; accepted 25 October 2002

A method for controlling the spins of atoms using optical near-fields

A. SHOJIGUCHI*, K. KITAHARA†, K. KOBAYASHI* &
M. OHTSU*‡
**ERATO Localized Photon Project, Japan Science and Technology, 687-1 Tsuruma, Machidashi, Tokyo 194-0004, Japan*
†Division of Natural Sciences, International Christian University, 10-2 Osawa 3-chome, Mitakashi, Tokyo 181-8585, Japan
‡Interdisciplinary Graduate School of Science and Engineering, Tokyo Institute of Technology, 4259 Nagatsuta-cho, Midori-ku, Yokohama, Kanagawa 226-8502, Japan

Key words. Carniglia–Mandel modes, cavity effect, evanescent field, planar boundary, spin control, spontaneous emission.

Summary

On the basis of the procedure for controlling the spins of atoms using circularly polarized evanescent light proposed by Hori *et al.* [(1996) Abstracts of the 1st Asia-Pacific Workshop on Near-field Optics] we discuss the influence of boundary conditions on the probability of spontaneous emission and thus on the spin polarization efficiency, which was not considered in the Hori *et al.* study. Using the Carniglia–Mandel mode expansion of electromagnetic fields, we derive the spontaneous emission and spin polarization probabilities of atoms near a dielectric surface, and show the atom–surface distance dependence and refractive index dependence. Numerical evaluation for the $6P_{1/2}$–$6S_{1/2}$ transition of a Cs atom indicates an increase in the efficiency of spin polarization by 30%.

1. Introduction

As a result of spatial localization and a unique dispersion relation originating from interaction with matter, optical near-fields produce intriguing phenomena that cannot be obtained with propagating far-fields. Some of these phenomena have been investigated extensively, both experimentally and theoretically, and their applicability to nano-photonics and atom-photonics has been discussed (Ohtsu *et al.*, 2002). Spin control of atoms, molecules, or quantum dots is another example that has attracted considerable attention in the scientific community. In this context, a method for controlling the spin of an atomic beam by using circularly polarized evanescent light whose angular momentum is perpendicular to the propagation direction has been proposed (Hori *et al.*, 1996; Ohdaira *et al.*, 2001). The authors neglected the dielectric surface effect, although it is well known that the spontaneous emission rate of atoms near a surface is modified. In addition, the polarization of emitted photons becomes anisotropic, and their directional dependence is not negligible when the atoms are very close to a surface. On the basis of their proposal, we examined the dielectric surface effects on spin-control efficiency, with the help of Carniglia–Mandel (CM) modes (Carniglia & Mandel, 1971; Inoue & Hori, 2001), which form a complete, orthonormal basis set for electromagnetic fields with an infinite surface boundary. Section 2 briefly outlines the spin-control method proposed by Hori *et al.* In Section 3, we derive the spontaneous emission and spin polarization probabilities of atoms near a dielectric planar surface, and discuss the spin-control efficiency, using the example of caesium atoms. Conclusions are drawn in Section 4, and the definitions and useful formulae of the CM modes are presented in the Appendix.

2. Spin-control method by optical near-fields

Following Hori *et al.* (1996), we outline a method that can be used to align the spins of atoms injected close to a dielectric surface. Suppose that the media below and above the plane have refractive indexes n and 1, respectively. Two s-polarized plane waves with amplitude E_0, monochromatic frequency ω, and wave number $k = n\omega/c \equiv nK$ are incident from the dielectric side as $E_0\mathbf{e}_x e^{ik(y\sin\theta+z\cos\theta)-i\omega t}$ and $E_0\mathbf{e}_y e^{ik(x\sin\theta+z\cos\theta)-i\omega t}$, where $\mathbf{e}_x$ and $\mathbf{e}_y$ are unit polarization vectors. If the incident angle θ exceeds the critical angle θ_c, two evanescent waves are generated above the surface. If the condition

$$nKx\sin\theta = nKy\sin\theta + \frac{\pi}{2} + 2l\pi, \quad (l = 0, 1, 2, 3, \dots) \qquad (1)$$

Correspondence: A. Shojiguchi. Tel.: +81 42 788 6045; fax: +81 42 788 6031; e-mail: akirasho@ohtsu. jst.go.jp

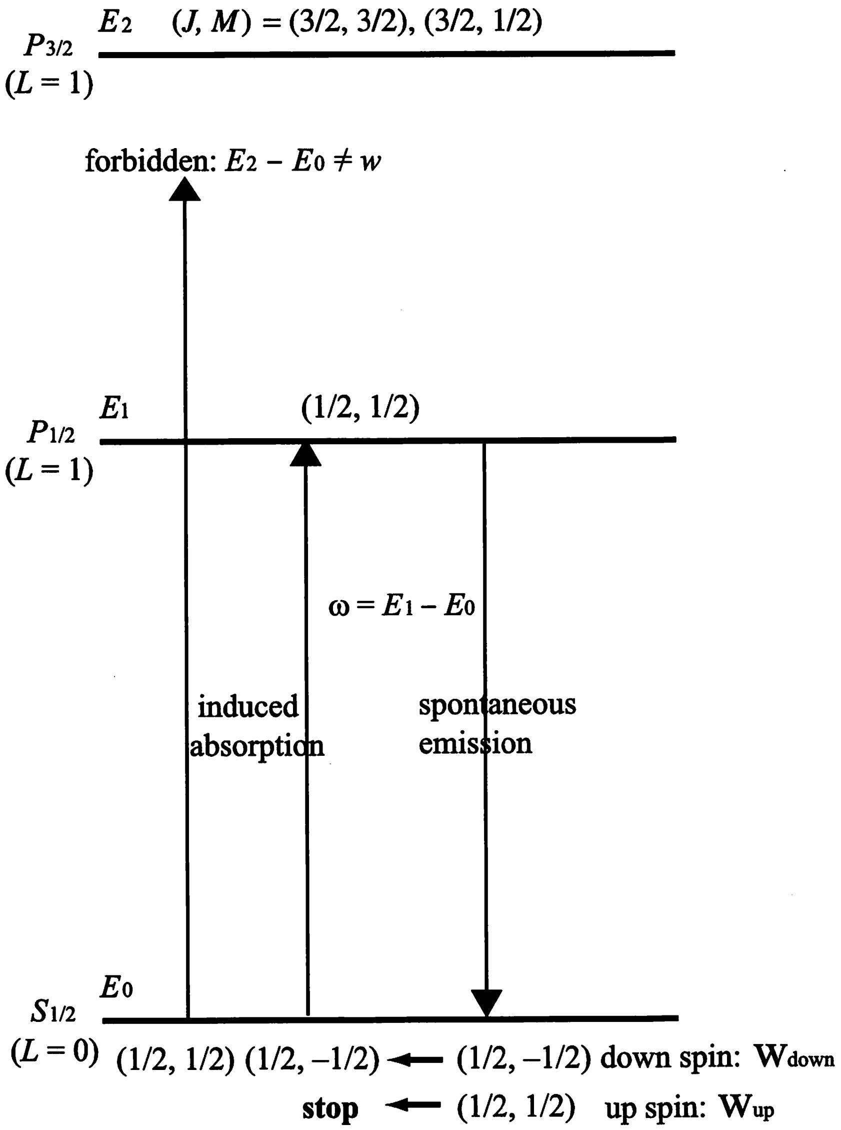

Fig. 1. Schematic energy levels and transition processes. Repeated pumping and relaxation processes result in the accumulation of the spin-up atoms.

is satisfied, the combined waves are converted into a circularly polarized evanescent wave as

$$E_{tr} = E(\boldsymbol{e}_x + i\boldsymbol{e}_y)\mathrm{e}^{iKyn\sin\theta - i\omega t - Kz\sqrt{n^2\sin^2\theta - 1}}, \tag{2}$$

$$E = \frac{2n\cos\theta}{n\cos\theta + i\sqrt{n^2\sin^2\theta - 1}}E_0. \tag{3}$$

Then, the stimulated absorption probability of atoms moving with velocity V along the line given by Eq. (1) can be written as

$$w_{i\to f} = |E|^2\mathrm{e}^{-2KQ_z\sqrt{n^2\sin^2\theta-1}}|\langle f|T_+|i\rangle|^2 2\pi\delta(\omega_{fi} + KVn\sin\theta - \omega), \tag{4}$$

where Q_z is the z component of the position of the centre of mass of each atom whose resonance frequency, initial and final states are denoted as ω_{fi}, $|i\rangle$, and $|f\rangle$, respectively, and T_+ is the spherical harmonic tensor that increases the z component of the total angular momentum of each atom by one. Let the initial state $|i\rangle$ be $|S_{1/2}\rangle$ for an alkali atom; then the valence electron is either in the spin-up state $(J, M) = (1/2, 1/2)$ or the spin-down state $(J, M) = (1/2, -1/2)$. The final state $|f\rangle$ can be either $|P_{1/2}\rangle$ or $|P_{3/2}\rangle$. However, we can selectively eliminate the $|P_{3/2}\rangle$ state by red detuning, and all the atoms in the spin-down state $(J, M) = (1/2, -1/2)$ are excited to the $|P_{1/2}\rangle$ state by stimulated absorption, whereas all the atoms in the spin-up state $(J, M) = (1/2, 1/2)$ remain in the same state. Because atoms in the $|P_{1/2}\rangle$ state relax to either the $(J, M) = (1/2, 1/2)$ or $(J, M) = (1/2, -1/2)$ state by spontaneous emission, repetitions of the pumping process lead to spin polarization of the final atoms, as depicted in Fig. 1. When the emitted photons are unpolarized, i.e. $|e_x|^2 = |e_y|^2 = |e_z|^2$, the ratio of relaxation probability w_{up} to w_{down} is given as

$$R = \frac{w_{up}}{w_{down}} = \frac{|e_z|^2}{|e_x|^2 + |e_y|^2} = \frac{1}{2}, \tag{5}$$

where w_{up} means the relaxation probability from the $|P_{1/2}\rangle$ state to the spin-up state, and w_{down} stands for the relaxation probability from the $|P_{1/2}\rangle$ state to the spin-down state. This indicates that one can efficiently align the spins of atoms as the ratio R increases.

3. Spontaneous emission under planar boundary conditions

In order to examine the effects of a planar boundary on the transition probabilities w_{up} and w_{down}, and their ratio R, discussed above, we use the CM modes (see Appendix), which form a complete, orthonormal basis set for the quantization of electromagnetic fields with an infinite planar boundary. Starting with the following total Hamiltonian of the system,

$$\mathcal{H} = \mathcal{H}_0 + \mathcal{H}', \tag{6}$$

$$\mathcal{H}_0 = \mathcal{H}_{elec} + \mathcal{H}_{rad} + \mathcal{T}, \tag{7}$$

$$\mathcal{H}' = -\frac{e}{m}\boldsymbol{p}\cdot\boldsymbol{A}(\boldsymbol{Q}, t), \tag{8}$$

the spontaneous emission rate per unit time is investigated. Here $\mathcal{H}_0$ is the unperturbed part, and consists of three parts, $\mathcal{H}_{elec}$, $\mathcal{H}_{rad}$ and $\mathcal{T}$, which describe a valence electron, the electromagnetic fields expressed as Eq. (A9) in terms of the CM modes, and the translational motion of an atom, respectively. The interaction of the valence electron with the electromagnetic fields $\mathcal{H}'$ is given by Eq. (8), where e, m, $\boldsymbol{p}$ and $\boldsymbol{A}(\boldsymbol{Q}, t)$ represent the electric charge, mass, momentum of the electron, and the vector potential at position $\boldsymbol{Q}$ of the centre of mass of the atom at time t, respectively. The explicit form of the vector potential is given as Eq. (A8) in the Appendix.

Using the time-dependent perturbation theory with respect to $\mathcal{H}'$ in Eq. (8), we can obtain the desired emission rate as

$$\begin{aligned} w_{\boldsymbol{k},\boldsymbol{\varepsilon}} &= \lim_{t\to\infty}\frac{1}{t}|\langle f|\Psi(t)\rangle|^2 \\ &= \frac{e^2\omega_{\beta\alpha}}{2\pi^2\varepsilon_0\hbar}\delta(\omega-\omega_{\beta\alpha})\mathrm{e}^{-i(\boldsymbol{K}^{*}-\boldsymbol{K})\cdot\boldsymbol{Q}}|\langle\beta|\boldsymbol{\varepsilon}\cdot\boldsymbol{r}|\alpha\rangle|^2|a(\lambda)|^2, \end{aligned} \tag{9}$$

where the final state $|f\rangle$ is assigned to state $|\beta, 1_{\boldsymbol{k},\boldsymbol{\varepsilon}}\rangle$ consisting of atomic state β and one photon state with wave vector $\boldsymbol{k}$ and polarization vector $\boldsymbol{\varepsilon}$, whereas $|\psi(t)\rangle$ is a time-evolved state from the initial state $|i\rangle = |\alpha, vac\rangle$ constructed from atomic state α and no photon state (vacuum), and the atomic resonance frequency is denoted as $\omega_{\beta,\alpha}$. Note that the explicit form of $\boldsymbol{\varepsilon}_{L(R)}(\boldsymbol{k}, \lambda, \boldsymbol{r})$ in Eq. (A4) is used as well as the conversion from $\langle\beta|\boldsymbol{e}\cdot\boldsymbol{p}|\alpha\rangle$ to $\langle\beta|\boldsymbol{e}\cdot\boldsymbol{r}|\alpha\rangle$, and that the Doppler shift due to atomic motion at velocity V is neglected.

For further evaluation, the following four cases of $w_{\boldsymbol{k},\boldsymbol{\varepsilon}}$ in Eq. (9) with respect to emitted photons are considered:

$$\text{Emitted photon} = \begin{cases} \text{homogeneous } (\theta < \theta_c) & \begin{cases} \boldsymbol{\varepsilon} = s\text{-polarization} \\ \boldsymbol{\varepsilon} = p\text{-polarization} \end{cases} \\ \text{evanescent } (\theta > \theta_c) & \begin{cases} \boldsymbol{\varepsilon} = s\text{-polarization} \\ \boldsymbol{\varepsilon} = p\text{-polarization} \end{cases} \end{cases}$$

As illustrated in Fig. 2, homogeneous waves are described by the R-mode, whereas evanescent waves are expressed in terms of the L-mode. From this classification, we can obtain the directional-dependent emission rate as

$$w^R_{up}(\boldsymbol{K}, s) = 0, \tag{10}$$

$$w^R_{up}(\boldsymbol{K}, p) = \frac{1}{4}F(k)\sin^2\theta', \tag{11}$$

$$w^L_{up}(\boldsymbol{k}, s) = 0, \tag{12}$$

$$w^L_{up}(\boldsymbol{k}, p) = F(k)\frac{n^2\cos^2\theta\sin^2\theta}{\cos^2\theta + n^2(n^2\sin^2\theta - 1)}\mathrm{e}^{-2Q_z\frac{\omega}{c}\sqrt{n^2\sin^2\theta-1}}, \tag{13}$$

$$w^R_{down}(\boldsymbol{K}, s) = \frac{1}{4}F(k), \tag{14}$$

$$w^R_{down}(\boldsymbol{K}, p) = \frac{1}{4}F(k)\cos^2\theta', \tag{15}$$

$$w^L_{down}(\boldsymbol{k}, s) = F(k)\frac{\cos^2\theta}{n^2 - 1}\mathrm{e}^{-2Q_z\frac{\omega}{c}\sqrt{n^2\sin^2\theta-1}}, \tag{16}$$

$$w^L_{down}(\boldsymbol{k}, p) = F(k)\frac{(n^2\sin^2\theta - 1)\cos^2\theta}{\cos^2\theta + n^2(n^2\sin^2\theta - 1)}\mathrm{e}^{-2Q_z\frac{\omega}{c}\sqrt{n^2\sin^2\theta-1}}, \tag{17}$$

$$F(k) = \frac{(ec)^2}{4\pi^2\hbar\omega}\omega^2_{\alpha\beta}\left|\left\langle a\frac{1}{2}\middle\|T^{(1)}\middle\|b\frac{1}{2}\right\rangle\right|^2\left|\left\langle\frac{1}{2}, 1; \frac{1}{2}, -1\middle|\frac{1}{2} - \frac{1}{2}\right\rangle\right|^2\delta(\omega - \omega_{\alpha\beta}), \tag{18}$$

where θ' represents the incident or transmitted angle on the vacuum side, while $\langle\frac{1}{2}, 1; \frac{1}{2}, -1|\frac{1}{2} - \frac{1}{2}\rangle$ and $\langle a\frac{1}{2}\|T^{(1)}\|b\frac{1}{2}\rangle$ denote the Clebsh–Gordan coefficient and the reduced matrix element, respectively. The notation for each expression on the left hand side of Eqs (10–17) is summarized in Table 1. Corresponding to the probability ratio R defined in Eq. (5), we integrate each directional-dependent emission rate in Eqs (10–17) with respect to the emission direction and sum them regarding the polarization as

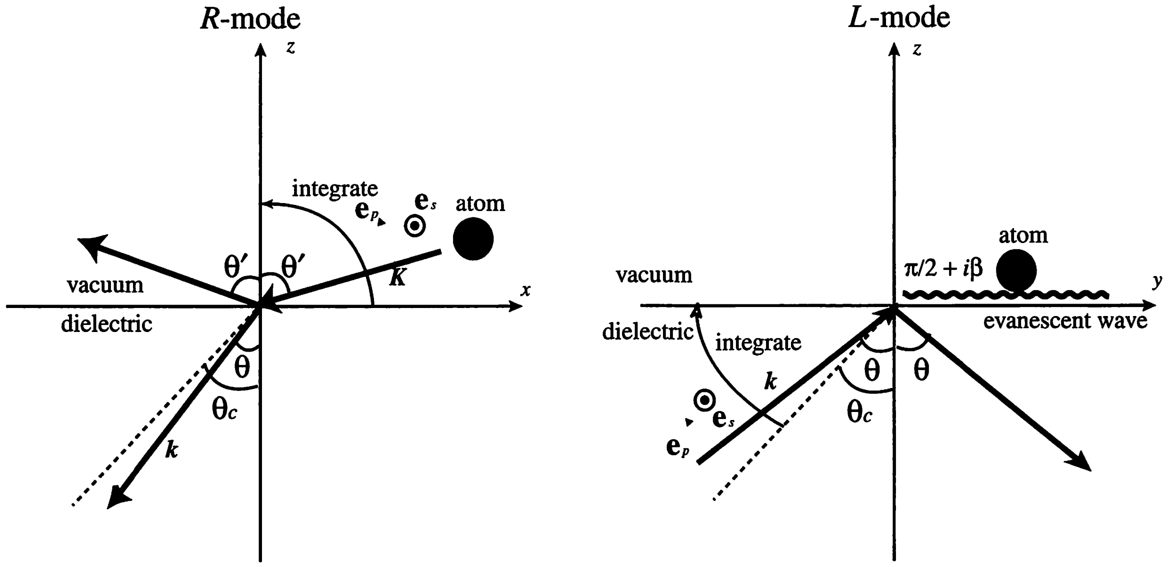

Fig. 2. Photon emission from an atom. The R-mode corresponds to homogeneous waves emitted by the atom, and the L-mode corresponds to evanescent waves. Integration range of θ' for the R-mode varies from 0 to $\pi/2$ and θ for the L-mode ranges from θ_c to $\pi/2$.

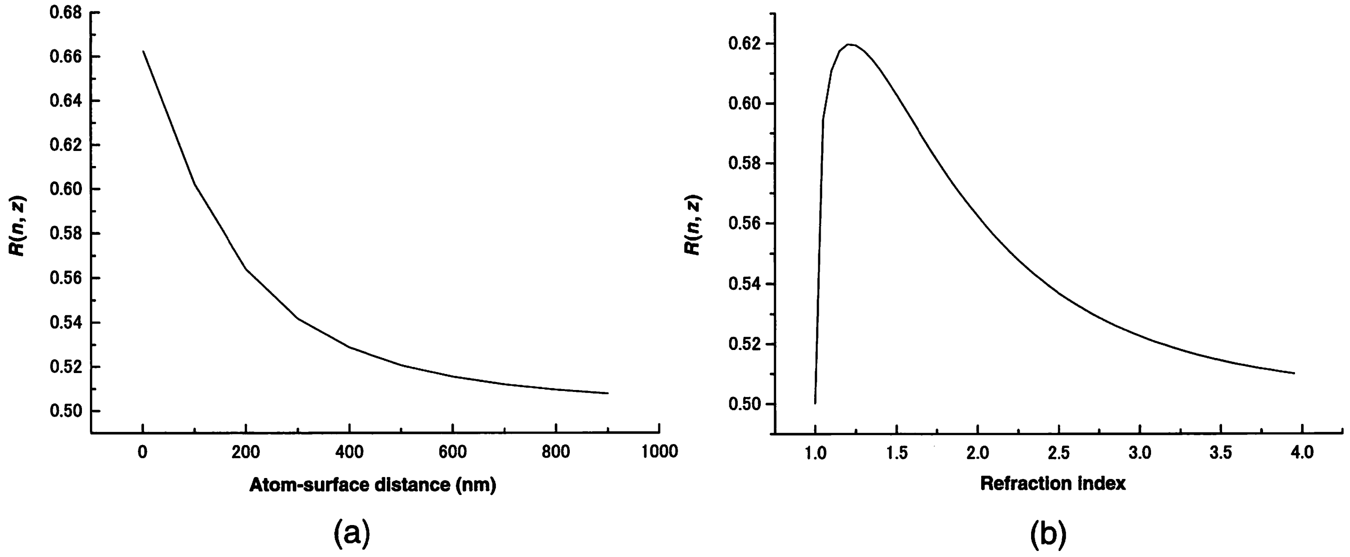

Fig. 3. Transition probability ratio $R(n, z) = w_{up}/w_{down}$ as a function of (a) atom–surface distance and (b) refractive index. We assume $n = 1.5$ in (a), and $z = 10$ nm in (b).

Table 1: Transition probabilities to the spin-up and spin-down states depending on the polarization for the R-mode and L-mode.

transition	homogeneous ! JRmode ! K		evanescent ! JLmode ! K	
$\|P_J, M\rangle \rightarrow \|S_{J'}, M'\rangle$	s-polarization	p-polarization	s-polarization	p-polarization
$\left\|P_{\frac{1}{2}}, \frac{1}{2}\right\rangle \rightarrow \left\|S_{\frac{1}{2}}, \frac{1}{2}\right\rangle$ (w_{up})	$w^R_{up}(\boldsymbol{K}, s)$	$w^R_{up}(\boldsymbol{K}, p)$	$w^L_{up}(\boldsymbol{k}, s)$	$w^L_{up}(\boldsymbol{k}, p)$
$\left\|P_{\frac{1}{2}}, \frac{1}{2}\right\rangle \rightarrow \left\|S_{\frac{1}{2}}, -\frac{1}{2}\right\rangle$ (w_{down})	$w^R_{down}(\boldsymbol{K}, s)$	$w^R_{down}(\boldsymbol{K}, p)$	$w^L_{down}(\boldsymbol{k}, s)$	$w^L_{down}(\boldsymbol{k}, p)$

$$w_{up} = \int d\Omega[w^{R}_{up}(K, s) + w^{R}_{up}(K, p)] + \int d\Omega'[w^{L}_{up}(k, s) + w^{L}_{up}(k, p)], \tag{19}$$

$$w_{down} = \int d\Omega[w^{R}_{down}(K, s) + w^{R}_{down}(K, p)]$$

$$+ \int d\Omega'[w^{L}_{down}(k, s) + w^{L}_{down}(k, p)]. \tag{20}$$

Here the integration range of θ' for the R-mode ranges from 0 to $\pi/2$, whereas θ for the L-mode ranges from θ_c to $\pi/2$. The ratio $R(n, z) = w_{up}/w_{down}$ with the refractive index n and the atom–surface distance z gives the final result, including the surface boundary effects.

As an example, we consider the transition from the $6P_{1/2}$ level to the $6S_{1/2}$ level of a Cs atom, which has a resonance energy of ≈ 1.38 eV. Figure 3(a) shows the atom–surface distance dependence of the ratio $R(n, z)$ calculated from Eqs (19 and 20). When the refractive index n is taken as 1.5, it follows from the figure that the ratio is larger than the free space value as the atoms come close to the surface, i.e. Cs atoms are more efficiently converted to the spin-up state. In addition, the ratio becomes 1/2 in Eq. (5) at the limit of an infinite atom–surface distance. Figure 3(b) shows the refractive index dependence of the ratio $R(n, z)$ when the atom–surface distance z is taken as 10 nm. We find that $R(n, z)$ has a maximum value at $n \sim 1.35$ and is enhanced by 30% compared with the value of 1/2 given in Eq. (5). This implies that the surface effects increase the spontaneous emission rate to the spin-up state. Although it is not shown in the figure, this result remains valid if the atom–surface distance is < 10 nm.

The results can be qualitatively understood as follows. The relaxation rate to the spin-up or spin-down state is approximated by

$$w_{up} \sim |\langle f|T_0|i\rangle|^2|e_z|^2, \quad w_{down} \sim |\langle f|T_-|i\rangle|^2|e_-|^2, \quad e_- = (e_x - ie_y)/\sqrt{2}. \tag{21}$$

With the help of the Wigner–Eckart theorem, we obtain the following relation

$$\langle f|T_0|i\rangle = \langle f|T_-|i\rangle/\sqrt{2}. \tag{22}$$

Thus, we can approximate the ratio R as

$$R(n, z) \sim \frac{|e_z|^2}{2|e_-|^2}. \tag{23}$$

The increase in the relaxation rate to the spin-up state comes from the increase in $|e_z|$, i.e. the z-component of the electromagnetic field, which can be produced by the image dipole due to the planar surface effect.

4. Conclusions

In terms of the CM mode expansion of electromagnetic fields, we investigated the effects of a dielectric planar surface on the spin-control method proposed by Hori *et al.* (1996). Using the derived formulae, we showed the dependence of the relaxation probability ratio $R(n, z) = w_{up}/w_{down}$ on the atom–surface distance and the refractive index for the $6P_{1/2}$–$6S_{1/2}$ levels of a Cs atom numerically. The main result indicates that the ratio has a maximum value at $n \sim 1.35$, which is enhanced by 30% over the free space value. This means that the surface effects increase the spontaneous emission rate to the spin-up state. Therefore, one can efficiently align the spins of atoms in repeated laser cycles of state-selective excitation and spontaneous emission.

Inoue & Hori (2001) recently discussed the spontaneous emission of atoms near a dielectric surface, using the CM modes, and showed the quantum interference effects on the angular dependence of the spontaneous emission with the help of the detector modes. It will be interesting to include these quantum effects in our studies in the near future. Because the CM modes form a basis set of the quantization of the electromagnetic fields, we can discuss the quantum properties of the evanescent field such as the possibility of the squeezed state of the evanescent field.

It will also be interesting to find a normal mode for other types of boundary, such as a fibre tip, and to discuss atom manipulation using such a probe (Kobayashi *et al.*, 2001), in the same manner as the CM mode for a planar boundary.

Acknowledgement

The authors are grateful to H. Hori for stimulating discussions.

References

Bialynicki-Birula, I. & Brojan, J. (1972) Completeness of evanescent waves. *Phys. Rev. D*, **5**, 485–487.

Carniglia, C. & Mandel, L. (1971) Quantization of evanescent electromagnetic waves. *Phys. Rev. D*, **3**, 280–296.

Hori, H., Kitahara, K. & Ohtsu, M. (1996) Comment on the possibility of longitudinal electromagnetic waves on the surface of dielectrics. *Abstracts of the 1st Asia-Pacific Workshop on Near Field Optics*, **49**.

Inoue, T. & Hori, H. (2001) Quantization of evanescent electromagnetic waves based on detector modes. *Phys. Rev. A*, **63**, 063805-1-16.

Kobayashi, K., Sangu, S., Ito, H. & Ohtsu, M. (2001) Near-field optical potential for a neutral atom. *Phys. Rev. A*, **63**, 013806-1-9.

Ohdaira, Y., Kijima, K., Terasawa, K., Kawai, M., Hori, H. & Kitahara, K. (2001) State-selective optical near-field resonant ionization spectroscopy of atoms near a dielectric surface. *J. Microsc.* **202**, 255–260.

Ohtsu, M., Kobayashi, K., Kawazoe, T., Sangu, S. & Yatsui, T. (2002) Nanophotonics: design, fabrication, and operation of nanometric devices using optical near fields. *IEEE J. Sel. Topics Quantum Electron.* **8**, in press.

Appendix

Here we present some useful expressions related to the CM mode of electromagnetic fields. In order to describe the electromagnetic field with a planar interface, we use the solutions $\boldsymbol{\varepsilon}_L$ and $\boldsymbol{\varepsilon}_R$ of the Helmholtz equation

$$\nabla^2 \boldsymbol{\varepsilon}_{L(R)}(\boldsymbol{k}, \lambda, \boldsymbol{r}) + \frac{n^2(\boldsymbol{r})\omega^2}{c^2}\boldsymbol{\varepsilon}_{L(R)}(\boldsymbol{k}, \lambda, \boldsymbol{r}) = 0, \quad \text{where}$$

$$n(\boldsymbol{r}) = \begin{cases} 1, & z > 0, \\ n, & z < 0, \end{cases} \tag{A1}$$

where λ stands for *s*- or *p*-polarization. In addition, the suffix *R* indicates the *R*-mode, in which plane waves are incident from the vacuum side, and *L* designates the *L*-mode, in which plane waves are incident from the dielectric side (see Fig. A1). From incident $\boldsymbol{\varepsilon}^I$, reflected $\boldsymbol{\varepsilon}^R$, and transmitted $\boldsymbol{\varepsilon}^T$ waves as solutions of Eq. (A1), the CM mode functions are defined as

$$\boldsymbol{\varepsilon}_L(\boldsymbol{k}, \lambda, \boldsymbol{r}) = \boldsymbol{\varepsilon}_L^I(\boldsymbol{k}, \lambda, \boldsymbol{r}) + \boldsymbol{\varepsilon}_L^R(\boldsymbol{k}, \lambda, \boldsymbol{r}) + \boldsymbol{\varepsilon}_L^T(\boldsymbol{k}, \lambda, \boldsymbol{r}), \tag{A2}$$

$$\boldsymbol{\varepsilon}_R(\boldsymbol{K}, \lambda, \boldsymbol{r}) = \boldsymbol{\varepsilon}_R^I(\boldsymbol{K}, \lambda, \boldsymbol{r}) + \boldsymbol{\varepsilon}_R^R(\boldsymbol{K}, \lambda, \boldsymbol{r}) + \boldsymbol{\varepsilon}_R^T(\boldsymbol{K}, \lambda, \boldsymbol{r}). \tag{A3}$$

Because these mode functions form a complete orthonormal set for transverse fields (Bialynicki-Birula & Brojan, 1972; Carniglia & Mandel, 1971), we can expand an arbitrary electric field using the CM modes as follows:

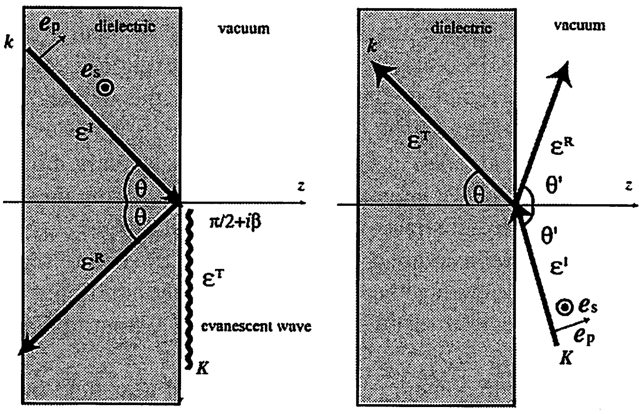

L-mode *R*-mode

Fig. A1. CM triplet modes: the *R*-mode (left) and the *L*-mode (right). Only the *L*-mode includes evanescent waves.

$$\hat{\boldsymbol{E}}(\boldsymbol{r}, t) = \frac{1}{(2\pi)^3}\sum_{\lambda}\left\{\int_{k_3>0} d^3k \sqrt{\frac{\hbar\omega}{\varepsilon_0}}(\boldsymbol{\varepsilon}_L(\boldsymbol{k}, \lambda, \boldsymbol{r})\hat{u}(\boldsymbol{k}, \lambda)e^{-i\omega t} + h.c.)\right.$$

$$\left. + \int_{K_3<0} d^3K \sqrt{\frac{\hbar\omega}{\varepsilon_0}}(\boldsymbol{\varepsilon}_R(\boldsymbol{K}, \lambda, \boldsymbol{r})\hat{v}(\boldsymbol{K}, \lambda)e^{-i\omega t} + h.c.)\right\}, \tag{A4}$$

where $\hat{u}$ and $\hat{v}$ obey the following commutation relations:

$$[\hat{u}(\boldsymbol{k}, \lambda), \hat{u}^\dagger(\boldsymbol{k}', \lambda')] = (2\pi)^3\hbar\delta(\boldsymbol{k} - \boldsymbol{k}')\delta_{\lambda\lambda'}, \tag{A5}$$

$$[\hat{v}(\boldsymbol{K}, \lambda), \hat{v}^\dagger(\boldsymbol{K}', \lambda')] = (2\pi)^3\hbar\delta(\boldsymbol{K} - \boldsymbol{K}')\delta_{\lambda\lambda'}, \tag{A6}$$

and the CM mode functions are described as

$$\boldsymbol{\varepsilon}_{R(L)}(\boldsymbol{k}, \lambda, \boldsymbol{r}) = \boldsymbol{e}(\lambda)a_{R(L)}(\lambda)e^{i\boldsymbol{k}\cdot\boldsymbol{r}}, \tag{A7}$$

with the polarization vector $\boldsymbol{e}(\lambda)$ and Fresnel's coefficient $a_{R(L)}(\lambda)$. Using the relation $\boldsymbol{E} = -\partial\boldsymbol{A}/\partial t$ for Eq. (A4), we can also express the vector potential in terms of the CM mode as

$$\boldsymbol{A}(\boldsymbol{r}, t) = -\frac{i}{(2\pi)^3}\sum_{\lambda}\left\{\int_{k_3>0} d^3k \sqrt{\frac{\hbar}{\varepsilon_0\omega}}(\boldsymbol{\varepsilon}_L(\boldsymbol{k}, \lambda, \boldsymbol{r})\hat{u}(\boldsymbol{k}, \lambda)e^{-i\omega t} - h.c.)\right.$$

$$\left. + \int_{K_3<0} d^3K \sqrt{\frac{\hbar}{\varepsilon_0\omega}}(\boldsymbol{\varepsilon}_R(\boldsymbol{K}, \lambda, \boldsymbol{r})\hat{v}(\boldsymbol{K}, \lambda)e^{-i\omega t} - h.c.)\right\}. \tag{A8}$$

Owing to the relation $\nabla \times \boldsymbol{E} = -\partial\boldsymbol{B}/\partial t$, analogous formulas hold for magnetic fields, with the annihilation operators $\hat{u}$ and $\hat{v}$ in common. Therefore, the Hamiltonian for the electromagnetic field is described by the CM modes as:

$$\mathscr{H} = \frac{1}{2}\int d^3r\{\boldsymbol{D}\cdot\boldsymbol{E} + \boldsymbol{B}\cdot\boldsymbol{H}\}$$

$$= \frac{1}{(2\pi)^3}\sum_{\lambda}\left\{\int_{K_3>0} d^3k\,\hbar\omega\,\hat{u}^\dagger(\boldsymbol{k}, \lambda)\hat{u}(\boldsymbol{k}, \lambda)\right.$$

$$\left. + \int_{K_3<0} d^3K\,\hbar\omega\,\hat{v}^\dagger(\boldsymbol{K}, \lambda)\hat{v}(\boldsymbol{K}, \lambda)\right\}. \tag{A9}$$

It follows that the CM modes form normal modes for the planar boundary condition and $\hat{u}$, $\hat{u}^\dagger$ and $\hat{v}$, $\hat{v}^\dagger$ are the annihilation and creation operators for *L*-mode and *R*-mode photons, respectively.

APPLIED PHYSICS LETTERS VOLUME 82, NUMBER 18 5 MAY 2003

Demonstration of a nanophotonic switching operation by optical near-field energy transfer

Tadashi Kawazoe,[a] Kiyoshi Kobayashi, and Suguru Sangu
Exploratory Research for Advanced Technology (ERATO), Japan Science and Technology Corporation (JST), 687-1 Tsuruma, Machida, Tokyo 194-0004, Japan
Motoichi Ohtsu[b]
Interdisciplinary Graduate School of Science and Engineering, Tokyo Institute of Technology, 4259 Nagatsuta, Midori-ku, Yokohama 226-8502, Japan

(Received 3 January 2003; accepted 27 February 2003)

We have demonstrated the operation of a nanophotonic switch that uses three CuCl quantum cubes with a size ratio of $1:\sqrt{2}:2$. The switching mechanism is based on resonant optical near-field energy transfer between the resonant quantized excitonic energy levels of the quantum cubes. Using near-field optical spectroscopy, we observed a switching rise time of less than 100 ps and a repetition rate of 80 MHz. These results suggest the possibility of making a nanophotonic switching device smaller than 20 nm with a figure of merit 10–100 times higher than that of a conventional photonic switch. © *2003 American Institute of Physics.* [DOI: 10.1063/1.1571977]

Optical fiber transmission systems require increased integration of photonic devices for higher data transmission rates. It is estimated that the size of photonic matrix switching devices should be reduced to a subwavelength scale, as in the near future it will be necessary to integrate more than 1000× 1000 input and output channels on a substrate.[1] Since conventional photonic devices, e.g., diode lasers and optical waveguides, have to confine lightwaves within their cavities and core layers, respectively, their minimum sizes are limited by the diffraction of light.[2] Therefore, they cannot meet the size requirement, which is beyond this diffraction limit. It can be readily understood that to support optical science and technology in the 21st century, optical nanotechnology that goes beyond the diffraction limit is required.

An optical near field is free from the diffraction of light and enables the operation and integration of nanometric optical devices. Namely, by using a localized optical near field as the carrier, which is transmitted from one nanometric element to another, the above requirements can be met. Based on this idea, we have proposed optical nanotechnology that uses the optical near field, i.e., nanophotonics, to realize nanometer-sized photonic devices and their integration.[1] The primary advantage of nanophotonics is the capacity to achieve functions that are based on local electromagnetic interactions, while realizing nanometer-sized photonic devices.

Since a nanometric all-optical switch (i.e., a nanophotonic switch) is a key device in such nanophotonic integrated circuits (ICs), we have been researching operation using a coupled quantum-dot (QD) system. In this letter, we report the demonstration of repetitive operation of a nanophotonic switch, using three CuCl QDs.[3] The optically forbidden energy transfer between neighboring CuCl QDs via optical near-field interaction, confirmed by the authors, is a key phenomenon for this operation.

We used cubic CuCl QDs, i.e., quantum cubes (QCs), in a NaCl matrix. It is well known that the translational motion of the exciton center of mass in CuCl QCs is quantized due to the small exciton Bohr radius.[4] When closely spaced QCs with quantized energy levels resonate with each other, near-field energy transfer occurs between them, even if the transfer is optically forbidden.[3] Figures 1(a) and 1(b) explain the "off" and "on" states of the proposed nanophotonic switch. Three QCs, $\mathrm{QC_{in}}$, $\mathrm{QC_{out}}$, and $\mathrm{QC_{control}}$, are used as the input, output, and control ports of the switch, respectively. Assuming an effective size ratio of $1:\sqrt{2}:2$, quantized energy levels (1,1,1) in $\mathrm{QC_{in}}$, (2,1,1) in $\mathrm{QC_{out}}$, and (2,2,2) in $\mathrm{QC_{control}}$ resonate with each other. Furthermore, energy levels (1,1,1) in $\mathrm{QC_{out}}$ and (2,1,1) in $\mathrm{QC_{control}}$ also resonate. In the off operation [Fig. 1(a)], almost all of the exciton energy in $\mathrm{QC_{in}}$ is transferred to the (1,1,1) level in the neighboring $\mathrm{QC_{out}}$, and finally, to the (1,1,1) level in $\mathrm{QC_{control}}$. Thus, the input energy escapes to $\mathrm{QC_{control}}$, and consequently, no optical output signals are generated from $\mathrm{QC_{out}}$. In the on state [Fig. 1(b)], by contrast, the escape routes to $\mathrm{QC_{control}}$ are blocked by the excitation of $\mathrm{QC_{control}}$, due to state filling in $\mathrm{QC_{control}}$ by applying the control signal; thus, the input energy is transferred to $\mathrm{QC_{out}}$ and an optical output signal is generated.

The coupling energy $V(r)$ of the optical near-field interaction is given by the Yukawa function $A\exp(-\mu r)/r$,[5] where r is the separation between the two QCs, A is the coupling coefficient, and μ is proportional to the effective mass of an optical near-field photon. Assuming that the separation r between the two QCs is 10 nm, the coupling energy, $V(r)$, is estimated to be on the order of 10^{-4} eV, which corresponds to a transfer time of 20 ps.[1] Since the near-field interaction is a local interaction, as indicated by $V(r)$, it is applicable to the operation of a nanophotonic switch and relevant devices in nanophotonic ICs.

We fabricated CuCl QCs embedded in a NaCl matrix

---

[a] Electronic mail: kawazoe@ohtsu.jst.go.jp

[b] Also at Exploratory Research for Advanced Technology, Japan Science and Technology Corporation, 687-1 Tsuruma, Machida, Tokyo 194-0004, Japan.

0003-6951/2003/82(18)/2957/3/$20.00

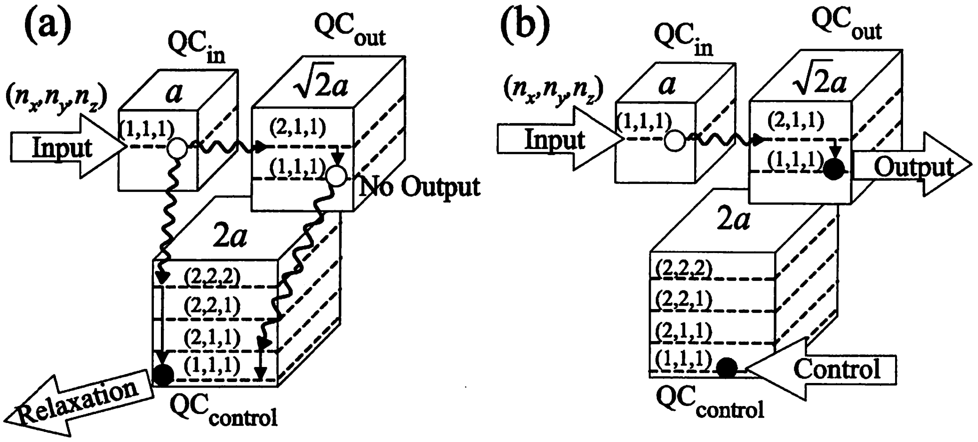

FIG. 1. Schematic explanation of a nanophotonic switch. The closely located CuCl QCs (QC$_{in}$, QC$_{out}$, and QC$_{control}$) with the effective side lengths of a $[=(L-a_B)]$, $\sqrt{2}a$, and $2a$, respectively, where L and a_B are the side lengths of the QCs and the exciton Bohr radius, respectively. n_x, n_y, and n_z represent quantum numbers of confined excitons. (a) and (b) show, respectively, the off and on states of the switch using three QCs.

using the Bridgman method.[6] By optimizing the successive annealing condition, we realized an average QC size of 4.3 nm. The sample was cleaved just before it was used in the near-field optical spectroscopy experiment in order to ensure a clean surface. The cleaved surface of the sample, which was 100 μm thick, was sufficiently flat for the experiment, i.e., its roughness was less than 50 nm, at least within the scanning area of a few μm. A double-tapered UV fiber probe was fabricated using chemical etching and coated with 150-nm-thick Al film. An aperture less than 50 nm in diameter was formed by the pounding method.[7]

To realize the switching operation, the fiber probe was carefully scanned to search for a trio of QCs that satisfied an effective size ratio of 1:$\sqrt{2}$:2 for the switching operation. Since the homogeneous linewidth of a CuCl QC increases with temperature,[8] the allowance in the resonatable size ratio is 10% at 15 K. The separation of the QCs must be less than 30 nm for the proposed switching operation, because the energy transfer time increases with separation; however, it must be shorter than the exciton lifetime. It is estimated that at least one trio of QCs exists in a 2 μm×2 μm scan area that satisfies these conditions. To demonstrate the switching operation, we found a QC trio in the sample whose sizes, L, were 3.5, 4.6, and 6.3 nm. Since their effective sizes $L-a_B$ were 2.8, 3.9, and 5.6 nm (a_B: exciton Bohr radius),[4] the size ratio was close to 1:$\sqrt{2}$:2 and they could be used as QC$_{in}$, QC$_{out}$, and QC$_{control}$, respectively. In the experiment, 379.5 and 385 nm second-harmonic generation (SHG) Ti:sapphire lasers, which were tuned to the (1,1,1) exciton energy levels of QC$_{in}$ and QC$_{control}$, respectively, were used as the input and the control light sources. The output signal was collected by the fiber probe, and its intensity was measured by a cooled microchannel plate after passing through three interference filters of 1 nm bandwidth tuned to the (1,1,1) exciton energy level in QC$_{out}$ at 383 nm.

Figures 2(a) and 2(b) show the spatial distribution of the output signal intensity in the off state, i.e., with an input signal only, and the on state, i.e., with input and control signals, using near-field spectroscopy at 15 K. The insets in Fig. 2 are schematic drawings of the existing QC trio used for the switching, which was confirmed by the near-field luminescence spectrum. Here, the separation of the QCs by less than 20 nm (drawings in Fig. 2) was theoretically estimated from time-resolved measurements, as explained in the next paragraph. In the off state, no output signal was observed, because the energy of the input signal was transferred to QC$_{control}$ and swept out as luminescence at 385 nm. To quench the output signal in the off state, which is generated by exciton accumulation in QC$_{control}$, the input signal density in QC$_{control}$ was regulated to less than 0.1 excitons. In the on state, we obtained a clear output signal in the broken circle. The output signal was proportional to the intensity of the control signal, where its density in QC$_{control}$ was 0.01–0.1 excitons. The internal quantum efficiency was close to 1.[9]

Next, the dynamic properties of the nanophotonic switch

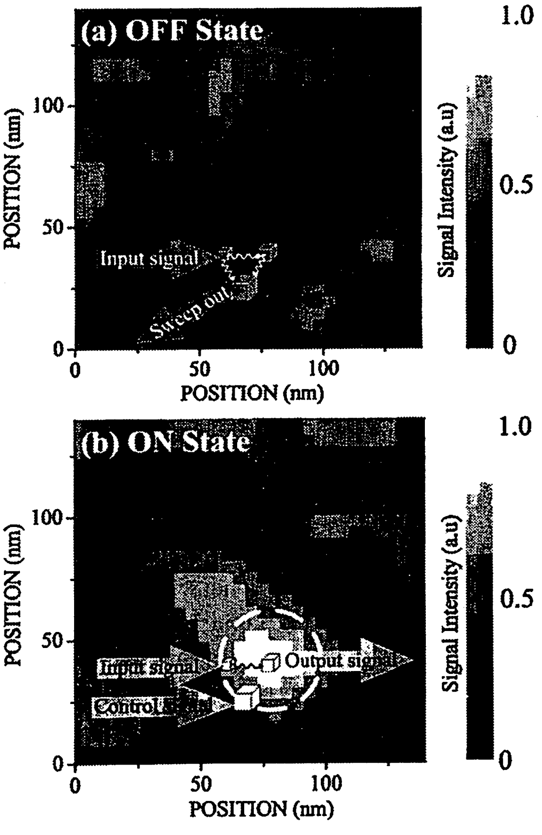

FIG. 2. Spatial distribution of the output signal from the nanophotonic switch measured by a near-field microscope, in the off (a) and on (b) states.

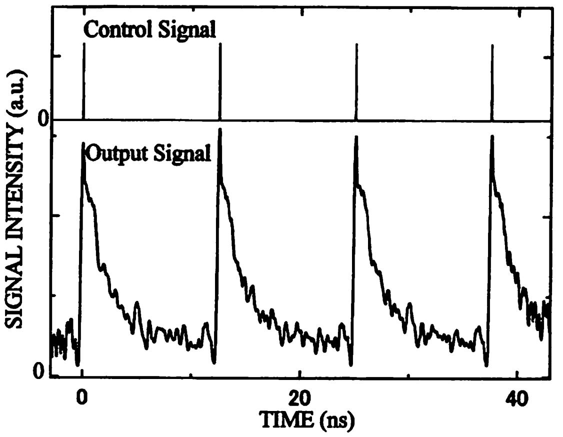

FIG. 3. Time evolution of the control pulse signal (upper part) and the output signal (lower part) from the nanophotonic switch at the broken circle in Fig. 2(b). The duration and repetition rate of the control pulse were 10 ps and 80 MHz, respectively.

were evaluated by using the time correlation single photon counting method. As a pulse-control light source, the 385 nm SHG of a mode-locked Ti–sapphire laser was used. The repetition rate of the laser was 80 MHz. To avoid cross talk of the input and control signals, which originates from spectral broadening for the pulse duration, the pulse duration of the mode-locked laser was set to be 10 ps. The time resolution of the experiment was 15 ps. Figure 3 shows the time evolution of the control pulse signal (upper part) applicable to $QC_{control}$ and the output signal (lower part) from QC_{out}. The output signal rises synchronously within less than 100 ps, with the control pulse, which agrees with the theoretically expected result based on the Yukawa model.[5] As this signal rise time is determined by the energy transfer time between the QCs, the separation between the QCs can be estimated from the rise time as being less than 20 nm;[10] the rise time can be shortened to a few ps by decreasing the separation of the QCs. Since the decay time of the output signal is limited by the exciton lifetime, this nanophotonic switch is able to operate at a few hundred MHz, and it is anticipated that the operation frequency can be increased to several GHz by means of exciton quenching using a plasmon coupling.[11] The on–off ratio was about 10, which is sufficient for use as an all-optical switch, and can be increased by a saturable absorber and electric field enhancement of the surface plasmon.[12]

The advantages of this nanophotonic switch are its small size and high-density integration capability based on the locality of the optical near field. The figure of merit (FOM) of an optical switch should be more important than the switching speed. Here, we have defined the FOM as $F = C/(Vt_{sw}P_{sw})$, where C, V, t_{sw}, and P_{sw} are the on–off ratio, the volume of the switch, the switching time, and the switching energy, respectively. The FOM of our demonstrated switch is 10–100 times higher than that of a conventional photonic switch, because its volume and switching energy are 10^{-5} times and 10^{-3} times smaller, respectively. By a conventional fabrication method, it is difficult to fabricate the nanophotonic devices, such as the QD *trio* functioning as the optical switch, because it is required that the designed sized QDs are placed at designed positions, which are closely spaced. Therefore, we are now researching materials, fabrication methods, and systems, such as ZnO dots,[13] near-field optical chemical vapor deposition,[14] and a plasmon waveguide,[15] respectively, for the realization of actual nanophotonic devices. Based on these results, we hope that this nanophotonic switching system will have applications in nanophotonic ICs and be a candidate for future data transmission systems.

In conclusion, we have demonstrated the switching operation of a nanophotonic switch using CuCl QCs embedded in a NaCl matrix. The size of the switch was estimated to be smaller than 20 nm. We experimentally showed that this optical switch can operate at a few hundred MHz. The FOM as an all-optical switch is 10–100 times higher than that of conventional optical switches. The proposed nanophotonic switch is expected to be a key device in future nanophotonic ICs.

[1] M. Ohtsu, K. Kobayashi, T. Kawazoe, S. Sangu, and T. Yatsui, IEEE J. Sel. Top. Quantum Electron. **8**, 839 (2002).
[2] A. Yariv, *Introduction to Optical Electronics* (Holt, Rinehart and Winston, New York, 1971).
[3] T. Kawazoe, K. Kobayashi, J. Lim, Y. Narita, and M. Ohtsu, Phys. Rev. Lett. **88**, 067404 (2002).
[4] N. Sakakura and Y. Masumoto, Phys. Rev. B **56**, 4051 (1997).
[5] K. Kobayashi, S. Sangu, H. Ito, and M. Ohtsu, Phys. Rev. A **63**, 013806 (2001).
[6] T. Itoh, Y. Iwabuchi, and M. Kataoka, Phys. Status Solidi B **145**, 567 (1988).
[7] T. Saiki and K. Matsuda, Appl. Phys. Lett. **74**, 2773 (1999).
[8] Landolt-Börnstein, *Physics of II–VI and I–VII Compounds, Semimagnetic Semiconductors*, Vol. 17b (Springer, Berlin, 1982).
[9] T. Kawazoe, K. Kobayashi, S. Sangu, and M. Ohtsu, J. Microsc. (to be published).
[10] S. Sangu, K. Kobayashi, A. Shojiguchi, T. Kawazoe, and M. Ohtsu, J. Appl. Phys. **93**, 2937 (2003).
[11] A. Neogi, C. W. Lee, H. O. Everitt, T. Kuroda, A. Tackeuchi, and E. Yablonovitch, Phys. Rev. B **66**, 153305 (2002).
[12] H. Raether, *Surface Plasmons*, Springer Tracts in Modern Physics, Vol. III (Springer, Berlin, 1988).
[13] T. Yatsui, T. Kawazoe, T. Shimizu, Y. Yamamoto, M. Ueda, M. Kourogi, M. Ohtsu, and G. H. Lee, Appl. Phys. Lett. **80**, 1444 (2002).
[14] T. Kawazoe, Y. Yamamoto, and M. Ohtsu, Appl. Phys. Lett. **79**, 1184 (2001).
[15] T. Yatsui, M. Kourogi, and M. Ohtsu, Appl. Phys. Lett. **79**, 4583 (2001).

JOURNAL OF APPLIED PHYSICS VOLUME 93, NUMBER 5 1 MARCH 2003

Excitation energy transfer and population dynamics in a quantum dot system induced by optical near-field interaction

S. Sangu,[a] K. Kobayashi, A. Shojiguchi, and T. Kawazoe
ERATO Localized Photon Project, Japan Science and Technology Corporation, 687-1 Tsuruma, Machida, Tokyo 194-0004, Japan

M. Ohtsu[b]
Interdisciplinary Graduate School of Science and Engineering, Tokyo Institute of Technology, 4259 Nagatsuta-cho, Midori-ku, Yokohama, Kanagawa 226-8502, Japan

(Received 11 June 2002; accepted 4 December 2002)

Energy transfer and exciton population dynamics in a two-quantum dot system coupled with a phonon heat-bath system are examined using the density matrix formalism. In such a system, optical near-field interactions induce energy transfer between quantum dots, and exciton–phonon interactions guarantee the unidirectional excitation energy transfer. Our theoretical investigation shows that the population dynamics change drastically depending on the coupling strengths due to optical near-field interactions and exciton–phonon heat-bath interactions. The temperature effect promotes frequent energy back-transfer from the heat-bath to the quantum dot system. Applying our theoretical formulation, we numerically calculate the time evolution of populations, and estimate energy transfer time or state-filling time for a CuCl quantum dot system. The estimated time is suitable for the elements in our proposed optical nano-switch and nano-photonic devices. © *2003 American Institute of Physics.* [DOI: 10.1063/1.1540739]

I. INTRODUCTION

In order to satisfy future demands for an increase in communication capacity and information processing, photonic devices must be ultrahighly integrated, and thus the size of each functional block will be so small that it is far beyond the diffraction limit of light. To this end, we have studied how to fabricate, operate, and control such devices using a novel technology, named nano-photonics,[1] which is defined as a technology that utilizes local electromagnetic interactions between a nanometric element and optical near fields. We have proposed a photochemical vapor deposition method using optical near fields to create nanometric structures with arbitrary position and size,[2–5] and have successfully fabricated Zn, Al, and ZnO nano-dots smaller than 50 nm.[4,5] Control of such nano-photonic devices requires coherent interactions between the nanometric element and optical near fields. So far, exciton populations in a single isolated quantum dot have been coherently controlled using a far-field light pulse.[6–9] Since our proposed nano-photonic devices are constructed from a collection of nanometric elements, spatially localized optical near fields are indispensable for the selective control and manipulation of the electronic states of a single nanometric object. In order to realize a nano-photonic device constructed using these methods, it is essential to investigate the mechanism of signal or energy transfer among nanometric objects via optical near fields, as well as to clarify the principles of operation.

The excitation energy transfer between nanometric objects has been extensively studied in various disciplines.[10–14] One of its basic underlying principles is the static dipole–dipole interaction between two objects.[10] In the nanometric regime, this involves a characteristic phenomenon: dipole-forbidden transition. The breakdown of the dipole selection rule for a quantum dot chain in scanning near-field optical microscopy has been shown in the framework of a semiclassical nonlocal theory.[12] Similarly, Mukai *et al.*[13] reported an optically forbidden energy transfer from an outer ring of loosely packed bacteriochlorophyll molecules to an inner ring of closely packed bacteriochlorophyll molecules in the light-harvesting antenna complex of photosynthetic purple bacteria. These observations imply that the local distribution structure of the electric dipole moments in a sample can be spatially resolved when the objects approach each other on a nanometer scale. Such energy transfer can occur between two quantum dots with dipole-forbidden energy levels, and this has been demonstrated experimentally.[14] In the nano-photonic devices discussed below, energy transfer is driven by optical near fields or photons dressed by the excitation of a macroscopic material system, such as the substrate, matrix, or an optical fiber probe.[15–17] Therefore this originates from a renormalized dipole–dipole interaction due to polariton mediation, not a static dipole–dipole interaction.

We have proposed a nano-photonic switch as a basic element of nano-photonic devices.[18] Figure 1 illustrates a switch that consists of three quantum dots (cubes) with discrete exciton-energy levels that depend on dot size. The one-side lengths of these cubes are chosen in the ratio $1:\sqrt{2}:2$, so that the adjacent dots have resonant energy levels. The principle of operation of the switch is as follows: as shown in Fig. 1(a), an exciton population is created at the (1,1,1)-level

---

[a] Author to whom correspondence should be addressed; electronic mail: sangu@ohtsu.jst.go.jp

[b] Also with ERATO Localized Photon Project, Japan Science and Technology Corporation, 687-1 Tsuruma, Machida, Tokyo 194-0004, Japan.

0021-8979/2003/93(5)/2937/9/$20.00

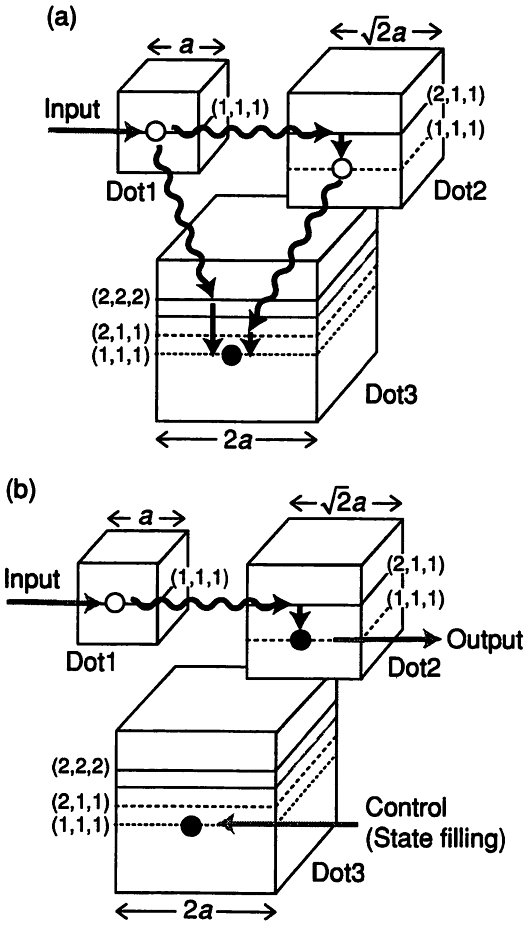

FIG. 1. A nano-photonic switch consisting of three quantum dots with discrete energy levels showing the (a) OFF and (b) ON states.

in dot 1 as an initial condition. Then the population is transferred to dots 2 and 3 as a result of optical near-field coupling. Owing to the fast relaxation between sublevels in each dot via exciton-phonon coupling, the population is transferred to lower energy levels, and finally collected at the lowest (1,1,1)-level in dot 3. This corresponds to the OFF-state of the switch, and, consequently, we obtain no output signals from the output port, i.e., the (1,1,1)-level in dot 2. By contrast, in the ON-state of the switch [Fig. 1(b)], the (1,1,1)-level in dot 3 is initially filled by the control field, isolating dot 3 from the other two dots. The input population only reaches the (1,1,1)-level in dot 2 and can be detected as output signals, either by near-field coupling to the detector or by far-field light emitted with electron–hole recombination.

From this explanation of the principle of operation, it follows that the key parameters determining the response time of the device are the coupling strength of two quantum dots via optical near fields, and that of the exciton and phonon heat bath. The purpose of this article is to analyze the dynamical properties of exciton populations by numerically clarifying the roles of the key parameters, based on our formulation of a quantum dot system that interacts with optical near fields and phonon fields. This allows us to discuss the dynamical properties of the proposed switch as a typical example of nano-photonic devices. We estimate the response time for CuCl quantum cubes, which have been extensively examined in experimental and theoretical studies of quantum dots.[19–22] For simplicity, we restrict ourselves to a two-quantum dot system (dots 1 and 2), and describe dynamics quantum mechanically using the density matrix formalism, since the energy transfer between the two quantum dots is followed by coherence of the resonant levels.

The article is organized as follows. Section II discusses energy transfer in a two-resonant level system based on our formulation of optical near-field interactions. As a competitor of optical near-field coupling, phonon heat-bath coupling is discussed in Sec. III. We show that the population dynamics are sensitive to the ratio of optical near-field coupling to exciton-phonon coupling and the temperature of the system. Section IV gives numerical results for the dynamics of CuCl quantum cubes. Finally, the concluding remarks are presented in Sec. V.

II. ENERGY TRANSFER INDUCED BY OPTICAL NEAR-FIELD INTERACTION

A typical optical near-field system consists of micro- and macroscopic material systems. In such a system, incident photons go through the macroscopic system and into the microscopic one, and any information that is determined by the microscopic system is via the macroscopic system. Therefore when we consider the population dynamics of a microscopic quantum dot system, it must incorporate the contribution of the macroscopic system. It is convenient to treat such a system in two steps. The first step describes photons and the macroscopic system in terms of the so-called polariton basis. Then in the second step, the interaction between the microscopic and macroscopic systems is expressed using the polariton basis. We develop a systematic formulation for the interaction, in which photons and macroscopic matter excitation are described as an elementary excitation mode, like exciton-polaritons, and then the effects of both photons and the macroscopic material system are renormalized into an effective two-body interaction between nanometric objects in the microscopic system.[15–17] Here, we call the effective interaction the optical near-field interaction. In the following sections, we first describe how the optical near-field interaction contributes to the dynamics of a two-quantum dot system with resonant energy levels using the density matrix, and then we derive an explicit form of the optical near-field interaction. As an example, a typical time scale is given for the energy transfer process in CuCl quantum cubes.

A. Interdot energy transfer via optical near fields

Let us consider a two-quantum dot system interacting with optical near fields, such as the one illustrated in Fig. 2. The model Hamiltonian of the system is written as

$$\begin{aligned}\hat{H}&=E_1\hat{A}^\dagger\hat{A}+E_1\hat{B}^\dagger\hat{B}+\sum_{\mathbf{k}} E(k)\hat{\xi}_{\mathbf{k}}^\dagger\hat{\xi}_{\mathbf{k}}+\hat{V},\\ \hat{V}&=-\sum_{\alpha=A}^{B}\hat{\boldsymbol{\mu}}_\alpha\cdot\hat{\mathbf{D}}(\mathbf{r}_\alpha),\end{aligned}\tag{1}$$

where $(\hat{A}^\dagger,\hat{A})$ and $(\hat{B}^\dagger,\hat{B})$ represent the creation and annihilation operators of an exciton in dots 1 and 2, respectively,

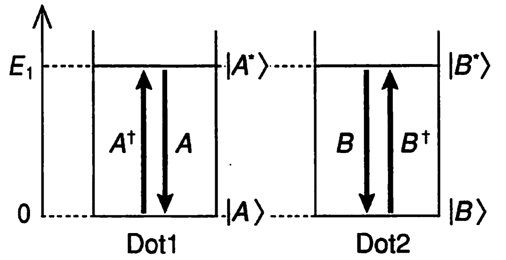

FIG. 2. Two-level quantum dots coupled via optical near fields.

with excitation energy E_1. The coupled modes of photons and the macroscopic material system, i.e., the exciton-polaritons,[23] are expressed by the creation and annihilation operators $(\hat{\xi}_{\mathbf{k}}^\dagger, \hat{\xi}_{\mathbf{k}})$ and the eigenenergy $E(k)$. The bare interaction $\hat{V}$ between the quantum dot system and the exciton-polariton fields is given by the multipolar QED Hamiltonian in the dipole approximation,[24] where $\hat{\boldsymbol{\mu}}_\alpha = \boldsymbol{\mu}_\alpha(\hat{\alpha}+\hat{\alpha}^\dagger)$ $(\hat{\alpha}=\hat{A},\hat{B})$ and $\hat{\mathbf{D}}(\mathbf{r}_\alpha)$ represent the dipole operator and electric displacement vector at position $\mathbf{r}_\alpha$, respectively. As mentioned above, $\hat{\mathbf{D}}(\mathbf{r}_\alpha)$ is expressed in terms of the exciton-polariton operators as

$$\begin{aligned} \hat{\mathbf{D}}(\mathbf{r}_\alpha) &= i\sqrt{\frac{2\pi\hbar}{V}} \sum_{\mathbf{k}} \sum_{\lambda=1}^{2} \mathbf{e}_{\mathbf{k}\lambda} f(k) (\hat{\xi}_{\mathbf{k}} e^{i\mathbf{k}\cdot\mathbf{r}_\alpha} - \hat{\xi}_{\mathbf{k}}^\dagger e^{-i\mathbf{k}\cdot\mathbf{r}_\alpha}), \\ f(k) &= \frac{\hbar ck}{\sqrt{E(k)}} \sqrt{\frac{E^2(k)-E_m^2}{2E^2(k)-E_m^2-\hbar^2c^2k^2}}, \end{aligned} \tag{2}$$

where $f(k)$ is the coupling coefficient between photons and the macroscopic material system, and E_m represents the eigenenergy of the macroscopic material system.[16,17] Vector $\mathbf{e}_{\mathbf{k}\lambda}$ is the unit vector normal to the exciton-polariton wave vector $\mathbf{k}$, and $\hbar$ and c are Planck's constant divided by 2π and the velocity of light in vacuum, respectively.

The dynamics of the system are governed by the following Liouville equation

$$\dot{\hat{\rho}}_{\text{total}}(t) = -\frac{i}{\hbar}[\hat{H}, \hat{\rho}_{\text{total}}(t)], \tag{3}$$

where $\hat{\rho}_{\text{total}}(t)$ represents the density operator of the total system,[25,26] expressed as the direct product of the microscopic system $\hat{\rho}(t)$ and the exciton-polaritons $\hat{\rho}_{\text{pol}}(t)$. In order to investigate the population dynamics in the microscopic material system, we take a trace of the exciton-polariton degrees of freedom on both sides of Eq. (3) and obtain the equation of motion for the density operator $\hat{\rho}(t) = \text{Tr}_{\text{pol}}[\hat{\rho}_{\text{total}}(t)]$ as

$$\begin{aligned} \dot{\hat{\rho}}(t) &= -\frac{i}{\hbar}[E_1(\hat{A}^\dagger\hat{A}+\hat{B}^\dagger\hat{B})+\hat{V}_{\text{dot}}, \hat{\rho}(t)], \\ \hat{V}_{\text{dot}} &= \text{Tr}_{\text{pol}}[\hat{V}\hat{\rho}_{\text{pol}}(t)], \end{aligned} \tag{4}$$

where $\text{Tr}_{\text{pol}}[\cdot]$ means to take a trace regarding the exciton-polariton degrees of freedom. We then prepare states $|\Phi_1\rangle = |A^*\rangle|B\rangle$ and $|\Phi_2\rangle = |A\rangle|B^*\rangle$ for the excited states in dots 1 and 2, respectively, in order to express Eq. (4) in the matrix form, where the weak excitation is assumed, i.e., only an exciton existing in the system. Note that the nonzero matrix elements of interaction $\hat{V}_{\text{dot}}$ are off-diagonal parts only; that is,

$$\begin{aligned} &\hbar U \equiv \langle\Phi_1|\hat{V}_{\text{dot}}|\Phi_2\rangle = \langle\Phi_2|\hat{V}_{\text{dot}}|\Phi_1\rangle, \\ &\langle\Phi_1|\hat{V}_{\text{dot}}|\Phi_1\rangle = \langle\Phi_2|\hat{V}_{\text{dot}}|\Phi_2\rangle = 0. \end{aligned} \tag{5}$$

Under the initial condition $\langle\Phi_1|\hat{\rho}(0)|\Phi_1\rangle = 1$, the matrix elements can be obtained exactly, and the population probability of staying in the excited state for dot 1 or 2 is given by the diagonal parts of the density matrix as

$$\begin{aligned} &\langle\Phi_1|\hat{\rho}(t)|\Phi_1\rangle = \sin^2(Ut), \\ &\langle\Phi_2|\hat{\rho}(t)|\Phi_2\rangle = \cos^2(Ut), \end{aligned} \tag{6}$$

As is well known, Eq. (6) shows that the temporal evolution of the population goes and returns between the two quantum dots, i.e., *nutation* occurs at Rabi frequency U.[10] In this way, the matter excitation energy can be transferred from one dot to a neighboring dot due to the interaction $\hat{V}$ as a coupling between the microscopic material system and the exciton-polariton field.

B. Optical near-field interaction between quantum dots

From the preceding section, it follows that the optical near-field interaction $\hbar U$ in Eq. (5) is a key parameter for determining the energy transfer process. The strength of the interaction has been derived systematically and consistently in our previous studies.[15–17] Here, we outline the derivation of the effective interaction, i.e., optical near-field interaction between two quantum dots, and give numerical results for the CuCl quantum cubes.

The exact eigenstates $|\Psi_\lambda\rangle$ of the total Hamiltonian $\hat{H}$ are divided into two groups: relevant states in P space $|\Psi_\lambda^P\rangle = P|\Psi_\lambda\rangle$ and irrelevant states in Q space $|\Psi_\lambda^Q\rangle = Q|\Psi_\lambda\rangle$. Here, P and Q represent projection operators with the properties $P+Q=1$, $P^2=P(Q^2=Q)$, and $P^\dagger=P(Q^\dagger=Q)$.[27] In the case shown in Fig. 2, for example, P space is constructed from the eigenstates of $\hat{H}_0$, i.e., a combination of the two energy levels for each quantum dot and the exciton-polariton vacuum state. In Q space, which is complementary to P space, the exciton-polariton states are not vacant. According to this notation, the exact state can be formally expressed by using the state in P space only as

$$\begin{aligned} &|\Psi_\lambda\rangle = \hat{J}P(P\hat{J}^\dagger\hat{J}P)^{-1/2}|\Psi_\lambda^P\rangle, \\ &\hat{J} = [1-(E_\lambda-\hat{H}_0)^{-1}Q\hat{V}]^{-1}, \end{aligned} \tag{7}$$

where E_λ represents the eigenenergy of the total Hamiltonian $\hat{H}$. Using Eq. (7), we can obtain the effective interaction $\hat{V}_{\text{eff}}$ as

$$\begin{aligned} &\langle\Psi_f|\hat{V}|\Psi_i\rangle = \langle\Psi_f^P|\hat{V}_{\text{eff}}|\Psi_i^P\rangle, \\ &\hat{V}_{\text{eff}} \equiv (P\hat{J}^\dagger\hat{J}P)^{-1/2}(P\hat{J}^\dagger\hat{V}\hat{J}P)(P\hat{J}^\dagger\hat{J}P)^{-1/2}. \end{aligned} \tag{8}$$

To further evaluate Eq. (8), we approximate operator $\hat{J}$ and eigenvalue E_λ perturbatively with respect to $\hat{V}$; that is, $\hat{J}$

$=1+(E_0^P-E_0^Q)^{-1}\hat{V}+\cdots$. Since the lowest order is $\langle\Psi_f^P|P\hat{V}P|\Psi_i^P\rangle=0$, Eq. (8) is rewritten within the second order as

$$\langle\Psi_f^P|\hat{V}_{\text{eff}}|\Psi_i^P\rangle=\sum_m \langle\Psi_f^P|\hat{V}|m^Q\rangle\langle m^Q|\hat{V}|\Psi_i^P\rangle \times\left(\frac{1}{E_{0i}^P-E_0^Q}+\frac{1}{E_{0f}^P-E_0^Q}\right), \tag{9}$$

where E_{0i}^P, E_{0f}^P, and E_0^Q represent the eigenenergies of unperturbed Hamiltonian $\hat{H}_0$ for the initial and final states in P space, and the intermediate state in Q space, respectively. Since we are primarily interested in the interdot interaction of Eq. (9), we set the relevant initial and final states in P space as $|\Psi_i^P\rangle=|A^*\rangle|B\rangle|0\rangle$ and $|\Psi_f^P\rangle=|A\rangle|B^*\rangle|0\rangle$, and then the intermediate states in Q space, $|m^Q\rangle=|A\rangle|B\rangle|\mathbf{k}\rangle$ and $|A^*\rangle|B^*\rangle|\mathbf{k}\rangle$, with a one exciton-polariton state $|\mathbf{k}\rangle$ providing nonzero contributions. Using these states, we can eliminate the exciton-polariton degrees of freedom, and obtain the optical near-field interaction between quantum dots as

$$\begin{aligned}\hbar U(\mathbf{r})&=\langle\Psi_f^P|\hat{V}_{\text{eff}}|\Psi_i^P\rangle\\ &=-\frac{\mu_A\mu_B}{6\pi^2}\int_0^\infty d^3k f^2(k)\\ &\quad\times\left\{\left[\frac{1}{E(k)+E_A}+\frac{1}{E(k)+E_B}\right]e^{i\mathbf{k}\cdot\mathbf{r}}\right.\\ &\quad\left.+\left[\frac{1}{E(k)-E_A}+\frac{1}{E(k)-E_B}\right]e^{-i\mathbf{k}\cdot\mathbf{r}}\right\},\end{aligned} \tag{10}$$

where $\mathbf{r}=\mathbf{r}_A-\mathbf{r}_B$ is the relative vector between the center positions of dots 1 and 2, and $\mu_{A(B)}$ is the transition dipole moment of dot 1(2). For the eigenenergy $E(k)$ of exciton-polaritons, the effective mass approximation

$$E(k)=\frac{\hbar^2k^2}{2m_p}+E_m \tag{11}$$

is used, where m_p and E_m denote the exciton-polariton mass and excitation energy of the macroscopic system, respectively. Substituting Eq. (11) into Eq. (10), one obtains the optical near-field interaction potential as a sum of the Yukawa functions:

$$\hbar U(r)=\frac{\mu_A\mu_B}{3(\hbar c)^2}\sum_{\alpha=A}^{B}[W_{\alpha+}Y(\Delta_{\alpha+}r)+W_{\alpha-}Y(\Delta_{\alpha-}r)], \tag{12}$$

where $W_{\alpha\pm}$ denotes the weight coefficient of each Yukawa function that is defined as

$$\begin{aligned}Y(\Delta_{\alpha\pm}r)&=\frac{e^{-\Delta_{\alpha\pm}r}}{r},\\ \Delta_{\alpha\pm}&=\frac{1}{\hbar c}\sqrt{2E_p(E_m\pm E_\alpha)},\end{aligned} \tag{13}$$

with the exciton-polariton effective mass rewritten as $E_p=m_pc^2$, and the relative distance $r=|\mathbf{r}_A-\mathbf{r}_B|$. The factor $\Delta_{\alpha-}$ becomes either real or imaginary depending on the magnitudes of E_m and E_α, which means that this component behaves as either a localized mode or a propagation mode. To be precise, Eq. (12) includes two additional terms that are independent of the parameters of the microscopic material system, but these terms are neglected in Eq. (12) as a far-field contribution.

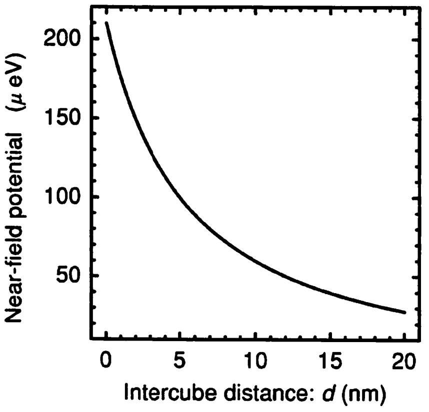

FIG. 3. The optical near-field interaction potential for two CuCl quantum cubes. The sizes of the quantum-cube pairs are set at $a=5$ and 7.1 nm (a 1:$\sqrt{2}$ ratio), respectively.

We can now estimate the strength of the effective interaction between two CuCl quantum cubes induced by optical near fields. When two-level exciton states are chosen as the microscopic material states in P space, the excitation energy of an exciton in a quantum cube is represented by

$$E_\alpha=\frac{\pi^2\hbar^2}{2Ma^2}(n_x^2+n_y^2+n_z^2)+E_g, \quad (n_x,n_y,n_z=1,2,3,\ldots), \tag{14}$$

where M and E_g denote the exciton mass and bulk exciton energy, respectively. In Fig. 3, the interaction potential is plotted as a function of the distance between the closest edges of the quantum cubes. The sizes of the quantum cubes are set at $a=5$ and 7.1 nm (a 1:$\sqrt{2}$ ratio) and $M=2.3m_e$ and $E_g=3.2022$ eV.[19] The transition dipole moments of the quantum cubes are estimated from the experimental value of the dot oscillator strength $f_{\text{QD}}=5$,[20] and theoretical conversion,[21] and $\mu_A=0.29$ and $\mu_B=0.49\ (\text{eV nm}^3)^{1/2}$ are obtained for $a=5$ and 7.1 nm, respectively. When we choose the distance $d=10$ nm, we find that the interaction potential is about 60 μeV from Fig. 3. Therefore a quarter of an oscillation period, $\pi/(4U)$, is about 10 ps, which corresponds to the time for the initial population to be transferred to its neighbor. This is sufficiently high speed and is suitable for a nano-photonic device from the viewpoint of size and speed.

III. DYNAMICS OF A QUANTUM DOT–HEAT-BATH COUPLING SYSTEM

In order to realize nano-photonic devices operated by the optical near-field interaction discussed above, unidirectional energy transfer must be guaranteed. One way is to utilize intra-sublevel transitions due to coupling to a lattice vibration. Therefore we examine a two-dot system coupled to a

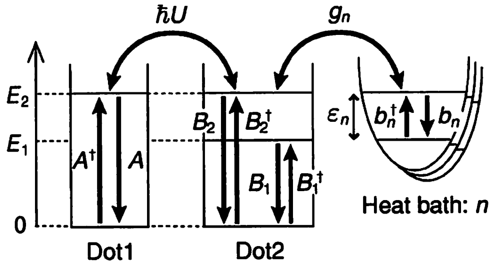

FIG. 4. Two-quantum-dot system. Dots 1 and 2 are resonantly coupled due to the optical near-field interaction, and the sublevels in dot 2 are coupled with the (phonon) heat-bath system.

phonon-(heat-) bath system as depicted schematically in Fig. 4. The Hamiltonian of such a system is modeled as

$$\begin{aligned}
&\hat H=\hat H_0+\hat H_{\mathrm{int}}+\hat H_{\mathrm{SR}},\\
&\hat H_0=E_2\hat A^\dagger\hat A+E_1\hat B_1^\dagger\hat B_1+E_2\hat B_2^\dagger\hat B_2+\hbar\sum_n\omega_n\hat b_n^\dagger\hat b_n,\\
&\hat H_{\mathrm{int}}=\hbar U(r)(\hat A^\dagger\hat B_2+\hat A\hat B_2^\dagger),\\
&\hat H_{\mathrm{SR}}=\hbar\sum_n(g_n\hat b_n^\dagger\hat B_1^\dagger\hat B_2+g_n^*\hat b_n\hat B_2^\dagger\hat B_1).
\end{aligned}\tag{15}$$

When we assume that initial and final states are constructed only in terms of one-exciton states, the creation (annihilation) operators of excitons can be written as follows; $\hat A^\dagger=|A^*\rangle\langle A|(\hat A=|A\rangle\langle A^*|)$, $\hat B_1^\dagger=|B_1^*\rangle\langle B|(\hat B_1=|B\rangle\langle B_1^*|)$, and $\hat B_2^\dagger=|B_2^*\rangle\langle B|(\hat B_2=|B\rangle\langle B_2^*|)$, where $|A\rangle$ and $|A^*\rangle$ are the ground and excited states in dot 1 and $|B\rangle$, $|B_1^*\rangle$, and $|B_2^*\rangle$ are the ground, and the lower and higher excited states in dot 2, similar to those in Fig. 2. We can readily understand the following commutation relations; $[\hat B_i^\dagger,\hat B_j]=\delta_{i,j}(|B_i^*\rangle\langle B_i^*|-|B\rangle\langle B|)$ and $[\hat B_i,\hat B_j]=[\hat B_i^\dagger,\hat B_j^\dagger]=0$ $(i,j=1,2)$. Therefore the operators are neither bosonic nor fermionic. Bosonic operators $(\hat b_n^\dagger,\hat b_n)$ are for the heat-bath system with eigenenergy $\hbar\omega_n$. For simplicity, the rotating wave approximation is used in the interaction Hamiltonian $\hat H_{\mathrm{int}}$ as $(\hat A+\hat A^\dagger)(\hat B_2+\hat B_2^\dagger)\approx\hat A^\dagger\hat B_2+\hat A\hat B_2^\dagger$. The heat-bath system is assumed to be a collection of multiple harmonic oscillators labeled by n. Note that the exciton-polariton degrees of freedom have already been traced out, and thus the strength of the optical near-field interaction $\hbar U(r)$ appears in Eq. (15). From Eq. (3), the equation of motion for the total system can be written as

$$\begin{aligned}
\dot{\hat\rho}^I(t)=&-\frac{i}{\hbar}[\hat H_{\mathrm{int}}+\hat H_{\mathrm{SR}}^I(t),\hat\rho(0)]-\frac{1}{\hbar^2}\int_0^t dt'\\
&\times[\hat H_{\mathrm{int}}+\hat H_{\mathrm{SR}}^I(t),[\hat H_{\mathrm{int}}+\hat H_{\mathrm{SR}}^I(t'),\hat\rho^I(t')]],
\end{aligned}\tag{16}$$

where the suffix I means the interaction picture, and the relation $\hat H_{\mathrm{int}}^I(t)=\hat H_{\mathrm{int}}$ is used.[25] In order to express the second-order temporal correlation clearly, the formal solution of Eq. (3) in the integral form is again substituted into the right-hand side of Eq. (3). Since we are interested in the exciton population in the two-dot system, we take a trace with respect to the degrees of freedom of the heat-bath system as $\hat\rho_S^I(t)=\mathrm{Tr}_R[\hat\rho^I(t)]$. Here, the density operator is assumed tobe a direct product of the quantum dot system part $\hat\rho_S^I(t)$ and the reservoir (heat-bath) system part $\hat\rho_R^I(t)$. If the reservoir system has a very large volume, deviation from the initial value can be neglected, and the density operator is approximated as

$$\hat\rho^I(t)=\hat\rho_S^I(t)\hat\rho_R^I(t)\approx\hat\rho_S^I(t)\hat\rho_R(0),\tag{17}$$

which corresponds to the Born approximation.[25] Taking a trace on both sides of Eq. (16) about the reservoir operator, we obtain

$$\begin{aligned}
\dot{\hat\rho}_S^I(t)=&-iU(r)[\hat A^\dagger\hat B_2+\hat A\hat B_2^\dagger,\hat\rho_S^I(t)]\\
&-\sum_n n(\omega_n,T)[(\{\hat C\hat C^\dagger,\hat\rho_S^I(t)\}-2\hat C^\dagger\hat\rho_S^I(t)\hat C)\otimes\gamma_n^r(t)\\
&-i[\hat C\hat C^\dagger,\hat\rho_S^I(t)]\otimes\gamma_n^i(t)]\\
&-\sum_n[1+n(\omega_n,T)][(\{\hat C^\dagger\hat C,\hat\rho_S^I(t)\}-2\hat C\hat\rho_S^I(t)\hat C^\dagger)\\
&\otimes\gamma_n^r(t)+i[\hat C^\dagger\hat C,\hat\rho_S^I(t)]\otimes\gamma_n^i(t)],
\end{aligned}\tag{18}$$

where the curly brackets $\{\cdot\}$ represent the anticommutation relation, and the notation $\otimes$ designates the convolution integral. In order to avoid verbose expressions, we make the following replacement; $\hat C^\dagger=\hat B_2^\dagger\hat B_1$ and $\hat C=\hat B_1^\dagger\hat B_2$. Since we assume that the reservoir system is in equilibrium, the terms including $\mathrm{Tr}_R[\hat b_n^\dagger\hat\rho_R(0)]$ and $\mathrm{Tr}_R[\hat b_n\hat\rho_R(0)]$ disappear in Eq. (18). The number of phonons in the equilibrium state is written as $n(\omega_n,T)=\mathrm{Tr}_R[\hat b_n^\dagger\hat b_n\hat\rho_R(0)]$, and it follows Bose–Einstein statistics as

$$n(\omega_n,T)=\frac{1}{e^{\hbar\omega_n/k_BT}-1}.\tag{19}$$

The real and imaginary parts of the function

$$\gamma_n(t)=|g_n|^2e^{i(\Delta\omega-\omega_n)t}\tag{20}$$

with $\hbar\Delta\omega=E_2-E_1$ are represented as $\gamma_n^r(t)$ and $\gamma_n^i(t)$, respectively, and are related to the relaxation (real part) and energy shift (imaginary part) of the energy level in dot 2 that originates from coupling to the heat-bath system. The convolution integral in Eq. (18) expresses a memory effect due to time delay in the heat-bath system. However, if the dynamics of the reservoir system are much faster than those of the two-dot system, one can approximate the density operator of the two-dot system as $\hat\rho_S^I(t-t')=\hat\rho_S^I(t)$ (a Markov approximation). Using this approximation, and rewriting the summation as $\Sigma_n=\int_0^\infty d\omega D(\omega)$, with $D(\omega)$ being the density of states for each phonon, we can express the convolution integral analytically as

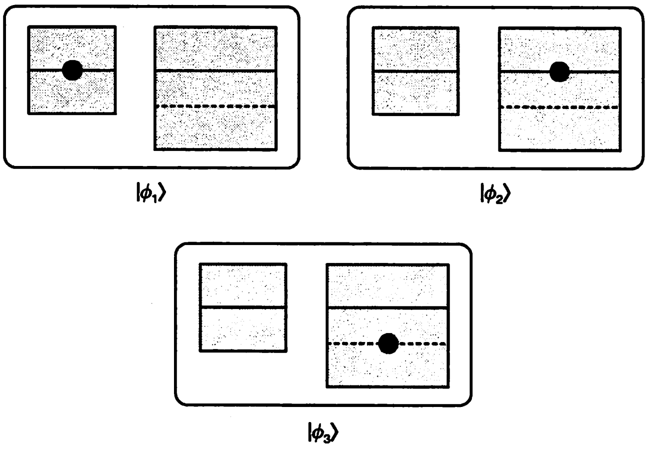

FIG. 5. Three bases of the single-exciton state in a two-quantum-dot system.

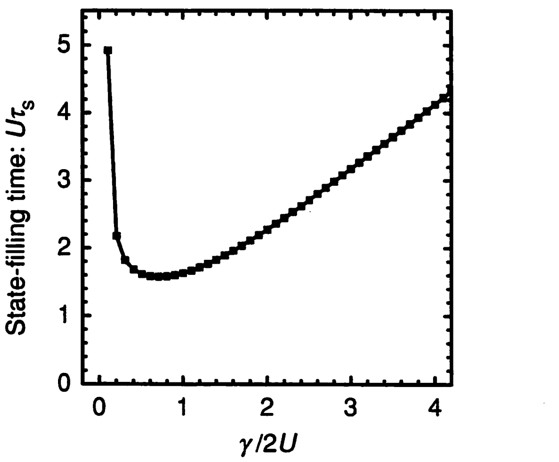

FIG. 6. The state-filling time τ_S plotted as a function of the ratio of the exciton-phonon coupling strength $\gamma/2$ to the interdot optical near-field coupling strength U.

$$\sum_n n(\omega_n,T)\hat{\rho}_S^I(t)\otimes\gamma_n(t)$$

$$=\hat{\rho}_S^I(t)\int_0^\infty d\omega n(\omega,T)D(\omega)|g(\omega)|^2\int_0^t dt' e^{i(\Delta\omega-\omega)t'}$$

$$\approx\hat{\rho}_S^I(t)\Bigg[\pi n(\Delta\omega,T)D(\Delta\omega)|g(\Delta\omega)|^2 + iP\int_0^\infty d\omega\frac{n(\omega,T)D(\omega)|g(\omega)|^2}{\Delta\omega-\omega}\Bigg]. \tag{21}$$

Here, we extend the upper limit of the time integration to infinity. The equation of motion for the dot system is finally reduced to

$$\dot{\hat{\rho}}_S^I(t)=-iU[\hat{A}^\dagger\hat{B}_2+\hat{A}\hat{B}_2^\dagger,\hat{\rho}_S^I(t)]-n\gamma(\{\hat{C}\hat{C}^\dagger,\hat{\rho}_S^I(t)\} -2\hat{C}^\dagger\hat{\rho}_S^I(t)\hat{C})-(1+n)\gamma(\{\hat{C}^\dagger\hat{C},\hat{\rho}_S^I(t)\} -2\hat{C}\hat{\rho}_S^I(t)\hat{C}^\dagger), \tag{22}$$

where $n\equiv n(\Delta\omega,T)$ and $\gamma=\pi D(\Delta\omega)|g(\Delta\omega)|^2$. The terms indicating the energy shift are neglected in Eq. (22) because the shift is usually small in the case of weak system–heat-bath coupling.

Let us consider one-exciton dynamics in the system, using three bases, as illustrated in Fig. 5. The equations of motion for the matrix elements are then read in the Schrödinger picture as

$$\begin{aligned}\dot{\rho}_{11}(t)&=iU(r)[\rho_{12}(t)-\rho_{21}(t)],\\ \dot{\rho}_{12}(t)-\dot{\rho}_{21}(t)&=2iU(r)[\rho_{11}(t)-\rho_{22}(t)]\\ &\quad-(1+n)\gamma[\rho_{12}(t)-\rho_{21}(t)],\\ \dot{\rho}_{22}(t)&=-iU(r)[\rho_{12}(t)-\rho_{21}(t)]-2(1+n)\gamma\rho_{22}(t)\\ &\quad+2n\gamma\rho_{33}(t),\\ \dot{\rho}_{33}(t)&=2(1+n)\gamma\rho_{22}(t)-2n\gamma\rho_{33}(t),\end{aligned} \tag{23}$$

where $\rho_{mn}(t)\equiv\langle\Phi_m|\hat{\rho}_S(t)|\Phi_n\rangle$ is employed. When the temperature, T, equals zero ($n=0$), Eq. (23) can be solved analytically. The diagonal parts representing the population probability for each energy level in dots 1 and 2, as well as the off-diagonal parts representing quantum coherence, are given as

$$\begin{aligned}\rho_{11}(t)&=\frac{1}{Z^2}e^{-\gamma t}\left[\frac{\gamma}{2}\sinh(Zt)+Z\cosh(Zt)\right]^2,\\ \rho_{22}(t)&=\frac{U^2}{Z^2}e^{-\gamma t}\sinh^2(Zt),\\ \rho_{33}(t)&=1-[\rho_{11}(t)+\rho_{22}(t)],\\ \rho_{12}(t)&=-\rho(t)_{21}\\ &=i\frac{U}{Z^2}e^{-\gamma t}\sinh(Zt)\left[\frac{\gamma}{2}\sinh(Zt)+Z\cosh(Zt)\right],\end{aligned} \tag{24}$$

where $Z\equiv\sqrt{(\gamma/2)^2-U^2}$, and initial conditions $\rho_{11}(0)=1$ and $\rho_{12}(0)=\rho_{21}(0)=\rho_{22}(0)=0$ are used. We define the state-filling time τ_S as $\rho_{33}(\tau_S)=1-e^{-1}$, which corresponds to the time for the excitation energy transfer from dot 1 to the lower energy level in dot 2. From Eq. (24), it follows that the temporal evolution of the population is quite different at $U>\gamma/2$ and $U<\gamma/2$. Although Eq. (24) seems to be undefined at $U=\gamma/2$ ($Z=0$), taking a limit value, there is a definite solution regardless of whether $Z\rightarrow+0$ or -0 is taken. In Fig. 6, the state-filling time τ_S is plotted as a function of the ratio of $\gamma/2$ to U. For $U>\gamma/2$, population $\rho_{22}(t)$ shows damped oscillation with envelope function $e^{-\gamma t}$; thus, τ_S is determined by the relaxation constant γ, i.e., $\tau_S\sim\gamma^{-1}$. By contrast, for $U<\gamma/2$, $\rho_{22}(t)$ decays monotonically. At first glance, as $\gamma/2$ increases, we expect τ_S to decrease monotonically because the population flows into the lower energy level more quickly; nevertheless, τ_S increases again, as shown in Fig. 6. This occurs because the upper energy level in dot 2 becomes effectively broad with increasing γ, which results in a decrease in the resonant energy transfer between the quantum dots. When the ratio $\gamma/2U$ is sufficiently large, τ_S increases linearly, as seen in Fig. 6. Therefore the state-filling time is not only determined by the optical near-field interaction strength between two dots, but also by the strength of coupling to the heat-bath system. From Fig. 6, it follows that the fastest energy transfer is obtained when $\gamma/2 \sim U$ is satisfied.

The term $2\gamma n \rho_{33}(t)$ on the right-hand side of the third equation in Eq. (23) indicates that the finite temperature effect due to the finite number of phonons $(n \neq 0)$ induces back transfer of the excitation energy from the heat-bath system to the two-dot system. Within the Born approximation adopted in Eq. (17), this term incoherently increases population $\rho_{22}(t)$. As population $\rho_{33}(t)$ increases, the back transfer becomes large, and gives residual populations $\rho_{11}(t)$ and $\rho_{22}(t)$ in the upper levels in both quantum dots.

IV. NUMERICAL RESULTS

In this section, we present numerical results for the population dynamics using Eqs. (23) and (24) for zero and finite temperatures in order to verify the theoretical considerations just presented, and to estimate the state-filling time for some practical cases. Suppose that the system consists of two CuCl quantum cubes embedded in a NaCl matrix. The cube size is set as $a:\sqrt{2}a$ $(a=5\text{ nm})$, so that the (1, 1, 1)-level of dot 1 is resonant with the (2, 1, 1)-level of dot 2. The variable parameters are the interaction strength U or the intercube spacing, the relaxation constant γ, and the temperature T of the heat-bath system.

In Figs. 7(a) and 7(b), the E_2- and E_1-level populations $\rho_{22}(t)$ and $\rho_{33}(t)$ in dot 2 are plotted for intercube spacings $d=5$, 10, and 15 nm $[U=1.51\times10^{-1}$, 0.90×10^{-1}, and $0.60\times10^{-1}\ (\text{ps})^{-1}]$, and $T=0$ K. The relaxation time γ^{-1} is assumed to be 1 ps based on another experimental study.[22] The populations for all three cases in Fig. 7(a) show monotonic decays because $U<\gamma/2$ is satisfied. From Fig. 7(b), the state-filling time τ_S is estimated for intercube spacings $d=5$, 10, and 15 nm as 22, 60, and 140 ps, respectively. This indicates that an energy transfer time of less than 100 ps can be realized when the two dots are located within 10 nm of each other.

Figure 8 shows the result for $\gamma^{-1}=10$ ps, which corresponds to weaker coupling between an exciton and the heat-bath system. Damped oscillation due to nutation between two resonant levels is clearly seen for $d=5$ nm in Fig. 8(a), where $U>\gamma/2$ is satisfied. Although $U>\gamma/2$ is also satisfied for $d=10$ and 15 nm, we cannot observe the oscillation because of the small amplitudes. From Fig. 8(b), the state-filling time τ_S for the three cases is estimated as 12, 18, and 25 ps, respectively. Compared with Fig. 7(b), the state-filling speed becomes faster in Fig. 8(b) in spite of the increase in γ^{-1} because U is nearly equal to $\gamma/2$. Figures 7 and 8 indicate that the interdot spacing should be adjusted so that the optical near-field coupling is of the same order as the exciton-phonon coupling in order to obtain the fastest energy transfer in the system.

Figures 9(a) and 9(b) show the temperature dependence of populations $\rho_{22}(t)$ and $\rho_{33}(t)$, respectively. The temperature is set at either $T=50$ or 100 K. These results are obtained using a Laplace transform, where singular points are derived numerically for the given numerical parameters. As mentioned in Sec. III, a finite temperature induces the incoherent back transfer of energy, and this results in residual populations at the upper energy levels in both quantum cubes. Figure 9(a) shows that the E_2-level population in dot 2 converges on a finite temperature-dependent value that can be derived numerically and is denoted by the horizontal dotted lines in Fig. 9(a). As shown in Fig. 9(b), however, the time evolution of the E_1-level population is almost independent of the temperature, except for a decrease in the amplitude because of the residual populations at upper energy levels.

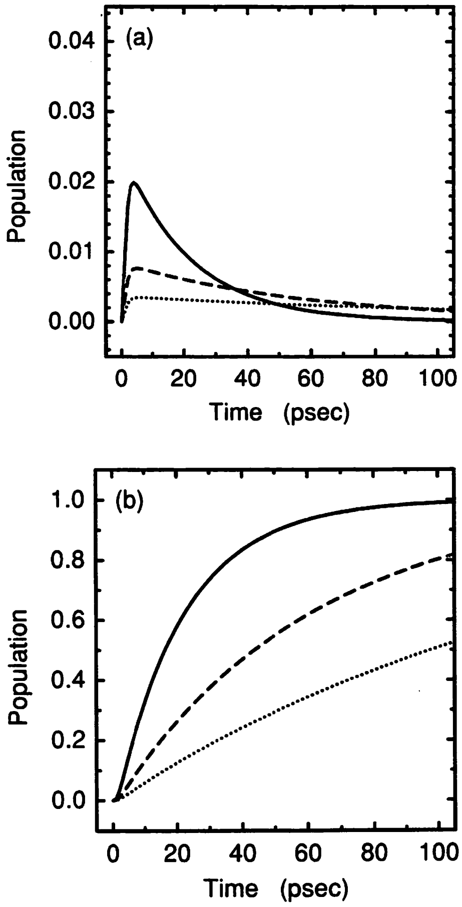

FIG. 7. Time-evolution of (a) E_1-level population $\rho_{22}(t)$ and (b) E_2-level population $\rho_{33}(t)$, where the relaxation time γ^{-1} and temperature T are set at 1 ps and 0 K, respectively. The solid, dashed, and dotted curves represent the cases for intercube spacings $d=5$, 10, and 15 nm, respectively.

V. CONCLUSIONS

With the ultimate goal of achieving a nano-photonic switch and a nano-photonic device, we have discussed excitation energy transfer in a two-quantum dot system and its dynamics using the density matrix formalism. Excitation energy can be transferred between two dots by an optical near-field interaction, and nutation occurs if both dots have resonant energy levels. The oscillation period depends on the optical near-field interaction strength. We have shown that the optical near-field interaction is expressed as a sum of Yukawa functions, and estimated that the period for CuCl quantum cubes is less than 100 ps at a 10-nm intercube distance.

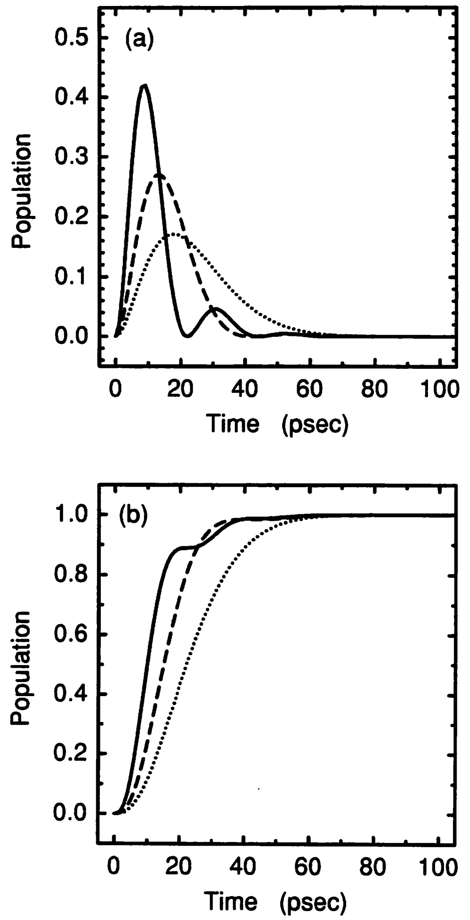

FIG. 8. Time-evolution of (a) E_1-level population $\rho_{22}(t)$ and (b) E_2-level population $\rho_{33}(t)$, where the relaxation time γ^{-1} and temperature are set at 10 ps and 0 K, respectively. The solid, dashed, and dotted curves represent the cases for intercube spacings $d=5$, 10, and 15 nm, respectively.

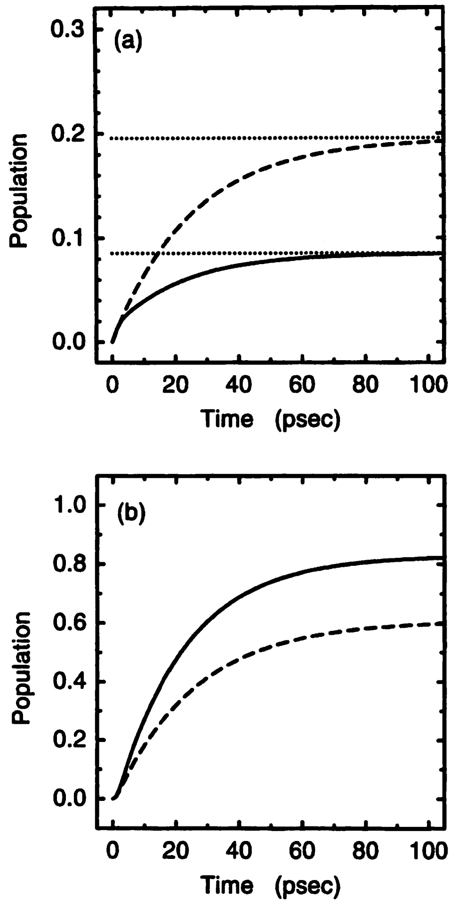

FIG. 9. Temperature dependence of (a) E_1-level population $\rho_{22}(t)$ and (b) E_2-level population $\rho_{33}(t)$, when $d=5$ nm and $\gamma^{-1}=1$ ps. The solid and dashed curves represent the cases for temperature $T=50$ and 100 K, respectively. The two dotted lines denote the limit values of E_1-level population for both temperatures at infinite time.

In order to guarantee irreversible energy transfer between two quantum dots, we have considered intra-sublevel transition via the exciton-phonon coupling that occurs in a two-quantum dot system with a size ratio of $1:\sqrt{2}$, and examined the population dynamics of the system. The state-filling time, defined as the time that it takes the population in dot 1 to be transferred to the lower energy level in dot 2, strongly depends on both the strength of optical near-field interaction U and the relaxation constant γ due to the phonon coupling. When $U>\gamma/2$ is satisfied, nutation between resonant energy levels appears as described by envelope function $e^{-\gamma t}$; thus, the state-filling time is determined by the constant γ for large U. By contrast, when $U<\gamma/2$ is satisfied and the population is transferred monotonically to the lower energy level, the state-filling time becomes long with increasing $\gamma/2U$. This is because the upper energy level is blurred. Therefore the fastest state-filling time is obtained when $U \sim \gamma/2$ is satisfied. Using CuCl quantum cubes, the state-filling time is numerically estimated as 22 and 12 ps when $\gamma^{-1}=1$ and 10 ps, which is suitable for a switching device.

The temperature effect was also examined within the Born–Markov approximation. Our analysis shows that the state-filling time is almost independent of the temperature. However, the finite temperature results in a residual population in the upper energy levels. This might degrade the ratio of the ON/OFF signals in a nano-switch.

The above theoretical modeling of the population dynamics in a two-quantum dot system assumes an ideally perfect resonance condition, which may be too tight to fabricate such a system with definite size ratios. In order to release the resonance condition, we estimate allowable tolerance, or size deviation of quantum dots from designed values. When the deviation from the resonant energy $\hbar\Delta\Omega$ in dot 2 is introduced, the factor on the right-hand side of the second equation in Eq. (24) is modified, and the ratio of that in off-resonance to on-resonance is approximately given as $\gamma^2/(\gamma^2+\Delta\Omega^2)$ $(\gamma/2 \gg U)$. Therefore we can achieve efficiency more than 50% even if the deviation $\Delta\Omega<\gamma$ is introduced. When the dot size and relaxation constant are set as 7.1 nm $(=5\sqrt{2}$ nm) and $\hbar\gamma=3$ meV, respectively, approximately 10% deviation of the dot size can be allowed. As the size of quantum dots is larger, the tolerable deviation is more relaxed. It is feasible to make such quantum dots by the recent advancement of nano-fabrication techniques. In fact, preliminary experimental results we obtained show the population dynamics as discussed in the article.

Our results and discussion might be valid within the Born–Markov approximation. Even if the Born approximation is admitted because of the large volume of the heat-bath system, the Markov approximation may not be guaranteed at low temperature, as assumed in the transformation in Eq. (21). Therefore we might need to deal with it more carefully, since it has been pointed out that non-Markov behavior manifests itself at low temperature.[25,28] The effects of non-Markov behavior on the dynamics are now under investigation.

We focused our attention on the energy transfer process in the nanometer scale, but it is quite important to investigate signal control, and to manipulate the electronic states of the components in a nano-photonic device, where we must deal with a two-exciton state, as shown in Fig. 1(b). Such analysis will be discussed elsewhere.

[1] M. Ohtsu, Proc. SPIE **3749**, 478 (1999).
[2] V. V. Polonski, Y. Yamamoto, M. Kourogi, H. Fukuda, and M. Ohtsu, J. Microsc. **194**, 545 (1999).
[3] G. H. Lee, Y. Yamamoto, M. Kourogi, and M. Ohtsu, Proc. SPIE **3791**, 132 (1999).
[4] Y. Yamamoto, M. Kourogi, M. Ohtsu, V. Polonski, and G. H. Lee, Appl. Phys. Lett. **76**, 2173 (2000).
[5] M. Ohtsu, K. Kobayashi, H. Ito, and G. H. Lee, Proc. IEEE **88**, 1499 (2000).
[6] T. H. Stievater, X. Li, D. G. Steel, D. Gammon, D. S. Katzer, D. Park, C. Piermarocchi, and L. J. Sham, Phys. Rev. Lett. **87**, 133603 (2001).
[7] H. Kamada, H. Gotoh, J. Temmyo, T. Takagahara, and H. Ando, Phys. Rev. Lett. **87**, 246401 (2001).
[8] H. Htoon, T. Takagahara, D. Kulik, O. Baklenov, A. L. Holmes, Jr., and C. K. Shih, Phys. Rev. Lett. **88**, 087401 (2002).
[9] N. H. Bonadeo, J. Erland, D. Gammon, D. Park, D. S. Katzer, and D. G. Steel, Science **282**, 1473 (1998).
[10] Th. Förster, in *Modern Quantum Chemistry*, edited by O. Sinanoğlu (Academic, New York, 1965), pp. 93–137.
[11] V. M. Agranovich and M. D. Galanin, *Electronic Excitation Energy Transfer in Condensed Matter* (North-Holland, Amsterdam, 1982).
[12] K. Cho, Y. Ohfuti, and K. Arima, Surf. Sci. **363**, 378 (1996).
[13] K. Mukai, S. Abe, and H. Sumi, J. Phys. Chem. B **103**, 6096 (1999).
[14] T. Kawazoe, K. Kobayashi, J. Lim, Y. Narita, and M. Ohtsu, Phys. Rev. Lett. **88**, 067404 (2002).
[15] K. Kobayashi and M. Ohtsu, J. Microsc. **194**, 249 (1999).
[16] K. Kobayashi, S. Sangu, and M. Ohtsu, in *Near-Field Optics: Principles and Applications*, edited by X. Zhu and M. Ohtsu (World Scientific, Singapore, 2000), pp. 82–88.
[17] K. Kobayashi, S. Sangu, H. Ito, and M. Ohtsu, Phys. Rev. A **63**, 013806 (2001).
[18] K. Kobayashi, T. Kawazoe, S. Sangu, and M. Ohtsu, in *Technical Digest of the 4th Pacific Rim Conference on Laser and Electro-Optics* (IEEE, Piscataway, NJ, 2001), pp. I192 and I193.
[19] N. Sakakura and Y. Masumoto, Phys. Rev. B **56**, 4051 (1997).
[20] T. Kataoka, T. Tokizaki, and A. Nakamura, Phys. Rev. B **48**, 2815 (1993).
[21] E. Hanamura, Phys. Rev. B **37**, 1273 (1988).
[22] Y. Masumoto, M. Ikezawa, B.-R. Hyun, K. Takemoto, and M. Furuya, Phys. Status Solidi B **224**, 613 (2001).
[23] J. J. Hopfield, Phys. Rev. **112**, 1555 (1958).
[24] D. P. Craig and T. Thirunamachandran, *Molecular Quantum Electrodynamics* (Academic, London, 1984).
[25] H. J. Carmichael, *Statistical Methods in Quantum Optics 1* (Springer-Verlag, Berlin, 1999).
[26] L. Mandel and E. Wolf, *Optical Coherence and Quantum Optics* (Cambridge University, Cambridge, England, 1995).
[27] P. Fulde, *Electron Correlations in Molecules and Solids* (Springer-Verlag, Berlin, 1995).
[28] K. Lindenberg and B. West, Phys. Rev. A **30**, 568 (1984).

Journal of Microscopy, Vol. 209, Pt 3 March 2003, pp. 261–266
Received 10 August 2002; accepted 25 October 2002

Demonstrating nanophotonic switching using near-field pump–probe photoluminescence spectroscopy of CuCl quantum cubes

T. KAWAZOE*, K. KOBAYASHI*, S. SANGU* & M. OHTSU*,†
**Exploratory Research for Advanced Technology (ERATO), Japan Science and Technology Corporation (JST), 687-1 Tsuruma, Machida, Tokyo 194-0004, Japan*
†Interdisciplinary Graduate School of Science and Engineering, Tokyo Institute of Technology, 4259 Nagatsuta, Midori-ku, Yokohama 226-8502, Japan

Key words. Nanophotonic device, near-field optical microscopy, optical near-field interaction, optical switch, photoluminescence spectroscopy, quantum dot.

Summary

We demonstrated a novel optical switching operation using three CuCl quantum cubes with a size ratio of $1 : \sqrt{2} : 2$. Their quantized excitonic energy levels resonate with one another, and the switching mechanism was based on the resonant near-field energy transfer between the quantum cubes. Using near-field pump–probe photoluminescence spectroscopy, we succeeded in controlling the near-field energy transfer and obtained a controlled (i.e. switched) signal in a differential photoluminescence spectrum with and without a pump beam. The internal quantum efficiency of the switching operation was close to 1. These results suggest the possibility of making a nanophotonic switching device smaller than 30 nm.

Introduction

Optical fibre transmission systems require increased integration of photonic devices if data transmission rates are to reach as high as 10 Tb s^{-1} by 2015. To support this increase, it is estimated that the size of photonic matrix switching devices should be reduced to a subwavelength scale, to integrate more than 1000 × 1000 input and output channels on a substrate. Because conventional photonic devices, e.g. diode lasers and optical waveguides, must confine the light wave within their cavities and core layers, respectively, their minimum sizes are limited by the diffraction of light. They cannot, therefore, meet this requirement because the required size is beyond this diffraction limit.

A nanometric all-optical switch (i.e. a nanophotonic switch) forms the nucleus of a nanophotonic integrated circuit. We used a coupled quantum-dot (QD) system to realize such a switch. The coupled QD system exhibits unique properties such as the Kondo effect (Goldhaber-Gordon *et al.*, 1998) and Coulomb blockade (Waugh *et al.*, 1995). It also reveals a variety of interactions, such as carrier tunnelling, Coulomb coupling and spin interaction. The optical near-field interaction can govern the coupling strength among QDs. Recently, we observed optically forbidden energy transfer between neighbouring CuCl QDs via the optical near-field interaction (Kawazoe *et al.*, 2002). Because the near-field interaction is a local interaction, it is applicable to nanophotonic switches. This study describes the principle of the nanophotonic switch and reports the experimental result of a switching operation for the first time.

Correspondence: T. Kawazoe. Tel. +81 42 788 6039; fax: +81 42 788 6031; e-mail: kawazoe@ohtsu.jst.go.jp

Principle of a nanophotonic switch

We used cubic CuCl QDs, i.e. quantum cubes (QCs), in a NaCl matrix to demonstrate the principle of the nanophotonic switch. It is well known that translational motion of the exciton centre of mass in CuCl QCs is quantized because of the small exciton Bohr radius (Ekimov *et al.*, 1985; Sakakura & Masumoto, 1997). The potential barrier of CuCl QCs in a NaCl crystal can be regarded as infinitely high, and the energy eigenvalues for the quantized Z_3 exciton energy level (n_x, n_y, n_z) in a CuCl QC with side length of L are given by

$$E_{n_x,n_y,n_z} = E_B + \frac{\hbar^2\pi^2}{2M(L-a_B)^2}(n_x^2+n_y^2+n_z^2), \qquad (1)$$

where E_B is the bulk energy of the Z_3 exciton, M is the translational mass of the exciton, a_B is its Bohr radius, n_x, n_y and n_z are quantum numbers (n_x, n_y, n_z = 1, 2, 3, ...), and $a = L - a_B$ corresponds to an effective side length found after considering the dead layer correction. The exciton energy levels with even quantum numbers are dipole-forbidden states that are optically forbidden (Tang *et al.*, 1993). However, we demonstrated for the first time that the optical near-field interaction is allowed for such energy levels (Kawazoe *et al.*, 2002).

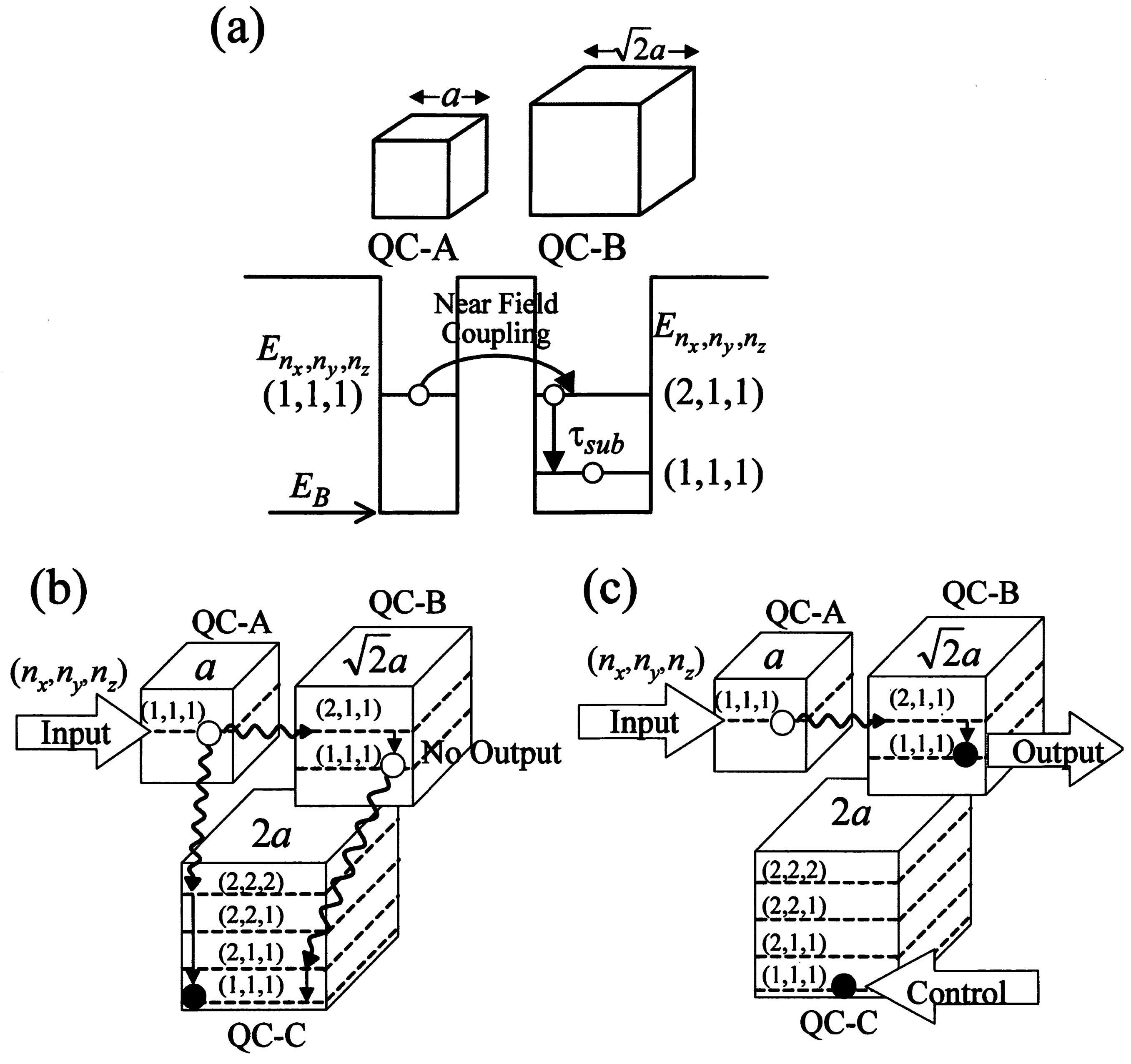

Fig. 1. Schematic explanation of a nanophotonic switch. (a) Upper: schematic drawings of closely located CuCl QCs A and B with the effective side lengths of $a(= (L - a_B))$ and $\sqrt{2}a$, respectively, where L and a_B are the side lengths of QCs and the exciton Bohr radius, respectively. Lower: their exciton energy levels. n_x, n_y and n_z represent quantum numbers of an exciton. E_B is the exciton energy level in a bulk crystal. (b) OFF and (c) ON states of the switch using three QCs, respectively.

Figure 1(a) explains the near-field energy transfer between two CuCl QCs (A and B) and shows their confined-exciton Z_3 energy levels. Assuming that the effective side lengths of QC-A and QC-B are a and $\sqrt{2}a$, respectively, Eq. (1) shows that the quantized (1,1,1) exciton energy level of QC-A resonates with the (2,1,1) level of QC-B. Under this resonant condition, the coupling energy of the optical near-field interaction is given by the following Yukawa function (Ohtsu *et al.*, 1998; Kobayashi *et al.*, 2001):

$$V(r) = A\frac{\exp(-\mu r)}{r} \tag{2}$$

Here, r is the separation between two QCs, A is the coupling coefficient, and μ is the effective mass of the Yukawa function given by

$$\mu = \frac{\sqrt{2E_{n_x,n_y,n_z}(E_{NaCl} + E_{n_x,n_y,n_z})}}{\hbar c}, \tag{3}$$

where E_{NaCl} is the exciton energy of the NaCl matrix. The value of the coupling coefficient A depends on experimental conditions. Assuming that the separation r between two QCs is 10 nm, the coupling energy, $V(r)$, is estimated to be of the order of 10^{-4} eV, which corresponds to a transition time of 20 ps, and is much shorter than the exciton lifetime of a few nanoseconds. Furthermore, the inter sublevel transition time, τ_{sub}, from higher exciton energy levels to the lowest, is generally less than a few picoseconds and is much shorter than the transition time (Suzuki *et al.*, 1996). Therefore, most of the exciton energy in CuCl QC-A will be transferred to the lowest exciton energy level in neighbouring QC-B and recombine radiatively in the lowest level in QC-B.

Figure 1(b) and (c) explains the OFF and ON states of a proposed nanophotonic switch using three QCs. QC-A, -B and -C are used as the input, output and control ports of the switch, respectively. Assuming an effective size ratio of $1 : \sqrt{2} : 2$, quantized energy levels (1,1,1) in QC-A, (2,1,1) in QC-B and (2,2,2) in QC-C resonate with each other (Eq. 1). Furthermore, energy levels (1,1,1) in QC-B and (2,1,1) in QC-C also resonate. As mentioned above, almost all of the exciton energy in QC-A will be transferred to the (1,1,1) level in neighbouring QC-B, and finally, to the (1,1,1) level in QC-C. Thus, the input energy escapes to QC-C; therefore, no optical output signals are generated from QC-B, which corresponds to the OFF state (Fig. 1b). In the ON state (Fig. 1c), by contrast, the escape routes to QC-C are blocked by the excitation of QC-C due to state filling in QC-C by applying the control signal; thus, the input energy is transferred to QC-B generating an optical output signal.

Experiments and discussions

We fabricated CuCl QCs embedded in a NaCl matrix using the Bridgman method and successive annealing, and found the average size of the QCs to be 4.3 nm. The sample was cleaved just before it was used in the near-field optical spectroscopy experiment in order to keep its surface clean. The cleaved surface of the sample, which was 100 μm thick, was sufficiently flat for the experiment, i.e. its roughness was < 50 nm, at least within the scanning area of a few micrometres. A double-tapered UV fibre probe was fabricated by chemical etching and coated with a 150 nm thick gold film. An aperture < 50 nm in diameter was fabricated using the pounding method (Saiki & Matsuda, 1999).

The curve in Fig. 2(a) is a far-field photoluminescence (PL) spectrum of the sample that was recorded with a probe–sample separation of 3 μm in collection mode (Ohtsu *et al.*, 1998) of a cryogenic near-field optical spectrometer at 15 K using a 325 nm He–Cd laser. It represents the collective PL intensity from several CuCl QCs, and is inhomogeneously broadened due to the size distribution of the QCs. The two curves in Fig. 2(b) represent differential spectra taken at two positions on a sample surface, and are the differences between the PL intensities measured with probe–sample separations of 3 μm and < 10 nm. These curves consist of many fine structures attributed to the contribution of the QCs near the apex of the probe because of the drastic increase in the measured PL intensity produced by decreasing the probe–sample separation to < 10 nm. Because the density of the QCs is 10^{17} cm^{-3}, the average separation between QCs is < 30 nm. Therefore, the spectral peaks in Fig. 2(b) originate from several QCs of different sizes. Among these, peaks X, Y and Z correspond to the confined Z_3-exciton energy levels of quantum number (1,1,1) for QCs with side lengths (L) of 3.5, 4.6 and 6.3 nm, respectively. As their effective side lengths a are 2.8, 3.9 and 5.6 nm, the size ratio is close to $1 : \sqrt{2} : 2$, which means that their quantized exciton levels resonate with one another. Therefore, if they are close to one another, the nanophotonic switching operation shown in Fig. 1 is expected.

To verify the switching operation, the fibre probe was carefully scanned to search for the trio of QCs that satisfied the conditions for the switching operation. As the homogeneous linewidth of a CuCl QC increases with temperature (Masumoto *et al.*, 1998), the allowance of a reasonable size ratio is 10% at 15 K. The separation among QCs must be < 50 nm for the proposed switching operation because the energy transfer time increases with separation (Eq. 2). However, it must be shorter than the exciton lifetime. It is estimated that at least one trio of QCs exists in a 2 μm × 2 μm scan area that satisfies these conditions.

Figure 3(a) shows the near-field PL intensity distribution from 6.3-nm QCs at a wavelength of 385 nm under 325 nm probe laser excitation. The inset shows a cross-sectional profile along the broken line across the solid circle in Fig. 3(a). The full-width at half maximum of the profile, which was limited by the spatial resolution of the fibre probe, was 30 nm. In the area enclosed by the solid circle, we found a trio of QCs suitable for the switching operation. Figure 3(b) shows the near-field PL spectrum at the centre of the area enclosed by the solid circle. The single PL peak from a 6.3 nm QC appeared at the wavelength of 385 nm. The other QCs of the QC trio in this area, which are 3.5 and 4.6 nm, did not show PL, because their energies are transferred to the 6.3 nm QC, as shown by Fig. 1(b).

Near-field PL pump–probe spectroscopy was carried out by fixing the fibre probe under the three excitation conditions: (i) with a pump laser only, (ii) with a probe laser only, and (iii) with pump and probe lasers. The second harmonic light of a CW Ti : sapphire laser (385 nm) and a 325 nm He : Cd laser were used as the light sources for the pump and probe, respectively. To clarify the PL difference with and without pumping, the differential PL intensity (PL_{diff}) was defined as

$$PL_{diff} = PL_{pump\&probe} - PL_{pump} - PL_{probe}, \tag{4}$$

where PL_{pump}, PL_{probe}, and $PL_{pump\&probe}$ are the PL intensities measured under conditions (i) (ii) and (iii), respectively.

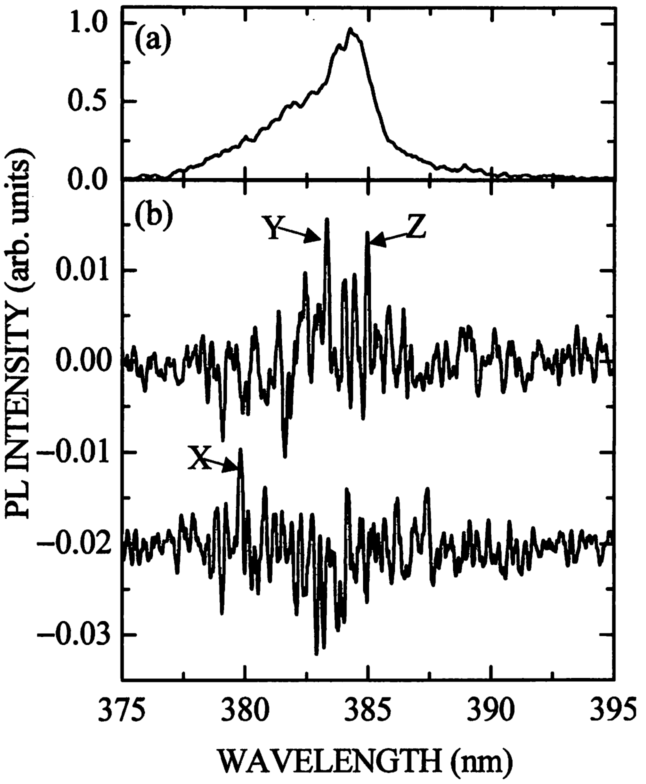

Fig. 2. (a) Far-field PL spectrum of a sample recorded with probe–sample separation of 3 μm for the collection-mode operation at 15 K. (b) The differential PL spectra, which is the intensity difference between PL spectra measured with probe–sample separations of 3 μm and < 10 nm. The peaks X, Y and Z indicated by arrows correspond to the wavelengths of lowest exciton state in QCs with the side lengths L of 3.5, 4.6 and 6.3 nm, respectively.

Figure 4(a) shows the PL_{diff} spectrum obtained at the centre of the area enclosed by the solid circle in Fig. 3(a). For comparison, Fig. 4(b) shows the PL_{diff} spectrum obtained at the centre of the area enclosed by the broken circle in Fig. 3(a). The vertical axes are normalized to the PL intensities from the 6.3 nm QC (i.e. at 385 nm of Fig. 3b). The pump laser light was used as the control light in Fig. 1(c) by tuning its wavelength to the (1,1,1) exciton energy level of a 6.3 nm QC. In Fig. 4(a), two satellite peaks appear at the positions of the (1,1,1) levels in the 4.6 and 3.5 nm QCs. The appearance of the satellite peaks means that the switching system proposed in Fig. 1 was constructed in the area enclosed by the solid circle. In other words, a trio of QCs with sizes of 3.5, 4.6 and 6.3 nm (i.e. their size ratio was $1:\sqrt{2}:2$) exists in this area, and pumping to the 6.3 nm QC blocks the energy transfer from the 3.5 and 4.6 nm QCs to the 6.3 nm QC due to the state filling of the 6.3 nm QC. Thus, the 3.5 and 4.6 nm QCs emit light that results in the satellite peaks in Fig. 4(a). This process corresponds to the ON state in Fig. 1(c). The satellite peaks never originate from exciton excitation levels (2,1,1) and (2,2,2), because they are optically forbidden, and satellite peaks from the other excitation levels, such as (2,2,1) and (3,1,1) in the 6.3 nm QC, have not been observed. The absence of satellite peaks from the 3.5 and 4.6 nm QCs in the PL_{diff} spectra at other positions, as shown in Fig. 4(b), supports our interpretation, which means that the proposed switching system is absent from the area enclosed by the broken circle in Fig. 3(a).

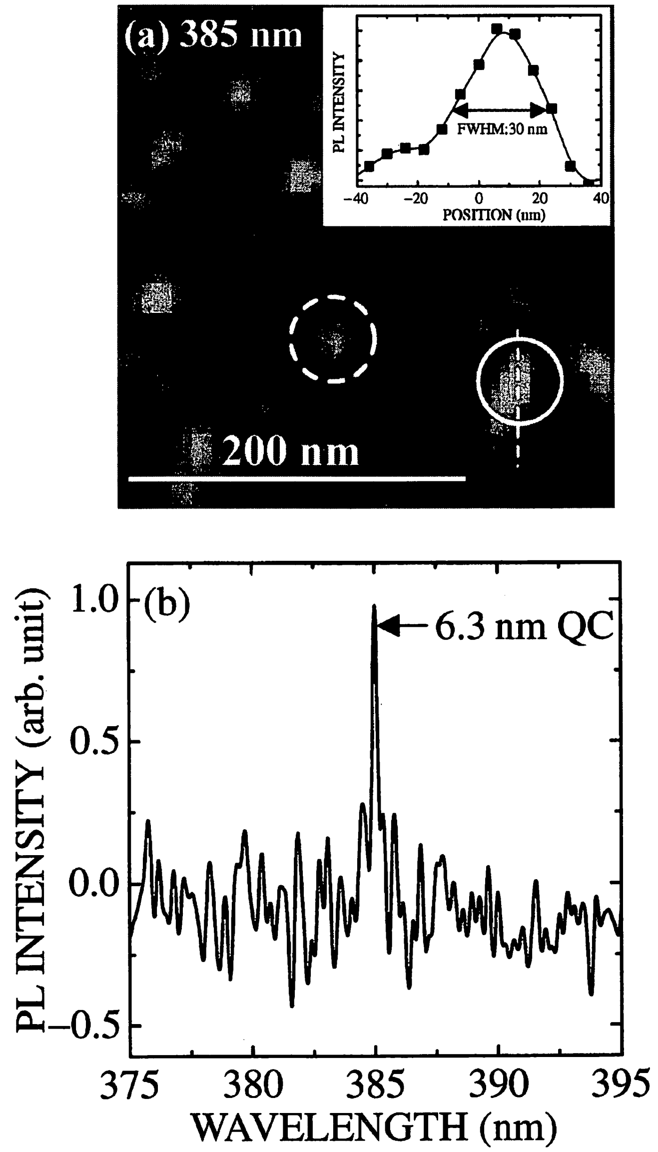

Fig. 3. (a) Spatial distributions of the near-field PL intensity for a peak of 6.3 nm QCs in Fig. 2(b). The inset shows a cross-sectional profile of the near-field PL intensity along with a broken line across a solid circle. (b) The near-field PL spectrum measured at the centre in the solid circle in (a).

The PL peak from the 4.6 nm QC corresponds to the output signal in Fig. 1(c), which is the first demonstration of our proposed near-field optical switching operation. The PL_{diff} intensity from the 4.6 nm QC, was 0.05 ± 0.02 times the PL intensity from the 6.3 nm QC in Fig. 3(b). This value is quite

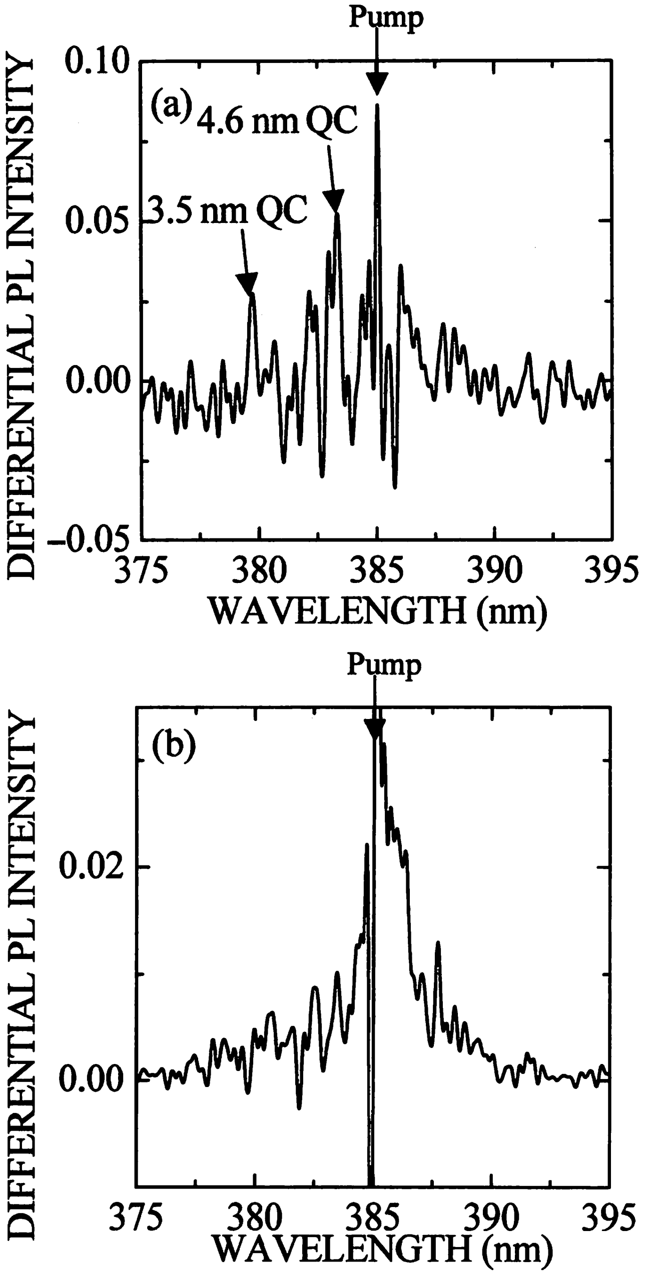

Fig. 4. Near-field differential PL spectra measured at the centre in the solid (a) and the broken (b) circles in Fig. 3(a). Vertical axes were normalized to the peak height of the curve in Fig. 3(b).

reasonable considering the pumping power density of 10 ± 3 W cm^{-2}, because the probability density of excitons in a 6.3 nm QC is 0.1 ± 0.05 (Landolt-Börnstein, 1982), which is close to the above-mentioned normalized output signal intensity. This result indicates that the internal quantum efficiency of the switching system is close to 1. We believe that this nanophotonic switch is smaller than 30 nm, as estimated from the full-width at half maximum shown in the inset of Fig. 3(a).

To fabricate the trio of QCs in a controlled manner, we developed the process of near-field optical chemical vapour deposition. Nanometric Zn patterns have been fabricated with high precision in their size and positions (Polonski *et al.*, 1999; Yamamoto *et al.*, 2000; Kawazoe *et al.*, 2001). Quantum size effects of the fabricated nanometric ZnO have also been observed (Yatsui *et al.*, 2002). A real nanophotonic switching device will be developed in the near future by using this fabrication process.

Conclusions

We proposed a nanophotonic switch using three different sized QCs. We demonstrated the switching operation in CuCl QCs embedded in a NaCl matrix using near-field pump–probe photoluminescence spectroscopy in the UV region. The optical switch was estimated to be smaller than 30 nm, and the internal quantum efficiency was close to 1. The proposed nanophotonic switch is expected to be a key device in future nanophotonic integrated circuits.

References

Ekimov, A.I., Eflos, Al.A., & Onushchenko, A.A. (1985) Quantum size effect in semiconductor microcrystals. *Solid State Commun.* **56**, 921–924.

Goldhaber-Gordon, D., Shtrikman, H., Mahalu, D., Abusch-Magder, D., Meirav, U. & Kastner, M.A. (1998) Kondo effect in a single-electron transistor. *Nature*, **391**, 156–159.

Kawazoe, T., Kobayashi, K., Lim, J., Narita, Y. & Ohtsu, M. (2002) Direct observation of optically-forbidden energy transfer between CuCl quantum cubes via optical near-field. *Phys. Rev. Lett.* **88**, 1–4, pp. 067404.

Kawazoe, T., Yamamoto, Y. & Ohtsu, M. (2001) Fabrication of a nanometric Zn dot by nonresonant near-field optical chemical-vapor deposition. *Appl. Phys. Lett.* **79**, 1184–1186.

Kobayashi, K., Sangu, S., Ito, H. & Ohtsu, M. (2001) Near-field optical potential for a neutral atom. *Phys. Rev. A*, **63**, 1–9, pp. 0138061.

Landolt-Börnstein (1982) *Physics of II–VI and I–VII Compounds, Semimagnetic Semiconductors*. Springer-Verlag, Berlin.

Masumoto, Y., Kawazoe, T. & Matsuura, N. (1998) Exciton-confined-phonon interaction in quantum dots. *J. Lumin.* **76/77**, 189–192.

Ohtsu, M. *et al.* (1998) *Near-Field Nano-Atom Optics and Technology* (ed. M. Ohtsu). Springer, Tokyo.

Ohtsu, M., Kobayashi, K., Kawazoe, T., Sangu, S. & Yatsui, T. (2002) Nanophotonics: design, fabrication, and operation of nanometric devices using optical near field. *IEEE J. Sel. Top. Quant. Electron*, **8**, 839–862.

Polonski, V., Yamamoto, Y., Kourogi, M., Fukuda, F. & Ohtsu, M. (1999) Nanometric patterning of zinc by optical near-field photochemical vapour deposition. *J. Microsc.* **194**, 545–551.

Saiki, T. & Matsuda, K. (1999) Near-field optical fiber probe optimized for illumination-collection hybrid mode operation. *Appl. Phys. Lett.* **74**, 2773–2775.

Sakakura, N. & Masumoto, Y. (1997) Persistent spectral-hole-burning spectroscopy of CuCl quantum cubes. *Phys. Rev. B*, **56**, 4051–4055.

Suzuki, T., Mitsuyu, T., Nishi, K. *et al.* (1996) Observation of ultrafast all-optical modulation based on intersubband transition in n-doped quantum wells by using free electron laser. *Appl. Phys. Lett.* **69**, 4136–4138.

Tang, Z.K., Yanase, A., Yasui, T., Segawa, Y. & Cho, K. (1993) Optical selection rule and oscillator strength of confined exciton system in CuCl thin films. *Phys. Rev. Lett.* 71, 1431–1434.

Waugh, F.R., Berry, M.J., Mar., D.J., Westervelt, R.M., Campman, K.L. & Gossard, A.C. (1995) Single-electron charging in double and triple quantum dots with tunable coupling. *Phys. Rev. Lett.* 75, 705–708.

Yamamoto, Y., Polonski, V., Lee, G.H., Kourogi, M. & Ohtsu, M. (2000) Fabrication of nanometric zinc pattern with photodissociated gas-phase diethylzinc by optical near field. *Appl. Phys. Lett.* 76, 2173–2175.

Yatsui, T., Kawazoe, T., Shimizu, T., Yamamoto, Y., Ueda, M., Kourogi, M. & Ohtsu, M. (2002) Observation of size-dependent features in the photoluminescence of zinc oxide nanocrystallites by near-field ultraviolet spectroscopy. *Appl. Phys. Lett.* 80, 1444–1446.

PAPER *Special Issue on Near-Field Optics and Its Applications*

Fabrication of a Ferromagnetic-Coated Fiber Probe with a Double-Layer Structure

Jungshik LIM[†a)], **Tadashi KAWAZOE**[††], **Takashi YATSUI**[††], *Nonmembers,*
and **Motoichi OHTSU**[†,††], *Regular Member*

SUMMARY We fabricated the first Fe-coated fiber probe for magneto-optical applications. In order to improve the optical confinement capability, we used a double-layer structure, with a thin coating of Au. The double-layer structure consisted of 50-nm-thick Fe and 50-nm-thick Au. A probe-to-probe experiment confirmed that the fabricated fiber probe had an effective optical confinement capability for optical near-field measurement.

key words: *optical near field, probe, fiber, ferromagnetic*

1. Introduction

Many types of apparatus have been used to observe nano structures, including scanning tunneling microscopes (STM) [1], atomic force microscopes (AFM) [2], near-field optical microscopes (NOM) [3], and so on. Since the probe in such equipment detects the physical and chemical responses of nanometric matter, the design of the probe should depend on what physical or chemical properties are to be measured [4]–[6]. For example, STM and AFM probes made of ferromagnetic materials have been reported [7], [8], and have unique functions, such as spin-polarized electron injection [9] and magnetic-force sensing [8], [10]. Similarly, fiber probes for NOM using ferromagnetic material have unique functions, such as a magnetic-force microscope (MFM) probe with photo-excitation ability. It is also expected to manifest the magneto-optical effects, such as Faraday effect, magnetic Kerr effect, and so on. Therefore, a ferromagnetic-coated fiber probe may act as a magneto-optical polarization controller for an optical near field. In a localized area, it is difficult to determine a light polarization due to the uncertainly relation between a wave number and a position, and controlling the polarization of an optical near field is challenging. However, localized matters, such as quantum dots and atoms, have light polarization selectivity in their electron transitions. We consider that the polarization control of an optical near field is possible, and is useful for optical near-field study. This paper reports the fabrication of an Fe-coated fiber probe with high optical confinement capability by introducing a double-layer coating structure for the light polarization control.

2. Fabrication of a Double-Layer Probe

To develop a fiber probe with magneto-optical properties, we selected Fe for the coating because of its large magneto-optical effect [11]. For practical near-field probe, optical properties are also important. Especially, optical confinement is one of the essential properties to realize an optical near field with high generation throughput and small spot size. We used finite deferential time domain (FDTD) calculations to determine the optimum parameters for effective optical confinement. The simulation results indicated that optical confinement is ineffective with an Fe film, because the plasma oscillation frequency is much lower than the optical frequency to be used. To overcome this difficulty, we propose using an Fe-coated fiber probe with a double-layer structure. We used a similar structure on another type of fiber probe, and successfully obtained a high-resolution image of Deoxyibo Nuclec Acid (DNA) [12]. Additionally, it is expected that the double-layer structure increases the magneto-optical effect [11].

Figures 1 (a)–(c) show the process used to fabricate a fiber probe with a double-layer structure. First, the fiber was sharpened to realize a double taper, using two buffered hydrogen fluoride solutions ($\mathrm{BHF_A}$ and $\mathrm{BHF_B}$) as etchants (Fig. 1 (a)) [3]. The two solutions contained different ratios of NH_4F solution (40 wt.%): HF acid (50 wt.%): H_2O, which were 1.7:1:1 ($\mathrm{BHF_A}$) and 10:1:1 ($\mathrm{BHF_B}$). After etching the fiber end with $\mathrm{BHF_A}$ for 60 min to obtain the first taper, it was etched with $\mathrm{BHF_B}$ for 120 min for the second. The typical cone angle of the first taper was 80°.

In order to improve the adhesion of coating materials to a sharpened fiber during a vacuum evaporation, a pre-coating is important. Usually, a thin layer of Cr is deposited before the vacuum evaporation of a metal film [13]. The magnetism of the coating on the fiber probe should be preserved, because the magneto-optical effect of the fiber probe originates from it. However, when evaporating Fe film, Cr forms an alloy with Fe, which can cause the magnetism of the fiber probe

---

Manuscript received July 10, 2002.
Manuscript revised August 11, 2002.

[†] The authors are with the Interdisciplinary Graduate School of Science and Engineering, Tokyo Institute of Technology, Yokohama-shi, 226-8502 Japan.

[††] The authors are with Exploratory Research for Advanced Technology, Japan Science and Technology Corporation, Machida-shi, 194-0004 Japan.

a) E-mail: jslim@ae.titech.ac.jp

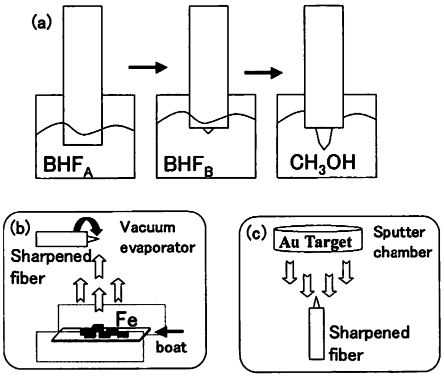

Fig. 1 Schematic explanation of the fabrication process. (a) Etching with two buffered hydrogen fluoride solutions (BHF_A and BHF_B) was used to sharpen the fiber end and the methanol treatment improved the adhesion of the Fe coating. (b) Fe vacuum evaporation. (c) Au sputtering.

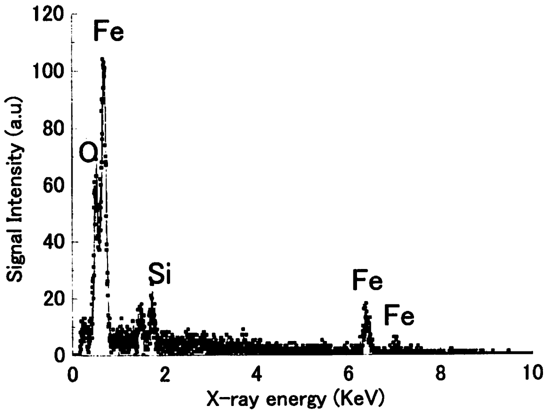

Fig. 2 EDX spectrum of the Fe-coated fiber. The Si and O peaks come from the fiber core (SiO_2). The Fe peaks are from the Fe coating on the fiber.

to decrease or disappear [14]. In order to overcome this difficulty, we adopted methanol treatment [15], instead of a Cr film, to realize homogenous Fe coating. Before the vacuum evaporation, the sharpened fiber was exposed to methanol for 30 sec to radicalize the fiber surface (Fig. 1(a)). The adhesion of Fe coating improved by the activation of the fiber surface.

Next, to coat the Fe film, we kept the Fe vacuum evaporation rate at 0.02–0.03 nm/sec (Fig. 1(b)) based on preliminary experimental results. Since Fe forms an alloy with the W in the heater boat at the temperature above melting point of Fe, the temperature was kept below this while sublimating the Fe. The typical evaporation time and resultant Fe thickness were 2000 s and 50 nm, respectively. Energy dispersive X-ray (EDX) was used to investigate the composition of the evaporated Fe coating on the sharpened fiber. Figure 2 shows an EDX spectrum of the Fe-coated sharpened fiber before Au sputtering. Signals from SiO_2 and Fe were observed, while no other significant signal was observed in the spectrum. This confirmed successfully coating with a high purity, uniform Fe film. Third, the Fe-coated fiber was coated with an Au film using the DC sputtering method (Fig. 1(c)). The typical deposition time and resultant Au thickness were 300 s and 50 nm, respectively. Figure 3 shows SEM images of the fabricated fiber probe with a double-layer structure consisting of 50-nm-thick Fe and 50-nm-thick Au.

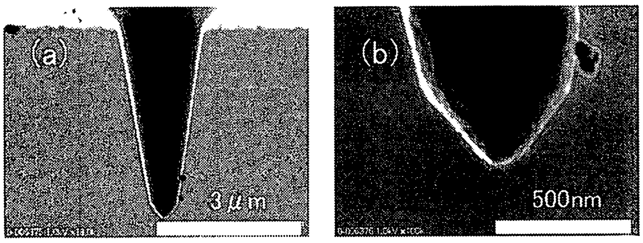

Fig. 3 SEM images of a fabricated fiber probe. (a) The entire probe. (b) A high-magnification SEM image of the fiber probe.

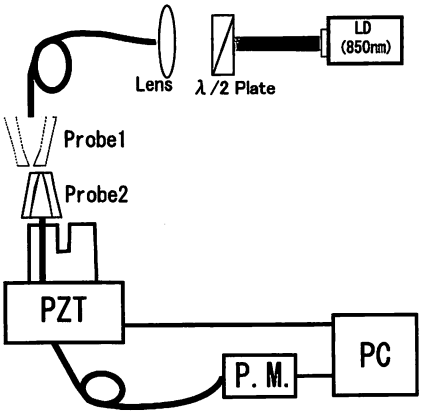

Fig. 4 Schematic drawing of the probe-to-probe experiment. LD: Laser Diode. PZT: Piezoelectric transducer. P.M.: Photomultiplier.

3. Evaluation of Optical Confinement

Figure 4 shows the instruments used to evaluate the optical confinement capability of the fabricated fiber probe, i.e., for measuring the spatial distribution of the optical near-field intensity on the fabricated fiber probe (Probe 1) by the probe-to-probe method [16]. The second probe (Probe 2) used for this evaluation was a double-tapered fiber probe that was fabricated by etching a fiber coated with a 1000-nm-thick layer of Au. A 30-nm diameter aperture was formed by the focused ion beam (FIB) technique. In the measurement, linearly polarized light from a laser diode (850 nm) was coupled into the single-mode fiber. The optical near-field intensity on Probe 1 was observed by scanning with Probe 2 and detecting the scattered light with a photo-multiplier, while the separation between the two probes was maintained within several nanometers using the shear-force technique [3].

Figure 5(a) shows the measured spatial distribu-

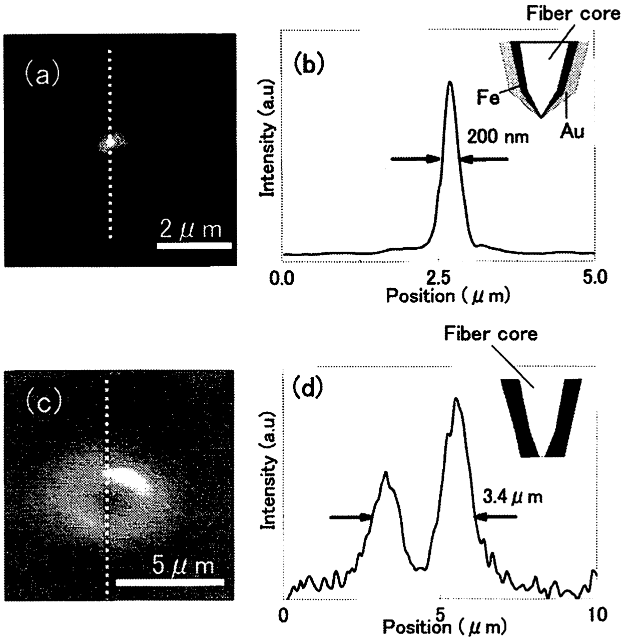

Fig. 5 Spatial distribution of the optical near-field intensity on Probe 1 measured in a probe-to-probe experiment. (a) Two-dimensional distribution and (b) cross-sectional profile of the distribution along the dotted line for the double-layer fiber probe (Au and Fe). (c) Two-dimensional distribution and (d) cross-sectional profile of the distribution along the dotted line for the Fe-coated fiber probe fabricated for comparison.

tion of the optical near-field intensity at the apex of the double-layer fiber probe (Probe 1). Figure 5(b) shows the cross-sectional profile along the dotted line in Fig. 5(a). It has a single peak and its full width at half maximum (FWHM) is 200 nm, which depends on the aperture diameter of Probe 2. The 30-nm diameter aperture of Probe 2 is much smaller than the FWHM of 200 nm. Therefore, the FWHM corresponds to the spatial resolution of the Probe 1. The spatial resolution of a probe corresponding to this value is less than $\lambda/4$ and is sufficient for spatially resolved near-field measurements [3]. For comparison, a fiber probe with a single-layer 250-nm Fe film and a 50-nm aperture was fabricated and evaluated. The measured spatial distribution of the optical near-field intensity was doughnut-shaped, as shown in Fig. 5(c). The FWHM of its cross-sectional profile along the dotted line in Fig. 5(c) was 3.4 μm (Fig. 5(d)). The doughnut-shape originates form ineffective optical confinement of the Fe layer, since the plasma frequency of Fe is much less than the used laser frequency (850 nm).

The improved optical confinement capability that is shown by Figs. 5(a) and (b) is attributed to the fact that the Au layer works as a cladding for the core Fe layer.

4. Conclusion

We fabricated a double-layer Fe-coated fiber probe for the first time. Methanol treatment was used to improve the adhesion of the Fe coating. In order to realize a sufficiently high optical confinement, an Au film was coated as a cladding layer. Evaluation by the probe-to-probe method confirmed that the confinement capability of the fiber probe was sufficient for use as a NOM probe.

References

[1] G. Binnig, H. Rohrer, C. Gerber, and E. Weibel, "Surface studies by scanning tunneling microscopy," Phys. Rev. Lett., vol.49, no.1, pp.57–60, July 1982.

[2] G. Binning, C.F. Quate, and C. Gerber, "Atomic force microscope," Phys. Rev. Lett., vol.56, no.9, pp.930–933, March 1986.

[3] M. Ohtsu, ed., Near-Field Nano/Atom Optics and Technology, Springer-Verlag, Tokyo, Berlin, Heidelberg, 1998.

[4] E.B. Cooper, S.R. Manalis, H. Fang, H. Dai, K. Matsumoto, S.C. Minne, T. Hunt, and C.F. Quate, "Terabit-per-square-inch data storage with the atomic force microscope," Appl. Phys. Lett., vol.75, no.22, pp.3566–3568, Nov. 1999.

[5] T. Shimizu, H. Tokumoto, S. Akita, and Y. Nakayama, "Stable atomic imaging of Si(111)-7×7 surface by scanning tunneling microscope with carbon nanotube tip," Surface Science, vol.486, no.3, pp.455–460, July 2001.

[6] R. Eckert, J.M. Freyland, H. Gersen, H. Heizelmann, G. Schürmann, W. Noell, U. Staufer, and N.F. de Rooij, "Near-field fluorescence imageing with 32 nm resolution based on microfabricated cantilevered probes," Appl. Phys. Lett., vol.77, no.23, pp.3695–3697, Dec. 2000.

[7] T. Kawagoe, Y. Suzuki, and S. Yuasa, "Observation of spin-polarized tunneling by scanning tunneling microscopy," J. Magnetism and Magnetic Materials, vol.239, no.1, pp.126–128, Feb. 2002.

[8] D. Rugar and P. Hansma, "Atomic force microscopy," Physics Today, vol.43, no.10, pp.23–30, Oct. 1990.

[9] D.W. Bullock, V.P. LaBella, Z. Ding, and P.M. Thibado, "Mapping the spin-injection probability on the atomic scale," J. of Superconductivity: Incorporating Novel Magnetism, vol.15, no.1, pp.37–42, Feb. 2002.

[10] P. Grutter, H.J. Mamin, and D. Rugar, Magnetic Force Microscopy, Scanning Probe Microscopy II, Springer-Verlag, New York, 1991.

[11] Y. Suzuki, T. Katayama, P. Bruno, S. Yuasa, and E. Tamura, "Oscillatory magnet-optical effect in a Au (001) film deposited on Fe: Experimental confirmation of a spin-polarized quantum size effect," Phys. Rev. Lett., vol.80, no.23, pp.5200–5203, June 1998.

[12] U.M. Rajagopalan, S. Mononobe, K. Yoshida, M. Yoshimoto, and M. Ohtsu, "Nanometer level resolving near-field optical microscope under optical feedback in the observation of a single-string deoxyibo nuclec acid," Jpn. J. Appl. Phys., vol.38, no.12A, pp.6713–6720, Dec. 1999.

[13] M.H. Lee, S.H. Bae, and A.S. Bhalla, "Thermal properties of a pyroelectric-ceramic infrared detector with metallic intermediate layer," Opt. Engineering, vol.37, no.6, pp.1746–1753, June 1998.

[14] R.M. Bozorth, Ferromagnetism; The Bell Telephone Laboratories series, Van Nostrand, New York, 1951.

[15] I. Yamaguchi, T. Terayama, T. Manabe, T. Tsuchiya, M. Sohma, T. Kumagai, and S. Mizuta, "Preparation of (111)-oriented epitaxial $Fe_{3-x}O_4$ films on-Al_2O_3 (0001) substrates by coating-pyrolysis process using postepitaxial topotaxy via (0001)-oriented-Fe_2O_3," J. Solid State Chem.,

vol.163, no.1, pp.239–247, Jan. 2002.
[16] T. Yatsui, M. Kourogi, and M. Ohtsu, "Highly efficient excitation of optical near-field on an apertured fiber probe with an asymmetric structure," Appl. Phys. Lett., vol.71, no.13, pp.1756–1758, Sept. 1997.

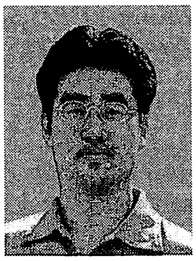

Jungshik Lim was born in Seoul, Korea in 1971. He received his B.S. in 2001 from Tokyo Institute of Tecnnology, and is currently working toward the M.E. degree at Tokyo Institute of Tecnnology, doing research focused on the fabrication of nano-structure using optical near-field technology. Mr. Lim is a member of the Japan Society of Applied Physics.

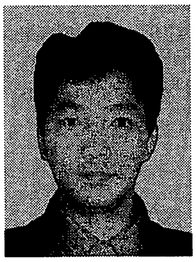

Tadashi Kawazoe was born in Kochi Prefecture, Japan, on April 5, 1967. He received the B.E., M.E., and Ph.D. degrees in physics from University of Tsukuba, Tsukuba, Japan, in 1990, 1993, and 1996, respectively. Since 1991, he has studied spin relaxation in semiconductor quantum wells and optical nonlinearities in semiconductor quantum dots at the Institute of Physics, University of Tsukuba, Tsukuba-city, Japan. In 1996, he joined in the faculty of Engineering, Yamagata University, Yamagata, Japan, as a Research Associate, engaged in research on nonlinear optical materials and devices. Since April 2000, he has been with Japan Science and Technology Corporation, Tokyo, Japan. His current research interests are in the areas of optical properties of nano materials, optical near field, and nanophotonic devices. Dr. Kawazoe is a member of the Japan Society of Applied Physics.

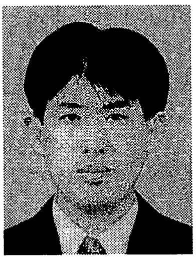

Takashi Yatsui was born in Tokyo, Japan, on January 21, 1972. He received the B.E. degree from Keio University, Tokyo, Japan, in 1995, and M.E. and D.E. degrees from Tokyo Institute of Technology, Tokyo, Japan, in 1997 and 2000, respectively. From 1999 to 2000, he was a Research Fellow of the Japan Society for the Promotion of Science. Since 2000, he has been a Researcher at the Japan Science and Technology Corporation, Tokyo. His current research interests include nanofabrication using optical near-field. Dr. Yatsui received 1st prize in Paper Contest from IEEE Student Branch at Tokyo Institute of Technology in 1998, and the excellent research presentation award form the Japan Society of Applied Physics in 2000, and Tejima Doctoral Dissertation Award from Tejima Foundation in 2001. Dr. Yatsui is a member of the Japan Society of Applied Physics.

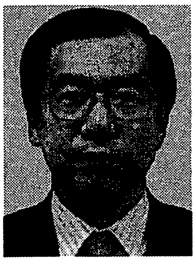

Motoichi Ohtsu received the B.E., M.E., and Dr.E. degrees in electronics engineering from the Tokyo Institute of Technology, Tokyo, Japan, in 1973, 1975, and 1978, respectively. In 1978, he was appointed a Research Associate, and in 1982, he became an Associate professor at the Tokyo Institute of Technology. From 1986 to 1987, while on leave from the Tokyo Institute of Technology, he joined the Crawford Hill Laboratory, AT&T Bell Laboratories, Holmdel, NJ. In 1991, he became a Professor at the Tokyo Institute of Technology. Since 1993, he has been concurrently the Leader of the "Photon Control" project of the Kanagawa Academy of Science and Technology, Kanagawa, Japan. Since 1998, he has been concurrently the Leader of the "Localized Photon" project of ERATO (Exploratory Research for Advanced Technology), JST (Japan Science and Technology Corporation), Japan. He has written over 320 papers and received 87 patents. He is the author and co-author of 39 books, including seven in English, entitled Highly Coherent Semiconductor Lasers (Artech House, Boston, 1991), Coherent Quantum Optics and Technology (Kluwer, Dordrecht, 1993), Frequency Control of Semiconductor Lasers (Wiley Interscience, New York, 1996), Near-Field Nano/Atom Optics and Technology (Springer Verlag, Berlin, 1998), Near-Field Nano-Optics (Kluwer Academic/Plenum Publishers, New York, 1999), Optical and Electronic Properties of Nano-matters (Kluwer Academic/KTK Scientific Publishers, Dordrecht/Tokyo, 2001), and Progress in Nano Electro-Optics (Springer Verlag, Berlin, 2002). In 1999, he was the Vice-President of the IEEE/LEOS Japan Chapter, and in 2000, he was appointed as the President. From 2000, he is an executive director of the Japan Society of Applied Physics. He served as a Technical Program Co-chair for the 4th Pacific Rim Conference on Lasers and Electro-Optics (CLEO/PR01), 2001. He has been a tutorial lecturer of the SPIE and the OSA. His main fields of interests are the nano-photonics and atom-photonics. Dr. Ohtsu is a member of the Japan Society of Applied Physics, the Institute of Electrical Engineering of Japan, the Optical Society of America, and American Physical Society. He has been awarded ten prizes from academic institutions, including the Issac Koga Gold Medal of URSI (International Union of Radio Science) in 1984, the Japan IBM Science Award in 1988, two awards from the Japan Society of Applied Physics in 1982 and 1990, and the Inoue Science Foundation Award in 1999.

PAPER *Special Issue on Near-Field Optics and Its Applications*

Lateral Integration of Zn and Al Dots with Nanometer-Scale Precision by Near Field Optical Chemical Vapor Deposition Using a Sharpened Optical Fiber Probe

Yoh YAMAMOTO[†], **Motonobu KOUROGI**[†,††], *Nonmembers*,
Motoichi OHTSU[†,††a)], *Regular Member*, **Geun Hyoung LEE**[††],
and **Tadashi KAWAZOE**[††], *Nonmembers*

SUMMARY *In-situ* position-controlled lateral deposition of nanometer-size Zn and Al dots on a sapphire substrate was accomplished by dissociating diethylzinc and trimethylaluminum using an optical near field on a sharpened optical fiber probe tip. The minimum diameters of the Zn and Al dots deposited were 37 and 25 nm, respectively, comparable with the apex diameter of the fiber probe. By changing the reactant molecules during deposition, nanometric Zn and Al dots were successively deposited on the same sapphire substrate with high precision. The distance between these dots was as short as 100 nm.

key words: *near-field, optical CVD, nano structures, nano fabrication*

1. Introduction

The integration of nano-scale photonic devices in future optical technology is the focus of much attention [1]. Such integration requires advanced nanofabrication techniques to realize high spatial resolution, precise control of size and position, and applicability to various materials. Self-organized growth has been widely investigated for such nano-fabrication [2]; however, its spatial precision is not sufficient. To improve precision, an e-beam [3], STM [4], and surface modification [5] have been used for site-control of the substrate. *In-situ* patterning of nano-scale structures has also been investigated using a scanning probe microscope, such as an STM [6]; however, this technique has the fatal disadvantage that it cannot deal with insulators, limiting its application.

In order to solve this problem, we recently demonstrated near-field optical chemical vapor deposition (NFO-CVD), which makes it possible to fabricate nano-scale structures while precisely controlling their size and position [7], [8]. The outstanding advantage of NFO-CVD is that the optical near-field effect enables deposition even using non-resonant photons [9]. Due to the photochemical reaction between the reactant molecules and the optical near field generated at the optical fiber probe, NFO-CVD is applicable to various materials, including metals, semiconductors, and insulators. By changing the reactant molecules during deposition, nano-scale structures made of different materials can be created on the same substrate. Furthermore, selective deposition is also possible by varying the photon energy, making NFO-CVD a powerful tool for the fabrication and integration of nano-scale photonic devices.

2. Experimental

In our previous work, we demonstrated the deposition of Zn dots 60 nm in diameter using an optical fiber probe with an aperture diameter of 60 nm [8]. Such apertured probes have been widely used for spatially resolved optical near-field imaging and spectroscopy. However, precise control of position while fabricating nano-scale structures is not straightforward because of the probe's flat tip. In order to improve precision, we used a sharpened UV optical fiber probe with an apex diameter of less than 50 nm. After forming a tapered probe by pulling and etching a pure silica core, the probe was coated with 20-nm-thick Al film [10]. Figure 1 shows an SEM image of the apex of the fiber probe. An optical near field generated in the region corresponding to the apex diameter of the tip disso-

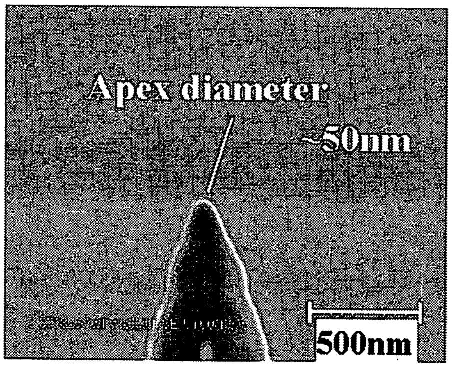

Fig. 1 A SEM image of a sharpened UV optical fiber probe.

Manuscript received June 13, 2002.

[†] The authors are with the Interdisciplinary Graduate School of Science and Engineering, Tokyo Institute of Technology, Yokohama-shi, 226-8502 Japan.

[††] The authors are with Japan Science and Technology Corporation, Machida-shi, 194-0004 Japan.

a) E-mail: ohtsu@ae.titech.ac.jp

ciates reactant molecules around the tip. Since the tip used for optical near-field generation is highly sensitive to the shear force with the substrate, the fiber probe facilitates precise position control during deposition. Moreover, the sharp tip enables reliable *in-situ* shear-force topographic imaging of the deposited nanoscale structures, immediately after deposition.

In the following section, we demonstrate the deposition of nano-scale dots of Zn and Al while controlling their size and position using the fiber probe described above. Furthermore, we integrated nanometric Zn and Al dots on the same substrate by changing the reactant molecules during deposition. The metals were deposited using the photodissociative reactions of diethylzinc (DEZ) and trimethylaluminum (TMA) with the second harmonic (SH) light (wavelength: 244 nm) of an argon ion laser [11]. In order to optimize the experimental parameters of the NFO-CVD, we carried out preliminary CVD experiments in which DEZ and TMA were dissociated using conventional propagating light. By referring to the EDS spectra of the deposited films, we determined the experimental parameters that resulted in deposited films of high quality Zn and Al. These parameters were used as the optimized parameters for NFO-CVD, as described below.

The SH light was coupled with the fiber probe used to generate an optical near field. The probe was installed in the deposition chamber and controlled using a scanning near-field optical microscope system. The vacuum chamber was evacuated to below 1.3×10^{-3} Pa and then filled with reactant gases. An atomic smooth sapphire [12] was used as the substrate, and kept at room temperature. During deposition, the substrate-probe distance was maintained within several nanometers using the shear-force feedback technique. The topographic profiles of the deposited patterns were measured by vacuum shear-force microscopy (VSFM) [13] with the same fiber probe.

3. Result and Discussion

Figure 2(a) shows the shear-force image of two nanometric Zn dots deposited on the sapphire substrate using the fiber probe in Fig. 1. The partial pressures of DEZ and the carrier gas (Ar) were 1.3 and 36 Pa, respectively. The deposition time, using SH light at 1 mW power, was 60 s. Figure 2(b) shows the cross sectional profile along the dashed line shown in Fig. 2(a). The full widths at half maximum (FWHM) of the two dots are 52 and 37 nm, which are comparable with the apex diameter of the fiber probe used. The distance between the two dots is 45 nm, which is as short as the FWHM of the dots. These results demonstrate the high precision of the nanometric deposition capability of this technique and its ability to control size and position.

Figure 3(a) shows shear-force images of five Al dots on a sapphire. These dots were deposited by dissociating TMA using SH light at 1 mW power. The deposition time was 60 s. The partial pressures of TMA and the carrier gas (Ar) were 1.3 and 64 Pa, respectively. The FWHM of one dot in Fig. 3(b) is 27 nm, which is comparable with the apex diameter of the probe used. This is the first report of the deposition of nanometric Al dots using this technique.

As the experimental results described above show, various materials can be deposited selectively by changing the reactant gases. Furthermore, the technique is not limited by the species of substrate or the material deposited. In addition to these advantages, the unique and most attractive advantage is the possibility of *in-situ* lateral integration of nano-scale structures of different materials with ease. Figure 4 proves this possibility, by showing shear-force images of Zn and Al dots deposited in close proximity with each other on a sapphire substrate: First, Zn dots were deposited under a DEZ partial pressure of 1.3 Pa, as shown in

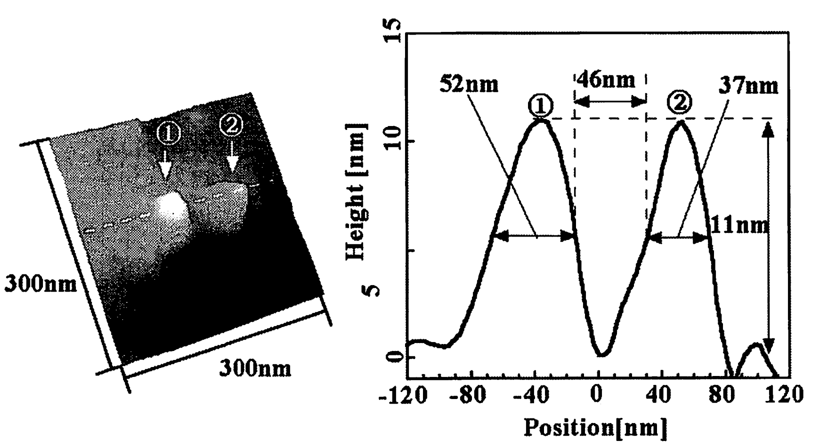

(a) (b)

Fig. 2 Closely spaced two nanometric Zn dots deposited on a sapphire substrate (a) Shear-force images. (b) Cross-sectional profile along the white dashed line in (a).

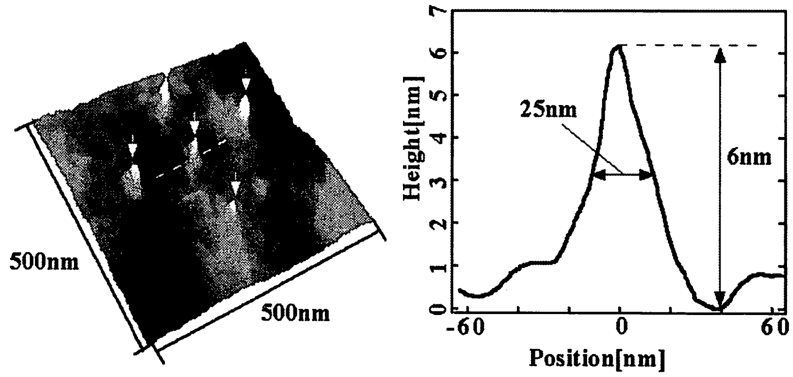

(a) (b)

Fig. 3 Five Al dots deposited on a sapphire substrate. (a) Shear-force images. White arrows indicate the Al dots. (b) Cross-sectional profile along the white dashed line in (a).

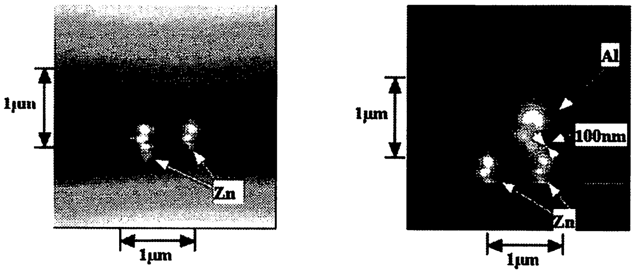

(a) (b)

Fig. 4 Zn and Al dots deposited closely on a sapphire substrate. (a) Shear-force images of Zn dots deposited by the first step of the process. (b) Shear-force images of Zn and Al dots.

Fig. 4(a). Next, Al dots were deposited under a TMA partial pressure of 1.3 Pa after the deposition chamber was evaporated to a pressure of 6.7×10^{-4} Pa. The final result is shown in Fig. 4(b). Here, the distance between Zn and Al dots is as short as 100 nm.

This technique enables the fabrication of nano-scale electro-luminescence (EL) devices on a p-type semiconductor substrate by assembling metallic Al wires and n-type ZnO nano-scale dots. We have already demonstrated the deposition of n-type ZnO dots by NFO-CVD and evaluated their UV light-emitting characteristics [14], [15]. Moreover, this technique is not limited to Zn, Al, and ZnO, but is applicable to various metals, semiconductors, and insulators.

4. Conclusion

In summary, we carried out the deposition of nano-scale Zn and Al dots on a sapphire substrate, while precisely controlling their size and position. Furthermore, we deposited Zn and Al dots in close proximity on the same substrate by changing the reactant gas. These results demonstrate that this technique enables the integration of nano-scale dots of different materials. Analysis of the nano-scale dots deposited is an important problem; however, we expect that it can be solved using *in-situ* near field Raman spectroscopy [16].

Acknowledgements

The authors would like to thank Doctor T. Yatsui of the Japan Science and Technology Corporation for his irreplaceable help and advice. They are grateful to Professor M. Konagai and Professor A. Yamada of the Tokyo Institute of Technology for useful advice.

References

[1] M. Ohtsu, "Near-field nano-optics toword nano/atom deposition," Technical Digest of SPIE, vol.3749, pp.478–479, Aug. 1999.

[2] D. Leonald, M. Krishnamurthy, C.M. Reaves, S.P. Denbaars, and P.M. Petroff, "Direct formation of quantum-sized dots from uniform coherent islands of InGaAs on GaAs surfaces," Appl. Phys. Lett., vol.63, no.23, pp.3203–3205, Dec. 1993.

[3] T. Tsutsui, K. Kawasaki, M. Mochizuki, and T. Matsubara, "Site controlled metal and semiconductor quantum dots on epitaxial fluoride films," Microelectronics Engineering, vol.47, p.135, 1999.

[4] S. Kohmoto, H. Nakamura, T. Ishikawa, and K. Asakawa, "Site-controlled self-organization of indivisiual InAs quamtum dots by scanning tunneling probe-assisted nanolithgraghy," Appl. Phys. Lett., vol.75, no.23, pp.3488–3490, Nov. 1999.

[5] E. Kuramochi, J. Temmyo, T. Tamamura, and H. Kamada, "Perfect spatial ordering of self-organized InGaAs/AlGaAs box-like structure array on GaAs(311)B substrate with silicon nitride dot array," Appl. Phys. Lett., vol.71, no.12, pp.1655–1657, Sept. 1997.

[6] R. Wiesendanger, "Fabrication of nanometer structure using STM," Appl. Surf. Sci., vol.54, pp.271–275, Aug. 1992.

[7] V.V. Polonski, Y. Yamamoto, M. Kourogi, H. Fukuda, and M. Ohtsu, "Nanometric patterning of zinc by optical near-field photochemical vapour deposition," J. Microscopy, vol.194, pp.545–547, May 1999.

[8] Y. Yamamoto, V. Polonski, G.H. Lee, M. Kourogi, and M. Ohtsu, "Fabrication of nanometric zinc pattern with photodissociated gas-phase diethylzinc by optical near field,"

Appl. Phys. Lett., vol.76, no.16, pp.2173–2175, April 2000.

[9] T. Kawazoe, Y. Yamamoto, and M. Ohtsu, "Fabrication of a nanometric Zn dot by nonresonant near-field optical chemical-vapor deposition," Appl. Phys. Lett., vol.79, no.8, pp.1184–1186, Aug. 2001.

[10] S. Mononobe, T. Saiki, T. Suzuki, S. Koshihara, and M. Ohtsu, "Fabrication of a triple tapered probe for near-field spectroscopy in UV region based on selective etching of a multistep index fiber," Opt. Commun., vol.146, no.1-6, pp.45–48, June 1998.

[11] D.J. Ehrlich, R.M. Osgood, Jr., and T.F. Deutsch, "Laser chemical technique for rapid direct writing of surface relief in silicon," Appl. Phys. Lett., vol.38, no.12, pp.1018–1020, June 1981.

[12] M. Yoshimoto, T. Maeda, T. Ohnishi, K. Koinuma, O. Ishiyama, M. Shinohara, M. Kubo, R. Miura, and A. Miyamoto, "Atomic-scale formation of ultrasmooth surfaces on sapphire substrates for high-quality thin film fabrication," Appl. Phys. Lett., vol.67, no.18, pp.2615–2617, Oct. 1995.

[13] V.V. Polonski, Y. Yamamoto, J.D. White, M. Kourogi, and M. Ohtsu, "Vacuum shear force microscopy application to high resolution work," Jpn. J. Appl. Phys., vol.38, no.7B, pp.L826–828, July 1999.

[14] G.H. Lee, Y. Yamamoto, M. Kourogi, and M. Ohtsu, "Fabrication of ZnO nanostructure using near-field optical technology," Proc. SPIE, vol.3791, pp.132–133, July 1999.

[15] G.H. Lee, Y. Yamamoto, M. Kourogi, and M. Ohtsu, "Blue shift of room temperature ultraviolet luminescence of ZnO deposited by photochemical vapor deposition," Thin Solid Films, vol.386, pp.117–120, 2001.

[16] Y. Narita, T. Tadokoro, T. Ikeda, T. Saiki, S. Mononobe, and M. Ohtsu, "Near-field Raman spectral measurement of polydiacetylene," Appl. Spectroscopy, vol.52, pp.1141–1143, Sept. 1998.

Yoh Yamamoto graduated from Waseda University in 1996. He completed the master'course at Tokyo Institute of Technology in 1998. He entered the doctor's course at Tokyo Institute of Technology in1998. He studies nanofabrication techniques with optical near field.

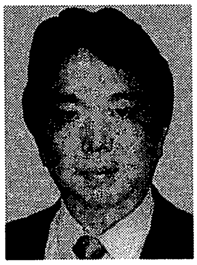

Motonobu Kourogi was born in Shiga, Japan, 1966. He received the B.S. degree from Shizuoka University, Shizuoka, Japan, in 1988, and M.S. and Ph.D. degrees from the Tokyo Institute of Technology, Tokyo, Japan, in 1990 and 1993, respectively. Since 1993 he has been with Tokyo Institute of Technology as a research Associate. His current research interests are frequency synthesis of lasers Dr. Kourogi is a member of the Japan Society of Applied Physics.

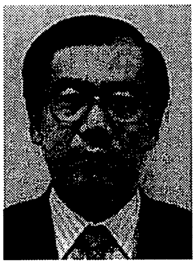

Motoichi Ohtsu received the B.E., M.E., and Dr.E. degrees in electronics engineering from the Tokyo Institute of Technology, Tokyo, Japan, in 1973, 1975, and 1978, respectively. In 1978, he was appointed a Research Associate, and in 1982, he became an Associate professor at the Tokyo Institute of Technology. From 1986 to 1987, while on leave from the Tokyo Institute of Technology, he joined the Crawford Hill Laboratory, AT&T Bell Laboratories, Holmdel, NJ. In 1991, he became a Professor at the Tokyo Institute of Technology. Since 1993, he has been concurrently the Leader of the "Photon Control" project of the Kanagawa Academy of Science and Technology, Kanagawa, Japan. Since 1998, he has been concurrently the Leader of the "Localized Photon" project of ERATO (Exploratory Research for Advanced Technology), JST (Japan Science and Technology Corporation), Japan. He has written over 320 papers and received 87 patents. He is the author and co-author of 39 books, including seven in English, entitled Highly Coherent Semiconductor Lasers (Artech House, Boston, 1991), Coherent Quantum Optics and Technology (Kluwer, Dordrecht, 1993), Frequency Control of Semiconductor Lasers (Wiley Interscience, New York, 1996), Near-Field Nano/Atom Optics and Technology (Springer Verlag, Berlin, 1998), Near-Field Nano-Optics (Kluwer Academic/Plenum Publishers, New York, 1999), Optical and Electronic Properties of Nano-matters (Kluwer Academic/KTK Scientific Publishers, Dordrecht/Tokyo, 2001), and Progress in Nano Electro-Optics (Springer Verlag, Berlin, 2002). In 1999, he was the Vice-President of the IEEE/LEOS Japan Chapter, and in 2000, he was appointed as the President. From 2000, he is an executive director of the Japan Society of Applied Physics. He served as a Technical Program Co-chair for the 4th Pacific Rim Conference on Lasers and Electro-Optics (CLEO/PR01), 2001. He has been a tutorial lecturer of the SPIE and the OSA. His main fields of interests are the nano-photonics and atom-photonics. Dr. Ohtsu is a member of the Japan Society of Applied Physics, the Institute of Electrical Engineering of Japan, the Optical Society of America, and American Physical Society. He has been awarded ten prizes from academic institutions, including the Issac Koga Gold Medal of URSI (International Union of Radio Science) in 1984, the Japan IBM Science Award in 1988, two awards from the Japan Society of Applied Physics in 1982 and 1990, and the Inoue Science Foundation Award in 1999.

Geun Hyoung Lee was born in Seoul, Korea on February 12, 1965. He received the B.E. and M.E. degrees in material science engineering from the Yonsei University, Seoul, in 1987 and 1990, respectively, and the Ph.D. degree in material science engineering from the Tokyo Institute of Technology, Tokyo, Japan, in 1998. He was a researcher from 1998 to 2000 at Japan Science and Technology Corporation, Tokyo. His main interests are the fabrication of nano-structure using optical near-field technology. He received the excellent research presentation award from the Japan Society of Applied Physics and the Outstanding student research award at the 4th International Conference on Laser Ablation, USA, both in 1997.

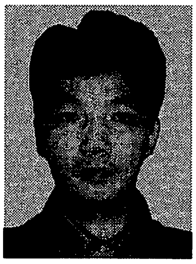

Tadashi Kawazoe was born in Kochi Prefecture, Japan, on April 5, 1967. He received the B.E., M.E., and Ph.D. degrees in physics from University of Tsukuba, Tsukuba, Japan, in 1990, 1993, and 1996, respectively. Since 1991, he has studied spin relaxation in semiconductor quantum wells and optical nonlinearities in semiconductor quantum dots at the Institute of Physics, University of Tsukuba, Tsukuba-city, Japan. In 1996, he joined in the faculty of Engineering, Yamagata University, Yamagata, Japan, as a Research Associate, engaged in research on nonlinear optical materials and devices. Since April 2000, he has been with Japan Science and Technology Corporation, Tokyo, Japan. His current research interests are in the areas of optical properties of nano materials, optical near field, and nanophotonic devices. Dr. Kawazoe is a member of the Japan Society of Applied Physics.

Nonlinear Optics, 2002, Vol. 29(10–12), pp. 563–569 Taylor & Francis
Taylor & Francis Group

COHERENT DIPOLE OSCILLATION INDUCED BY LOCALIZED PHOTONS

A. SHOJIGUCHI[a,*], K. KOBAYASHI[a], S. SANGU[a], K. KITAHARA[b]
and M. OHTSU[a,c]

[a]*ERATO Localized Photon Project, Japan Science and Technology, Tokyo, 194-0004, Japan;* [b]*Division of Natural Sciences, International Christian University, Tokyo, 181-8585, Japan;* [c]*Interdisciplinary Graduate School of Sciences and Engineering, Tokyo Institute of Technology, Kanagawa, 226-8502, Japan*

(Received 22 July 2002; In final form 11 August 2002)

This paper describes a novel model for the dynamics of the dipole coherence in two-level quantum dots (QDs) interacting with localized photons. The model is based on the fact that the coupling on a nanometer scale between QDs via optical near fields represented by localized photons is much stronger than that via propagating far fields. The model predicts that an intriguing phenomenon such as a collective dipole oscillation occurs if the initial quantum states are locally manipulated. The origin of this kind of collective behaviour is discussed in view of Dicke's superradiance.

Keywords: Dipole coherence; Localized photon; Exciton; Optical near fields; Collective dipole oscillation; Dicke's superradiance

1 INTRODUCTION

Recent progress in nanotechnology has enabled us to explore the excitonic processes and control quantum states in an isolated semiconductor quantum dot (QD) or several coupled quantum dots that are also isolated from one

---

[*] Corresponding author.

ISSN 1058-7268 print; ISSN 1029-2500 online
DOI: 10.1080/1058726021000045414

another [1]. It seems that in the near future, the excition dynamics will be experimentally investigated with the help of the near-field optical techniques [2] by the local excitation of arbitrarily selected QDs. Optical near fields, free from the diffraction limit, are localized around the matter, *e.g.*, around a near-field probe tip or a QD system, and thus they can be reasonably treated either as a short-range effective interaction of QDs or as localized photonic degrees of freedom. Moreover, the near-field coupling strength between QDs is much stronger than the far-field one in the nanometer regime. One then expects essentially different dynamics from what has been obtained with optical far fields that cannot, due to the diffraction limit, selectively excite QDs arranged at a nanometer scale. In this paper, we report intriguing phenomena that appear in such an initially locally coupled QD system via localized photons, on the basis of a novel model that takes both localized photonic and excitonic degrees of freedom into account explicitly.

2 THEORY OF COHERENT OSCILLATION

We consider a model system consisting of N two-level QDs closely configured in a ring (Fig. 1(a)) and localized photons on each QD. An exciton in a QD can interact only with localized photons in the same QD while the localized photons can hop between the nearest neighbour sites. This model is based on the unique property of localization or non-propagation of the optical near fields [3] mentioned above, and is preferable for an intuitive understanding of coherent excitation transfer between the QDs and its manipulation by the localized photons. The model Hamiltonian H can be written in the following form:

$$H = H_a + H_b + H_{\text{int}}, \tag{1a}$$

$$H_a = \varepsilon \sum_{n=1}^{N} a_n^{\dagger} a_n + V \sum_{n=1}^{N} (a_{n+1}^{\dagger} a_n + a_n^{\dagger} a_{n+1}), \tag{1b}$$

$$H_b = E \sum_{n=1}^{N} b_n^{\dagger} b_n, \tag{1c}$$

$$H_{\text{int}} = U \sum_{n=1}^{N} (a_n^{\dagger} b_n + a_n b_n^{\dagger}), \tag{1d}$$

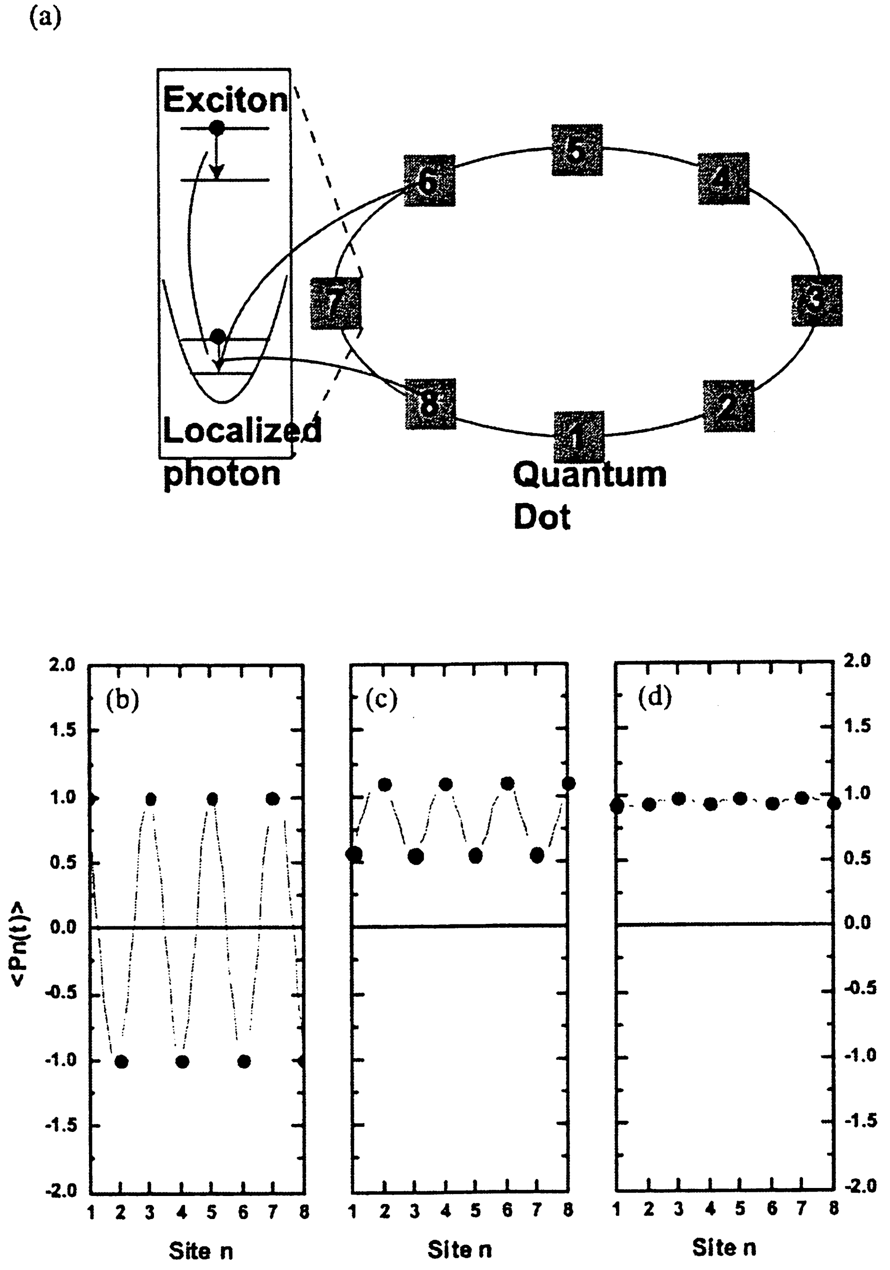

FIGURE 1 (a) Schematic diagram of a model system: N two-level QDs labelled by the site number are closely configured in a ring and interacting with localized photons. (b)–(d) Time evolution of the dipole coherence for the system size $N = 8$. The vertical and horizontal axes represent the dipole coherence and the QD site, respectively. From (b) to (d), a collective oscillation is growing, which originated from a local manipulation of the initial non-radiative state (a).

where H_a and H_b describe localized photons and excitons in QDs, respectively, and the intradot interaction between the localized photons and the excitons is denoted as H_{int}. Creation and annihilation operators for a localized photon and an exciton in each QD labelled by n are expressed as $(a_n^\dagger, a_n)$ and $(b_n^\dagger, b_n)$, respectively. The localized photon operators satisfy the bosonic commutation relation while the exciton operators obey the fermionic commutation relation in a single site and the bosonic one between different sites. The constant energies of the localized photons and excitons are assumed to be ε and E, respectively. The hopping energy of the localized photons is represented as V, and U is for the conventional dipolar coupling between the localized photons and excitons in the rotating wave approximation.

In order to investigate the coherent excitation dynamics of the system, we examine the time evolution of the expectation value of the dipole coherence at an arbitrary QD n, $\langle P_n(t)\rangle = \langle b_n(t) + b_n^\dagger(t)\rangle$, under a variety of initial conditions. Since the Heisenberg equations of motion for $b_n(t)$ and $a_n(t)$ are nonlinearly coupled, it would be rational to solve them considering H_{int} as a perturbation H_{int}. Defining the Liouville operators as

$$L\bullet = \frac{1}{\hbar}[H, \bullet], \quad L_{\mathrm{int}}\bullet = \frac{1}{\hbar}[H_{\mathrm{int}}, \bullet], \quad L_0\bullet = \frac{1}{\hbar}[H_0, \bullet], \tag{2}$$

we have formal solutions of $b_n(t)$ and $b_n^\dagger(t)$ as follows:

$$b_n(t) = G(t)b_n(0), \quad b_n(t) = G(t)b_n(0). \tag{3}$$

Here the operator $G(t)$ is defined as $G(t) = \exp(iLt)$, which satisfies the following equation:

$$\frac{\mathrm{d}G(t)}{\mathrm{d}t} = iLG(t) = i(L_0 + L_{\mathrm{int}})G(t). \tag{4}$$

Then the perturbative solution of $G(t)$ in the second order is obtained as

$$\begin{aligned} G^{(2)}(t) &= G_0(t) + i\int_0^t G_0(t-s)L_{\mathrm{int}}G_0(s)\,\mathrm{d}s \\ &\quad - \int_0^t \mathrm{d}s \int_0^s \mathrm{d}u G_0(t-s)L_{\mathrm{int}}G_0(s-u)L_{\mathrm{int}}G_0(u) \end{aligned} \tag{5}$$

with $G_0(t) = \exp(iL_0 t)$, and the expectation value of the exciton operator $b_n(t)$ can be written as

$$\begin{aligned}\langle b_n(t)\rangle &= \langle b_n(0)\rangle \exp(-i\Omega t)\\ &\quad + g^2 \sum_{j=1}^{N} \Gamma_j(t) \left(\sum_{m=1}^{N} P_{nj} P_{mj} (1 - \delta_{nm}) \langle W_n(0)\rangle \langle b_m(0)\rangle - P_{nj}^2 \langle b_n(0)\rangle \right)\end{aligned} \tag{6}$$

Here $E = \hbar\Omega$, $U = \hbar g$, and

$$\Gamma_j(t) = e^{-i\Omega t} \int_0^t e^{is(\Omega-\lambda_j)}\, \mathrm{d}s \int_0^s e^{iu(\Omega-\lambda_j)}\, \mathrm{d}u. \tag{7}$$

In addition, we employ the eigenvalue λ_j and the matrix elements of the diagonalizing operator P, noticing that the Hamiltonian H_a in Eq. (1b) can be diagonalized in terms of the mixed photon operator $v_j = \sum_{n=1}^{N} P_{nj} a_n$ as

$$H_a = \sum_j \hbar \lambda_j v_j^{\dagger} v_j, \quad [v_j, v_j^{\dagger}] = \delta_{jj'}. \tag{8}$$

The population difference at a time t, $W_n(t) = b_n^{\dagger}(t) b_n(t) - b_n(t) b_n^{\dagger}(t)$, is also incorporated in Eq. (6), as another state parameter to be manipulated locally. The expressions given by Eq. (6) and its Hermitian conjugate provide a final result as

$$\begin{aligned}\langle P_n(t)\rangle &= \langle P_n(0)\rangle \left(\cos\Omega t - g^2 \sum_j c_j(t) P_{nj}^2 \right)\\ &\quad + g^2 \sum_j \sum_{m \neq n} c_j(t) P_{nj} P_{mj} \langle P_m(0)\rangle \langle W_n(0)\rangle,\end{aligned} \tag{9}$$

where the real part of $\Gamma_j(t)$ in Eq. (7) is denoted by $c_j(t)$. It is noteworthy that the sign of the dipole coherence of nth QD $\langle P_n(t)\rangle$, depends on the product of the initial dipole coherence and population difference from the second line of Eq. (9), which indicates a possibility of the local manipulation leading to a collective behaviour of the system.

3 RESULTS AND DISCUSSION

On the basis of Eq. (9), we numerically investigate the dynamics of dipole coherence depending on initial conditions. Suppose the dipole coherence is initially set only at QD 1 as $\langle P_n(0)\rangle = \delta_{n1}$ and all the population differences $\langle W_n(0)\rangle$ as -1 with the material parameters ε, V, and Ω given. Then the dipoles of QDs 4, 5, and 6 oscillate with an opposite sign to those of other QDs. If the population differences in QDs 4, 5, and 6 are set opposite to those of other QDs at $t = 0$, we find a collective oscillation of all QDs dipoles. This indicates that an appropriate local manipulation of the quantum states in the QDs at $t = 0$ can induce a collective oscillation of all the dipoles of the system.

Figures 1(b)–(d) illustrate the more intriguing non-radiative case, where the alternating dipole coherences are initially set by an optical near-field probe, *i.e.*, the total dipole of the system is vanishing as $\langle P_n(0)\rangle = (-1)^{n+1}$ for $n = 1, 2, \ldots, N =$ even. It follows from Figs 1(b) to 1(d) that a collective oscillation of the dipoles is growing. The point of the matter is a local manipulation by which the sign of the population difference in each QD is set opposite to that of the corresponding dipole coherence as $\langle W_n(0)\rangle = -\langle P_n(0)\rangle$. Note that this kind of collective phenomenon never manifests itself if all the QDs are excited by optical far fields as $\langle W_n(0)\rangle = -1$ or 1 for all n. Therefore this kind of collective behaviour is inherent in the optical near fields.

The dipole-ordered state discussed above is close to Dicke's superradiant state whose maximum intensity of radiation is given by $(N/2)\{1 + (N/2)\}$. Our analysis for the total QD number of $N = 8$ shows a maximum value of about 15 corresponding to 20 as the Dicke value. This reduction of the maximum value from 20 to 15 is consistent with the result obtained with the XY model [4]. The mechanism of this ordering is explained using the following effective Hamiltonian

$$H_{\text{eff}} = \sum_n \hbar\Omega b_n^\dagger b_n + \sum_n \sum_{m\neq n} J_{nm} b_n^\dagger b_m, \tag{10}$$

which is derived from Eqs. (1a)–(1d) with the help of the unitary transformation [5] and elimination of the localized photonic degrees of freedom. The hopping energy J_{nm} of excitons is explicitly expressed as

$$J_{nm} = \sum_j \frac{g^2}{\Omega - \lambda_j} P_{nj} P_{mj} = J_{mn}, \tag{11}$$

which is not constant as in the XY model. Using Eq. (10), we can write the dipole coherence in QD n at time t as

$$\langle P_n(t)\rangle = \langle P_n(0)\rangle \cos[(\Omega + J_{nn})t] + \sum_{m\neq n} J_{nm} t \langle W_n(0)\rangle \langle P_m(0)\rangle \sin(\Omega t), \quad (12)$$

which shows that the sign of $\langle P_n(t)\rangle$ is governed by the sign of J_{nm} as well as the product of $\langle W_n(0)\rangle$ and $\langle P_m(0)\rangle$. When $\langle W_n(0)\rangle$ is -1 for all n and only the dipole coherence of QD 1 $\langle P_1(0)\rangle$ is initially generated, with the same material parameters discussed above, it follows from our analysis that the signs of J_{1n} for $n = 4, 5$, and 6 are opposite to those of others. Therefore if the population difference of QDs 4, 5, and 6 can be initially inverted to have the value 1, the directions of all the dipoles of the system are aligned at time t, and this results in the dipole-ordered state. In addition, one can control the sign of the hopping energy J_{nm} by choosing the material parameters, and can have, *e.g.*, a "ferromagnetic" state with all parallel dipoles, or an "anti-ferromagnetic" state with alternating anti-parallel dipoles.

In summary we have presented a novel model of an N two-level-QD system interacting with localized photons, on the basis of the unique non-propagation property of optical near fields. The dynamics of the dipole coherence have been examined, and a collective oscillation has been predicted after a local manipulation of the initial quantum states of QDs. We have discussed the mechanism of this collective phenomenon, using an equivalent effective Hamiltonian.

References

[1] Stievater, T. H., Xiaoqin Li, Steel, D. G., Gammon, D., Katzer, D. S., Park, D., Piermarocchi, C. and Sham, L. J. (2001). *Phys. Rev Lett.*, **87**, 133603; Kamada, H., Gotoh, H., Temmyo, J., Takagahara, T. and Ando, H. (2001); *ibid.*, **87**, 246401; Kawazoe, T., Kobayashi, K., Lim, J., Narita, Y. and Ohtsu, M. *ibid.*, **88**, 067404; Htoon, H., Takagahara, T., Kulik, D., Baklenov, O., Holmes, A. L. Jr. and Shih, C. K. (2002). *ibid.*, **88**, 087401.

[2] Ohtsu, M., Kobayashi, K., Kawazoe, T., Sangu, S. and Yatsui, T. (2002). *IEEE Journal of Selected Topics Quantum Electronics*, **8**, 839.

[3] Kobayashi, K., Sangu, S., Ito, H. and Ohtsu, M. (2001). *Phys. Rev. A*, **63**, 013806; Inoue, T. and Hori, H. (2001). *ibid.*, **63**, 063805.

[4] Tokihiro, T., Manabe, Y. and Hanamura, E. (1993). *Phys. Rev. B*, **47**, 2019.

[5] Kittel, C. (1987). *Quantum Theory of Solids*, 2nd revised printing. John Wiley & Sons, New York, p. 148.

APPLIED PHYSICS LETTERS VOLUME 81, NUMBER 19 4 NOVEMBER 2002

Fabrication of nanometric single zinc and zinc oxide dots by the selective photodissociation of adsorption-phase diethylzinc using a nonresonant optical near field

T. Yatsui[a] and T. Kawazoe
Exploratory Research for Advanced Technology, Japan Science and Technology Corporation, 687-1 Tsuruma, Machida, Tokyo 194-0004, Japan

M. Ueda, Y. Yamamoto, M. Kourogi,[b] and M. Ohtsu[b]
Interdisciplinary Graduate School of Science and Engineering, Tokyo Institute of Technology, 4259 Nagatsuta, Midori-ku, Yokohama, Kanagawa 226-8502, Japan

(Received 20 May 2002; accepted 17 September 2002)

We demonstrated a deposition of nanometer-scale Zn dots using the selective photodissociation of adsorption-phase diethylzinc with a nonresonant optical near field, where the photon energy is lower than that of the absorption edge of gas-phase diethylzinc. We achieved nanometric prenucleation by dissociating diethylzinc molecules adsorbed on a substrate. Subsequent deposition was performed by dissociating the adsorbed molecules on the prenucleated Zn. The topographic image of the deposited Zn dot had a full width at half maximum (FWHM) of 25 nm. Furthermore, the photoluminescence intensity distribution from a single ZnO dot fabricated using laser annealing had a FWHM of 85 nm. © *2002 American Institute of Physics.* [DOI: 10.1063/1.1520337]

Ultrahigh integration of photonic switching arrays is necessary to increase data transmission rates and the capacity of future optical transmission systems. To accomplish this, the size of all switching devices must be reduced beyond the diffraction limit of light. We have already proposed a nanophotonic integrated circuit (IC) that is composed of nanometer-scale dots and wires. In this circuit, the optical near field acts as a carrier to transfer signals.[1] We previously reported near-field nonlinear absorption spectroscopy of InGaAs single quantum dots[2] and near-field optical energy transfer among resonant energy states of CuCl quantum dots.[3] These are used in the operation of nanometer-scale photonic switches.

To fabricate nanophotonic IC, nanometer-scale dots must be deposited on a substrate with nanometer-scale controllability in size and position. This is necessary so that the optical near-field energy can be transferred from one dot to another. To achieve this level of controllability, we demonstrated the feasibility of nanometer-scale chemical vapor deposition (CVD) using optical near-field techniques,[4] and have demonstrated the deposition of 60 nm Zn dots with high controllability.[5] Since high-quality ZnO nanocrystallites can be obtained by oxidizing Zn nuclei,[6,7] this technique could be used to produce high quality ZnO nanocrystallites: a promising material for use in nanometer-scale light-emitters and switching devices in nanophotonic IC.

However, conventional optical CVD method uses a light source that resonates the absorption band of metalorganic (MO) vapor and has a photon energy that exceeds the dissociation energy.[5,8] Thus, it utilizes a two-step process: gas-phase photodissociation and subsequent adsorption. In this process, resonant photons excite molecules from the ground state to the excited electronic state and the excited molecules relax to the dissociation channel, and then the dissociated Zn atoms adsorb to the substrate.[9] However, we found that the dissociated MO molecules migrate on the substrate before adsorption, which limits the minimum lateral size of deposited dots [Fig. 1(a)].

A promising method for avoiding this migration is dissociation and deposition in the adsorption phase [Fig. 1(b)]. Here, we propose and demonstrate a three-step deposition technique for nanometer-scale Zn dots [Fig. 1(c)]: (1) adsorbing MO molecular layers of diethylzinc (DEZn) on a substrate, (2) nanometer-scale prenucleation of Zn, and (3) subsequent selective deposition on the prenucleated Zn with the photodissociation of adsorption-phase DEZn, using an

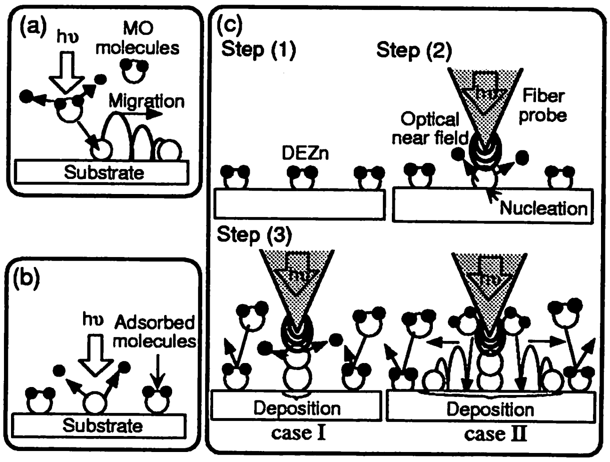

FIG. 1. Schematic diagrams of the photodissociation of the (a) gas-phase and (b) adsorption-phase MO molecules. (c) Schematic diagram of photodissociation using an optical near field. Step (1): adsorbing the DEZn molecules on the substrate. Step (2): dissociation by the optical near field and prenucleation. Step (3): deposition by an optical near field in an atmosphere of DEZn gas under nonresonant (proposed, case I) and resonant (conventional, case II) conditions for gas-phase DEZn.

---

[a] Electronic mail: yatsui@ohtsu.jst.go.jp

[b] Also with Japan Science and Technology Corporation, 687-1 Tsuruma, Machida, Tokyo 194-0004, Japan.

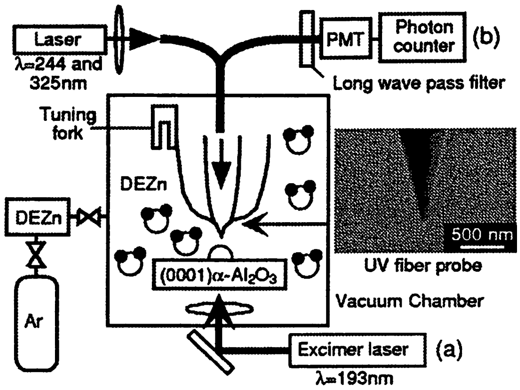

FIG. 2. The experimental setup for near-field optical deposition. (a) Excimer laser annealing. (b) Spatially resolved near-field spectroscopy.

optical near field whose photon energy is lower than that of the absorption edge of gas-phase DEZn and higher than that of the absorption edge of adsorption-phase DEZn [i.e., the conditions are nonresonant for gas-phase DEZn and resonant for adsorption-phase DEZn (case I)].

Figure 2 shows the experimental setup for near-field optical deposition.[5] DEZn was used as a reactive molecular gas source. Since the absorption band edge wavelength (λ) of the gas-phase DEZn was 270 nm,[8] we used He–Cd laser light (λ = 325 nm) (case I) as the light source; it is nonresonant to gas-phase DEZn. Note that the photon energy remained higher than the dissociation energy of DEZn (2.26 eV). For comparison, the second harmonic of an Ar^+ laser was used as the light source; it resonates the gas-phase DEZn because it has a wavelength (λ = 244 nm) shorter than that of the absorption band edge λ [case II in step (3) in Fig. 1(c)].[8]

To efficiently generate the optical near field, we used a sharpened UV fiber probe with a pure silica core and fluorine-doped cladding. This probe was fabricated using a pulling/etching technique. A scanning electronic microscopic image of a fiber probe with an apex diameter of 30 nm is shown in the inset of Fig. 2.[10] Since propagating nonresonant light that leaks from the probe does not dissociate the gas-phase DEZn, we used a fiber probe without the metal coating to generate a nonresonant optical near field at the apex for selective dissociation and deposition. Since the deposition time was sufficiently short, the deposition of Zn on the fiber probe was negligible. The separation between the fiber probe and the (0001) sapphire substrate was kept within several nanometers by shear-force feedback control. Immediately after the Zn dots were deposited, their sizes and shapes were measured by *in situ* vacuum shear-force microscopy,[11] using the same probe used for deposition. Furthermore, to confirm that the deposited dots were Zn, we fabricated a UV-emitting ZnO dot by oxidizing the Zn dot immediately after deposition. Laser annealing was employed for this oxidization,[7] that is, the deposited Zn dot was irradiated with a pulse of an ArF excimer laser (λ = 193 nm, pulse width-30 ns, fluence-120 mJ/cm^2) in a high-pressure oxygen environment (5 Torr) [Fig. 2(a)]. To evaluate the optical properties of the oxidized dot, the photoluminescence (PL) intensity distribution was measured using an illumination and collection mode (IC-mode) near-field optical microscope. For this measurement, a He–Cd laser (λ = 325 nm) was used as the light source, the signal collected through a fiber probe, and a long wave (λ >360 nm) pass filter was focused on a photomultiplier tube to count photons [Fig. 2(b)].

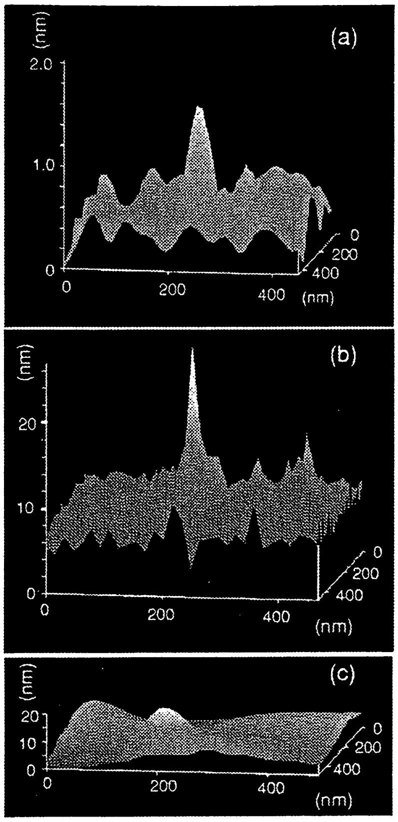

FIG. 3. Bird's-eye views of a shear-force topographical image of Zn deposited using (a) λ = 325 nm without gas-phase DEZn, (b) λ = 325 nm in an atmosphere of DEZn gas, and (c) λ = 244 nm in an atmosphere of DEZn gas.

Figure 3(a) shows a topographical image of a prenucleated Zn dot, when a He–Cd laser (λ = 325 nm) was used as a nonresonant light source. The laser output power was 100 μW and the irradiation time was 120 s. Before irradiating the optical near field, 10 mTorr DEZn gas was introduced into the vacuum chamber (the total pressure including Ar buffer gas ranged from 200 to 300 mTorr). Next, the chamber was evacuated to a pressure below 1×10^{-6} Torr. Prenucleation of the Zn dot was carried out after evacuation [step (2) in Fig. 1(c)]. Figure 3(b) shows a topographical image of a Zn dot deposited by dissociating the adsorbed DEZn layers on a prenucleated Zn dot using λ = 325 nm in an atmosphere of DEZn gas [case I, step (3) in Fig. 1(c)] with a partial pressure of 10 mTorr. The laser output power was 100 μW and the irradiation time was 120 s. For comparison, Fig. 3(c) shows a topographical image of Zn deposited using a resonant optical near field (λ = 244 nm) in an atmosphere of DEZn gas [case II, step (3) in Fig. 1(c)] with a partial pressure of 10 mTorr. The laser output power was 15 mW and the irradiation time was 60 s.

In Fig. 4, curves A, B, and C show cross-sectional profiles through the Zn dots in Figs. 3(a), 3(b), and 3(c), respectively. Curve A indicates that nanometer-scale nucleation 1 nm high resulted from dissociating adsorbed DEZn on the sapphire substrate using a nonresonant optical near field. Curve B shows a sharp profile with a full width at half maximum (FWHM) of 25 nm and a height of 16 nm. It is clear that the nonresonant propagating light (λ = 325 nm) that

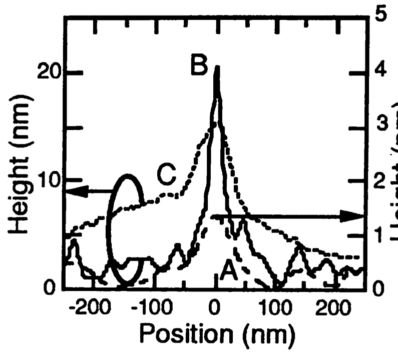

FIG. 4. Cross-sectional profiles through deposited Zn dots. Curves A (dashed-and-dotted line), B (solid line), and C (dashed line) show $\lambda = 325$ nm without gas-phase DEZn, $\lambda = 325$ nm in an atmosphere of DEZn gas, and $\lambda = 244$ nm in an atmosphere of DEZn gas.

leaked from the probe did not dissociate the gas-phase DEZn and, as a result, deposition occurred only on the prenucleated Zn dot. In contrast to curves A and B, curve C has tails on both sides of the peak. These tails correspond to the Zn deposited due to the photodissociation of the gas-phase DEZn by the resonant optical near field and the simultaneous propagating light.

The absorption edge of adsorption-phase DEZn was not determined. However, we attribute the selective photodissociation of the adsorption-phase DEZn observed when using a nonresonant optical near field ($\lambda = 325$ nm; lower energy than the absorption edge of the gas-phase DEZn molecules) to the redshift in the absorption spectrum in DEZn with respect to that in the gas-phase; that is, it resonates the adsorption-phase DEZn. The redshift may be attributed to perturbations of the free-molecule potential surface in the adsorbed phase.[8,12] Since the resonant optical near field ($\lambda = 244$ nm; higher energy than the absorption edge of the gas-phase DEZn molecules) dissociates both the adsorption-phase and gas-phase DEZn, it results in a deposited-dot profile with side tails (curve C in Fig. 4). Furthermore, the very sharp profile and high aspect ratio of the Zn dots without tails (curve B in Fig. 4) demonstrates that the gas-phase DEZn was selectively adsorbed on the prenucleated Zn, and that the deposition was a result of the selective photodissociation of adsorption-phase DEZn on the prenucleated Zn when using the nonresonant optical near field in an atmosphere of DEZn gas.

Figure 5(a) shows the PL intensity distribution of an oxidized dot [Fig. 3(a)] integrated for the wavelength region longer than 360 nm using a long wave pass filter [Fig. 2(b)]. The low collection efficiency due to the IC-mode configuration did not establish the spectrum. To overcome this difficulty, a Zn thin film was deposited using the same CVD process, except the optical near field was replaced by far-field propagating light. After it was annealed with an excimer laser, we found that the PL intensity of the spontaneous emission from the free exciton was ten times greater than that of the deep-level green emission. Thus, we concluded that the PL in Fig. 5(a) originated from spontaneous emission from the free exciton. Figure 5(b) is the cross-sectional profile along the dashed white line in Fig. 5(a). Note that the FWHM in Fig. 5(b) is smaller than the dot size, which was estimated using a shear-force microscope [Fig. 3(a)]. This originates from the high spatial resolution capability of the IC-mode near-field microscope. The next stage of this study will be a more detailed evaluation of the optical properties of single ZnO nanocrystallites.

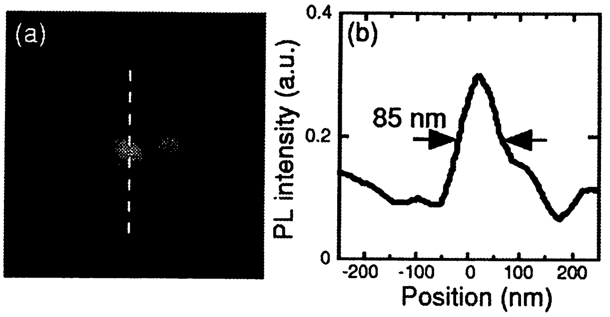

FIG. 5. Spatial distribution of the optical near-field PL intensity ($\lambda > 360$ nm) of an oxidized Zn dot. (a) The image is of a 750×750 nm^2 area. (b) Cross-sectional profile along the dashed white line in (a).

In summary, we investigated the mechanics of near-field optical deposition. By selectively photodissociating adsorption-phase DEZn using an optical near field under nonresonant conditions in gas-phase DEZn, we deposited a Zn dot with a FWHM as low as 25 nm. Furthermore, using IC-mode near-field spectroscopy, we obtained spatially resolved PL spectra from a single ZnO dot. Since our disposition method is based on a photodissociation reaction, it could be widely used to fabricate size- and position-controlled nanometer-scale structures in other metals, semiconductors, and insulators.

The authors would like to thank Prof. A. Yamada of Tokyo Institute of Technology for useful discussions.

[1] M. Ohtsu, Proc. SPIE **3749**, 478 (1999).
[2] T. Matsumoto, M. Ohtsu, K. Matsuda, T. Saiki, H. Saito, and K. Nishi, Appl. Phys. Lett. **75**, 3246 (1999).
[3] T. Kawazoe, K. Kobayashi, J. S. Lim, Y. Narita, and M. Ohtsu, Phys. Rev. Lett. **88**, 067404 (2002).
[4] V. V. Polonski, Y. Yamamoto, M. Kourogi, H. Fukuda, and M. Ohtsu, J. Microsc. **194**, 545 (1999).
[5] Y. Yamamoto, M. Kourogi, M. Ohtsu, V. Polonski, and G. H. Lee, Appl. Phys. Lett. **76**, 2173 (2000).
[6] S. Cho, J. Ma, Y. Kim, Y. Sun, G. Wong, and J. B. Ketterson, Appl. Phys. Lett. **75**, 2761 (1999).
[7] T. Aoki, Y. Hatanaka, and D. C. Look, Appl. Phys. Lett. **76**, 3257 (2000).
[8] R. R. Krchnavek, H. H. Gilgenm, J. C. Chenm, P. S. Shaw, T. J. Licata, and R. M. Osgood, J. Vac. Sci. Technol. B **5**, 20 (1987).
[9] R. L. Jackson, J. Chem. Phys. **96**, 5938 (1992).
[10] *Near-field Nano/Atom Optics and Technology*, edited by M. Ohtsu (Springer, Tokyo, 1999), Chap. 3.
[11] V. V. Polonski, Y. Yamamoto, J. D. White, M. Kourogi, and M. Ohtsu, Jpn. J. Appl. Phys., Part 2 **38**, L 826 (1999).
[12] C. J. Chen and R. M. Osgood, Jr., Chem. Phys. Lett. **98**, 363 (1983).

Nanophotonics: Design, Fabrication, and Operation of Nanometric Devices Using Optical Near Fields

Motoichi Ohtsu, *Senior Member, IEEE*, Kiyoshi Kobayashi, *Member, IEEE*, Tadashi Kawazoe, Suguru Sangu, and Takashi Yatsui

Invited Paper

***Abstract*—This paper reviews progress in nanophotonics, a novel optical nanotechnology, utilizing local electromagnetic interactions between a few nanometric elements and an optical near field. A prototype of a nanophotonic integrated circuit (IC) is presented, in which the optical near field is used as a carrier to transmit a signal from one nanometric dot to another. Each section of this paper reviews theoretical and experimental studies carried out to assess the possibility of designing, fabricating, and operating each nanophotonic IC device. A key device, the nanophotonic switch, is proposed based on optical near-field energy transfer between quantum dots (QDs). The optical near-field interaction is expressed as the sum of the Yukawa function, and the oscillation period of the nutation of cubic CuCl QDs is estimated to be less than 100 ps. To guarantee one-directional (i.e., irreversible) energy transfer between two resonant levels of QDs, intrasublevel transitions due to phonon coupling are examined by considering a simple two-QD plus phonon heat bath system. As a result, the state-filling time is estimated as 22 ps for CuCl QDs. This time is almost independent of the temperature in the Born–Markov approximation. Using cubic CuCl QDs in a NaCl matrix as a test sample, the optical near-field energy transfer was experimentally verified by near-field optical spectroscopy with a spatial resolution smaller than 50 nm in the near-UV region at 15 K. This transfer occurs from the lowest state of excitons in 4.6-nm QDs to the first dipole-forbidden excited state of excitons in 6.3-nm QDs. To fabricate nanophotonic devices and ICs, chemical vapor deposition using an optical near field is proposed; this is sufficiently precise in controlling the size and position of the deposited material. A novel deposition scheme under nonresonant conditions is also demonstrated and its origin is discussed. In order to confirm the possibility of using a nanometric ZnO dot as a light emitter in a nanophotonic IC, spatially and spectrally resolved photoluminescence imaging of individual ZnO nanocrystallites was carried out with a spatial resolution as high as 55 nm, using a UV fiber probe, and the spectral shift due to the quantum size effect was found. To connect the nanophotonic IC to external photonic devices, a nanometer-scale waveguide was developed using a metal-coated silicon wedge structure. Illumination (wavelength: 830 nm) of the metal-coated silicon wedge (width: 150 nm) excites a TM plasmon mode with a beam width of 150 nm and propagation length of 2.5 μm. A key device for nanophotonics, an optical near-field probe with an extremely high throughput, was developed by introducing a pyramidal silicon structure with localized surface plasmon resonance at the metallized probe tip. A throughput as high as 2.3% was achieved. Finally, as an application of nanophotonics to a high-density, high-speed optical memory system, a novel contact slider with a pyramidal silicon probe array was developed. This slider was used for phase-change recording and reading, and a mark length as short as 110 nm was demonstrated.**

***Index Terms*—Nanofabrication, nanophotonic switch, optical memory, optical near fields, plasmon waveguide, quantum dots, silicon probe.**

I. INTRODUCTION

We first present three possible technical problems that are faced by the future optical industry in order to explain the motivation behind the work reviewed here [1]. 1) Optical fiber transmission systems require increased integration of photonic devices if data transmission rates are to reach as high as 10 Tb/s by the year 2015. To support this increase, it is estimated that the size of photonic matrix switching devices should be reduced to a subwavelength scale, to integrate more than 1000 × 1000 input and output channels on a substrate. Since conventional photonic devices, e.g., diode lasers and optical waveguides, have to confine the lightwave within their cavities and core layers, respectively, their minimum sizes are limited by the diffraction of light. Therefore, they cannot meet this requirement, because the required size is beyond this diffraction limit. 2) Progress in DRAM technology requires improved photolithography. It is anticipated that it should be possible to fabricate patterns narrower than 50 nm by the year 2010. Although several methods using special light sources, e.g., an extreme ultraviolet (UV) light source and a synchrotron radiation light source, have been developed, they require linewidth that far exceeds the diffraction limit of visible light. 3) It has been estimated that optical memory systems will require a recording density as high as 1 $\mathrm{Tb/in^2}$ by the year 2010, which is more than 100 times higher than that of a DVD. Since the mark length for 1 $\mathrm{Tb/in^2}$ is as short as 25 nm, recording such small marks far exceeds the diffraction limit of light.

Manuscript received March 28, 2002.

M. Ohtsu is with the Interdisciplinary Graduate School of Science and Engineering, Tokyo Institute of Technology, Yokohama 226-8502, Japan, with the Exploratory Research for Advanced Technology (ERATO), Localized Photon Project, Japan Science and Technology Corporation, Tokyo 194-0004, Japan, and also with the Near-field Photonics Group, Kanagawa Academy of Science and Technology, Kawasaki 213-0012, Japan (e-mail: ohtsu@ae.titech.ac.jp).

K. Kobayashi, T. Kawazoe, S. Sangu, and T. Yatsui are with the Exploratory Research for Advanced Technology (ERATO), Localized Photon Project, Japan Science and Technology Corporation, Tokyo 194-0004, Japan (e-mail: kkoba@ohtsu.jst.go.jp; kawazoe@ohtsu.jst.go.jp; sangu@ohtsu.jst.go.jp; yatsui@ohtsu.jst.go.jp).

Digital Object Identifier 10.1109/JSTQE.2002.801738.

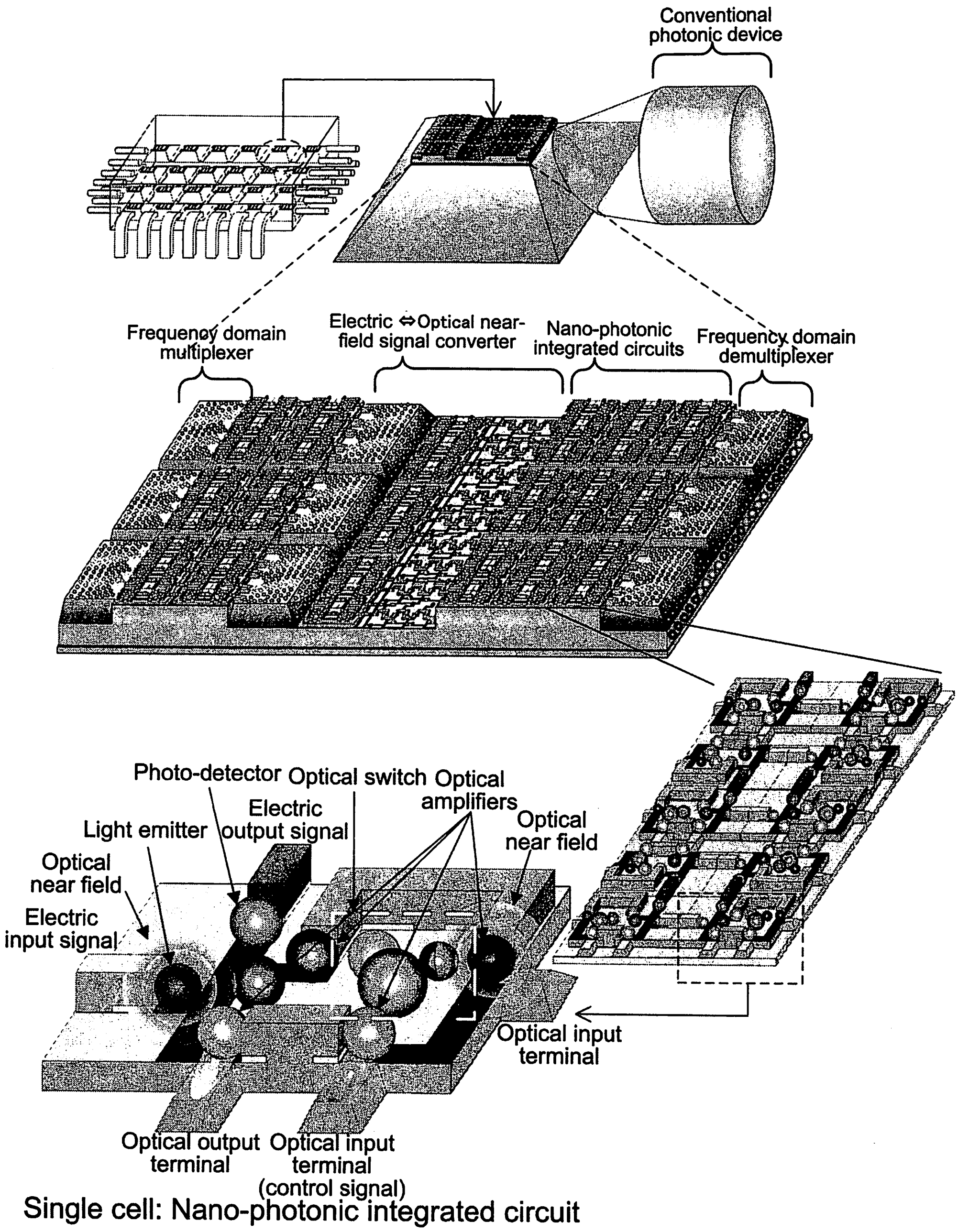

Fig. 1. Basic structure of a nanophotonic integrated circuit.

From these three points, it can be readily understood that a novel optical nanotechnology that goes beyond the diffraction limit is required in order to support the optical science and technology of the 21st century. To meet this requirement, M. Ohtsu has proposed a novel technology, called nanophotonics [2]. Nanophotonics is defined as a technology that utilizes local electromagnetic interactions between a small nanometric element and an optical near field. Since an optical near field is free from the diffraction of light due to its size-dependent localization and resonance features, nanophotonics enables the fabrication, operation, and integration of nanometric devices. The primary advantage of nanophotonics is its capacity to realize novel functions based on local electromagnetic interactions. It should be noted that some of the conventional concepts of wave optics, such as interference, are no longer essential in nanophotonics. Instead, concepts of surface elementary excitation and nanofabrication technology are essential.

To solve the first technical problem requires an advanced photonic integrated circuit (IC). The degree of integration must greatly exceed that of a conventional diffraction-limited photonic IC. Quantum dot lasers and photonic crystals, composed of many nanometric elements, cannot meet this requirement because they use conventional lightwaves as a carrier for signal transmission. Instead, it is indispensable to use a localized optical near field as the carrier, and transmit it from one nanometric element to another. Fig. 1 schematically explains the basic structure of such an IC, called a nanophotonic IC, proposed by the authors [3]. The light emitters, optical switches, input/output (I/O) terminals, and photodetectors in this IC all consist of nanometric dots and wires. The optical near field generated at one quantum dot is transferred to an adjacent dot in order to transmit the signal. A switching device is used to modulate the optical near-field energy. To connect this IC with external conventional photonic devices, narrow waveguides are used as I/O terminals. Here, it should be noted that the nanometric size of each device and the high degree of integration are no more than a secondary advantage of this IC. The primary advantage is that novel functions and operations are realized based on the local electromagnetic interactions in a nanometric system buried in a macroscopic heat bath, as will be demonstrated in the following sections.

Section II outlines the theory of the nanophotonic switch, which is a key device in the nanophotonic IC. Its function is based on a unique optical near-field energy transfer, which is allowed between nanometric elements by the exchange of near-field photons. Experimental verification of this transfer is described in Section III. To fabricate nanophotonic devices and ICs requires a high degree of control and reproducibility of the size and position of the fabricated nanostructures, which should be as high as several nanometers. Section IV-A reviews the chemical vapor deposition process developed to meet this requirement, using an optical near field. An advantage of this method is that it allows the selective growth of various materials, i.e., metals, insulators, and semiconductors, by the choice of light source. It should be noted that this deposition method also solves Problem 2 above. Further, as described in Section IV-A, an essential feature is that it allows nonresonant dissociation, which is an intrinsic phenomenon induced by an optical near field. Section IV-B reviews the quantum size effect of nanometric ZnO to demonstrate the capability of using it as a light emitter in a nanophotonic IC. Section V reviews a novel plasmon waveguide to be used as an I/O terminal of the nanophotonic IC. For work in nanophotonics, a key device is a probe to generate/detect optical near fields with high efficiency and high resolution. Section VI reviews the progress in the development of this device. Finally, to solve Problem 3, Section VII reviews a high-density, high-speed optical memory system that uses an optical near field. Section VIII summarizes the main points discussed in this paper.

II. THEORETICAL STUDY OF A NANOPHOTONIC SWITCH

A. Principle of a Nanophotonic Switch

Optical near-field energy transfer between semiconductor quantum dots (QDs) can be used to design a nanophotonic switch, which is the most essential device in the nanophotonic IC of Fig. 1. As an example, we employ cubic CuCl QDs in a NaCl matrix to describe the principle of this switch. It has been well known that translational motion of the exciton center of mass is quantized due to the small exciton Bohr radius for CuCl QDs [4]–[6]. The potential barrier of CuCl QDs in an NaCl crystal can be regarded as infinitely high, and the energy eigenvalues for the quantized Z_3 exciton energy level (n_x, n_y, n_z) in a cubic CuCl QD with the side length of L is given by

$$E_{n_x,n_y,n_z} = E_B + \frac{\hbar^2\pi^2}{2M(L-a_B)^2}\left(n_x^2+n_y^2+n_z^2\right) \qquad (1)$$

where E_B is the bulk Z_3 exciton energy, M is the translational mass of exciton, a_B is its Bohr radius, n_x, n_y, and n_z are quantum numbers $(n_x, n_y, n_z = 1, 2, 3, \ldots)$, and $a = L - a_B$ corresponds to an effective side length found through consideration of the dead layer correction [4]. The exciton energy levels with even quantum numbers are dipole-forbidden states, that is optically forbidden [7]. However, the optical near-field interaction is allowed for such energy levels [8].

Fig. 2(a) illustrates the different-sized cubic CuCl QDs (I and O) and confined-exciton Z_3 energy levels. According to (1), there exists a resonance between the quantized exciton energy level of quantum number (1, 1, 1) for the QD-I with effective side length a and that of quantum number (2, 1, 1) for the QD-O with effective side length $\sqrt{2}a$. Under this type of resonant condition, the coupling energy of the optical near-field interaction is given by the following Yukawa function [8], [9] (refer to Section II-B2):

$$V(r) = A\frac{\exp(-\mu r)}{r}. \qquad (2)$$

Here, r is the separation between two QDs, A is the coupling coefficient, and μ is the effective mass of the Yukawa function given by

$$\mu = \frac{\sqrt{2E_{n_x,n_y,n_z}\left(E_{\mathrm{NaCl}} + E_{n_x,n_y,n_z}\right)}}{\hbar c} \qquad (3)$$

where E_{NaCl} is the exciton energy of an NaCl matrix. Since the value of the coupling coefficient A depends on experimental conditions, we estimate it from the result of the previous work on the interaction between a Rb atom and the optical near-field probe-tip [8]. As a result, the value of A for a 5-nm cubic CuCl QD is found to be more than ten times larger than that for the Rb-atom case, since the coupling coefficient A is proportional to the oscillator strength and square of the photon energy [8], [10]. Assuming that the separation r between two QDs is 10 nm, the coupling energy $V(r)$ is in the order of 10^{-4} eV, which corresponds to a transition time of 20 ps, and is much shorter than the exciton lifetime of a few nanoseconds. Further, an intersublevel transition time τ_{sub}, from higher exciton energy levels to the lowest one, is generally less than a few picoseconds and is much shorter than the transition time due to optical near-field coupling [11]. Therefore, most of the energy of the exciton in a CuCl QD-I transfer to the lowest exciton energy level in the neighboring QD-O and recombine radiatively in the lowest level.

Fig. 2(b) and (c) illustrates the OFF and ON states of the proposed nanophotonic switch using three QDs, including two QDs of Fig. 2(a). The QD-I, O, and C are used as the input, output, and control ports of the switch, respectively. The quantized energy sublevels (1, 1, 1) in QD-I, (2, 1, 1) in QD-O, and (2, 2, 2) in QD-C resonate with each other. Additionally, the energy sublevels (1, 1, 1) in QD-O and (2, 1, 1) in QD-C also resonate. As was described above, almost all the energy of the excitation in the QD-I transfer to the energy sublevels (1, 1, 1) in the neighboring QD-O and, finally, it transfers to the energy sublevels (1, 1, 1) in the QD-C. In the OFF state [Fig. 2(b)], the input energy escapes to the QD-C, and then the output signal is obstructed. In the ON state [Fig. 2(c)], the escape passes to the QD-C are blocked by the excitation of the QD-C and, thus, the input energy goes through the QD-O giving an output signal. This switching operation is studied theoretically in Section II-B.

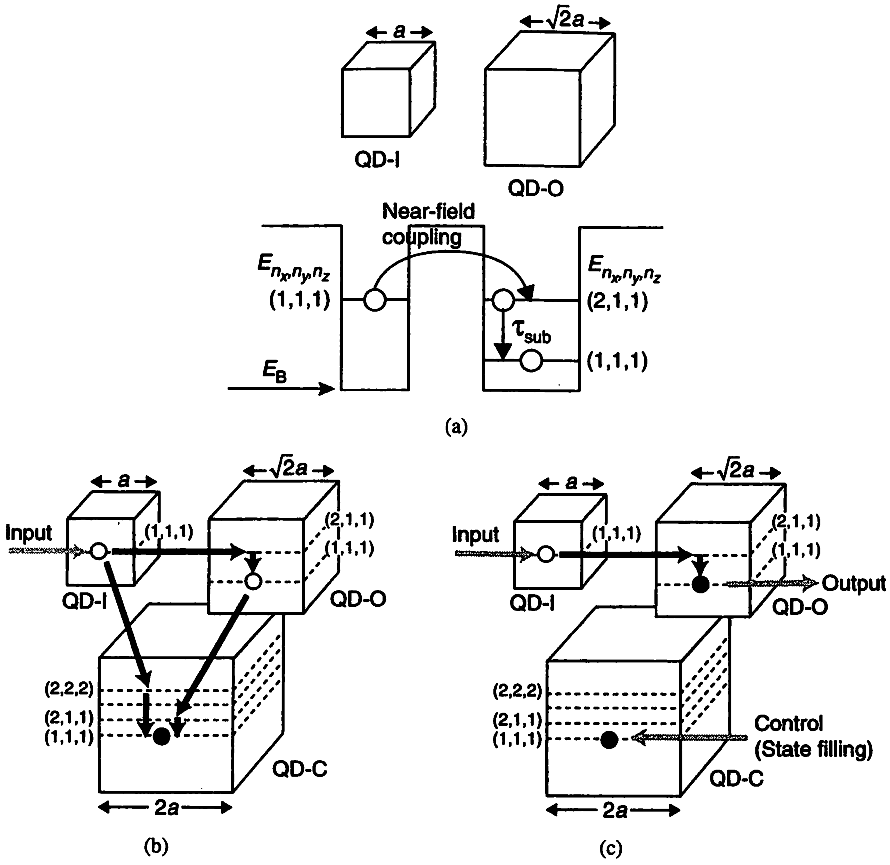

Fig. 2. Schematic explanation of a nanophotonic switch. (a) Upper: Schematic drawings of closely located cubic CuCl QDs I and O with the effective side lengths of $a(=(L-a_B))$ and $\sqrt{2}a$, respectively, where L and a_B are the side lengths of QDs and the exciton Bohr radius, respectively. Lower: Their exciton energy levels. n_x, n_y, and n_z represent quantum numbers of an exciton. E_B is the exciton energy level in a bulk crystal. (b) OFF state. (c) ON state.

B. Energy Transfer Induced by Optical Near-Field Interaction

We will discuss the physical principles and phenomena behind the nanophotonic switch of Fig. 2, i.e., energy transfer phenomena induced by optical near field between two resonant energy levels in a QD and its adjacent QD [12]. Optical near-field interaction (coupling) between QDs as an origin of the energy transfer will be derived microscopically within the quantum theoretical framework. As an example, a typical coupling strength and time scale of the process will be given for cubic CuCl QDs. We will also formulate a QD-heat bath system interacting with optical near field to clarify critical parameters for the proposed device, and examine the dynamics of the system numerically in order to simulate the switching behavior of the device.

A typical optical near-field system is a microscopic system (consisting of QDs and optical near field), which is coupled by a macroscopic matter systems (consisting of a substrate, incident photons, and so on). It is convenient to treat this system in two steps. 1) Photons and the macroscopic matter system are described in terms of a so-called polariton basis where photons are dressed by macroscopic matter excitations, not free photons. 2) The interaction between the microscopic and macroscopic systems is expressed by using the polariton basis.

We have developed a systematic formulation by using the projection operator method, in which photons and macroscopic matter excitations are described on an equal footing in terms of an elementary excitation mode like exciton–polaritons, and then the effects of both macroscopic matter system and photons are renormalized into an effective two-body interaction between nanometric objects in the microscopic system [8], [13]–[16]. Here, we call this effective interaction as optical near-field interaction. On the basis of the formulation, we first illustrate interdot energy transfer phenomena, with QDs as nanometric objects, and then derive an explicit form of the optical near-field interaction. As an example, we give a typical time scale for the energy transfer process in cubic CuCl QDs.

1) Interdot Energy Transfer via Optical Near Field: Let us first consider a two-QD system interacting with optical near field, as schematically depicted in Fig. 3, in order to illustrate how excitation energy is transferred between the QDs. The QD1 and QD2 correspond to the QD-I and QD-O in Fig. 2, respectively. The model Hamiltonian of the system is written as

$$\begin{aligned}\hat{H} &= \hat{H}_0 + \hat{V}\\ \hat{H}_0 &= E_1\hat{A}^\dagger\hat{A} + E_1\hat{B}^\dagger\hat{B} + \sum_{\vec{k}} E(k)\hat{\xi}^\dagger_{\vec{k}}\hat{\xi}_{\vec{k}}\\ \hat{V} &= -\sum_{\alpha=A}^{B} \hat{\vec{\mu}}_\alpha \cdot \hat{\vec{D}}(\vec{r}_\alpha)\end{aligned} \tag{4}$$

where $(\hat{A}^\dagger, \hat{A})$ and $(\hat{B}^\dagger, \hat{B})$ represent the excitation creation and annihilation operators in QD1 and QD2, respectively, and with E_1 being the excitation energy. The optical near field is modeled as exciton–polariton field, and the creation and annihilation operators and the eigenenergy for exciton–polariton [17]–[21] are denoted as $(\hat{\xi}^\dagger_{\vec{k}}, \hat{\xi}_{\vec{k}})$ and $E(k)$, respectively. The

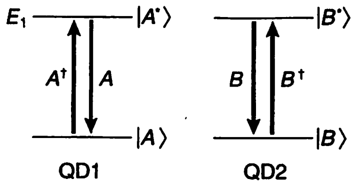

Fig. 3. Two-level QD system coupled by the optical near field.

interaction $\hat{V}$ between the QD system and the optical near field expressed by exciton–polariton is given by the multipolar QED Hamiltonian in the dipole approximation [22], [23], with $\hat{\vec{\mu}}_\alpha$ and $\hat{\vec{D}}(\vec{r}_\alpha)$ representing the dipole operator and the electric displacement vector at position $\vec{r}_\alpha$. As mentioned above, $\hat{\vec{D}}(\vec{r}_\alpha)$ is expressed in terms of the exciton–polariton operators as

$$\begin{aligned}\hat{\vec{\mu}}_A &= \vec{\mu}_A(\hat{A}+\hat{A}^\dagger)\\ \hat{\vec{\mu}}_B &= \vec{\mu}_B(\hat{B}+\hat{B}^\dagger)\\ \hat{\vec{D}}(\vec{r}_\alpha) &= i\sqrt{\frac{2\pi\hbar}{V}}\sum_{\vec{k}\lambda}\vec{e}_{\vec{k}\lambda}f(k)(\hat{\xi}_{\vec{k}}e^{i\vec{k}\cdot\vec{r}_\alpha}-\hat{\xi}^\dagger_{\vec{k}}e^{-i\vec{k}\cdot\vec{r}_\alpha})\\ f(k) &= \frac{\hbar ck}{\sqrt{\hbar E(k)}}\sqrt{\frac{E^2(k)-E_m^2}{2E^2(k)-E_m^2-\hbar^2c^2k^2}}\end{aligned} \tag{5}$$

where $f(k)$ is the coupling coefficient between photons and the macroscopic matter system, and E_m designates the excitation energy of the macroscopic matter system [8], [14], [16]. The vector $\vec{e}_{\vec{k}\lambda}$ is the unit vector normal to the exciton–polariton wave vector $\vec{k}$, and $\hbar$ and c are the Planck constant divided by 2π and the velocity of light in a vacuum, respectively.

Dynamics of the system, including energy transfer, is now governed by the following Liouville equation:

$$\dot{\hat{\rho}}_{\text{total}}(t) = -\frac{i}{\hbar}[\hat{H},\hat{\rho}_{\text{total}}(t)] \tag{6}$$

with the density operator $\hat{\rho}_{\text{total}}(t)$ [24]–[27]. Tracing out the exciton–polariton degrees of freedom from both sides of (6), we obtain an equation of motion for the density operator $\hat{\rho}(t)$ in mean-field approximation [27] as

$$\begin{aligned}\dot{\hat{\rho}}(t) &= -\frac{i}{\hbar}[\hat{V}_{\text{dot}},\hat{\rho}(t)]\\ \hat{\rho}(t) &= \mathrm{Tr}_{\text{pol}}[\hat{\rho}_{\text{total}}(t)]\\ \hat{V}_{\text{dot}} &= \mathrm{Tr}_{\text{pol}}[\hat{V}].\end{aligned} \tag{7}$$

Here, the notation Tr_{pol} means to take a trace of the subsequent operator regarding the exciton–polariton degrees of freedom. Note that we have obtained (7) in the interaction representation. We then prepare two states $|\phi_1\rangle = |A^*\rangle|B\rangle$ for the excited state in QD1 and $|\Phi_2\rangle = |A\rangle|B^*\rangle$ for the excited state in QD2, in order to construct the matrix elements of $\hat{\rho}(t)$ and to express (7) in the matrix form. It should be noted that the nonzero matrix elements of the interaction operator $\hat{V}_{\text{dot}}$ are the off-diagonal parts only as

$$\hbar U \equiv \langle\Phi_2|\hat{V}_{\text{dot}}|\Phi_1\rangle = \langle\Phi_1|\hat{V}_{\text{dot}}|\Phi_2\rangle \tag{8}$$

and thus

$$\langle\Phi_1|\hat{V}_{\text{dot}}|\Phi_1\rangle = \langle\Phi_2|\hat{V}_{\text{dot}}|\Phi_2\rangle = 0. \tag{9}$$

Under the initial condition of $\langle\Phi_1|\hat{\rho}(0)|\Phi_1\rangle = 1$, the matrix elements of the density operator can be exactly solved, and population probability of staying in the excited state for QD1 or QD2 is given by the diagonal part of the density matrix as

$$\begin{aligned}\langle\Phi_1|\hat{\rho}(t)|\Phi_1\rangle &= \cos^2(Ut)\\ \langle\Phi_2|\hat{\rho}(t)|\Phi_2\rangle &= \sin^2(Ut).\end{aligned} \tag{10}$$

Equation (10) shows, as is well known, that the time evolution of the population goes and returns between both QDs, i.e., *nutation* occurs with the Rabi flopping frequency U [25], [27]. In this way, the matter excitation energy is transferred from one QD to another neighboring QD due to the interaction $\hat{V}$ as a coupling between the QDs and the exciton–polariton field (optical near field).

2) Optical Near-Field Interaction Between Quantum Dots: From the preceding section, it follows that $\hbar U$ in (8) is a key parameter of the interdot energy transfer process. According to our previous studies [8], [13]–[16], we show how to obtain $\hat{V}_{\text{dot}}$ in a systematic and consistent way, depending on the choice of $|\Phi_1\rangle$ and $|\Phi_2\rangle$. In other words, we outline a derivation of the optical near-field interaction between QDs.

First, exact eigenstates $|\Psi_\lambda\rangle$ of the total Hamiltonian $\hat{H}$ are divided into two groups. One contains relevant states in P-space $|\Psi_\lambda^P\rangle = P|\Psi_\lambda\rangle$ and the other contains irrelevant states in Q-space $|\Psi_\lambda^Q\rangle = Q|\Psi_\lambda\rangle$, where P and Q represent the projection operators with the properties $P+Q=1, P^2 = P(Q^2 = Q)$, and $P^\dagger = P(Q^\dagger = Q)$ [8], [13], [14], [28]–[32]. Referring to Fig. 3, for example, P-space can be constructed from the eigenstates of $\hat{H}_0$, i.e., a combination of two energy levels for each QD and the exciton–polariton vacuum state. Q-space is complementary to P-space and the exciton–polariton states are not vacant. Then the exact states $|\Psi_\lambda\rangle$ can be formally expressed by using the states only in P-space as [8], [13], [14], [28]

$$\begin{aligned}|\Psi_\lambda\rangle &= \hat{J}P(P\hat{J}^\dagger\hat{J}P)^{-1/2}\left|\Psi_\lambda^P\right\rangle\\ \hat{J} &= [1-(E_\lambda-H_0)^{-1}Q\hat{V}]^{-1}\end{aligned} \tag{11}$$

where E_λ denotes the eigenenergy for $\hat{H}|\Psi_\lambda\rangle = E_\lambda|\Psi_\lambda\rangle$. Using (11), we can thus obtain the effective interaction $\hat{V}_{\text{eff}}$ that corresponds to $\hbar U$ or $\hat{V}_{\text{dot}}$ in (8) as

$$\begin{aligned}\langle\Psi_f|\hat{V}|\Psi_i\rangle &= \left\langle\Psi_f^P\middle|\hat{V}_{\text{eff}}\middle|\Psi_i^P\right\rangle\\ \hat{V}_{\text{eff}} &\equiv (P\hat{J}^\dagger\hat{J}P)^{-1/2}P\hat{J}^\dagger\hat{V}\hat{J}P(P\hat{J}^\dagger\hat{J}P)^{-1/2}.\end{aligned} \tag{12}$$

For further evaluation of (12), we need to know the explicit form of the operator $\hat{J}$ as well as the eigenvalue E_λ. If we expand the operator $\hat{J}$ in the order of $\hat{V}$, and approximate the eigenvalue E_λ as an unperturbed value, then we have the perturbative solution of $\hat{J}$ as $\hat{J} = 1+(E_0^P-E_0^Q)^{-1}\hat{V}+\cdots$. Since it is easy to show $\langle\Psi_f^P|P\hat{V}P|\Psi_i^P\rangle = 0$, (12) can be rewritten within the second order as

$$\begin{aligned}\langle\Psi_f^P|\,\hat{V}_{\text{eff}}\,|\Psi_i^P\rangle &= \sum_m\langle\Psi_f^P|\,\hat{V}|m^Q\rangle\langle m^Q|\hat{V}\,|\Psi_i^P\rangle\\ &\quad\times\left(\frac{1}{E_{0i}^P-E_0^Q}+\frac{1}{E_{0f}^P-E_0^Q}\right)\end{aligned} \tag{13}$$

where E_{0i}^P, E_{0f}^P, and E_0^Q stand for the eigenenergies of unperturbed Hamiltonian $\hat{H}_0$ for the initial and final states in P-space, and the intermediate state $|m^Q\rangle$ in Q-space, respectively.

Since we are primarily interested in the interdot interaction part of (13), we set the relevant initial and final states in P-space as $|\Psi_i^P\rangle = |A^*\rangle|B\rangle|0\rangle$ and $|\Psi_f^P\rangle = |A\rangle|B^*\rangle|0\rangle$. Then it is easily shown that only two states in Q-space, $|m^Q\rangle = |A\rangle|B\rangle|\vec{k}\rangle$ and $|A^*\rangle|B^*\rangle|\vec{k}\rangle$ with one exciton–polariton state $|\vec{k}\rangle$, can provide nonzero contributions. Through the above procedure, we can eliminate the explicit exciton–polariton (optical near field) degrees of freedom, and have an effective two-body interaction, i.e., optical near-field interaction between QDs as

$$\begin{aligned} U(\vec{r}) &\equiv \frac{1}{\hbar}\left\langle \Psi_f^P \middle| \hat{V}_{\text{eff}} \middle| \Psi_i^P \right\rangle \\ &= -\frac{\mu_A\mu_B}{6\pi^2}\int_0^\infty d^3k f(k) \\ &\quad \times \left\{ \left[\frac{1}{E(k)+E_A} + \frac{1}{E(k)+E_B}\right] e^{i\vec{k}\cdot\vec{r}} \right. \\ &\quad \left. + \left[\frac{1}{E(k)-E_A} + \frac{1}{E(k)-E_B}\right] e^{-i\vec{k}\cdot\vec{r}} \right\} \end{aligned} \tag{14}$$

where $\vec{r} = \vec{r}_A - \vec{r}_B$ is the relative distance vector, and $\mu_{A(B)}$ is the transition dipole moment of QD1(2). Approximating the energy dispersion $E(k)$ of exciton–polaritons with effective mass m_p as

$$E(k) = \frac{\hbar^2 k^2}{2m_p} + E_m \tag{15}$$

and substituting (15) into (14), one can finally obtain the optical near-field interaction potential as a sum of the Yukawa functions

$$U(r) = \frac{\mu_A\mu_B}{3(\hbar c)^2}\sum_{\alpha=A}^{B}\left[W_{\alpha+}Y(\Delta_{\alpha+}r) + W_{\alpha-}Y(\Delta_{\alpha-}r)\right]. \tag{16}$$

Here $W_{\alpha\pm}$ designates the weight factor of each Yukawa function that is defined as

$$\begin{aligned} Y(\Delta_{\alpha\pm}r) &= \frac{e^{-\Delta_{\alpha\pm}r}}{r} \\ \Delta_{\alpha\pm} &= \frac{1}{\hbar c}\sqrt{2E_p(E_m \pm E_\alpha)} \end{aligned} \tag{17}$$

with the exciton–polariton effective mass rewritten as $E_p = m_p c^2$, and the relative distance $r = |\vec{r}_A - \vec{r}_B|$. The factor $\Delta_{\alpha-}$ becomes either real or pure imaginary depending on the magnitude of E_m and E_α, which means that this component behaves as either a localized or a propagation mode. To be precise, (16) includes additional two terms that are independent of the parameters of the microscopic system, i.e., the QDs, but those terms are neglected in (16) as a far-field contribution.

We can now, as an example, estimate the strength of the effective interaction between two cubic CuCl QDs induced by optical near field, i.e., the optical near-field interaction. We choose two-level exciton states as the microscopic matter states in P-space. The excitation energy of an exciton in a cubic QD is represented by (1) of Section II-A. In Fig. 4, the interaction potential is plotted as a function of the distance d between the closest edges of the cubic QDs. The effective side length a $(=L - a_B)$ of the cubic QDs are set as $a = 5$ and 7.1 nm whose ratio is $1 : \sqrt{2}$, and $M = 2.3m_e$ and $E_B = 3.20$ eV are used [4]. We estimated the transition dipole moments of the QDs from the experimental value of the QD oscillator strength $f_{\text{dot}} = 5$ [10] and the theoretical conversion formula [33], which are $\mu_A = \mu_B = 0.29\ (\text{eV}\cdot\text{nm}^3)^{1/2}$ and $\mu_A = 0.29$, $\mu_B = 0.49\ (\text{eV}\cdot\text{nm}^3)^{1/2}$ for $a = 5$ and 7.1 nm, respectively. When we choose the distance $d = 10$ nm, we find from Fig. 4 that the interaction potential is about 60 μeV. Thus, it follows from (10) that half of an oscillation period, π/U, is about 30 ps, which corresponds to the time for the initial population of a QD to be transferred to its neighbor. This is a very high speed and suitable for a nanophotonic device.

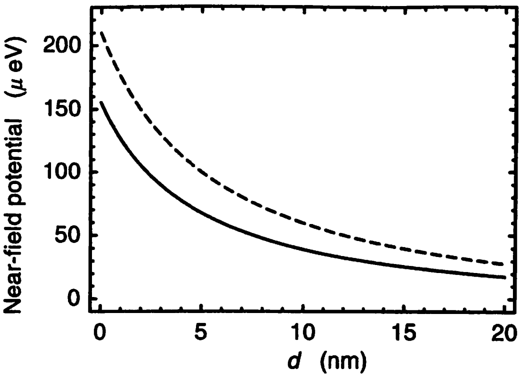

Fig. 4. Optical near-field interaction potential for two cubic CuCl QDs. The solid and dashed curves represent the results for the cubic QD pairs with the same sizes a, and with the size ratio $a : \sqrt{2}a$ ($a = 5$ nm), respectively.

C. Dynamics of a Quantum Dot-Heat Bath Coupling System

From the discussion of the previous section, the population between two resonant levels of QDs undergoes nutation induced by the optical near-field interaction and, thus, we have to include some mechanisms to guarantee the one-directional or irreversible energy transfer on which a nanophotonic device relies. One way is to allow intrasublevel transitions due to a phonon coupling. We, therefore, examine a two-QD system coupled to a phonon (heat) bath system illustrated in Fig. 5. The Hamiltonian of such a system is modeled as

$$\begin{aligned} \hat{H} &= \hat{H}_0 + \hat{H}_{\text{int}} + \hat{H}_{\text{SR}} \\ \hat{H}_0 &= E_1\hat{A}^\dagger\hat{A} + E_2\hat{B}^\dagger\hat{B} + (E_1 - E_2)\hat{C}^\dagger\hat{C} + \sum_n \varepsilon_n\hat{b}_n^\dagger\hat{b}_n \\ \hat{H}_{\text{int}} &= \hbar U(r)(\hat{A}^\dagger\hat{B}\hat{C} + \hat{A}\hat{B}^\dagger\hat{C}^\dagger) \\ \hat{H}_{\text{SR}} &= \hbar\sum_n(g_n\hat{b}_n^\dagger\hat{C} + g_n^*\hat{b}_n\hat{C}^\dagger) \end{aligned} \tag{18}$$

where $(\hat{A}^\dagger, \hat{A})$ and $(\hat{B}^\dagger, \hat{B})$ are fermionic operators for the creation and annihilation of an exciton in QD1 and in the lower energy level of QD2, respectively. Fermionic operators $(\hat{C}^\dagger, \hat{C})$ and bosonic operators $(\hat{b}_n^\dagger, \hat{b}_n)$ are for the $E_2 - E_1$ levels of QD2

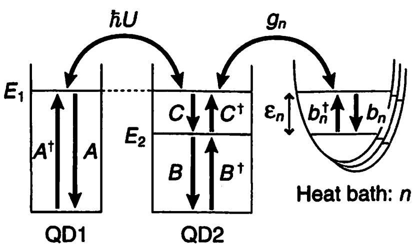

Fig. 5. Two-QD system. Dot 1 and 2 are resonantly coupled due to the optical near-field interaction, and the sublevels in Dot 2 are coupled with the lattice vibration.

and for the heat bath system, respectively. The heat bath system is assumed to be a collection of many harmonic oscillators labeled n. From (6), the equation of motion for the total system can be written as

$$\begin{aligned}\dot{\hat{\rho}}^I(t) =& -\frac{i}{\hbar}\left[\hat{H}_{\rm int} + \hat{H}^I_{\rm SR}(t), \hat{\rho}^I(0)\right] \\ & -\frac{1}{\hbar^2}\int_0^t dt'\left[\hat{H}_{\rm int} + \hat{H}^I_{\rm SR}(t), \left[\hat{H}_{\rm int} + \hat{H}^I_{\rm SR}(t'), \hat{\rho}^I(t')\right]\right]\end{aligned} \tag{19}$$

where the suffix I means the interaction picture, and the relation $\hat{H}^I_{\rm int}(t) = \hat{H}_{\rm int}$ is used [26]. In order to express the second-order temporal correlation clearly, the formal solution $\hat{\rho}^I(t)$ of (6) in the integral form is substituted again into the right-hand side (rhs) of (6). Since we are mainly interested in exciton dynamics in the two-QD system, we take a trace with respect to the degrees of freedom of the heat-bath system as $\hat{\rho}^I_S(t) = {\rm Tr}_R[\hat{\rho}^I(t)]$. Here, the density operator is assumed to be a direct product of the QD system part $\hat{\rho}^I_S(t)$ and the reservoir (heat-bath) system part $\hat{\rho}^I_R(t)$. If the reservoir system has a large volume or many degrees of freedom, the deviation from the initial value can be neglected, and the density operator can be approximated as (Born approximation)

$$\hat{\rho}^I(t) = \hat{\rho}^I_S(t)\hat{\rho}^I_R(t) \approx \hat{\rho}^I_S(t)\hat{\rho}^I_R(0). \tag{20}$$

Taking a trace of both sides of (19) about the reservoir operator, we obtain

$$\begin{aligned}\dot{\hat{\rho}}^I_S(t) =& -iU(r)\left[\hat{A}^\dagger\hat{B}\hat{C} + \hat{A}\hat{B}^\dagger\hat{C}^\dagger, \hat{\rho}^I_S(t)\right] \\ & -\sum_n n(\omega_n, T)\left[\left(\left\{\hat{C}\hat{C}^\dagger, \hat{\rho}^I_S(t)\right\} - 2\hat{C}^\dagger\hat{\rho}^I_S(t)\hat{C}\right)\right. \\ & \left.\otimes\,\gamma^r_n(t) - i\left[\hat{C}\hat{C}^\dagger, \hat{\rho}^I_S(t)\right]\otimes\gamma^i_n(t)\right] \\ & -\sum_n[1 + n(\omega_n, T)]\left[\left(\left\{\hat{C}^\dagger\hat{C}, \hat{\rho}^I_S(t)\right\}\right.\right. \\ & \left.\left. -\ 2\hat{C}\hat{\rho}^I_S(t)\hat{C}^\dagger\right)\otimes\gamma^r_n(t) + i\left[\hat{C}^\dagger\hat{C}, \hat{\rho}^I_S(t)\right]\otimes\gamma^i_n(t)\right]\end{aligned} \tag{21}$$

where the $\{\cdot\}$ stands for the anticommutator, and $\otimes$ designates the convolution integral. Since we assume the reservoir system to be in an equilibrium state, the terms including ${\rm Tr}_R[\hat{b}^\dagger_n\hat{\rho}^I_R(0)]$ and ${\rm Tr}_R[\hat{b}_n\hat{\rho}^I_R(0)]$ do not appear in (21). The number of phonons in the equilibrium state is written as $n(\omega_n, T) = {\rm Tr}_R[\hat{b}^\dagger_n\hat{b}_n\hat{\rho}_R(0)]$ to follow the Bose–Einstein statistics as [25]–[27]

$$n(\omega_n, T) = \frac{1}{e^{\hbar\omega_n/k_BT} - 1}. \tag{22}$$

The real and imaginary parts of the function

$$\gamma_n(t) = |g_n|^2 e^{i(\Delta\omega - \omega_n)t} \tag{23}$$

with $\hbar\Delta\omega = E_1 - E_2$ are represented as $\gamma^r_n(t)$ and $\gamma^i_n(t)$, which are related to a relaxation (real part) and energy shift (imaginary part) from the energy level in QD2 because of coupling to the heat bath system. The convolution in (21) expresses the effect of time delay for the transition between sublevels because of the coupling to the phonon (heat) bath system. However, if the dynamics of the reservoir (heat bath) system are much faster than that of the two-QD system, one can approximate the density operator of the two-QD system as $\hat{\rho}^I_S(t - t') = \hat{\rho}^I_S(t)$ (Markov approximation). Using this approximation, and rewriting the summation as $\sum_n = \int_0^\infty d\omega\, D(\omega)$, with $D(\omega)$ being the density of states for each phonon, we can express the convolution analytically as

$$\begin{aligned}&\sum_n n(\omega_n, T)\hat{\rho}^I_S(t)\otimes\gamma_n(t) \\ &= \hat{\rho}^I_S(t)\int_0^\infty d\omega\, n(\omega, T) \\ &\quad\times D(\omega)|g(\omega)|^2\int_0^t dt'\, e^{i(\Delta\omega-\omega)t'} \\ &\approx \hat{\rho}^I_S(t)\left[\pi n(\Delta\omega, T)D(\Delta\omega)|g(\Delta\omega)|^2\right. \\ &\quad\left. +\ iP\int_0^\infty d\omega\,\frac{n(\omega, T)D(\omega)|g(\omega)|^2}{\Delta\omega - \omega}\right].\end{aligned} \tag{24}$$

Here, we extend the upper limit of the time integration to infinity. The density operator is finally reduced to

$$\begin{aligned}\dot{\hat{\rho}}^I_S(t) =& -iU\left[\hat{A}^\dagger\hat{B}\hat{C} + \hat{A}\hat{B}^\dagger\hat{C}^\dagger, \hat{\rho}^I_S(t)\right] \\ & - n\gamma\left(\left\{\hat{C}\hat{C}^\dagger, \hat{\rho}^I_S(t)\right\} - 2\hat{C}^\dagger\hat{\rho}^I_S(t)\hat{C}\right) \\ & - (1 + n)\gamma\left(\left\{\hat{C}^\dagger\hat{C}, \hat{\rho}^I_S(t)\right\} - 2\hat{C}\hat{\rho}^I_S(t)\hat{C}^\dagger\right)\end{aligned} \tag{25}$$

where $n \equiv n(\Delta\omega, T)$ and $\gamma = \pi|g(\Delta\omega)|^2 D(\Delta\omega)$. The terms indicating the energy shift are neglected in (25) because it is small in the weaker system-bath coupling $\hat{H}_{\rm SR}$.

Let us now discuss one-exciton dynamics or energy transfer in the system based on (25), using the three bases illustrated in Fig. 6. The equations of motion for the matrix elements are read in the Schrödinger picture as

$$\begin{aligned}\dot{\rho}_{11}(t) &= iU(r)[\rho_{12}(t) - \rho_{21}(t)] \\ \dot{\rho}_{12}(t) - \dot{\rho}_{21}(t) &= 2iU(r)[\rho_{11}(t) - \rho_{22}(t)] \\ &\quad - (1 + n)\gamma[\rho_{12}(t) - \rho_{21}(t)] \\ \dot{\rho}_{22}(t) &= -iU(r)[\rho_{12}(t) - \rho_{21}(t)] \\ &\quad - 2(1 + n)\gamma\rho_{22}(t) + 2n\gamma\rho_{33}(t) \\ \dot{\rho}_{33}(t) &= 2(1 + n)\gamma\rho_{22}(t) - 2n\gamma\rho_{33}(t).\end{aligned} \tag{26}$$

When the temperature T is equal to zero ($n = 0$), (26) can be analytically solved. The diagonal parts representing the popula-

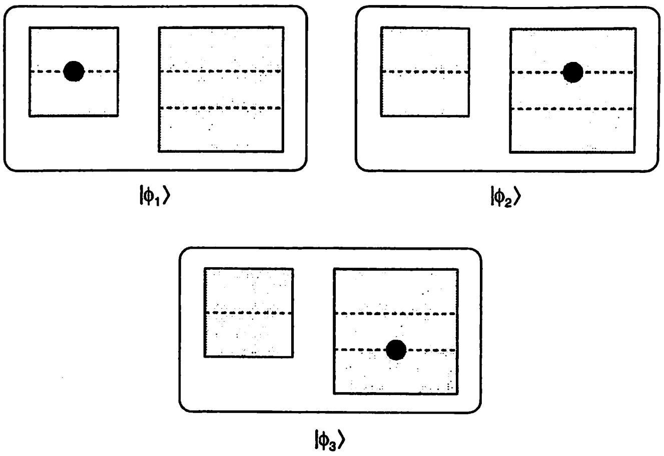

Fig. 6. Three bases of single-exciton states in a two-QD system.

tion probability for each energy level in QD1 and QD2 as well as the off-diagonal parts representing quantum coherence are given as

$$
\begin{aligned}
\rho_{11}(t) &= \frac{1}{Z^2} e^{-\gamma t} \left[\frac{\gamma}{2}\sinh(Zt) + Z\cosh(Zt)\right]^2 \\
\rho_{22}(t) &= \frac{U^2}{Z^2} e^{-\gamma t}\sinh^2(Zt) \\
\rho_{33}(t) &= 1 - [\rho_{11}(t) + \rho_{22}(t)] \\
\rho_{12}(t) &= -\rho_{21}(t) \\
&= i\frac{U}{Z^2} e^{-\gamma t}\sinh(Zt) \\
&\quad \times \left[\frac{\gamma}{2}\sinh(Zt) + Z\cosh(Zt)\right] \qquad (27)
\end{aligned}
$$

where $Z = \sqrt{(\gamma/2)^2 - U^2}$ and $\rho_{11}(0) = 1$ are used. We define the state-filling time τ_s as $\rho_{33}(\tau_s) = 1 - e^{-1}$, which corresponds to the time for excitation energy transfer from QD1 to the lower energy level in QD2. From (27), it follows that time evolution of the population drastically changes when the condition for the coupling strength is varied from $U < \gamma/2$ to $U > \gamma/2$. Although (27) seems to be undefined at $U = \gamma/2$ $(Z = 0)$, we have a definite solution regardless of whether $Z \to +0$ or -0 are taken. In Fig. 7, the state-filling time τ_s is plotted as a function of the ratio of $\gamma/2$ to U. For $U > \gamma/2$, the population $\rho_{22}(t)$ shows damped oscillation with an envelope function $e^{-\gamma t}$ and, thus, τ_s is determined by the relaxation constant γ, i.e., $\tau_s \sim \gamma^{-1}$. On the other hand, for $U < \gamma/2, \rho_{22}(t)$ decays monotonically. At first glance, as $\gamma/2$ increases, we expect τ_s to become shorter, i.e., the population seems to flow into the lower level more quickly, but on the contrary, the time τ_s becomes long as shown in Fig. 7. The reason is that the upper energy level becomes effectively broad and results in a decrease of the resonant energy transfer between the QDs. When the ratio $\gamma/2U$ is large enough, τ_s increases linearly from Fig. 7. Therefore, the state-filling time is determined not only by the optical near-field interaction strength between two QDs, but also by the coupling strength to the heat bath (phonon bath) system. It follows from Fig. 7 that the fastest energy transfer time τ_s is obtained when the condition $\gamma/2 \sim U$ is satisfied, and that τ_s is proportional to $\gamma/2U^2$ as $\gamma/(2U)$ becomes large.

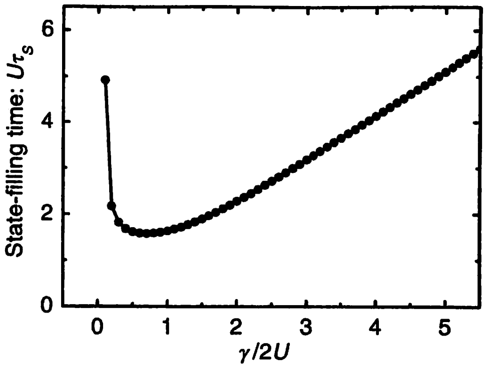

Fig. 7. State-filling time τ_s against the ratio of exciton–phonon (heat) bath coupling strength $\gamma/2$ to intradot optical near-field coupling strength U.

The last term $2\gamma n\rho_{33}(t)$ on the rhs of the third equation in (26) indicates that the temperature effect due to the finite number of phonons $(n \neq 0)$ induces back transfer of the excitation energy from the heat bath to the two-QD system. Within the Born approximation adopted in (20), this term incoherently increases the population $\rho_{22}(t)$. As the population $\rho_{33}(t)$ increases, the back transfer becomes large, and gives nonnegligible contributions to the upper-level populations $\rho_{11}(t)$ and $\rho_{22}(t)$.

D. Numerical Results

We present numerical calculation results for the population dynamics, using (26) and (27) for finite and zero temperature in order to verify the above theoretical considerations and to estimate the state-filling time for some practical cases. Here, we assume that the system consists of two cubic CuCl QDs embedded in NaCl matrix [12]. The effective side length of the cubes is set as $a : \sqrt{2}a$ $(a = 5$ nm) so that the (1, 1, 1) level of QD1 is resonant with the (2, 1, 1) level of QD2. The variable parameters are the interaction strength U or the intercube spacing, the relaxation constant γ, and the temperature of the heat bath system.

In Fig. 8, the E_1- and E_2-level populations $\rho_{22}(t)$ and $\rho_{33}(t)$ in QD2 are plotted in the cases of the intercube spacing $d = 5, 10$, and 15 nm [$U = 1.5 \times 10^{-1}, 0.90 \times 10^{-1}$, and 0.60×10^{-1} (ps)$^{-1}$], and $T = 0$ K. The relaxation time γ^{-1} is set as 1 ps based on another experiment [34]. The populations for all three cases in Fig. 8(a) show monotonic decays as we expected because the condition $U < \gamma/2$ is satisfied. From Fig. 8(b), the state-filling time τ_s is estimated for the distance $d = 5, 10$, and 15 nm as 22, 60, and 140 ps, respectively. This indicates that energy transfer time of less than 100 ps can be realized when the two QDs are located within a distance of 10 nm.

Fig. 9 gives the result for $\gamma^{-1} = 10$ ps, corresponding to a weaker coupling between an exciton and the heat bath system. Damped oscillations due to nutation between two resonant levels are clearly seen for $d = 5$ nm in Fig. 9(a), where the condition $U > \gamma/2$ is satisfied. Although in the cases of $d = 10$ and 15 nm, the condition $U > \gamma/2$ also satisfied, we cannot observe the oscillation because of the small amplitude. From Fig. 9(b), the state-filling times τ_s for the three cases are estimated as 12, 18, and 25 ps. Compared with Fig. 8(b), the state-filling speed becomes faster in Fig. 9(b) in spite of the increase in γ^{-1} because U is nearly equal to $\gamma/2$. These two

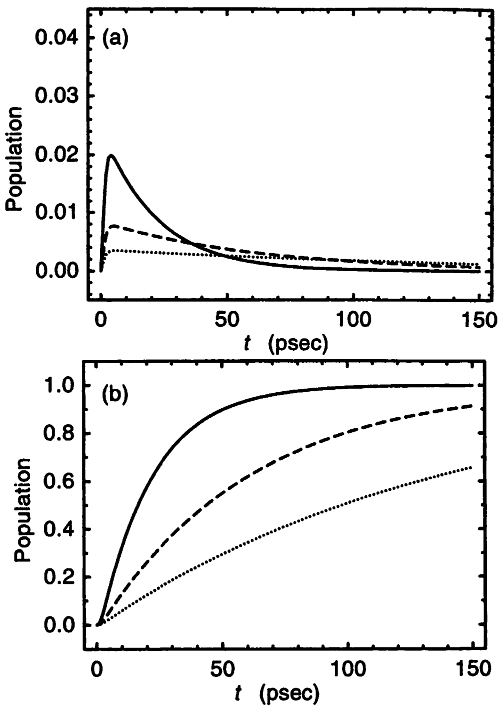

Fig. 8. Time-evolution of (a) E_1-level population $\rho_{22}(t)$ and (b) E_2-level population $\rho_{33}(t)$, where the relaxation time γ^{-1} is set as 1 ps, and the temperature is set as 0 K. The solid, dashed, and dotted curves represent the cases of interdot spacing $d = 5, 10$, and 15 nm, respectively.

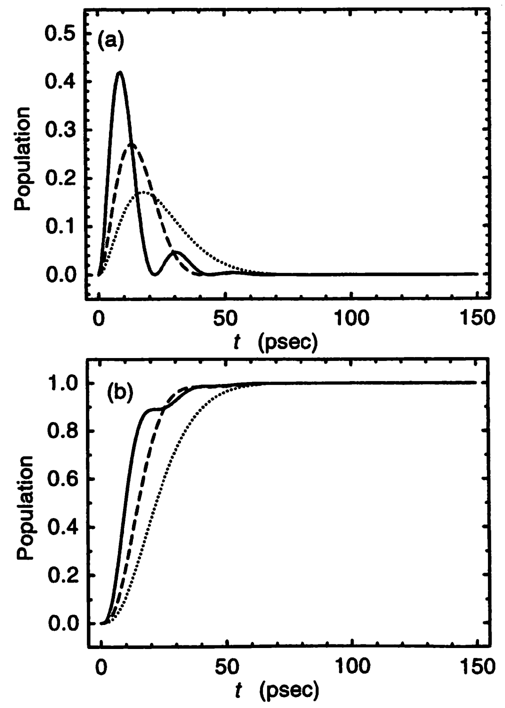

Fig. 9. Time-evolution of (a) E_1-level population $\rho_{22}(t)$ and (b) E_2-level population $\rho_{33}(t)$, where the relaxation time γ^{-1} is set as 10 ps, and the temperature is 0 K. The solid, dashed, and dotted curves represent the cases of interdot spacing $d = 5, 10$, and 15 nm, respectively.

graphs indicate that the interdot spacing should be adjusted so that the optical near-field coupling is of the same order as the exciton–phonon coupling in order to obtain the fastest energy transfer in the system.

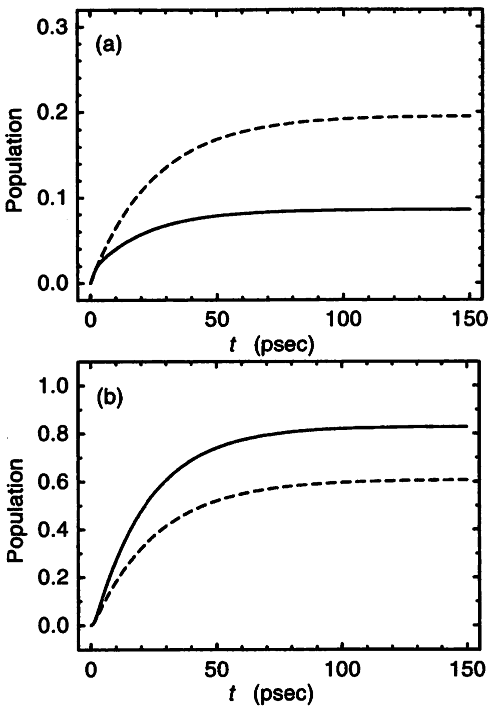

Fig. 10. Temperature dependence of (a) E_1-level population $\rho_{22}(t)$ and (b) E_2-level population $\rho_{33}(t)$ when $d = 5$ nm and $\gamma^{-1} = 1$ ps are fixed. The solid and dashed curves represent the cases of the temperature $T = 50$ and 100 K, respectively.

Fig. 10 shows the temperature dependence of the population $\rho_{22}(t)$ and $\rho_{33}(t)$. The temperature is set as either $T = 50$ or 100 K. These results are obtained by using a Laplace transform, where the singular points are derived numerically for the given numerical parameters. As mentioned in the previous section, the finite temperature induces incoherent back transfer of energy, and this results in residual populations in the upper energy levels in both QDs. Fig. 10(a) shows that there are finite-convergent values depending on the temperature. However, we find from Fig. 10(b) that the state-filling time does not change so drastically.

The results and discussions described above might be valid within the Born–Markov approximation. Even if the Born approximation is allowed because of the large volume of the heat bath system, the Markov approximation may not be guaranteed at low temperatures, as assumed in the transformation in (24). Therefore, we might deal with it more carefully, since it is said that non-Markov behavior manifests itself at low temperatures [26], [35]. The effects of non-Markov behavior on the dynamics are now under investigation. We have focused our attention on the energy transfer process in the nanometric regime, or signal transfer in a nanophotonic switch, but it is quite important to investigate the control of signals in such a system.

III. OBSERVATION OF A DIPOLE FORBIDDEN ENERGY TRANSFER FOR A NANOPHOTONIC SWITCH

This section reviews our experimental studies on optical near-field interaction between QDs described in Section II [12]. Recently, Mukai *et al.* reported ultrafast "optically forbidden" energy transfer from an outer ring of loosely packed bacteriochlorophyll molecules, called B800, to an inner ring of closely packed bacteriochlorophyll molecules, called B850, in the light-harvesting antenna complex of photosynthetic purple bacteria [36]. They theoretically showed that this transfer is possible when the point transition dipole approximation is violated due to the size effect of B800 and B850. From our viewpoint, this energy transfer is due to the optical near-field interaction between B800 and B850. Similarly, the energy can be transferred from one QD to another by the optical near-field interaction in the QD's system, even though it is a dipole-forbidden transfer.

Cubic CuCl QDs embedded in NaCl is a promising candidate for an optical near-field coupling system that exhibits this optically forbidden energy transfer. This is because, for this system, other possibilities of energy transfer, such as carrier tunneling, Coulomb coupling, and so on, can be neglected. This is also because carrier wave function is localized in QDs due to a deep potential depth of more than 4 eV and the Coulomb interaction is weak due to small exciton Bohr radius of 0.68 nm. Conventional optical energy transfer is also negligible, since the energy levels of nearly perfect cubic CuCl QDs are optically forbidden, and are confined to the energy levels of exciton with an even principal quantum number [7]. However, Sakakura *et al.* observed the optically forbidden transition in a hole-burning experiment using CuCl QDs [4]. Although they attributed the transition to an imperfect cubic shape, the experimental and simulation results did not show such imperfection. We believe that the transition was due to the energy transfer between the CuCl QDs, via the optical near-field interaction similar to the optically forbidden energy transfer between B800 and B850 in the above-mentioned photosynthetic system. However, this type of energy transfer has not yet been directly observed. This section describes the direct observation of energy transfer from the exciton state in a CuCl QD to the optically forbidden exciton state in another CuCl QD by near-field optical spectroscopy.

We fabricated cubic CuCl QDs embedded in a NaCl matrix by the Bridgman method and successive annealing, and found the average size of the QDs to be 4.3 nm. The sample was cleaved just before the near-field optical spectroscopy experiment in order to keep the clean sample surface. The cleaved surface of the 100-μm-thick sample was sufficiently flat for the experiment, i.e., its roughness was less than 50 nm at least within a few micrometer squares. A 325-nm He-Cd laser was used as a light source. A double-tapered UV fiber probe was fabricated by chemical etching and a 150-nm-thick gold film was coated. A 50-nm-diameter aperture was fabricated by the pounding method [37].

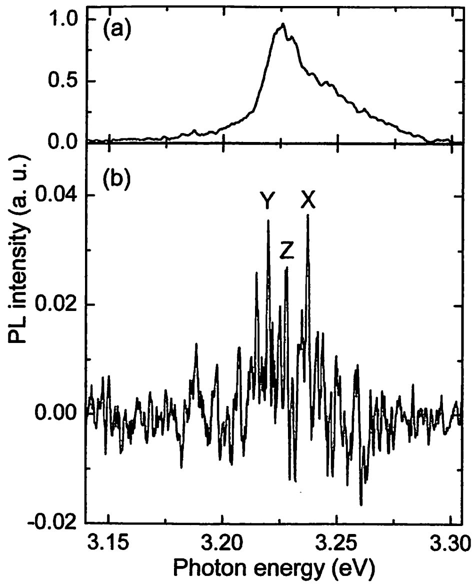

Fig. 11. (a) Far-field PL spectrum of a sample recorded with probe-sample separation of 3 μm for the collection-mode operation at 15 K. (b) The differential PL spectrum, which is the intensity difference between PL measured with the probe-sample separations of 3 μm and of less than 10 nm. The spectral peaks X, Y, and Z correspond to the wavelengths of lowest exciton state in cubic QDs with the side lengths of 4.6, 6.3, and 5.3 nm, respectively.

The curve in Fig. 11(a) shows a far-field photoluminescence (PL) spectrum of the sample that was recorded with a probe-sample separation of 3 μm in the collection-mode operation [9] of the cryogenic near-field optical spectrometer at 15 K. It represents the collective PL intensity from several CuCl QDs, and is inhomogeneously broadened owing to the size distribution of the QDs. The curve in Fig. 11(b) represents the differential spectrum, which is the difference between the PL intensities measured with probe-sample separations of 3 μm and of less than 10 nm. This curve consists of many fine structures, which are attributed to the contribution of the QDs near the apex of the probe because of the drastic increase in the measured PL intensity for a probe-sample separation less than 10 nm. Since the average density of the QDs is 10^{17} cm^{-3}, average separation between the QDs is less than 30 nm. Therefore, the spectral peaks in Fig. 11(b) originate from several QDs of different sizes. Among these, the peaks X and Y correspond to the confined Z_3-exciton energy levels of quantum number (1, 1, 1) for the QDs with side lengths (L) of 4.6 and 6.3 nm, respectively. Their effective side lengths a are 3.9 and 5.6 nm, whose size ratio is close to $1 : \sqrt{2}$ and, thus, the (1, 1, 1) and (2, 1, 1) quantized exciton levels of these QDs are resonant with each other to be responsible for optical near-field energy transfer. It means that these QDs can be used as the input and output ports of the nanophotonic switch of Fig. 2.

Fig. 12(a) and (b) shows the spatial distributions of the PL intensity, i.e., near-field optical microscope images, for peaks X and Y of Fig. 11(b), respectively. The spatial resolution, which depends on the aperture diameter of the fiber probe, was smaller than 50 nm. These images clearly establish anticorrelation features in their intensity distributions, as manifested by the dark and bright regions surrounded by white broken curves. Fig. 12(c) shows the spatial distribution of the PL intensity of peak Z in Fig. 11(b), which corresponds to the QDs with side length of 5.3 nm. Their sizes do not satisfy the resonant condition given by (1) and, thus, this figure does not show any anticorrelation features. In Fig. 12(d), the anticorrelation features of the PL intensity of X and Y are demonstrated by cross-sectional profiles taken along the dotted lines in Fig. 12(a) and (b), respectively. This figure also shows the cross-sectional profile of Z [Fig. 12(c)], which does not shows anticorrelation features with X and Y.

In order to confirm the anticorrelation feature more quantitatively, Fig. 13 shows the values of the cross-correlation coeffi-

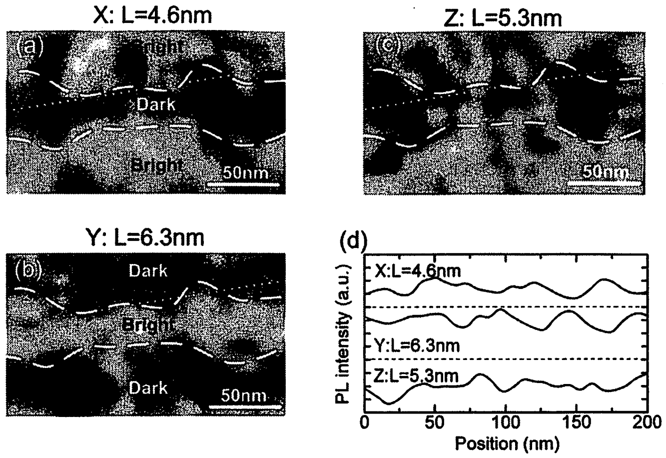

Fig. 12. (a)–(c) Spatial distributions of the near-field PL intensity for peaks X, Y, and Z in Fig. 11(b), respectively. (d) Cross-sectional profiles along the dotted lines in (a)–(c).

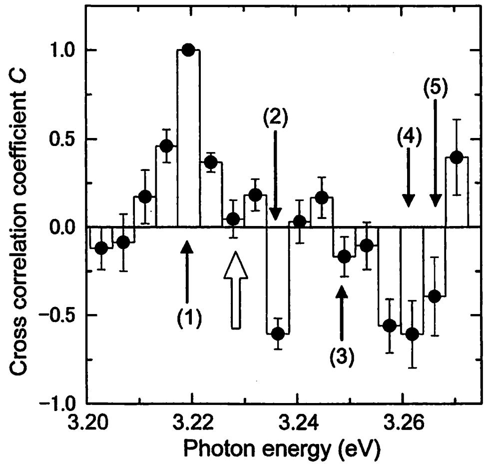

Fig. 13. Values of the cross-correlation coefficient C between the spatial distributions of the PL intensity emitted from the (n_x, n_y, n_z) level of exciton in a cubic QD with 6.3-nm side length and that from the (1, 1, 1) level in a cubic QD with the different side length L. They have been normalized to that of the autocorrelation coefficient of the PL intensity from the (1, 1, 1) level in a 6.3-nm QD, which is identified by an arrow (1). The other four arrows (2)–(5) represent the cross-correlation coefficient C between higher levels in a 6.3-nm QD and other sized QDs. They are between: (2) the (2, 1, 1) level in a 6.3-nm QD and the (1, 1, 1) level in a 4.6-nm QD, (3) the (2, 2, 1) level in a 6.3-nm QD and the (1, 1, 1) level in a 3.9-nm QD, (4) the (3, 1, 1) level in a 6.3-nm QD and the (1, 1, 1) level in a 3.6-nm QD, and (5) the (2, 2, 2) level in a 6.3-nm QD and the (1, 1, 1) level in a 3.5-nm QD. For reference, a white arrow represents the value of C between the (2, 1, 1) level in a 6.3-nm QD and the nonresonant (1, 1, 1) level in a 5.3-nm QD.

cient C between the spatial distribution of the intensity of the PL emitted from the (n_x, n_y, n_z) level of exciton in a QD with 6.3-nm side length and that from the (1, 1, 1) level in a QD with a different side length L. They have been normalized to that of the autocorrelation coefficient of the PL intensity from the (1, 1, 1) level in a 6.3-nm QD, which is identified by an arrow (1) in Fig. 13. To calculate the values of C, spatial Fourier transform was performed on the series of PL intensity values in the chain of pixels inside the region surrounded by the broken white curves in Fig. 12. The large negative value of C identified by an arrow (2) clearly shows the anticorrelation feature between Fig. 12(a) and (b), i.e., between the (2, 1, 1) level in a 6.3-nm QD and the (1, 1, 1) level in a 4.6-nm QD. This anticorrelation feature can be understood by noting that these spatial distributions in PL intensity represent not only the spatial distributions of the QDs, but also some kind of resonant interaction between the QDs. This interaction induces energy transfer from 4.6-nm QDs to 6.3-nm QDs. Interpreting this, most of 4.6-nm QDs "accidentally" located close to 6.3-nm QDs cannot emit light, but instead transfer the energy to the 6.3-nm QDs. As a result, in the region containing embedded 6.3-nm QDs, the PL intensity in Fig. 12(a) from 4.6-nm QDs is low, while the corresponding position in Fig. 12(b) is high. As we mentioned above, it is reasonable to attribute the origin of the interaction to the optical near-field energy transfer. For reference, we note the dark area outside the broken curves in Fig. 12(b). This occurs because there are very few 6.3-nm QDs. From the absorption spectra of the sample, it is estimated that the population of 6.3-nm QDs is one-tenth the population of 4.6-nm QDs. As a result, the corresponding area in Fig. 12(a) is bright due to absence of the energy transfer. On the other hand, the spatial distributions of the PL intensities from other QDs do not show any anticorrelation features. This is confirmed by comparing Fig. 12(a)–(c). The white arrow in Fig. 13 indicates the relationship between Fig. 12(b) and (c). The negligibly small value of C identified by this arrow proves the absence of the anticorrelation feature between the exciton energy levels in a 6.3-nm QD and the (1, 1, 1) level in a 5.3-nm QD due to their nonresonant condition.

Further, arrows (3)–(5) also represent large negative values of C, which means the existence of the anticorrelation feature between higher levels in 6.3-nm QD and other sized QDs due to the resonant optical near-field energy transfer. They are: (3) the (2, 2, 1) level in a 6.3-nm QD and the (1, 1, 1) level in a 3.9-nm QD, (4) the (3, 1, 1) level in a 6.3-nm QD and the (1, 1, 1) level in a 3.6-nm QD, and (5) the (2, 2, 2) level in a 6.3-nm QD and the (1, 1, 1) level in a 3.5-nm QD. The large anticorrelation coefficients C, identified by arrows (4) and (5) in Fig. 13, can be attributed also to multiple energy transfer: Since the (1, 1, 1) levels in 3.6-nm and 3.5-nm QDs resonate or nearly resonate to the (2, 1, 1) level in a 4.6-nm QD, there is another route of energy transfer in addition to direct transfer from the 3.5-nm and 3.6-nm QDs to 6.3-nm QDs, i.e., the transfer via the 4.6-nm QDs.

The anticorrelation features appear for every pair of QDs if the resonant conditions of the confinement exciton energy levels are satisfied. Fig. 14 shows two-dimensional (2-D) plots of cross correlation coefficient C between two QDs. White solid lines indicate the QDs pairs with resonant energy levels of (2, 1, 1)–(1, 1, 1), (2, 2, 1)–(1, 1, 1), (3, 1, 1)–(1, 1, 1), and (2, 2, 2)–(1, 1, 1), respectively. Large negative C appears along the solid lines due to optical near-field energy transfer between QDs.

IV. FABRICATION AND CHARACTERIZATION OF NANOPATTERNS BY OPTICAL NEAR FIELD

A. Nonresonant Near-Field Optical Chemical Vapor Deposition of Zn

To realize the proposed nanophotonic switch and nanophotonic IC in Fig. 1, an advanced nanofabrication technique is required that realizes high spatial resolution, high precision in

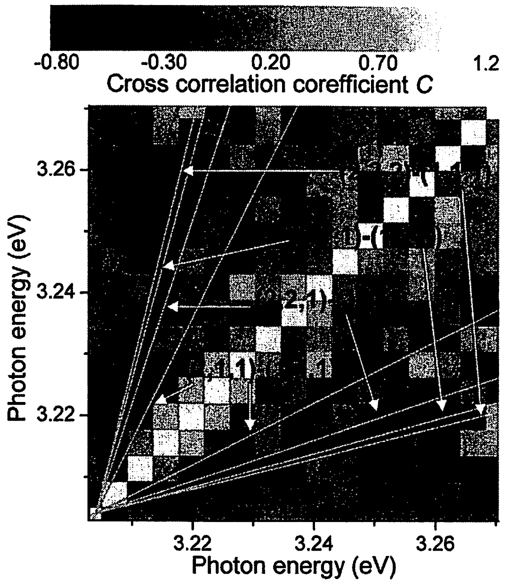

Fig. 14. 2-D plots of cross correlation coefficient C between two cubic QDs. White solid lines show the QDs pairs with resonant energy levels of (2, 1, 1)-(1, 1, 1), (2, 2, 1)-(1, 1, 1), (3, 1, 1)-(1, 1, 1), and (2, 2, 2)-(1, 1, 1), respectively.

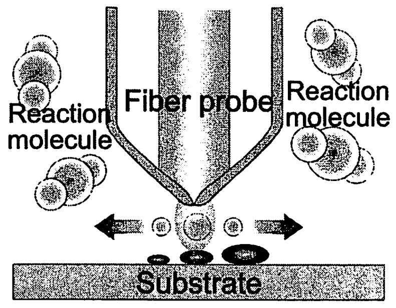

Fig. 15. Principle of the NFO-CVD. Vapors of the organometallic molecules are dissociated by the photochemical reaction with the optical near-field on the probe tip.

controlling size and position, and is applicable to various materials. Self-organized growth has been employed for nanofabrication [38]; however, its spatial precision is not sufficiently high to meet this requirement. To improve the precision, an e-beam [39], scanning tunneling microscope (STM) [40], and surface modification [41] are used for site-control of the substrate. *In situ* patterning of nanoscale structures using a scanning probe microscope, such as STM [42], has also been investigated; however, it has a fatal disadvantage in that it limits the materials that can be deposited because it cannot deal with insulators. By the conventional optical chemical vapor deposition (CVD), vapors of organometallic molecules are dissociated by the photochemical reaction with the far-field light; however, it is difficult to deposit subwavelength-sized materials due to the diffraction limit of light.

Fig. 15 shows the principle of near-field optical CVD (NFO-CVD), which has been proposed by the authors in order to solve these problems by utilizing high spatial resolution capability of the optical near field. Nanometric Zn, Al, and ZnO dots and loops have been successfully deposited by this method [37], [43]–[45]. As an example, Fig. 16 shows the shear-force topographic images of the deposited Zn and Al dots, whose sizes are less than 50 nm. It has been confirmed from these results that the precision of the deposited position was as high as about 1 nm [44]. As an outstanding advantage, we recently found that the photodissociation can take place even in nonresonant conditions, which is due to the inherent properties of the optical near field [46].

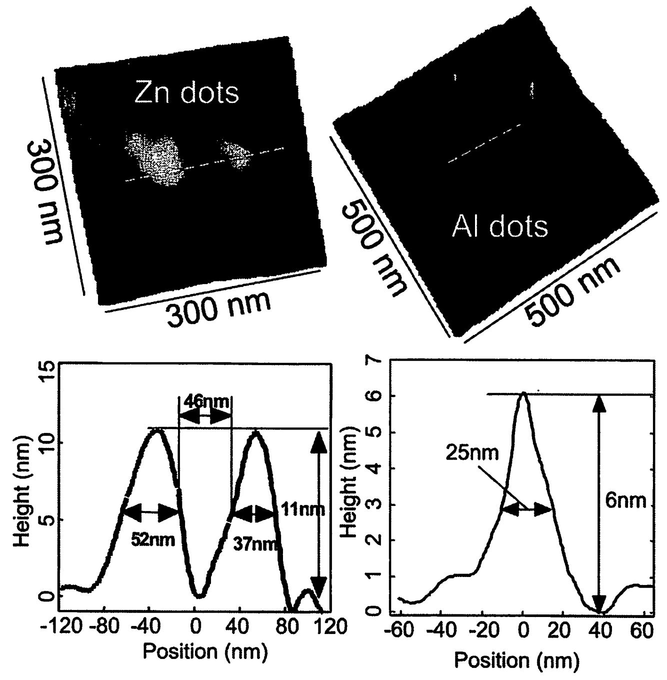

Fig. 16. Upper: Shear-force topographic images of Zn dots and Al dots deposited by NFO- CVD. Lower: Cross-sectional profiles of the deposited Zn and Al patterns along the broken lines in the upper figures, respectively.

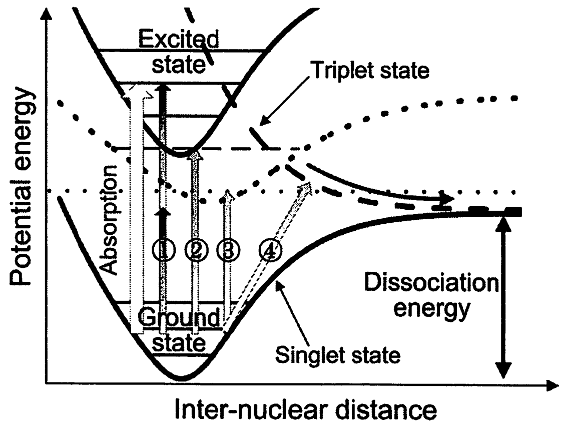

Fig. 17. Potential curves of an electron in DEZn molecular orbitals. Solid and broken curves correspond to singlet and triplet states of DEZn molecule, respectively. The relevant energy levels of the molecular vibration modes are also represented by horizontal lines.

This section discusses nonresonant NFO-CVD of nanometric Zn dots, i.e., the possible mechanisms of diethylzinc (DEZn) dissociation by the nonresonant optical near field. Fig. 17 shows potential curves of an electron in the DEZn molecular orbitals drawn as a function of the inter-nuclear distance of a C–Zn bond, which are involved in photodissociation [47]. The relevant energy levels of the molecular vibration modes are also

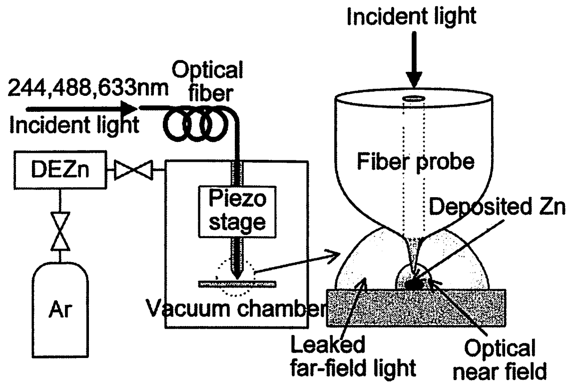

Fig. 18. Experimental setup for NFO-CVD under nonresonant condition. An atomic smooth sapphire was used as a substrate for deposition.

represented by horizontal lines on each potential curve. When a conventional far-field light is used, photoabsorption dissociates DEZn, as is indicated by a white arrow in this figure [48]. In contrast, there are four possible mechanisms of photodissociation when a nonresonant optical near field is used. They are the following. 1) *Two-photon absorption process, as indicated by the two arrows* ①. It is possible due to the high energy density of the optical near field at the apex of the high throughput fiber probe. 2) *The transition, shown by arrow* ②, *to the intermediate energy level (a broken line on the dotted curve) induced by the fiber probe and successive relaxation to the dissociative triplet state.* This induced intermediate level is created by several reasons, such as the energy shift of the excitation level in the molecule due to the interaction between molecules and the fiber probe, activation of the optically forbidden energy levels to the allowed levels for the optical near field, and so on. Similar activation of the optically forbidden energy levels has been observed in dye molecules and coupled QDs [12], [36]. 3) *The transition to an excited state of a molecular vibration mode whose energy is higher than the dissociation energy (2.26 eV), as indicated by the dotted line and arrow* ③. Although this transition is prohibited by the wavenumber conservation law for conventional far-field light, it is allowed in the present case because of the large uncertainty in the wavenumber of the subwavelength-sized optical near field. 4) *Direct transition from the singlet ground state to the dissociative triplet state is represented by arrow* ④. A spatially homogeneous far-field light cannot interact with the polarization of a DEZn molecule, as is easily understood by referring to the Franck–Condon principle. Thus, the far-field light interacts only with electrons. However, since the optical near field has a very large spatial gradient with a nanometric decay length, it can interact with the polarization of the molecule. As a result of this interaction, atoms in the molecule can be translated directly, as indicated by arrow ④.

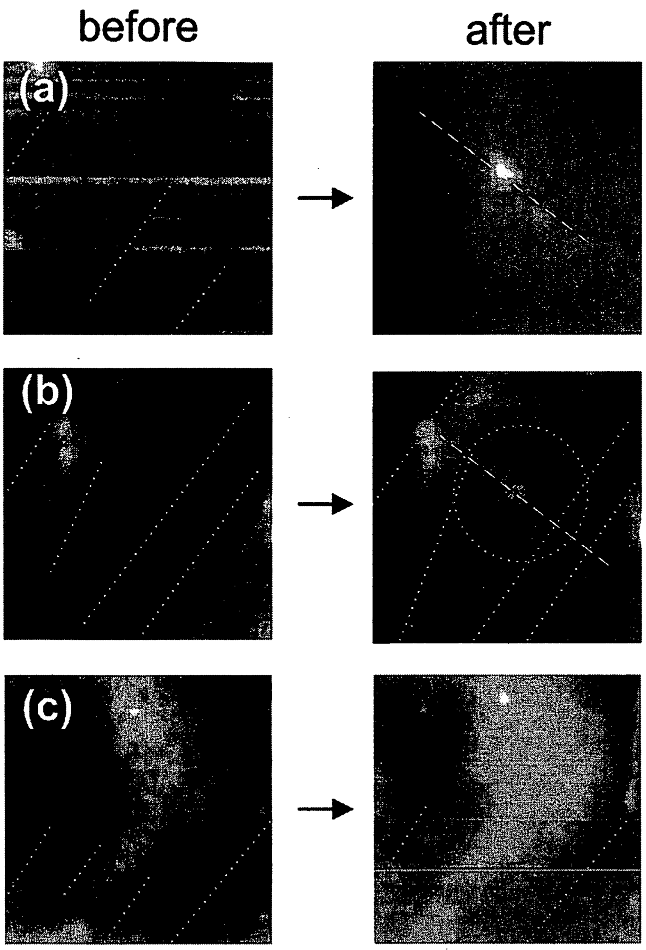

Fig. 19. Shear-force topographic images before and after NFO-CVD at wavelengths of (a) $\lambda = 244$, (b) 488, and (c) 633 nm. The image sizes are 300 × 300 nm. The observed laser output power and the irradiation time for deposition were (a) 1.6 μW and 60 s, (b) 150 μW and 75 s, and (c) 240 μW and 300 s.

Fig. 18 shows the experimental setup used to confirm the NFO-CVD under nonresonant condition. An atomic smooth sapphire (0001) was used as a substrate for deposition [49]. Ultrahigh purity argon (Ar) was used as a buffer gas and DEZn as a reacting molecular gas source. The second harmonic ($\lambda = 244$ nm) of an Ar^+ laser was used as a light source that resonates the absorption band of DEZn [47]. The fundamental frequencies of Ar^+ ($\lambda = 488$ nm) and He–Ne ($\lambda = 633$ nm) lasers were used as nonresonant light sources. In order to investigate simultaneously the deposition effect of far-field light, a bare fiber probe, i.e., a fiber probe without the metal coating, was used for CVD. This fiber probe was fabricated by pulling and etching a pure silica core fiber. Therefore, the far-field light leaked through the circumference of the fiber probe, while the optical near field was generated at the apex. The laser output power from the fiber probe was measured with a photodiode placed behind the sapphire substrate. Topographic profiles of the deposited Zn dots were measured using a shear-force microscope. During deposition, the partial pressure of DEZn was 100 mtorr and the total pressure in the chamber was 3 torr. It should be noted that the deposition of Zn on the fiber probe and the resultant decrease in the efficiency of optical near-field generation were negligible because the deposition time was sufficiently short, as has been confirmed by the previous works [44], [50].

Fig. 19 shows the shear-force topographic images before and after NFO-CVD on the sapphire substrate with atomic-level steps for (a) $\lambda = 244$, (b) 488, and (c) 633 nm. For Fig. 19(a) ($\lambda = 244$ nm), the laser power was 1.6 μW and the irradiation time was 60 s. A white circle at the center of the right figure

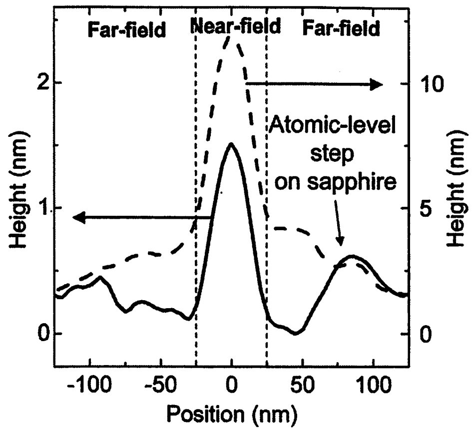

Fig. 20. Cross-sectional profiles of the deposited Zn patterns. Broken and solid curves represent cross-sectional profiles along the broken lines on the right-hand side of Fig. 19(a) and (b), respectively.

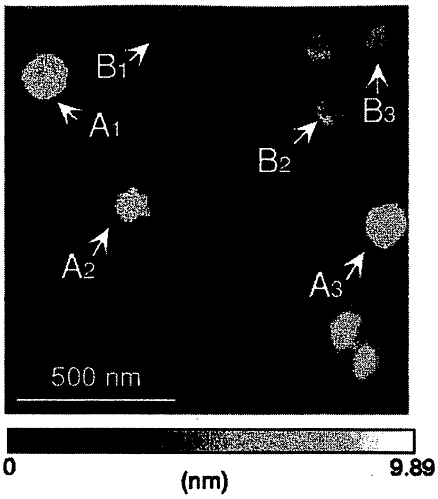

Fig. 21. Shear-force topographic image of polycrystalline ZnO.

represents a Zn dot deposited by an optical near field. However, since the bare fiber probe also leaked strong far-field light, a Zn film was deposited around the dot, which covered the atomic-step structures on a substrate. For Fig. 19(b), the laser power was 150 μW and the irradiation time was 75 s. The photon energy at this wavelength ($\lambda = 488$ nm) is higher than the dissociation energy of DEZn, but it is still lower than the absorption edge of DEZn [47]. Under this condition, it is amazing to find a Zn dot less than 50 nm in diameter at the center of the broken circle on the right figure. For Fig. 19(c) ($\lambda = 633$ nm), the laser power was 240 μW and the irradiation time was 300 s. Despite the higher power and longer irradiation time, there was no Zn deposition, which means that the thermal effect of laser irradiation is negligible for Zn deposition.

In Fig. 20, the broken curve represents the cross-sectional profile of the Zn pattern deposited at $\lambda = 244$ nm, taken along the broken line in Fig. 19(a). The solid curve is a cross-sectional profile of the Zn pattern deposited at 488 nm along the broken line in Fig. 19(b). These curves confirm that Zn dots with a full-width at half-maximum (FWHM) of 30 nm were deposited in the region where the optical near field is dominant. The broken curve has tails of 4-nm height on both sides of the peak, which correspond to the film deposited by the leaked far-field light. In contrast to this, the solid curve has no tails. Thus, it is clear that the leaked 488-nm far-field light did not deposit a Zn film. This result agrees with previous work using conventional optical CVD for Zn deposition with a far-field light with $\lambda = 300$ nm [51]. Therefore, it is confirmed that a Zn dot of Fig. 19(b) was deposited under a nonresonant condition, despite the presence of leaked far-field light.

Although more studies are required to identify the mechanism of this nonresonant deposition among the four possible candidates given above, the experimental results and the suggested mechanisms described here show numerous potential advantages. As an example, this technique makes it possible to use various light sources and gas sources, which have never been used in conventional far-field optical CVD. Thus, it can be claimed that the nonresonant NFO-CVD is a powerful nanofabrication technique.

B. Observation of Size-Dependent Features in the Photoluminescence of ZnO Nanocrystallites

As an application of NFO-CVD, nanometric ZnO has been produced by oxidizing the deposited Zn [45]. Since free-excitons in ZnO can emit a UV light, it is possible to use a nanometric ZnO dot as a light emitter in the nanophotonic IC of Fig. 1. In order to confirm this possibility, this section evaluates its PL characteristics of ZnO nanocrystallites, especially its size-dependent features by using an optical near-field technique [52], [53]. ZnO has a wide bandgap of 3.37 eV and a larger exciton binding energy (60 meV) than those of GaN (28 meV) or ZnSe (19 meV). Recently, several groups have reported room-temperature UV lasing [54], [55].

For quantitative evaluation of the size-dependent features, ZnO nanocrystallites were prepared by conventional optical CVD, not by NFO-CVD. This method is composed of two steps.

- Step 1) 200-nm-thick Zn nanocrystallites were grown on a sapphire (0001) substrate at room temperature by optical CVD. DEZn was used as a gas source. The partial pressures of DEZn and the Ar buffer gas were 10 and 200 mtorr, respectively. The second harmonic (SH) light of an Ar^+ laser ($\lambda = 244$ nm) was used as the light source for the photodissociation of DEZn [56], whose power and spot size were 10 mW and 600 μm, respectively.
- Step 2) The deposited Zn nuclei were thermally oxidized in ambient oxygen at 1 atm and 750 °C for 30 min [55]. This method is applicable to NFO-CVD [57] in order to deposit nanometric ZnO dots with high precision in the size and position because depositing Zn at room temperature in Step 1) avoids thermal drift of the substrate and the probe.

Fig. 21 shows a shear-force topographic image of oxidized Zn, obtained using a sharpened fiber probe with an apex diameter of 100 nm. Hexagonal (A_1–A_3) and square (B_1–B_3) nanocrystallites can be seen, which proves that oxidized Zn is

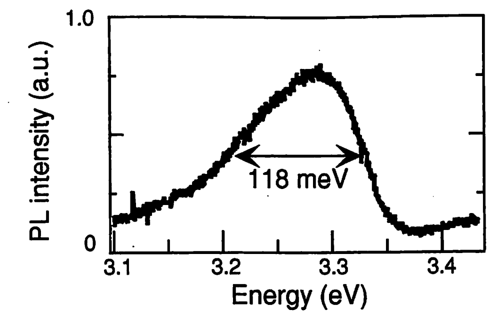

Fig. 22. Far-field PL spectrum of polycrystalline ZnO at room temperature.

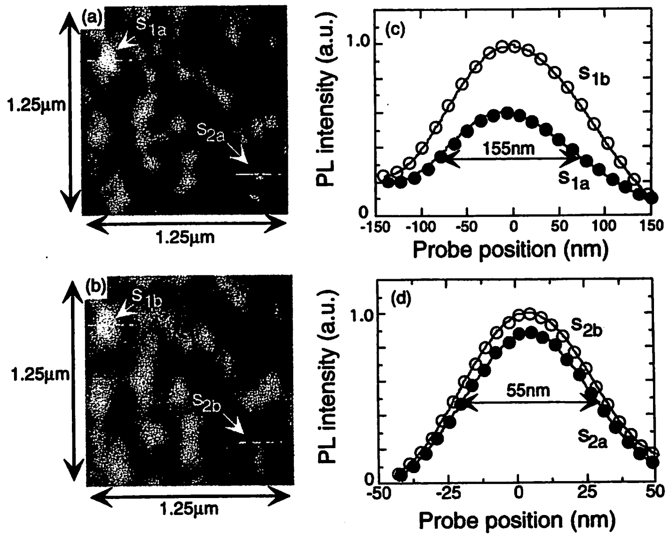

Fig. 23. Monochromatic PL images of polycrystalline ZnO obtained at wavelengths of (a) 370 and (b) 380 nm. (c) Closed and open circles represent cross-sectional profiles along the broken lines through spots s_{1a} and s_{1b}, respectively. (d) Closed and open circles represent cross-sectional profiles along the broken lines through spots s_{2a} and s_{2b}, respectively.

composed of many nanocrystallites with various orientations. The grain sizes were in the range of 30–160 nm.

Fig. 22 shows a far-field PL spectrum at room temperature, measured by using an He–Cd laser ($\lambda = 325$ nm) as a light source. The emission peak energy was close to the reported value of 3.26 eV ($\lambda = 380$ nm), which corresponds to spontaneous emission from the free exciton in high-quality ZnO nanocrystallites [54]. The FWHM of the PL spectrum was about 118 meV, which is comparable with the 117 meV of molecular beam epitaxy grown ZnO nanocrystallites at room temperature [58]. These results imply that the oxidized Zn is composed of high-quality ZnO nanocrystallites. Furthermore, since ZnO has a wurtzite structure, the hexagonal and square nanocrystallites shown in Fig. 21 represent nanocrystallites oriented along the c axis [54] and in other directions, respectively. These results imply that fabricated ZnO nanocrystallites are polycrystalline.

Using a collection-mode near-field optical spectrometer, we measured spatially and spectrally resolved PL spectra, for which a UV fiber probe with an 80-nm aperture diameter was used. Fig. 23(a) and (b) shows monochromatic PL images, in which the detection wavelengths were 370 ± 2.5 and 380 ± 2.5 nm, respectively. The closed and open circles in Fig. 23(c) represent cross-sectional profiles along the broken lines through spots s_{1a} and s_{1b} in Fig. 23(a) and (b), respectively. Those in Fig. 23(d) are for spots s_{2a} and s_{2b} in Fig. 23(a) and (b). Note that the FWHM of spots s_{1a} and s_{2a} was 155 and 55 nm, respectively, which is comparable to the grain sizes of ZnO nanocrystallites. This indicates that each emission spot originated from an individual ZnO nanocrystallite.

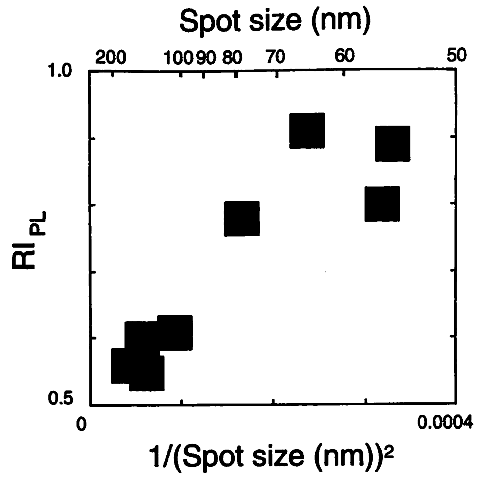

Fig. 24. Monochromatic PL images of polycrystalline ZnO obtained at wavelengths of (a) Relative PL intensity RI_{PL}[=(PL intensity at 370 ± 2.5 nm)/(PL intensity at 380 ± 2.5 nm)] of ZnO nanocrystallites as a function of spot size.

One technical problem was that the sensitivity of near-field optical spectrometer was not sufficiently high in order to evaluate precisely the spectral profile of individual ZnO nanocrystallites. To solve this problem, we defined the relative PL intensity RI_{PL} by (PL intensity at a detection wavelength of 370 ± 2.5 nm)/(PL intensity at a detection wavelength of 380 ± 2.5 nm). This parameter RI_{PL} can be used to evaluate the magnitude of the blue-shift of the PL spectral peak because it increases with decreasing the spectral peak wavelength. Fig. 24 shows the measured relation between the value of RI_{PL} and the PL spot size of ZnO nanocrystallites, where the spot sizes were estimated from the FWHM of Fig. 23. An outstanding feature of this figure is that the RI_{PL} is larger for a smaller spot size. It means that the smaller ZnO nanocrystallites have shorter wavelength at its PL spectral peak, which is attributed to the quantum size effect in ZnO nanocrystallites. Although this size-dependent feature of the PL intensity has ever been evaluated for an ensemble of nanocrystallites using a conventional diffraction-limited optical method [55], the present results are the first to evaluate individual nanocrystallites using a spatially resolved optical near-field method.

Since Zn dots with the size less than 50 nm have been fabricated by the NFO-CVD [57], fabrication and integration of nanophotonic devices are expected by assembling high-quality ZnO nanocrystallites by optical near-field method.

V. PLASMON WAVEGUIDE FOR OPTICAL FAR/NEAR-FIELD CONVERSION

A. *Principle of a Plasmon Waveguide*

A nanometric optical waveguide is required for far/near field conversion in order to connect the nanophotonic IC with external conventional diffraction-limited photonic devices, as is

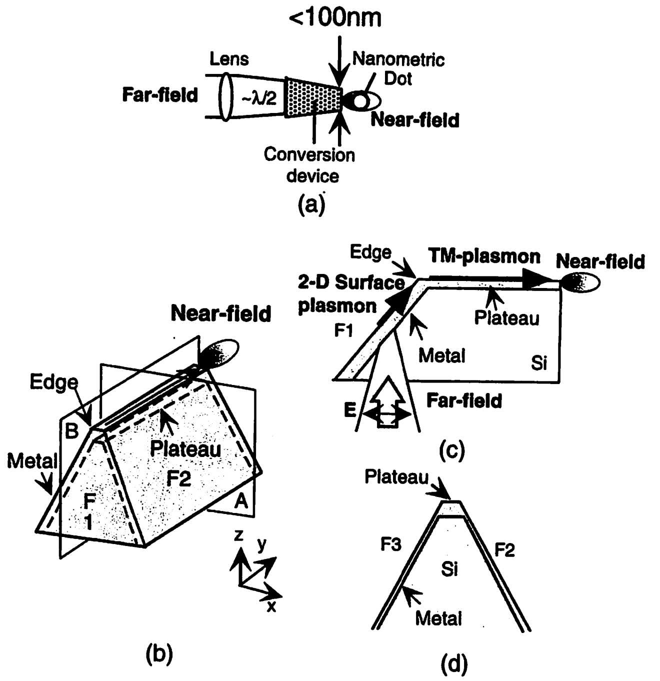

Fig. 25. Monochromatic PL images of polycrystalline ZnO obtained at wavelengths of (a) Optical far/near field conversion device. (a) Schematic explanation of operation. (b) Bird's-eye view of a plasmon waveguide. The x and y axes are perpendicular and parallel to the plateau axis, respectively. (c) Cross section along the plane B (yz plane) in (b). (d) Cross section along the plane A (xz plane) in (b).

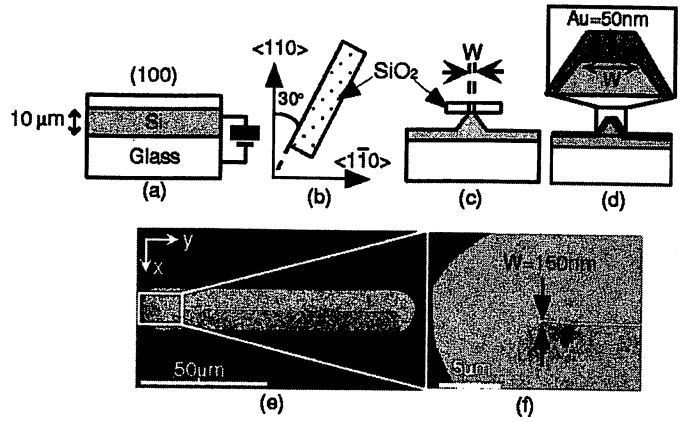

Fig. 26. Fabrication processes for a plasmon waveguide. (a) Anodic bonding. (b) Mask alignment. (c) Anisotropic etching for fabrication of the silicon wedge. W: plateau width. (d) Metal coating. (e) and (f) SEM images of the metal-coated silicon wedge, $W = 150$ nm.

schematically explained by Fig. 25(a). Performances required for this waveguide include: 1) high conversion efficiency; 2) a sub-100-nm width of a guided beam for efficient coupling of the converted optical near field to nanometric dots; and 3) a super-wavelength propagation length to avoid direct coupling of the propagating far-field light to the nanometric dots.

A cylindrical metal core waveguide is a promising candidate to realize a sub-100-nm beam width, through which the TM plasmon mode propagates [59]. However, the TM plasmon mode is not easily excited by far-field light due to mode mismatching. To overcome this difficulty, we employed a metal-coated silicon wedge structure [Fig. 25(b)] [60]. The main part consists of a silicon wedge, which is coated with a thin metal film. An incoming far-field light, which is polarized parallel to the y axis, is first transformed into the 2-D surface plasmon mode on the surface F1 [Fig. 25(c)]. Next, the 2-D surface plasmon mode is converted into the one-dimensional (1-D) TM plasmon mode at the edge between F1 and the plateau. This conversion occurs because of the scattering coupling at the edge [61]. Finally, the TM plasmon mode propagates along the plateau in a manner similar to an edge mode in a tetrahedral tip [62]. Since the metal film deposited on the plateau is sufficiently thicker than on the other surfaces (F1–F3) due to the normal evaporation process, the plateau acts as a metal core waveguide [Fig. 25(d)]. Finally, the TM plasmon mode at the outlet of the waveguide is converted to the optical near field.

Advantages of this plasmon waveguide are as follows. a) High conversion efficiency from the 2-D surface plasmon mode to the 1-D TM plasmon mode due to the scattering coupling, which meets the requirement 1) [61], [63]. b) The beam width decreases to as narrow as 1 nm with decreasing the core diameter, since this waveguide does not have a cutoff [59]. It meets the requirement 2). c) The propagation length of the TM-plasmon mode is sufficiently long. As an example, the propagation length is 2.5 μm (at $\lambda = 830$ nm) for the TM plasmon with a gold core (diameter $D = 40$ nm) insulated by air [59]. It meets the requirement 3).

The plasmon waveguide was fabricated in four steps. i) A (100)-oriented silicon wafer was bonded to the glass substrate by anodic bonding [Fig. 26(a)] [64]. ii) In order to avoid any deformation of the convex corners [65], the patterned rectangular mask was tilted 30° with respect to the $\langle 110 \rangle$ crystal orientation of silicon [Fig. 26(b)]. iii) The silicon wedge was fabricated by anisotropic etching (40 g KOH + 60 g H_2O + 40 g isopropyl alcohol, 80 °C). By maintaining the silicon wedge height lower than 10 μm, its propagation loss can be kept sufficiently low [Fig. 26(c)]. iv) After removing the SiO_2 layer, the silicon wedge was coated with a 50-nm-thick gold layer [Fig. 26(d)]. SEM images of the fabricated waveguide are shown by Fig. 26(e) and (f).

B. Excitation and Observation of 1-D Plasmon Mode

The spatial distribution of the electric-field energy on the plateau of metallized silicon wedge was measured by scanning a fiber probe with an aperture diameter D_a of 60 nm. In order to excite the plasmon mode, linearly polarized light ($\lambda = 830$ nm) was focused onto the surface F1. Fig. 27(a) and (b) shows the bird's-eye views of the observed electric-field energy distributions on the wedges with plateau width $W = 1$ μm and 150 nm for TM polarization (the incident light polarization is parallel to the y axis), respectively. Fig. 27(c) and (d) are for TE polarization (parallel to the x axis). Comparing Fig. 27(a) and (c) [or Fig. 27(b) and (d)], it is confirmed that the propagating mode was excited efficiently only by TM polarized incident light. Closed and open circles in Fig. 28(a) and (b) show the cross-sectional profiles along the lines in Fig. 27(a) (A–A' and a–a') and (b) (B–B' and b–b'), respectively. In these figures, transmission was defined as the ratio of the light power detected by the

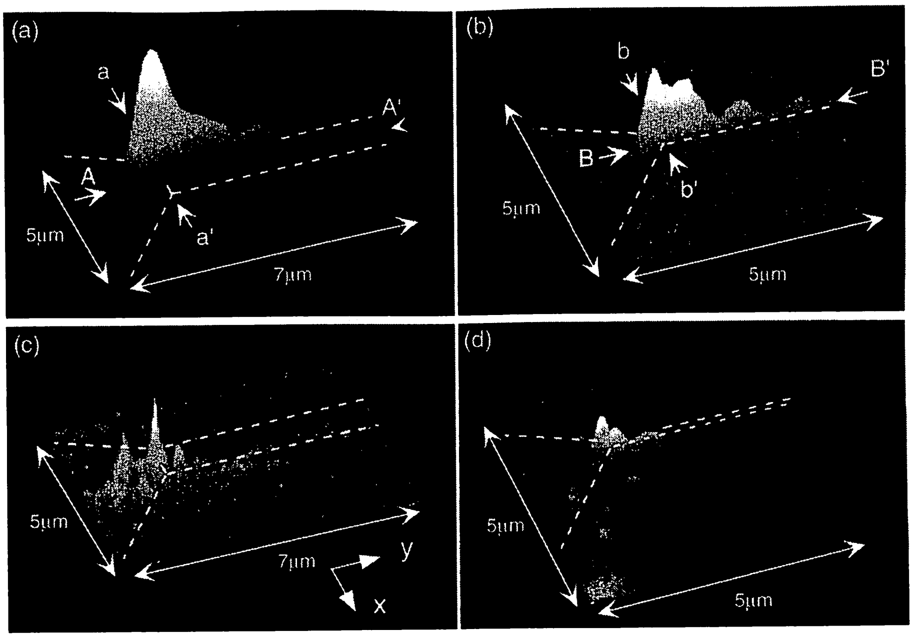

Fig. 27. Bird's eye views of the electric-field energy distribution (λ = 830 nm) on the silicon wedge plateau. (a) TM polarization: $W = 1$ μm. (b) TM polarization: $W = 150$ nm. (c) TE polarization: $W = 1$ μm. (d) TE polarization: $W = 150$ nm.

fiber probe to the input light power. From the dotted exponential curve in Fig. 28(a) fitted to the open circles, the propagation length is estimated as 2.5 μm for the 150-nm wedge. This value is comparable to the theoretical value for TM plasmon mode in a cylindrical metal core waveguide with $D = 40$ nm, which consists of a gold core and air cladding ($\lambda = 830$ nm) [59]. From the solid exponential curve in Fig. 28(a) fitted to the closed circles, the propagation length for $W = 1.0$ μm is estimated as 4.0 μm, which is longer than that for $W = 150$ nm. This is because, as W increases, the effective refractive index approaches that of surface plasmon at the planar boundary between gold and air [59]. These experimental results confirm that the observed excitation along the plateau was the TM plasmon mode.

Fig. 28(b) shows that FWHM of the cross-sectional profiles was 150 nm for $W = 150$ nm, which can be decreased by minor improvements of the waveguide design in order to meet the requirement 2). Further, note that the transmission was 5.0×10^{-3} for $W = 150$ nm, which is ten times higher than that of a fiber probe with $D_a = 150$ nm [66]. This efficient excitation of the TM plasmon mode is attributed to the scattering coupling at the edge between F1 and the plateau in Fig. 25(b) [61], [63] and, thus, it meets the requirement 1). Finally, the propagation length estimated above is longer than the incident light wavelength, which meets the requirement 3).

In the case when this waveguide is used in the UV region in order to excite nanometric ZnO, CuCl, and so on, higher coupling efficiency could be expected by introducing a grating coupler in order to convert the propagating far-field light to the 2-D plasmon mode.

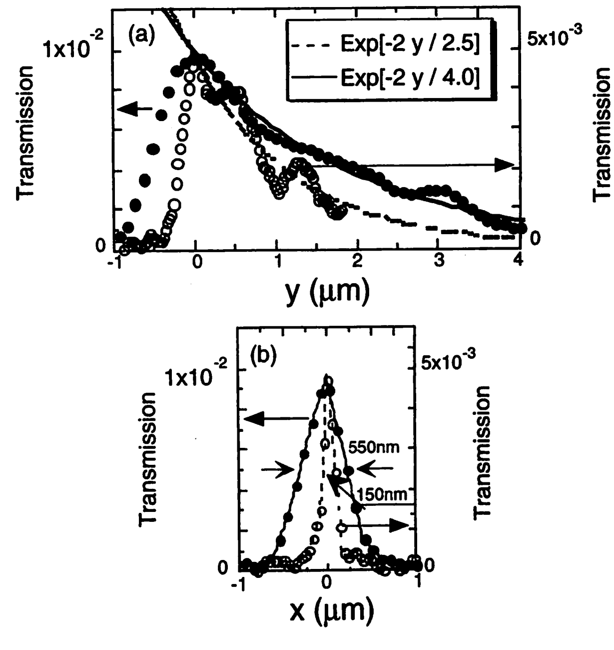

Fig. 28. (a) Cross-sectional profiles along A–A' (closed circles) and B–B' (open circles) in Fig. 27(a) and (b), respectively. Solid and dotted exponential curves were fitted to the experimental values of closed and open circles, respectively. (b) Cross-sectional profiles along a–a' (closed circles) and b–b' (open circles) in Fig. 27(a) and (b), respectively.

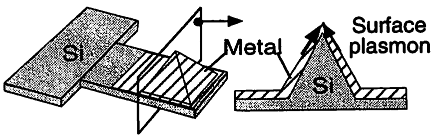

Fig. 29. Structure of a metallized pyramidal silicon probe.

VI. A KEY DEVICE FOR GENERATION/DETECTION OF OPTICAL NEAR FIELD WITH HIGH THROUGHPUT AND RESOLUTION

A. Metallized Pyramidal Silicon Probe

A key device for nanophotonics is the one generating or detecting optical near field. Such a device, i.e., a fiber probe has been fabricated by selective chemical etching, which was developed by the authors [67]. Recently, several groups have reported cantilevered probes based on micromachining

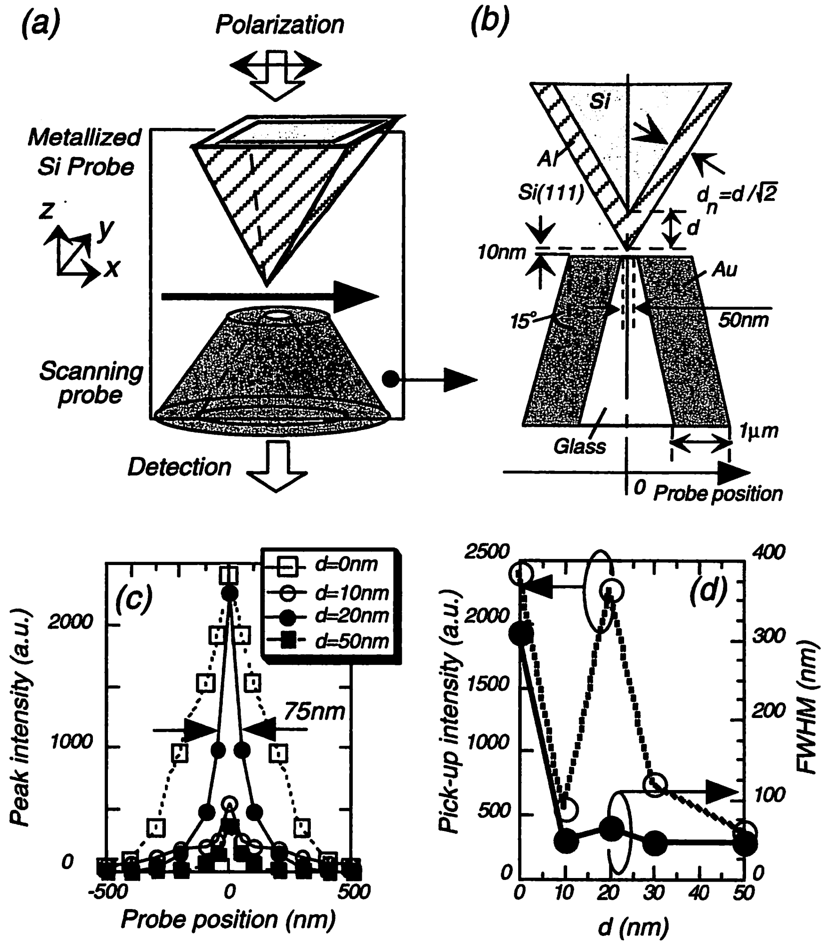

Fig. 30. (a) FDTD geometry of the probe-to-probe method. (b) Cross section along the xz plane in (a). d = aluminum thickness. (c) Thickness dependence of the calculated distributions. (d) Thickness dependence of peak intensity and FWHM of the profiles in (c).

[68]–[71]. High throughput and small spot size are expected due to high refractive indices of their cores; however, they have not yet been realized for applications to nanophotonics. This section reviews the successful fabrication of a probe with extremely high throughput, introducing a pyramidal silicon structure and localized surface plasmon resonance at the metallized probe tip.

In order to realize a nanometric spot size at the probe tip, a metallic probe is a promising candidate, through which the surface plasmon mode propagates. Since a metallic core waveguide does not have a cutoff, the spot size of the propagating mode decreases with decreasing the core diameter [59]. However, the plasmon mode is not easily excited by the propagating mode inside the dielectric core due to mode mismatching. In order to overcome this difficulty, we employed a pyramidal silicon probe that is entirely coated with a thin metal film, as is schematically explained by Fig. 29. Due to the high refractive indices of the core and the thin metal film, light propagates inside the silicon core and is converted into the surface plasmon mode at the metallic tip.

To find the optimum tip parameters, numerical calculations were carried out for the geometry shown in Fig. 30(a) and (b) by using the finite-difference time-domain (FDTD) method [72]. Fig. 30(a) is for the probe-to-probe method used to measure the spatial distribution of the optical near-field energy $180 \times 180 \times 150$ cells with the cell size of $10 \times 10 \times 10$ nm. As shown in Fig. 30(b), the pyramidal silicon probe (refractive index $n = 3.67$ at $\lambda = 830$ nm) was coated with Al film ($n = 2.74 - i8.3$) [73], and the four sidewalls resulted from (111) silicon crystal planes. A scanning probe with a glass core ($n = 1.53$) was used to detect the optical near-field energy on the probe tip. The scanning probe with a cone angle of 30° was coated with a 1-μm-thick Au ($n = 0.19 - i5.4$) layer, and had an aperture with a diameter D_a of 50 nm. Separation between the probes was fixed to 10 nm. The pyramidal silicon probe was illuminated with a linearly polarized light ($\lambda = 830$ nm).

Fig. 30(c) shows the thickness dependence of the calculated cross-sectional profiles of the detected optical near-field energy, which represents that the peak energy for the metallized silicon probe (metal thickness $d = 20$ nm) is as high as that of the bare silicon tip ($d = 0$ nm) and the FWHM is 75 nm. The thickness dependence of the peak energy and FWHM is illustrated in Fig. 30(d), which indicates that the metallized silicon structure produced a spot size as small as 50 nm ($<\lambda/10$). Since efficient excitation of the surface plasmon is obtained with a 15-nm-thick aluminum coating ($\approx d/\sqrt{2}$) on silicon in the Kretschmann configuration [74], these size-dependent features are attributed to localized surface plasmon resonance [75]. As a result of these numerical calculations, the optimum Al thickness was found to

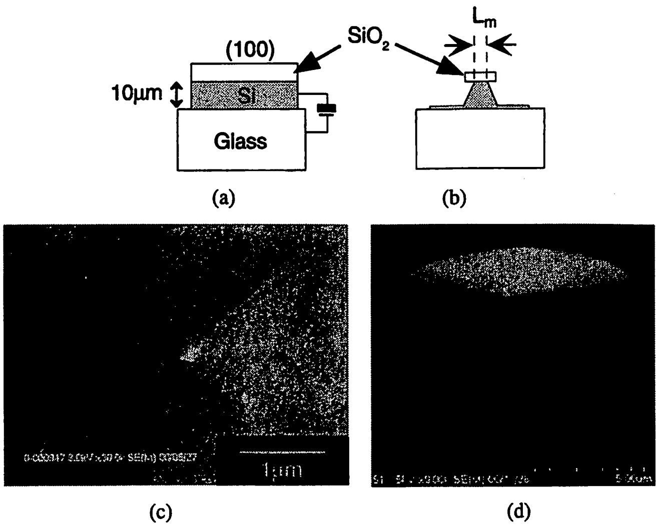

Fig. 31. Fabrication processes for a pyramidal silicon probe. (a) Anodic bonding. (b) Anisotropic etching for fabrication of the silicon wedge. L_m: mesa length. (c) SEM image of the fabricated pyramidal silicon probe. (d) Magnified image of (c).

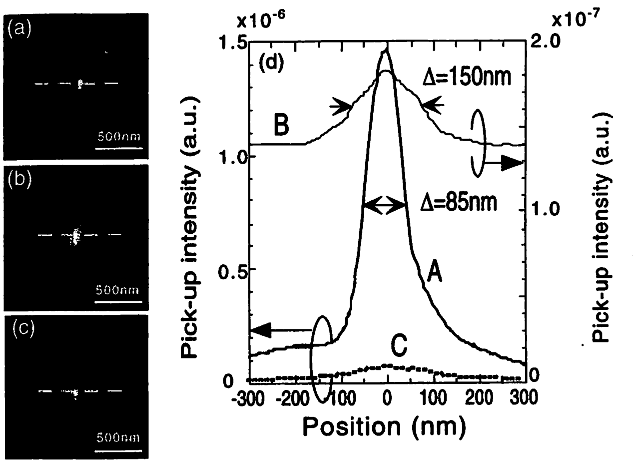

Fig. 32. Observed spatial distributions of the optical near-field energy of the (a) metallized pyramidal silicon probe ($d = 20$ nm), (b) bare pyramidal silicon probe ($d = 0$ nm), and (c) triple-tapered probe with $D_a = 60$ nm. (d) Curves A, B, and C are the cross-sectional profiles along the dashed white lines in (a)–(c), respectively.

B. Fabrication of a Metallized Pyramidal Silicon Probe and Observation of Localized Plasmon Resonance

Based on the optimization in Section VI-A, a pyramidal silicon probe was fabricated in three steps:

- Step 1) A (100)-oriented silicon wafer was bonded to a glass substrate by anodic bonding [Fig. 31(a)] [64].
- Step 2) The probe was fabricated by anisotropic etching [Fig. 31(b)]. By maintaining the silicon probe height at less than 10 m, the propagation loss is kept sufficiently low.
- Step 3) After removing the SiO_2 layer, the probe was coated with an Al layer ($d = 20$ nm). Fig. 31(c) and (d) shows scanning electron microscope (SEM) images of our sharpened (mesa length $L_m < 10$ nm) pyramidal silicon probe with an Al layer.

Spatial distribution of the optical near-field energy on the pyramidal silicon probe was measured using the probe-to-probe method, i.e., it was scanned with an apertured probe with $D_a =$ 50 nm with a cone angle of 30°. The separation between the probes was kept within 10 nm using the shear-force feedback technique. For comparison, we also measured the optical near-field energy of a triple-tapered fiber probe with $D_a = 60$ nm. The throughput of this triple-tapered fiber probe has been calibrated to be 1.5×10^{-3} [66], which is the highest among existing fiber probes due to the interference characteristics of the guided modes [66].

Fig. 32 (a)–(c) shows the observed spatial distributions of the optical near-field energy for the metallized pyramidal silicon probe ($d = 20$ nm), the bare pyramidal silicon probe ($d =$ 0 nm), and the triple-tapered fiber probe with $D_a = 60$ nm, respectively. Curves A–C in Fig. 32(d) are cross-sectional profiles along the dashed white lines in Fig. 32(a)–(c), respectively. Note that the FWHM of the metallized pyramidal silicon probe is 85 nm ($\sim\lambda/10$) (curve A), which is in good agreement with the value in Fig. 30(c). Further, the peak energy of the metallized pyramidal silicon probe is five and 15 times larger than those of the bare pyramidal silicon and the triple-tapered probes, respectively. Such effective excitation of the optical near field by the metallized silicon probe is attributed to localized surface plasmon resonance. These results indicate that the metallized pyramidal silicon structure resulted in high throughput (2.3%) and small spot size (85 nm) simultaneously.

Considering the aperture diameter ($D_a = 50$ nm) of the fiber probe used for detection, the spot size of the metallized pyramidal silicon probe ($d = 20$ nm) should have the capability of higher resolution, e.g., 50 nm or higher should be possible. Higher throughput is expected by combining the pyramidal silicon probe tip and the microfabricated solid immersion lens [76]. Further, by using the transparent material with high refractive index in the UV region, such as Si_3N_4, GaP, GaN, and so on, the plasmon resonance effect described here can be applicable also to the blue-violet region.

VII. APPLICATION TO HIGH-DENSITY AND HIGH-SPEED OPTICAL MEMORY

A. Optical Near-Field Slider

Nanophotonics can be applied to next-generation optical storage system with 1 Tb/in^2 recording density and 1-Gb/s data transmission rate. A super-resolution near-field structure [77] and a planar probe mounted on an optical slider [78] were proposed recently for this application. Though these methods do not require shear-force feedback, the optical near-field energies on the subwavelength apertures are too low because the incident light is focused by a conventional lens. We review here an advanced system using a contact slider as a more promising candidate to realize high recording density on a phase-change recording medium and fast data transmission rate. Our metallized pyramidal silicon probe technology of Section VI is applied to this system.

Structures of the system and the slider are illustrated in Fig. 33 [79]. A metallized pyramidal silicon probe array is arranged on a surface of the slider. The probes in the array are designed by utilizing the results of Section VI. Advantages of such a slider are as follows. 1) the probe array with sub-10-μm heights has

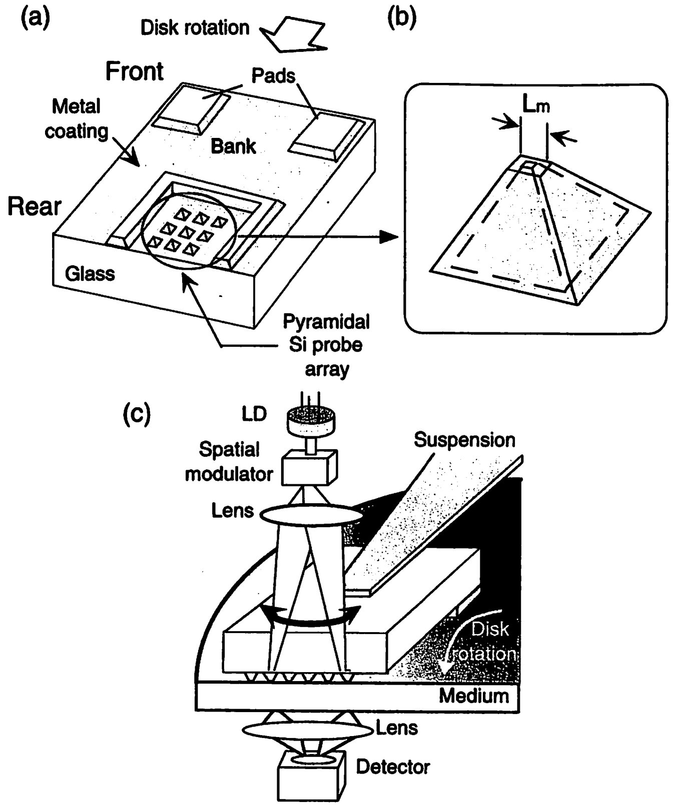

Fig. 33. (a) Contact slider with a pyramidal silicon probe array. (b) Pyramidal silicon probe, L_m: mesa length. (c) Data storage system with the slider.

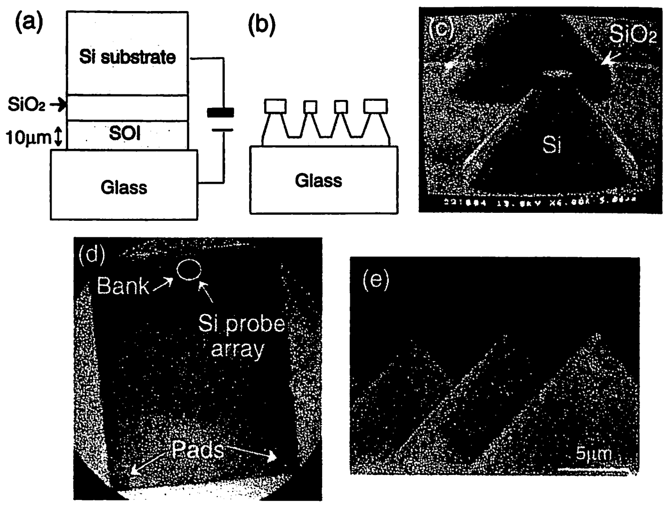

Fig. 34. Fabrication processes of a contact slider with a pyramidal silicon probe array. (a) Anodic bonding. (b) Anisotropic etching for fabrication the probe array, the bank, and the pads. (c) SEM image as the result of Step 1). (d) Optical image as the result of Step 4). (e) Magnified SEM image of the fabricated pyramidal silicon probe array.

high durability because it is bonded to a thick glass substrate. 2) Since the height of the probe tips and the pads are determined by the uniformity of the thickness of silicon wafer, ultrahigh homogeneity in the heights of the probes and pads can be obtained. 3) Use of a probe array with many probe tips increases the total data transmission rate by parallel readout [80]–[82]. For this readout, the incident light is spatially modulated by an electrooptics method, and the scattered light from each probe is detected as a time-sequential signal.

B. Fabrication of Optical Near-Field Slider and Recording-Readout Experiments

Since the key issue in realizing a pyramidal silicon probe array is high homogeneity in the heights of the probes, the probe array is fabricated from a (100)-oriented silicon-on-insulator (SOI) wafer in four steps.

Step 1) A 10-μm SOI wafer is bonded to the glass substrate by anodic bonding [Fig. 34(a)] [64].

Step 2) After removal of the silicon substrate from the SOI wafer by wet etching, the probe array, the bank, and the pads are fabricated by anisotropic etching (40g KOH + 60 g H_2O + 40 g isopropyl alcohol, 80 °C) [Fig. 34(b)]. Note that the height homogeneity is maintained by the remaining the SiO_2 layer [see Fig. 34(c)].

Step 3) The slider is quarried with a dicing saw.

Step 4) After removal of the SiO_2 layer, the slider is coated with 30-nm-thick aluminum.

Fig. 34(d) and (e) shows an optical image of the contact slider and a SEM image of the pyramidal silicon probe array fabricated on the slider, respectively. The height dispersions of the probes and pads are decreased to less than 10 nm due to the uniformity of thickness of the SOI wafer. The slider is designed by use of the design criteria [83] for a contact-type hard-disk head so that its jumping height over the phase-change recording medium is maintained to be less than 10 nm. Furthermore, since the phase-change recording medium is fragile, we designed the bank so that the contact stress becomes 100 times lower than the yield stress of the magnetic disk at a constant linear velocity (v_{CL}) of 0.3 m/s, corresponding to a data transmission rate of 10 Mb/s for a data density of 1 Tb/in^2. To increase the data transmission rate 100 times, i.e., to realize a 1-Gb/s data transmission rate for recording density of 1 Tb/in^2, we fabricated 100 probe elements on the inner part of the bank for parallel readout.

In recording and readout experiments (see Fig. 35), an as-deposited AgInSbTe film was used as a phase-change recording medium. We compared the signal transmitted through phase-changed marks recorded with a single element of the probe array and that with a focused propagating light ($\lambda = 830$ nm). The slider was in contact with a phase-change recording medium coated with a thin lubricant film. The frequency of the rectangularly modulated signal with 50% duty was changed from 0.16 to 2.0 MHz at $v_{\mathrm{CL}} = 0.43$ m/s. The recording optical powers for a pyramidal silicon probe with a mesa length L_m of 150 nm (see the SEM image in Fig. 35) and a focused propagating light with an object lens (N.A., 0.4) were 200 and 15 mW, respectively. Readout was carried out at $v_{\mathrm{CL}} = 0.43$ m/s. The reading optical powers for the pyramidal silicon probe and the focused propagating light were 20 and 3.6 mW, respectively. The resolution bandwidth was 30 kHz.

Measured dependences of the carrier-to-noise ratio (CNR) on the mark length are shown in Fig. 36. Compared with the closed circles, open circles indicate that shorter crys-

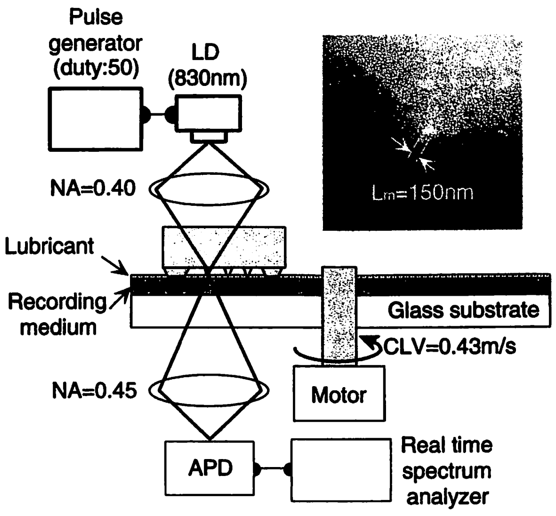

Fig. 35. Experimental setup for phase-change recording-reading by the contact slider. Inset: SEM image of the pyramidal silicon probe tip used for optical near-field recording-reading.

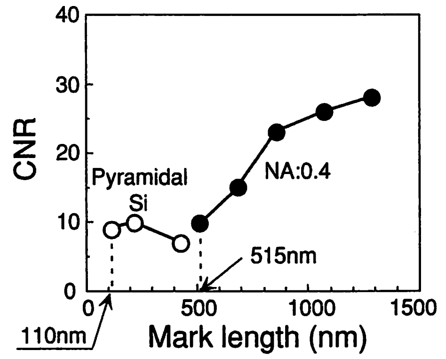

Fig. 36. Dependence of the CNR on mark length. Open circles: by an optical near field with the pyramidal silicon probe. Closed circles: by a propagating light focused with an object lens.

talline phase-changed marks beyond the diffraction limit were recorded and read out by an optical near field on the pyramidal silicon probe. The shortest mark length was 110 nm at $v_{\mathrm{CL}} = 0.43$ m/s, corresponding to a data transmission rate of 2.0 Mb/s. This is the first phase-change recording-readout with a contact slider. The constant CNR of the pyramidal silicon probe shown by the open circles in this figure is due to the small spot size of the optical near field for recording-readout and the narrow recorded mark width, which are as small as L_m of the pyramidal silicon probe. These results indicate that further increases in CNR and decreases in mark length are possible by means of tracking during readout.

The data transmission rate of 2.0 Mb/s can be increased to 200 Mb/s by parallel readout with all elements of the probe array. Further, it is expected that the recording density can be increased to as high as 1 Tb/in^2 by further improvements in the plasmon resonance effect at the pyramidal silicon probe tip.

VIII. SUMMARY

This paper reviewed nanophotonics, a novel optical nanotechnology utilizing local electromagnetic interactions between a small number of nanometric elements and an optical near field. Its potential for high integration beyond the diffraction limit of light can solve the technical problems of the future optical industry. A prototype nanophotonic integrated circuit was presented. All the devices in this circuit involve nanometric dots and wires, and an optical near field is used as a carrier to transmit the signal. As a key device, we proposed a nanophotonic switch based on optical near-field energy transfer between QDs.

Using a density matrix formulation, we theoretically showed that the optical near-field interaction is expressed as the sum of the Yukawa function, and estimated that the oscillation period of the nutation for cubic CuCl QDs is less than 100 ps at a 10-nm inter-QD distance, which is sufficiently short for the switching operation. In order to guarantee one-directional (i.e., irreversible) energy transfer between two resonant levels of QDs, we examined intrasublevel transitions due to phonon coupling by considering a simple two-QD plus phonon heat-bath system, and formulated the population dynamics of the system. As a result, we found that the state-filling time strongly depended on both the strength of the optical near-field interaction and the relaxation rate due to phonon coupling. To numerically evaluate CuCl QDs, the state-filling time was estimated as 22 ps, which is sufficiently short for the switching operation. Our analysis also showed that the state-filling time was almost independent of the temperature within the Born–Markov approximation. However, the finite temperature results in a residual population in the upper energy levels, which might degrade the aspect ratio of the ON–OFF signals of the switch. The optical near-field energy transfer to be used for the nanophotonic switch was experimentally studied using cubic CuCl QDs in a NaCl matrix as a test sample. Using near-field optical spectroscopy with a spatial resolution smaller than 50 nm in the near-UV region at 15 K, we observed the optical near-field energy transfer occurring from the lowest state of excitons in 4.6-nm QDs to the first dipole-forbidden excited state of excitons in 6.3-nm QDs.

To fabricate nanophotonic devices and ICs, we developed a new technique of chemical vapor deposition that uses an optical near field. Reviewing the experimental results of depositing nanometric Zn and Al patterns, we confirmed that this technique was sufficiently precise in controlling the size and position of the deposited material. Furthermore, we demonstrated a novel deposition scheme under nonresonant conditions and discussed its origin. In order to confirm the possibility of using a nanometric ZnO dot as a light emitter in a nanophotonic IC, we performed spatially and spectrally resolved PL imaging of individual ZnO nanocrystallites with a spatial resolution as high as 55 nm using a UV fiber probe. We observed the quantum size effect in ZnO nanocrystallites, i.e., the intensities of higher energy components of the PL spectrum increased as the spot size decreased.

To connect the nanophotonic IC with external photonic devices, we developed a nanometer-scale waveguide using a metal-coated silicon wedge structure. Propagation of the TM plasmon mode was observed using a near-field optical microscope. Illumination ($\lambda = 830$ nm) of the metal-coated silicon wedge ($W = 150$ nm) caused a TM plasmon mode with beam width of 150 nm and propagation length of 2.5 μm.

To improve the performance of a key device for nanophotonics, we realized an optical near-field probe with an extremely high throughput by introducing a pyramidal silicon structure and localized surface plasmon resonance at the metallized probe tip. Throughput as high as 2.5% was achieved for a spot size of 85 nm.

To apply nanophotonics to a high-density, high-speed optical memory system, we proposed and fabricated a novel contact slider with a pyramidal silicon probe array, with high homogeneity in the heights of the probes. We carried out phase-change recording/reading using this slider. Illuminating one element of the silicon probe array with a laser beam (λ = 830 nm), we demonstrated mark lengths as short as 110 nm.

ACKNOWLEDGMENT

The authors gratefully acknowledge fruitful discussion with Prof. H. Hori, Prof. N. Onishi, and Prof. I. Banno (Yamanashi University), Prof. K. Kitahara and Dr. A. Shojiguchi (International Christian University), Dr. H. Nejo (National Institute for Materials Science), Prof. H. Ito and Dr. M. Kourogi (Tokyo Institute of Technology). They authors are also grateful to Prof. Y. Masumoto and his co-workers (Tsukuba University) for valuable discussions. Further, the authors would like to thank Dr. S. Mitsugi and Prof. K. Goto (Tokai University) for their help with the numerical calculations.

REFERENCES

[1] M. Ohtsu, "Overview," in *Near-Field Optics: Principles and Applications*, X. Zhu and M. Ohtsu, Eds. Singapore: World Scientific, 2000, pp. 1–8.

[2] ——, "Near-field nano-optics toward nano/atom deposition," in *Tech. Dig. 18th Congr. Int. Commission for Optics, SPIE*, vol. 3749, 1999, pp. 478–479.

[3] ——, "Nanotechnology and nano/atom photonics by optical near field," *Proc. SPIE-Int. Soc. Opt. Eng.*, vol. 4416, pp. 1–13, 2001.

[4] N. Sakakura and Y. Masumoto, "Persistent spectral-hole-burning spectroscopy of CuCl quantum cubes," *Phys. Rev. B, Condens. Matter*, vol. 56, pp. 4051–4055, Aug. 1997.

[5] A. I. Ekimov, Al. L. Eflos, and A. A. Onushchenko, "Quantum size effect in semiconductor microcrystals," *Solid State Commun.*, vol. 56, pp. 921–924, 1985.

[6] T. Itoh, S. Yano, N. Katagiri, Y. Iwabuchi, C. Gourdon, and A. I. Ekimov, "Interface effect on the properties of confined excitons in CuCl microcrystals," *J. Lumin.*, vol. 60–61, pp. 396–399, 1994.

[7] Z. K. Tang, A. Yanase, T. Yasui, Y. Segawa, and K. Cho, "Optical selection rule and oscillator strength of confined exciton system in CuCl thin films," *Phys. Rev. Lett.*, vol. 71, pp. 1431–1434, Aug. 1993.

[8] K. Kobayashi, S. Sangu, H. Ito, and M. Ohtsu, "Near-field optical potential for a neutral atom," *Phys. Rev. A, Gen. Phys.*, vol. 63, pp. 0 138 061-1–9, Jan. 2001.

[9] M. Ohtsu, Ed., *Near-Field Nano/Atom Optics and Technology*. Heidelberg, Germany: Springer-Verlag, 1998, ch. 9.

[10] T. Kataoka, T. Tokizaki, and A. Nakamura, "Mesoscopic enhancement of optical nonlinearity in CuCl quantum dots: Giant-oscillator strength effect on confined excitons," *Phys. Rev. B, Condens. Matter*, vol. 48, pp. 2815–2818, July 1993.

[11] T. Suzuki, T. Mitsuyu, K. Nishi, H. Ohyama, T. Tomimasu, S. Noda, T. Asano, and A. Sasaki, "Observation of ultrafast all-optical modulation based on intersubband transition in n-doped quantum wells by using free electron laser," *Appl. Phys. Lett.*, vol. 69, pp. 4136–4138, Dec. 1996.

[12] T. Kawazoe, K. Kobayashi, J. Lim, Y. Narita, and M. Ohtsu, "Direct observation of optically forbidden energy transfer between CuCl quantum cubes via near-field optical spectroscopy," *Phys. Rev. Lett.*, vol. 88, pp. 067 404-1–4, Feb. 2002.

[13] K. Kobayashi and M. Ohtsu, "Quantum theoretical approach to a near-field optical system," *J. Microsc.*, vol. 194, pp. 249–254, May/June 1999.

[14] ——, "Quantum theory and virtual photon model of near field optics," *Proc. SPIE-Int. Soc. Opt. Eng.*, vol. 3791, pp. 10–20, 1999.

[15] K. Kobayashi, S. Sangu, H. Ito, and M. Ohtsu, "Effective probe-sample interaction: Toward atom deflection and manipulation," in *Near-Field Optics: Principles and Applications*, X. Zhu and M. Ohtsu, Eds. Singapore: World Scientific, 2000, pp. 82–88.

[16] S. Sangu, K. Kobayashi, and M. Ohtsu, "Optical near fields as photon-matter interacting systems," *J. Microsc.*, vol. 202, pp. 278–285, May 2001.

[17] J. J. Hopfield, "Theory of the contribution of excitons to the complex dielectric constant of crystals," *Phys. Rev.*, vol. 112, pp. 1555–1567, Dec. 1958.

[18] M. Orrit, C. Aslangul, and P. Kottis, "Quantum-mechanical-model calculations of radiative properties of a molecular crystal. I. Polaritons and abnormal decays of excitons in one- and two-dimensional systems," *Phys. Rev. B, Condens. Matter*, vol. 25, pp. 7263–7280, June 1982.

[19] J. Knoester and S. Mukamel, "Intermolecular forces, spontaneous emission, and superradiance in a dielectric medium: Polariton-mediated interactions," *Phys. Rev. A, Gen. Phys.*, vol. 40, pp. 7065–7080, Dec. 1989.

[20] B. Huttner and S. M. Barnett, "Quantization of the electromagnetic field in dielectrics," *Phys. Rev. A, Gen. Phys.*, vol. 46, pp. 4306–4322, Oct. 1992.

[21] G. Juzeliūnas and D. L. Andrews, "Quantum electrodynamics of resonant energy transfer in condensed matter," *Phys. Rev. B, Condens. Matter*, vol. 49, pp. 8751–8763, Apr. 1994.

[22] C. Cohen-Tannoudji, J. Dupont-Roc, and G. Grynberg, *Photons and Atoms*. New York: Wiley, 1989.

[23] D. P. Craig and T. Thirunamachandran, *Molecular Quantum Electrodynamics*. London, U.K.: Academic, 1984.

[24] H. Haken, *Light*. Amsterdam, The Netherlands: North-Holland, 1986, vol. 1.

[25] L. Mandel and E. Wolf, *Optical Coherence and Quantum Optics*. Cambridge, U.K.: Cambridge Univ. Press, 1995.

[26] H. J. Carmichael, *Statistical Methods in Quantum Optics 1*. Berlin, Germany: Springer-Verlag, 1999.

[27] V. May and O. Kühn, *Charge and Energy Transfer Dynamics in Molecular Systems*. Berlin, Germany: Wiley-VCH, 2000.

[28] H. Hyuga and H. Ohtsubo, "Breakdown of the Siegert theorem and the many-body charge density operators," *Nucl. Phys. A*, vol. 294, pp. 348–356, 1978.

[29] R. Zwanzig, "On the identity of three generalized master equations," *Physica*, vol. 30, pp. 1109–1123, 1964.

[30] H. Mori, "Transport, collective motion, and Brownian motion," *Prog. Theor. Phys.*, vol. 33, pp. 423–455, 1965.

[31] C. R. Willis and R. H. Picard, "Time-dependent projection-operator approach to master equations for coupled systems," *Phys. Rev. A, Gen. Phys.*, vol. 9, pp. 1343–1358, Mar. 1974.

[32] P. Fulde, *Electron Correlations in Molecules and Solids*, 3rd ed. Berlin, Germany: Springer-Verlag, 1995.

[33] E. Hanamura, "Very large optical nonlinearity of semiconductor microcrystallites," *Phys. Rev., B Condens. Matter*, vol. 37, pp. 1273–1279, Jan. 1988.

[34] Y. Masumoto, M. Ikezawa, B.-R. Hyun, K. Takemoto, and M. Furuya, "Homogeneous width of confined excitons in quantum dots at very low temperatures," *Phys. Stat. Sol. B*, vol. 224, no. 3, pp. 613–619, 2001.

[35] K. Lindenberg and B. West, "Statistical properties of quantum systems: The linear oscillator," *Phys. Rev. A, Gen. Phys.*, vol. 30, pp. 568–582, July 1984.

[36] K. Mukai, S. Abe, and H. Sumi, "Theory of rapid excitation-energy transfer from B800 to optically-forbidden exciton state of B850 in the antenna system LH2 of photosynthetic purple bacteria," *J. Phys. Chem. B*, vol. 103, pp. 6096–6102, Mar. 1999.

[37] V. V. Polonski, Y. Yamamoto, M. Kourogi, H. Fukuda, and M. Ohtsu, "Nanometric patterning of zinc by optical near-field photochemical vapor deposition," *J. Microsc.*, vol. 194, pp. 545–551, May/June 1999.

[38] D. Leonard, M. Krishnamurthy, C. M. Reaves, S. P. Denbaars, and P. M. Petroff, "Direct formation of quantum-sized dots from uniform coherent islands of InGaAs on GaAs surfaces," *Appl. Phys. Lett.*, vol. 63, pp. 3203–3205, Dec. 1993.

[39] T. Tsutsui, K. Kawasaki, M. Mochizuki, and T. Matsubara, "Site controlled metal and semiconductor quantum dots on epitaxial fluoride films," *Microelectron. Eng.*, vol. 47, pp. 135–137, June 1999.

[40] S. Kohmoto, H. Nakamura, T. Ishikawa, and K. Asakawa, "Site-controlled self-organization of individual InAs quantum dots by scanning tunneling probe-assisted nanolithography," *Appl. Phys. Lett.*, vol. 75, pp. 3488–3490, Nov. 1999.

[41] E. Kuramochi, J. Temmyo, T. Tamamura, and H. Kamada, "Perfect spatial ordering of self-organized InGaAs/AlGaAs box-like structure array on GaAs (311)B substrate with silicon nitride dot array," *Appl. Phys. Lett.*, vol. 71, pp. 1655–1657, Sept. 1997.

[42] R. Wiesendanger, "Fabrication of nanometer structures using STM," *Appl. Surf. Sci.*, vol. 54, pp. 271–277, Jan. 1992.

[43] V. V. Polonski, Y. Yamamoto, J. D. White, M. Kourogi, and M. Ohtsu, "Vacuum Shear-force microscopy application to high resolution work," *Jpn. J. Appl. Phys.*, pt. 2, vol. 38, pp. L826–L829, July 1999.

[44] Y. Yamamoto, M. Kourogi, M. Ohtsu, V. Polonski, and G. H. Lee, "Fabrication of nanometric Zinc pattern with photodissociated gas-phase diethylzinc by optical near-field," *Appl. Phys. Lett.*, vol. 76, pp. 2173–2175, Apr. 2000.

[45] G. H. Lee, Y. Yamamoto, M. Kourogi, and M. Ohtsu, "Fabrication of ZnO nanostructure using near-field optical technique," *Proc. SPIE–Int. Soc. Opt. Eng.*, vol. 3791, pp. 132–139, 1999.

[46] T. Kawazoe, Y. Yamamoto, and M. Ohtsu, "Fabrication of a nanometric Zn dot by nonresonant near-field optical chemical vapor deposition," *Appl. Phys. Lett.*, vol. 79, pp. 1184–1186, Aug. 2001.

[47] R. L. Jacson, "Vibrational energy of the monoalkyl zinc product formed in the photodissociation of dimethyl zinc, diethyl zinc, and dipropyl zinc," *J. Chem. Phys.*, vol. 96, pp. 5938–5951, Apr. 1992.

[48] H. Okabe, *Photochemistry*. New York: Wiley, 1978.

[49] M. Yoshimoto, T. Maeda, T. Ohnishi, H. Koinuma, O. Ishiyama, M. Shinohara, M. Kubo, R. Miura, and A. Miyamoto, "Atomic-scale formation of ultrasmooth surfaces on sapphire substrates for high-quality thin film fabrication," *Appl. Phys. Lett.*, vol. 67, pp. 2615–2617, Nov. 1995.

[50] M. Ohtsu, K. Kobayashi, H. Ito, and G. Lee, "Nanofabrication and atom manipulation by optical near-field and relevant quantum optical theory," *Proc. IEEE*, vol. 88, pp. 1499–1518, Sept. 2000.

[51] M. Shimizu, H. Kamei, M. Tanizawa, T. Shiosaki, and A. Kawabata, "Low temperature growth of ZnO film by photo-MOCVD," *J. Cryst. Growth*, vol. 89, pp. 365–370, 1988.

[52] T. Yatsui, T. Shimizu, Y. Yamamoto, M. Kourogi, G. H. Lee, and M. Ohtsu, "Near-field ultraviolet photoluminescence spectroscopy for evaluating the crystallinity of polycrystalline zinc oxide," *Appl. Phys. Lett.*, vol. 79, no. 15, pp. 2369–2371, 2001.

[53] T. Yatsui, T. Kawazoe, T. Shimizu, Y. Yamamoto, M. Ueda, M. Kourogi, G. H. Lee, and M. Ohtsu, "Observation of size-dependent features in the photoluminescence of zinc oxide nanocrystallites by near-field ultraviolet spectroscopy," *Appl. Phys. Lett.*, vol. 80, no. 8, pp. 1444–1446, 2002.

[54] Z. K. Tang, G. K. L. Wong, P. Yu, M. Kawasaki, A. Ohtomo, H. Koinuma, and Y. Segawa, "Room-temperature ultraviolet laser emission from self-assembled ZnO microcrystallite thin films," *Appl. Phys. Lett.*, vol. 72, no. 25, pp. 3270–3272, 1998.

[55] S. Cho, J. Ma, Y. Kim, Y. Sun, G. Wong, and J. B. Ketterson, "Photoluminescence and ultraviolet lasing of polycrystalline ZnO thin films prepared by the oxidation of the metallic Zn," *Appl. Phys. Lett.*, vol. 75, no. 18, pp. 2761–2763, 1999.

[56] R. R. Krchnavek, H. H. Gilgenm, J. C. Chenm, P. S. Shaw, T. J. Licata, and R. M. Osgood, "Photodeposition rates of metal from metal alkyls," *J. Vac. Sci. Technol. B, Microelectron. Process. Phenom.*, vol. 5, pp. 20–26, 1987.

[57] Y. Yamamoto, T. Kawazoe, G. H. Lee, T. Shimizu, M. Kourogi, and M. Ohtsu, "In-situ lateral fabrication of Zinc and Aluminum nanodots by near field optical chemical vapor deposition," in *Tech. Dig. Pacific Rim Conf. Lasers and Electro-Optics*, vol. 4, 2001, pp. I520–I521.

[58] Y. Chen, D. M. Bagnall, H. J. Ko, K. T. Park, H. Hiraga, Z. Zhu, and T. Yao, "Plasma assisted molecular beam epitaxy of ZnO on *c*-plane sapphire: Growth and characterization," *J. Appl. Phys.*, vol. 87, pp. 3912–3918, 1998.

[59] J. Takahara, S. Yamagishi, H. Taki, A. Morimoto, and T. Kobayashi, "Guiding of a one-dimensional optical beam with nanometer diameter," *Opt. Lett.*, vol. 22, no. 7, pp. 475–477, 1997.

[60] T. Yatsui, M. Kourogi, and M. Ohtsu, "Plasmon waveguide for optical far/near-field conversion," *Appl. Phys. Lett.*, vol. 79, no. 27, pp. 4583–4585, 2001.

[61] D. Marcuse, *Light Transmission Optics*. New York: Van Nostrand, 1972, ch. IV.

[62] U. C. Fischer, J. Koglin, and H. Fuchs, "The tetrahedral tip as a probe for scanning near-field optical microscopy at 30 nm resolution," *J. Microsc.*, vol. 176, pp. 231–237, 1994.

[63] T. Yatsui, M. Kourogi, and M. Ohtsu, "Highly efficient excitation of optical near-field on an apertured fiber probe with an asymmetric structure," *Appl. Phys. Lett.*, vol. 71, no. 13, pp. 1756–1758, 1997.

[64] T. R. Anthony, "Dielectric isolation of silicon by anodic bonding," *J. Appl. Phys.*, vol. 58, pp. 1240–1247, 1998.

[65] B. Puers and W. Sansen, "Compensation structures for convex corner micromachining in silicon," *Sens. Actuators*, vol. A21-A23, pp. 1036–1041, 1990.

[66] T. Yatsui, M. Kourogi, and M. Ohtsu, "Increasing throughput of a near-field optical fiber probe over 1000 times by the use of a triple-tapered structure," *Appl. Phys. Lett.*, vol. 73, no. 15, pp. 2090–2092, 1998.

[67] M. Ohtsu, Ed., *Near-Field Nano/Atom Optics and Technology*. Tokyo, Japan: Springer-Verlag, 1998, ch. 3.

[68] W. Noell, M. Abraham, K. Mayr, A. Ruf, J. Barenz, O. Hollricher, O. Marti, and P. Güthner, "Micromachined aperture probe tip for multifunctional scanning probe microscopy," *Appl. Phys. Lett.*, vol. 70, no. 10, pp. 1236–1238, 1997.

[69] S. Heisig, H.-U. Danzebrink, A. Leyk, W. Mertin, S. Münster, and E. Oesterschulze, "Monolithic gallium arsenide cantilever for scanning near-field microscopy," *Ultramicroscopy*, vol. 71, no. 1, pp. 99–105, 1998.

[70] H.-U. Danzebrink, A. Castiaux, C. Girard, X. Bouju, and G. Wilkening, "Transmission scanning near-field optical microscopy with uncoated silicon tips," *Ultramicroscopy*, vol. 71, no. 1, pp. 371–377, 1998.

[71] R. Eckert, J. M. Freyland, H. Gersen, H. Heinzelmann, G. Schürmann, W. Noell, U. Staufer, and N. F. de Rooji, "Near-field fluorescence imaging with 32 nm resolution based on microfabricated cantilevered probes," *Appl. Phys. Lett.*, vol. 77, no. 23, pp. 3695–3697, 2000.

[72] S. Mitsugi, Y. J. Kim, and K. Goto, "Finite-difference-time-domain analysis for electro-magnetic field distribution on near-field optical recording probe head," *Opt. Rev.*, vol. 8, pp. 120–125, 2001.

[73] E. D. Palik, Ed., *Handbook of Optical Constants of Solids*. New York: Academic, 1985.

[74] H. Raether, Ed., *Surface Plasmons*. Berlin, Germany: Springer-Verlag, 1988.

[75] G. T. Boyd, T. Rasing, J. R. R. Leite, and Y. R. Shen, "Local-field enhancement on rough surfaces of metals, semimetals, and semiconductors with the use of optical second-harmonic generation," *Phys. Rev. B, Condens. Matter*, vol. 30, pp. 519–526, July 1984.

[76] D. A. Fletcher, K. B. Crozier, C. F. Quate, G. S. Kino, and K. E. Goodson, "Near-field infrared imaging with a microfabricated solid immersion lens," *Appl. Phys. Lett.*, vol. 77, no. 14, pp. 2109–2111, 2000.

[77] J. Tominaga, T. Nakano, and N. Atoda, "An approach for recording and readout beyond the diffraction limit with an Sb thin film," *Appl. Phys. Lett.*, vol. 73, no. 15, pp. 2078–2080, 1998.

[78] H. Yoshikawa, Y. Andoh, M. Yamamoto, K. Fukuzawa, T. Tamamura, and T. Ohkubo, "7.5-MHz data-transfer rate with a planar aperture mounted upon a near-field optical slider," *Opt. Lett.*, vol. 25, no. 1, pp. 67–69, 2000.

[79] T. Yatsui, M. Kourogi, K. Tsutsui, J. Takahashi, and M. Ohtsu, "High density/speed optical near field recording/reading with a pyramidal silicon probe on a contact slider," *Opt. Lett.*, vol. 25, no. 17, pp. 1279–1281, 2000.

[80] Y. J. Kim, K. Kurihara, K. Suzuki, M. Nomura, S. Mitsugi, M. Chiba, and K. Goto, "Fabrication of micro-pyramidal probe array with aperture for near-field optical memory applications," *Jpn. J. Appl. Phys.*, vol. 39, no. 3B, pp. 1538–1541, 2000.

[81] T. Yatsui, M. Kourogi, K. Tsutsui, J. Takahashi, and M. Ohtsu, "Sub-wavelength-sized phase-change recording with a silicon planar apertured probe," *Proc. SPIE–Int. Soc. Opt. Eng.*, vol. 3791, pp. 76–84, 1999.

[82] D. W. Pohl, "Some thoughts about scanning probe microscopy, micromechanics, and storage," *IBM J. Res. Dev.*, vol. 39, pp. 701–711, 1995.

[83] C. S. Bhatia and A. K. Menon, *Tribology of Contact/Near-Contact Recording for Ultra High Density Magnetic Storage*. New York: Amer. Soc. Mech. Eng., 1996, vol. 6.

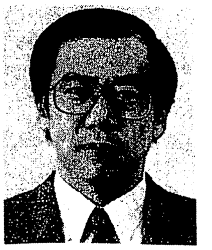

Motoichi Ohtsu (M'88–SM'90) received the B.E., M.E., and Dr. E. degrees in electronics engineering from the Tokyo Institute of Technology, Tokyo, Japan, in 1973, 1975, and 1978, respectively.

In 1978, he was appointed a Research Associate, and in 1982, he became an Associate Professor at the Tokyo Institute of Technology. From 1986 to 1987, while on leave from the Tokyo Institute of Technology, he joined the Crawford Hill Laboratory, AT&T Bell Laboratories, Holmdel, NJ. In 1991, he became a Professor at the Tokyo Institute of Technology. Since 1993, he has been concurrently the Leader of the "Photon Control" project of the Kanagawa Academy of Science and Technology, Kanagawa, Japan. Since 1998, he has been concurrently the Leader of the "Localized Photon" project of Exploratory Research for Advanced Technology (ERATO), Japan Science and Technology Corporation. He has authored more than 320 papers and holds 87 patents. He is the author and coauthor of 39 books, including seven in English, titled *Highly Coherent Semiconductor Lasers* (Norwood, MA: Artech House, 1991), *Coherent Quantum Optics and Technology* (Dordrecht, The Netherlands: Kluwer, 1993), *Frequency Control of Semiconductor Lasers* (New York: Wiley/Interscience, 1996), *Near-Field Nano/Atom Optics and Technology* (Berlin, Germany: Springer Verlag, 1998), *Near-Field Nano-Optics* (New York: Kluwer/Plenum, 1999), *Optical and Electronic Properties of Nano-matters* (Dordrecht, The Netherlands: Kluwer, 2001), and *Progress in Nano Electro-Optics* (Berlin, Germany: Springer-Verlag, 2002).

Dr. Ohtsu is a member of the Japan Society of Applied Physics, the Institute of Electronics, Information and Communication Engineering of Japan, the Institute of Electrical Engineering of Japan, the Optical Society of America, and the American Physical Society. In 1999, he was Vice-President of the IEEE/LEOS Japan Chapter, and in 2000, he was appointed as the President. From 2000, he has been an Executive Director of the Japan Society of Applied Physics. He served as a Technical Program Co-chair for the 4th Pacific Rim Conference on Lasers and Electro-Optics (CLEO/PR01), 2001. He has been a tutorial lecturer of the SPIE and the Optical Society of America. His main fields of interests are nanophotonics and atom-photonics. He has been awarded ten prizes from academic institutions, including the Issac Koga Gold Medal of International Union of Radio Science (URSI) in 1984, the Japan IBM Science Award in 1988, two awards from the Japan Society of Applied Physics in 1982 and 1990, and the Inoue Science Foundation Award in 1999.

Kiyoshi Kobayashi (M'94) was born in Okayama, Japan, on November 25, 1953. He received the D.S. degree in physics from the University of Tsukuba, Tsukuba, Japan, in 1982.

After graduation, he joined IBM Japan as a Research Staff Member at Tokyo Research Laboratory, Tokyo, Japan. Since 1998, he has been the theoretical group leader of the "Localized Photon" project for the Exploratory Research for Advanced Technology (ERATO) at the Japan Science and Technology Corporation, Tokyo. His main fields of interest are theory on near field optics and its application to nano/atom photonics.

Dr. Kobayashi is a member of the Physical Society of Japan, the Japan Society of Applied Physics, the American Physical Society, and the Optical Society of America.

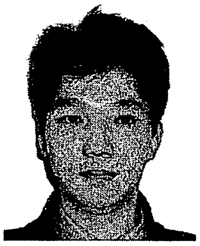

Tadashi Kawazoe was born in Kochi, Japan, on April 5, 1967. He received the B.E., M.E., and Ph.D. degrees in physics from University of Tsukuba, Tsukuba, Japan, in 1990, 1993, and 1996, respectively.

Since 1991, he has studied spin relaxation in semiconductor quantum wells and optical nonlinearities in semiconductor quantum dots at the Institute of Physics, University of Tsukuba. In 1996, he joined the faculty of Engineering, Yamagata University, Yamagata, Japan, as a Research Associate, engaged in research on nonlinear optical materials and devices. Since April 2000, he has been with Japan Science and Technology Corporation, Tokyo, Japan. His current research interests are in the areas of optical properties of nano materials, optical near field, and nanophotonic devices.

Dr. Kawazoe is a member of the Japan Society of Applied Physics.

Suguru Sangu was born in Hokkaido, Japan, on November 10, 1971. He received the B.E. degree from the Muroran Institute of Technology, Hokkaido, Japan, in 1994, and the M.E. and Ph.D. degrees in electronics and information engineering from Hokkaido University, Hokkaido, Japan, in 1996 and 1999, respectively.

Since 1999, he has been a Researcher of the "Localized Photon" project for the Exploratory Research for Advanced Technology (ERATO) at the Japan Science and Technology Corporation, Tokyo, Japan. His current research interests are the theory on near-field optics and its application to nano-photonics.

Dr. Sangu is a member of the Japan Society of Applied Physics.

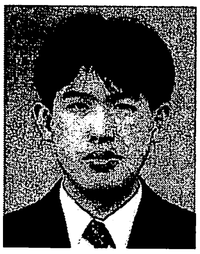

Takashi Yatsui was born in Tokyo, Japan, on January 21, 1972. He received the B.E. degree from Keio University, Tokyo, Japan, in 1995, and M.E. and D.E. degrees from the Tokyo Institute of Technology, Tokyo, Japan, in 1997 and 2000, respectively.

From 1999 to 2000, he was a Research Fellow of the Japan Society for the Promotion of Science. Since 2000, he has been a Researcher at the Japan Science and Technology Corporation, Tokyo, Japan. His current research interests include nanofabrication using optical near-field.

Dr. Yatsui is a member of the Japan Society of Applied Physics. He received the First Prize in Paper Contest from IEEE Student Branch at Tokyo Institute of Technology in 1998, the Excellent Research Presentation Award from the Japan Society of Applied Physics in 2000, and the Tejima Doctoral Dissertation Award from the Tejima Foundation in 2001.

WHAT IS NANOPHOTONICS?

M. Ohtsu*
Interdisciplinary Graduate School of Science and Technology, Tokyo Institute of Technology
4259 Nagatsuta-cho, Midori-ku, Yokohama, Kanagawa 2265-8502, Japan
E-mail: ohtsu@ae.titech.ac.jp

This talk reviews recent progress in nanophotonics which was proposed by myself several years ago in order to open a new field of optical science and technology beyond the diffraction limit of light. Nanophotonics is defined as a technology that utilizes local electromagnetic interactions between a few nanometric element and an optical near field. Since an optical near field is free from the diffraction of light due to its size-dependent localization and size-dependent resonance features, nanophotonics enables fabrication, operation, and integration of nanometric devices. Thus, this technology can solve the technical problems that are faced by the future optical industry. They are (1) increased integration of photonic devices if the data transmission rates of optical fiber transmission systems are to reach as high as 10Tb/s by the year 2015, (2) sub-100nm width pattern fabrication by photo-lithography for increasing the DRAM capacity by the year 2010, and (3) recording and readout of 25 nm pit pattern for realizing 1 Tb/in^2 recording density of the optical memory systems by the year 2010.

The primary advantage of nanophotonics is its capacity to realize novel functions based on local electromagnetic interaction. It should be noted that some of the conventional concepts of wave-optics, such as interference, are no longer essential in nanophotonics. Instead, concepts of surface elementary excitation and nano-fabrication technology are essential.

Novel nanophotonic devices and their integration are proposed and theoretical/experimental studies on their functions are reviewed. Chemical vapor deposition by optical near field is also demonstrated to deposit a variety of nanometric materials on a substrate.

(*) also with ERATO Localized Photon Project, Japan Science and Technology Corporation, 687-1 Tsuruma, Machida-shi, Tokyo 194-0004, Japan

QMD3

Nanophotonic Switching using CuCl Quantum Cubes

T. Kawazoe[1], **K. Kobayashi**[1], **S. Sangu**[1], **and M. Ohtsu**[1, 2]
[1] Exploratory Research for Advanced Technology (ERATO), Japan Science and
Technology Corporation (JST), 687-1 Tsuruma, Machida, Tokyo 194-0004, Japan
Tel:+81-42-788-6039, Fax:+81-42-788-6031, e-mail: kawazoe@ohtsu.jst.go.jp

[2] Interdisciplinary Graduate School of Science and Engineering,
Tokyo Institute of Technology, 4259 Nagatsuta, Midori-ku, Yokohama 226-8502, Japan

Abstract: We report the first demonstration of repeated near-field optical switching using cubic CuCl quantum dots by time-resolved optical near-field measurement. Its figure of merit is 10~100 times greater than that of conventional photonic switches.

OCIS codes: (230.1150) All-optical device; (999.9999) Nanometric Optical Control; (999.9999) Nanophotonic devices

Coupled quantum dot (QD) system have unique properties that distinguish them from single QD system. The optical near-field interaction [1] is interesting, as it can govern the coupling strength of QDs. Recently, we observed an optically forbidden energy transfer between neighboring cubic CuCl QDs, *i.e.*, quantum cubes (QCs), via the optical near field [2]. Controlling this nanometric energy transfer enables nanophotonic switching [3].

Figure 1 shows the schematic mechanism of a nanophotonic switch that we propose to realize ultra highly integrated switch array devices for future high-speed, large-capacity optical communication system. Assuming three QCs with side lengths L (input cube), $\sqrt{2}L$ (output cube), and $2L$ (control cube), energy levels (2,2,2) in the control cube, (2,1,1) in the output cube, and (1,1,1) in the control cube resonate with each other. Here, (n_x, n_y, n_z) refers to the quantum numbers for the sublevels in the QCs. When the separation of the cubes is less than 30 nm, the resonance levels in each cube are coupled with the optical near field. Consequently, the energy transfer occurs among the QCs. Without a control signal, the input signal to the control cube relaxes, and the output signal is obstructed (OFF state). With a control signal, energy transfer to the control cube is blocked by the filling of the control cube, and the input signal then goes through the output cube giving an output signal (ON state).

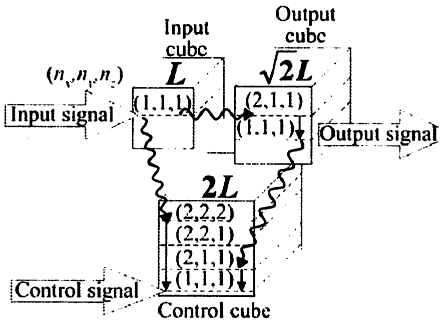

Fig.1. Schematic mechanism of the proposed nanophotonic switch using quantum cubes. The arrows input, output, and control refer to the switching system interface.

We used the CuCl QCs embedded in a NaCl matrix as test samples to verify the nanophotonic switching operation, as CuCl QCs offer the similar discrete energy levels to the exciton described in Fig.1 [4]. Figures 2 (a) and (b) show the spatial distribution of an output signal intensity in the OFF, *i.e.*, with an input signal only, and ON, *i.e.*, with input and control signal, state respectively using a near-field microscope at 15 K. The insets in Fig.2 are schematic drawings of the existing QC *trio* used for the switching, which was confirmed from the luminescence spectrum. The QC sizes of the *trio*, obtained from the wavelengths of their luminescence, were 3.5, 4.6, and 6.3 nm, and the effective size ratio, considering with the exciton Bohr radius, was $1:\sqrt{2}:2$. Therefore, they satisfy the switching condition shown in Fig.1. Here their separations of QCs (drawings in Fig.2) were theoretically estimated from the time-resolved measurement explained in the next paragraph.

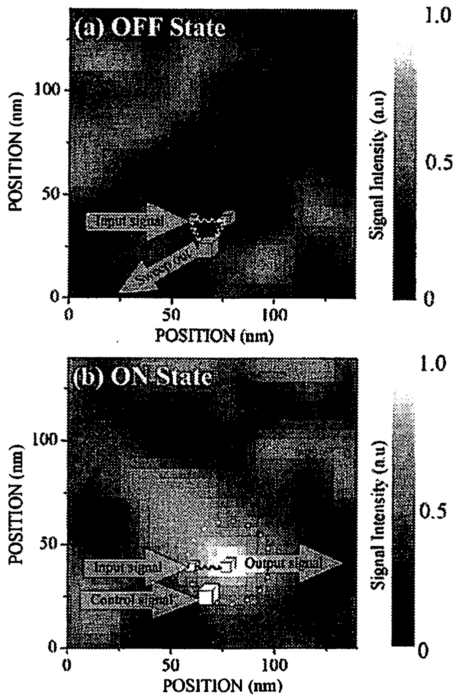

Fig.2. Spatial distributions of the output signal from the nanophotonic switch in the OFF (a) and ON (b) states, measured using a near-field microscope.

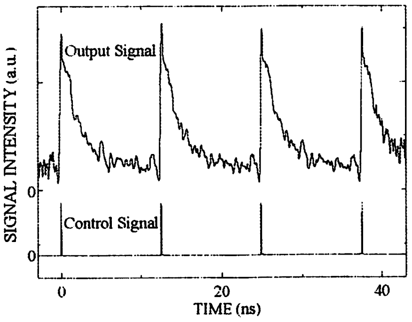

Fig.3. Temporal evolutions of the output (upper) and control pulse (lower) signals from the nanophotonic switch located at the dotted circle in Fig.2 (b).

The dynamic properties of the switch were measured using a time correlation single photon counting method. As a pulse-control-light source, 385-nm SHG of a mode locked Ti-sapphire laser was used. The repetition rate and the pulse duration of the laser were 80 MHz and 10 ps, respectively. The temporal resolution of the experiment was 15 ps. Figure 3 shows the temporal evolution of the controlled output and control pulse signals from the QC *trio*. The output signal synchronously rises within less than 100 ps of the control pulse, and this nanophotonic switch can operate at a few hundred MHz considering the decay time of the output signal. The separations among the QCs can be estimated from the rise time. The ON-OFF ratio is about 10, which is sufficient for an all-optical switch. The advantages of this nanophotonic switch are its small size and high-density integration ability based on the locality of the optical near-filed. Its figure of merit, $F=C/(V\cdot t_{sw}\cdot P_{sw})$, as an optical switch is 10~100 times greater than all other optical switches, where C, V, t_{sw}, and P_{sw} are the ON-OFF ratio, volume, switching time, and switching energy. We consider this nanometric optical switching system is suitable to ultra high-density nanophotonic ICs.

References

1. K. Kobayashi, S. Sangu, H. Ito, and M. Ohtsu, Phys. Rev. A **63**, 013806 (2000)
2. T. Kawazoe, K. Kobayashi, J. Lim, Y. Narita and M. Ohtsu, Phys. Rev. Lett. **88**, 6, 067404 (2002).
3. M. Ohtsu, K. Kobayashi, T. Kawazoe, S. Sangu, and T. Yatsui, IEEE J. Sel. Top. Quant. Electron, **8** 839 (2002).
4. N. Sakakura and Y. Masumoto, Phys. Rev. B **56**, 4051 (1997).

Ultraviolet-emission and lasing from ZnO nanostructures fabricated by a simple method involving the low-temperature oxidation of metallic Zn

T.-W. Kim[1], T. Kawazoe[1], S. Yamazaki[2], J. Lim[2], T. Yatsui[1], and M. Ohtsu[1,2]
[1] Japan Science and Technology Corporation, 687-1, Tsuruma, Machida, Tokyo194-0004, Japan
[2] Interdisciplinary Graduate School of Science and Engineering, Tokyo Institute of Technology, Yokohama, Kanagawa 226-8502, Japan
Email: twkim90@ohtsu.jst.go.jp

Abstract: we report deep-level emission-free UV emission and lasing from ZnO nanostructures fabricated via a simple method involving the low-temperature oxidation of metallic Zn.

OCIS codes: (250.0250) Optoelectronics; (160.3380) Laser materials; (250.5230) Photoluminescence; (260.7190) Ultraviolet

The nanostructures of wide-band gap semiconductors such as GaN and ZnO, have attracted much attention for applications to nanophotonic devices in the ultraviolet (UV) region [1,2]. In particular, ZnO is a promising material for fabricating the devices that emit UV light at room temperature (RT) at high efficient via an exciton recombination process. However, most of the ZnO nanostructures previously reported have suffered from deep-level emissions, which have been attributed to intrinsic defects such as ionized oxygen vacancies or interstitial Zn [3,4]. Such deep-level emissions deteriorate excitonic emission at the near band edge and lead to low efficiency UV light emission. In this paper, we report deep-level emission-free UV emission and lasing from ZnO nanostructures fabricated using a simple method that involves low-temperature oxidation of metallic Zn.

To fabricate ZnO nanostructures, i.e., dots or crystallites, we used a simple method of fabrication, in which metallic Zn nanodots prepared on CaF_2 (111) substrates by thermal evaporation of pure metallic Zn powder (99.999-%) were transformed into ZnO nanodots by thermal oxidation at 380 °C for 6 h.

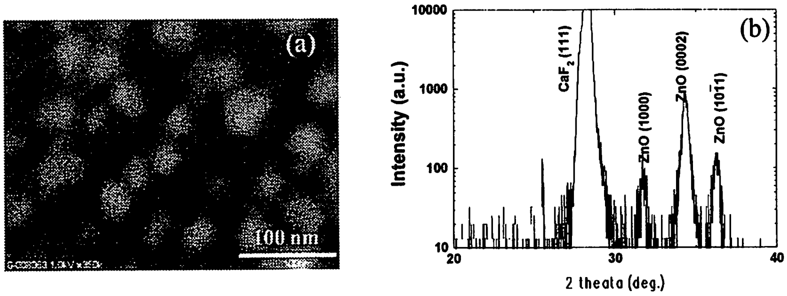

Fig. 1. SEM image (a) and XRD pattern (b) of ZnO nanodots fabricated by thermal oxidation at 380 °C, for 6 h.

Scanning electron microscopy (SEM) images showed ZnO nanodots with diameters from 10 nm to 60 nm (Fig. 1(a)). X-ray diffraction (XRD) measurements revealed the ZnO diffraction peaks and the mean diameter of the ZnO nanodots determined using Scherrer's formula was ca. 30 nm (Fig. 1 (b)). RT photoluminescence (PL) measurements using a cw He-Cd laser (325 nm) showed a strong peak at 3.28 eV, which was ascribed to free excition recombination. In contrast, the deep-level emission intensity around 2.5 eV was negligibly weak, i.e., two orders of magnitude lower than that of the near-band emission (Fig. 2). The results suggest that sufficient oxygen is able to diffuse into the metallic Zn nanodots, even at temperature as low as 380 °C, allowing fabrication of pure ZnO nanodots with extremely low concentrations of the defect associated with the deep-level emission [5]. Furthermore, we optically pumped polycrystalline ZnO films composed of ZnO nanocrystallites fabricated using the same process. Figure 3 shows the PL spectra of a ZnO polycrystalline film optically pumped at RT by 5th harmonic generation (213 nm) of a Nd:YAG laser. At a low excitation energy (0.022 mJ), a single broad spontaneous-emission peak of ZnO was observed at 3.246 eV (Fig. 3 (a)). As the excitation intensity was increased, a sharp peak appeared at around 3.12 eV (Fig. 3 (a), (b)). This sharp peak is a typical characteristic of laser action.

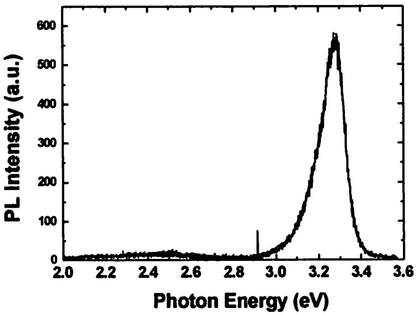

Fig. 2. PL spectrum of ZnO nanodots measured at room temperature using a cw He-Cd laser (325 nm).

The threshold intensity for lasing was estimated at ~7 MW/cm^2 from a plot of luminescence intensity versus pumping power. Recently, Cao *et al.* demonstrated laser action in self-formed cavities via scattering in ZnO polycrystalline films [6].

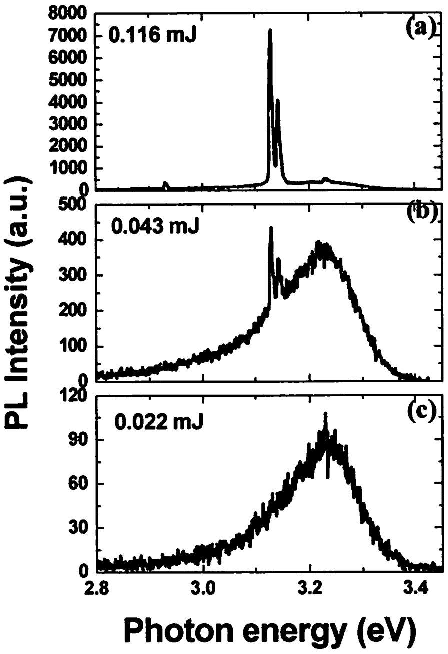

Fig. 3. PL spectra of ZnO polycrystalline films composed of ZnO nanocrystallites measured at room temperature using 5th harmonic generation (213 nm) of a Nd:YAG laser.

In conclusion, we demonstrated deep-level emission-free UV emission and lasing from ZnO nanostructures fabricated using a low temperature oxidation process. We believe that this process is a simple, promising approach for fabricating ZnO nanodots of sufficiently high quality for use as nanoscale UV light emitters and an alternative UV laser source; both are key components in photonic devices.

References

[1]. M. H. Huang *et al.*, "Room-temperature ultraviolet nanowires nanolasers", Science **292**, 1897-1899 (2001)
[2]. H. M. Kim *et al.*, "Growth of GaN nanorods by a hydride vapor phase epitaxy method", Adv. Mater. **14**, 991-993 (2002)
[3]. Y. B. Li *et al.*, "ZnO nanobelts grown Si substrate", Appl. Phys. Lett. **81**, 144-146 (2002)
[4]. M. H. Huang *et al.*, "Catalytic growth of zinc oxide nanowires by vapor transport", Adv. Mater. **13**, 113-115 (2002)
[5]. K. Vanheusden *et al.*, "Mechanism behind green photoluminescence in ZnO phosphor powders", J. App. Phys.**79**, 7983-7990 (1996)
[6]. H. Cao *et al.*, "Ultraviolet lasing in resonators formed by scattering in semiconductor polycrystalline films", Appl. Phys. Lett.**73**, 3656-3658 (1998)

QTuK6

A nanophotonic switch: transient dynamics and switching operation

Suguru Sangu,[1] Kiyoshi Kobayashi,[1] Tadashi Kawazoe,[1]
Akira Shojiguchi,[1] and Motoichi Ohtsu[1,2]
[1]ERATO Localized Photon Project, Japan Science and Technology Corporation, 687-1 Tsuruma, Machida, Tokyo 194-0004, Japan. Tel: +81-42-788-6043, Fax: +81-42-788-6031, E-mail:sangu@ohtsu.jst.go.jp
[2]Interdisciplinary Graduate School of Science and Engineering, Tokyo Institute of Technology, 4259 Nagatsuda-cho, Midori-ku, Yokohama, Kanagawa 226-8502, Japan

Abstract: The operation of a nanophotonic switch was investigated theoretically. An increase in the exciton population with fast vibrations was obtained in the state-filling condition. We also found that the population decay time can be shortened by changing the state-filling time.

OCIS codes: (230.3990) Microstructure devices; (320.5390) Picosecond phenomena

Recently, functional nanometric devices operated by optical near fields have been intensively studied in order to satisfy future demands for optical information processing and communication [1]. We have proposed a novel class of devices that are constructed from a few quantum dots coupled via optical near fields, *i.e.*, *nanophotonic devices*. The exciton population dynamics in a nanophotonic switch, one such device, has been investigated both experimentally [2] and theoretically [1]. In this paper, we theoretically discuss principles of operating such a switch by controlling the excited state of matter, and demonstrate switching using three cubic quantum dots of appropriate sizes.

Figure 1 shows a model of the nanophotonic switch, in which each neighboring pair of quantum dots has a resonant energy level that is determined by setting the sizes as $1(\mathrm{I}):2(\mathrm{C}):\sqrt{2}(\mathrm{O})$. An input signal creates an exciton at the (1,1,1)-level in QD-I, and this is transferred to the resonant energy levels of the adjacent quantum dots via optical near-field coupling [3]. While some energy levels with even total quantum numbers are optically (dipole) forbidden and are not directly excited by far-field light, optical near fields allow such transitions because their spatial localization resolves the wave function of each nanometric quantum dot far beyond the diffraction limit of light. The ON or OFF state of the switch corresponds to an occupied or unoccupied lowest (1,1,1)-level, respectively, in QD-C. When this energy level is occupied, which is called *state-filling*, the excitation ultimately reaches the (2,1,1)-level in QD-C or the (1,1,1)-level in QD-O, leading to an output signal. The lowest energy level in each quantum dot is coupled to a free photon bath to sweep out the excitation radiatively and to a laser photon bath to control this device with a light pulse. Intra-sublevel transitions by phonon interaction guarantee unidirectional energy transfer.

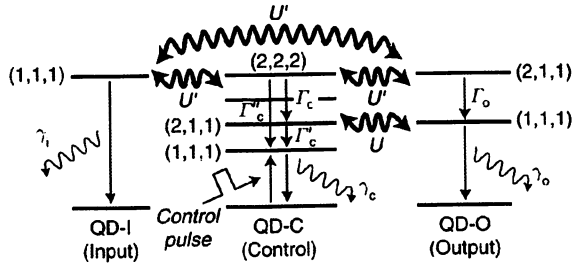

Fig. 1. Theoretical model of a nanophotonic switch.

Based on this model, we derived a master equation for density matrix elements, and calculated the dynamics numerically. As an initial population, a steady state is prepared, where the (1,1,1)-level in QD-I is excited weakly and continuously. The output signal (luminescence intensity) is proportional to the (1,1,1)-level population in QD-O. Figure 2 shows the temporal evolution of the population in QD-O after an incoherent short pulse (10 ps) is applied to QD-C. This situation corresponds to transition from the OFF state to the ON state. When state-filling is achieved instantaneously, the population increases and fast vibrations appear. These vibrations manifest themselves only in the state-filling condition, which is apparently caused by nutation between the (2,1,1) and (1,1,1)-levels in QD-C and O when the intra-sublevel transition in QD-C is restrained. Another characteristic feature, slow population decay, is observed in the later stage, and is approximately twice that of an isolated quantum dot. This phenomenon cannot be reproduced using the rate equation approach. Primary reason for this decay is that, in the two resonant energy levels coupled via optical near fields, one is dipole allowed, but the other is forbidden and cannot sweep out the population as a free photon in the case of the state-filling condition. Therefore, this is an inherent effect of optical near fields.

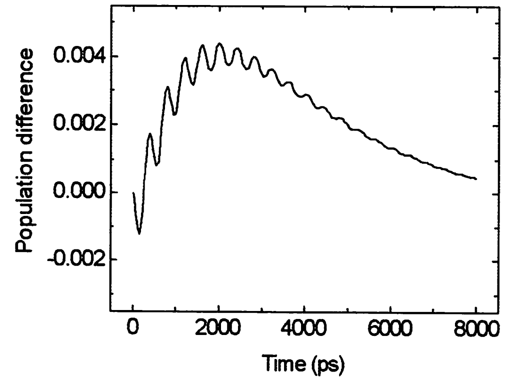

Fig. 2. Temporal evolution of the (1,1,1)-level population from the steady state in QD-C. The adjustable parameters are set as follows: optical near-field coupling $U^{-1} = U'^{-1} = 130$ ps, radiative relaxation time $\gamma_i^{-1} = 16.8$ ns, $\gamma_c^{-1} = 2.1$ ns, and $\gamma_o^{-1} = 5.9$ ns, and non-radiative relaxation time $\Gamma_c^{-1} = 20$ ps, $\Gamma'^{-1}_c = 10$ ps, $\Gamma''^{-1}_c = 30$ ps, and $\Gamma_o^{-1} = 20$ ps.

Furthermore, we found an important feature of the switching operation in this system. At first glance, it seems as though the excited population in the (1,1,1)-level in QD-O cannot be removed until the slow decay occurs (see Fig. 2). With control light illumination, however, the excitation in the system reaches a stable state faster than the spontaneous emission time. We postulate that the effect originates from stimulated emission and absorption in QD-C. In one of the calculated results (Fig. 3), the change from ON to OFF takes only a few 100 ps, and this can be optimized by varying some parameters, such as the inter-dot spacing, quantum-dot size, and dot and phonon bath materials.

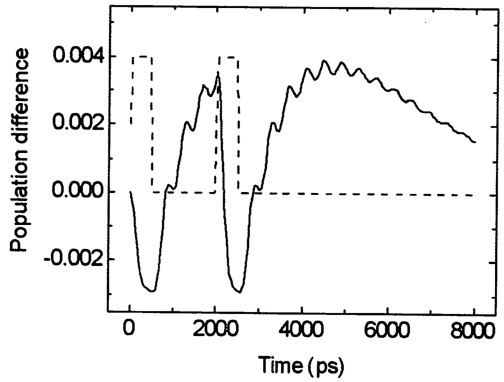

Fig.3. Demonstration of the switching operation using two control pulses. The solid and dashed curves represent the population at the (1,1,1)-level in QD-C and the temporal profile of the control pulses, respectively. The same parameters used to calculate Fig. 2 are adopted, and each pulse width is 500 ps.

To conclude, we discussed the operation of a nanophotonic switch when a control signal exists. After an instantaneous control pulse is applied, the output population increases with fast vibrations, and then decays slowly. By changing the control pulse width, the population decay time can be shortened to achieve faster ON-OFF switching. These characteristics were demonstrated numerically, and we obtained switching on the order of a few 100 ps with such a device.

[1] M. Ohtsu, K. Kobayashi, T. Kawazoe, S. Sangu, and T. Yatsui, "Nanophotonics: design, fabrication, and operation of nanometric devices using optical near fields," IEEE J. Sel. Top. Quant. Electron. **8**, 839-862 (2002).
[2] T. Kawazoe, K Kobayashi, J. Lim, Y. Narita, and M. Ohtsu, "Direct observation of optically forbidden energy transfer between CuCl quantum cubes via near-field optical spectroscopy," Phys. Rev. Lett. **88,** 067404 (2002).
[3] K. Kobayashi and M. Ohtsu, "Quantum theoretical approach to a near-field optical system," J. Microsc. **194**, 249-254 (1999).

QWA12

Non-Adiabatic Nanometric Near-Field Optical Chemical Vapor Deposition using Visible Light for Ultraviolet Metal-Organic Gas Source

T. Kawazoe1), K. Kobayashi1), S. Takubo2), and M. Ohtsu1),2)
1) Exploratory Research for Advanced Technology (ERATO), Japan Science and
Technology Corporation (JST), 687-1 Tsuruma, Machida, Tokyo 194-0004, Japan
Tel:+81-42-788-6039, Fax:+81-42-788-6031, e-mail: kawazoe@ohtsu.jst.go.jp

2) Interdisciplinary Graduate School of Science and Engineering,
Tokyo Institute of Technology, 4259 Nagatsuta, Midori-ku, Yokohama 226-8502, Japan

Abstract: Photodissociation using optical near field of diethylzinc becomes non-adiabatic due to the steep spatial gradient of optical power. Therefore, diethylzinc becomes active even for visible light, although it is active only for UV propagating light.

OCIS codes: (220.4610) Optical fabrication; (260, 5130) Photochemistry; (999.9999); Optical Near Field

The application of near-field optical chemical vapor deposition (NFO-CVD) to nanostructure fabrication has the potential to realize high-density nanometric integrated photonic devices [1]. Previously, we utilized the high spatial resolution capability of the optical near field to deposit 20-nm-wide Zn wires [2] and 40-nm Zn and 25-nm Al dots [1]. The size of objects deposited by conventional far-field optical CVD techniques is limited by diffraction. Optical CVD utilizes a two-step process: photodissociation and adsorption. For photodissociation, the far-field light must resonate the reacting molecular gasses in order to excite molecules from the ground state to the excited electronic state. The Frank-Condon principle claims that this resonance is essential for excitation [3]. The excited molecules then relax to the dissociation channel, and the dissociated Zn atoms adsorb to the substrate surface. The usual metal-organic gas source for optical CVD has the excited electron state in the ultraviolet wavelength region. For NFO-CVD, however, photodissociation can take place in nonresonant conditions, *i.e.*, for visible light, due to the inherent properties of the optical near field [4]. This technique makes it possible to use various light and gas sources to deposit a variety of nanometric materials, and is very useful.

In the experiment, ultra-high purity argon was used as a buffer gas and diethylzinc (DEZn) as a reacting molecular gas source. The fiber probe used for NFO-CVD was a high-throughput, single-tapered UV fiber probe. The apex of the fiber probe was 30 nm. In order to investigate the deposition effect of nonresonant far-field light, a fiber probe without the usual metal coating was used for deposition, *i.e.*, a bare fiber probe. Therefore, the optical far field was generated by light leaking through the circumference of the fiber probe, while the optical near field was generated at the apex. The laser output power from the fiber probe was measured with a photo-diode placed behind the sapphire substrate. The deposited Zn dots were measured using a shear-force microscope. During deposition, the partial pressure of DEZn was 100 mTorr. Details of the Zn deposition procedures have been reported previously [4, 5].

Figure 1 shows shear-force topographic images after NFO-CVD on a sapphire substrate with light sources of $\lambda = 325$ (a), 488 (b), and 684 (c) nm. Zn dots smaller than the light wavelength were deposited below the apex of the fiber probe, despite the leakage of far-field light from the bare fiber probe to the circumference. Namely, deposition does not occur for far-field light at these wavelengths, but for near-field light. This result agrees with previous work using conventional optical CVD for Zn deposition with a far-field light with $\lambda = 300$ nm [6].

Figure 2 shows the photon-flux dependencies of the deposition rate of Zn. For λ=325 nm, the deposition rate was proportional to the photon flux. For $\lambda = 488$ and 684 nm, higher-order dependencies of the deposition rate appeared and were fit by third-order functions. In discussions of the experimental results, we clarified that the photodissociation process for NFO-CVD is a non-adiabatic process that does not follow the Frank-Condon principle, which implies direct excitation of molecule vibration mode and direct transition to the dissociation channel. These phenomena arise from the steep spatial gradient of optical power, which is caused by the spatial locality of the optical near field.

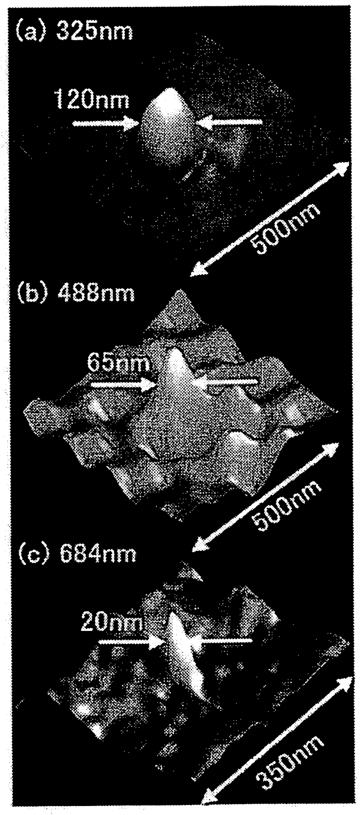

Fig.1. Shear-force topographic images after NFO-CVD on a sapphire substrate using three light sources: (a) He-Cd laser: λ = 325 nm; (b) Ar^+ laser: λ = 488 nm; (c) Diode laser: λ = 684 nm.

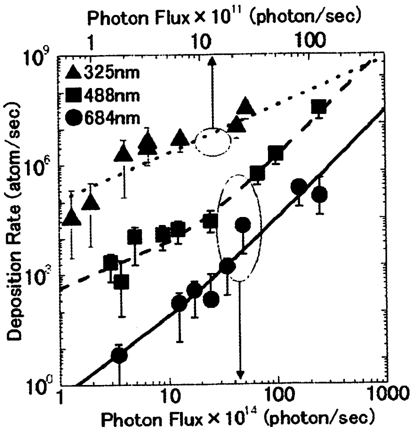

Fig.2. The photon-flux dependencies of the rate of Zn deposition. The solid, broken, and dotted curves fit the results by $Y=A\cdot X$: λ=325nm, $Y=A'\cdot X+B'\cdot X^2+C'\cdot X^3$: λ=488nm, and $Y=B''\cdot X^2+C''\cdot X^3$: λ=684nm, where Y and X are the deposition rate and photon flux, respectively.

References

1. M. Ohtsu, K. Kobayashi, T. Kawazoe, S. Sangu, and T. Yatsui, IEEE J. Sel. Top. Quant. Electron 8, 839 (2002).
2. V. V. Polonski, Y Yamamoto, J. D. White, M. Kourogi, and M. Ohtsu, Japan. J. Appl. Phys. Part 2 38, L826 (1999).
3. J. G. Calvert and J. N. Patts Jr., *Photochemistry* (Wiley, New York, 1966).
4. T. Kawazoe, Y. Yamamoto, and M. Ohtsu, Applied Physics Letters 79, 1184, (2001).
5. Y. Yamamoto, M. Kourogi, M. Ohtsu, V. Polonski, and G. H. Lee, Appl. Phys. Lett. 76, 2173 (2000).
6. M. Shimizu, H. Kamei, M. Tanizawa. T. Shiosaki and A. Kawabata, J. Crystal Growth 89, 365 (1988).

Plasmon condenser for optical far/near-field conversion

T. Yatsui[*], **W. Nomura**[**], **M. Kourogi**[**], **and M. Ohtsu**[*, **]
[*] *Ohtsu Project, ERATO, Japan Science and Technology Corporation*
687-1 Tsuruma, Machida, Tokyo, Japan 194-0004
+81 42-788-6040, +81 42-788-6031, yatsui@ohtsu.jst.go.jp
[**] *Interdisciplinary Graduate School of Science and Engineering, Tokyo Institute of Technology,*
4259 Nagatsuta, Midori-ku, Yokohama, Japan 226-8502
+81 45-924-5455, +81 45-924-5599

Abstract: We successfully fabricated a plasmon condenser for optical far/near-field conversion by introducing a microscatterer, which works as a high-efficiency coupler to a one-dimensional plasmon waveguide.

OCIS codes: (230.3120) Integrated optics devices, (240.6680) Surface plasmons

For future optical transmission systems, nanophotonic integrated circuits [1], which are composed of sub-100 nm scale dots, are necessary to increase data transmission rates and capacity. To realize this, they must be coupled with external conventional diffraction-limited photonic devices using a nanometer-scale optical waveguide for far/near-field conversion. To meet this requirement, we have reported a plasmon waveguide using a metallized silicon wedge structure that converts far-field light into an optical near field via one-dimensional (1D) plasmon mode [2]. To couple with the 1D plasmon mode efficiently, we propose here a plasmon condenser with a microscatterer that focuses a two-dimensional (2D) surface plasmon (SP) and converts it to 1D plasmon mode efficiently.

As a plasmon condenser, carbon columns were aligned using a focused ion beam. They were positioned on the circumference of a circle of radius R in order to phase-match the scattered plasmon waves at the focal point. The angular position of the nth column is given by $kR-kR\cos(\alpha_n)=2\pi n$ (see Fig. 1) [3]. Furthermore, to increase the efficiency of light scattering, a microscatterer was deposited at the focal point of the plasmon condenser. To excite 2D SP mode and increase the near-field optical energy at the microscatterer, 50-nm-thick gold coating was applied. In order to investigate the plasmon enhancement due to the microscatterer, we compared the spatial distribution of palsmon condensers without and with the microscatterer. The spatial distribution of the optical near-field energy was observed with a collection mode near-field optical microscope at λ = 785 nm and arrangement for 2D SP excitation in the Kretschmann configuration.

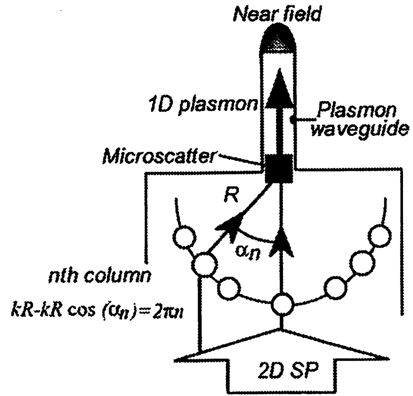

Fig. 1. Model of a plasmon condenser with a microscatterer.

Figures 2(a) and 2(b) show the respective topographical and near-field optical images of the plasmon condenser without the microscatterer. Figures 2(c) and 2(d) are for the plasmon condenser with the microscatterer. In Fig. 2(e), curves A, B, and C show cross-sectional profiles along the dashed white lines A-A', B-B' [in Fig. 2(b)], and C-C' [in Fig. 2(d)], respectively, where the pick-up intensity was normalized by the incident power of 2D SP in front of the plasmon condenser. Note that the peak intensity of curves B and C is twice and 7 times that of curve A, respectively, and the full width at half maximum of curve C is 350 nm. These results confirm that the plasmon condenser focuses 2D SP and the microscatterer enhances the light scattering.

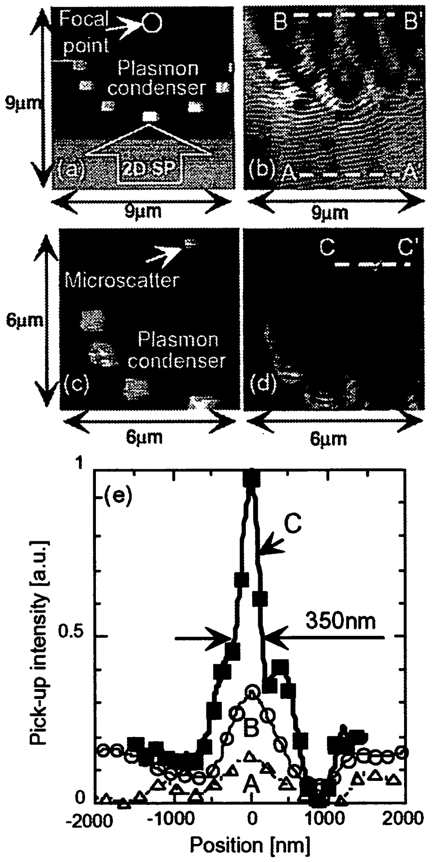

Fig. 2. (a) Topographical image of the plasmon condenser. (b) Near-field optical image of (a). (c) Topographical image of the plasmon condenser with a microscatterer. (d) Near-field optical image of (c). (e) Curves A, B, and C show cross-sectional profiles along the dashed white lines of A-A', B-B', and C-C', respectively.

Using these structures in a far/near-field conversion device, higher conversion efficiency from 2D SP to 1D plasmon mode is expected.

References

1. M. Ohtsu, K. Kobayashi, T. Kawazoe, S. Sangu, and T. Yatsui, "Nanophotonics: design, fabrication, and operation of nanometric devices using optical near fields," IEEE Journal of Selected Topics in Quantum Electronics **8**, 839-862 (2002).
2. T. Yatsui, M. Kourogi, and M. Ohtsu, "Plasmon waveguide for optical far/near-field conversion," Appl. Phys. Lett. **79**, 4583-4585 (2001).
3. I. I. Smolyaninov, D. L. Mazzoni, J. Mait, and C. C. Davis, "Experimental study of surface-plasmon scattering by individual surface defects," Phys. Rev. B **56**, 1601-1610 (1997).

Controlling the growth of Zn nanoparticles in a non-resonant optical near field using size-dependent resonance

T. Yatsui*, S. Takubo**, J. Lim**, T. Kawazoe*, M. Kourogi**, and M. Ohtsu*,**
*Ohtsu Project, ERATO, Japan Science and Technology Corporation
687-1 Tsuruma, Machida, Tokyo, Japan 194-0004
+81 42-788-6040, +81 42-788-6031, yatsui@ohtsu.jst.go.jp
** Interdisciplinary Graduate School of Science and Engineering, Tokyo Institute of Technology,
4259 Nagatsuta, Midori-ku, Yokohama, Japan 226-8502
+81 45-924-5455, +81 45-924-5599

Abstract: We report that a nonresonant optical near field can dramatically influence and regulate the growth of zinc nanoparticles during photochemical vapor deposition. A single 15-nm dot was fabricated in a highly controlled manner.

OCIS codes: (220.4610) Optical fabrication, (310.1860) Deposition and fabrication

We have proposed a nanophotonic integrated circuit to realize the ultrahigh integration of photonic switching arrays for future optical transmission systems [1]. It is composed of sub-100 nm scale dots, which must be fabricated with nano-scale controllability in size and position. We have proposed near-field optical chemical vapor deposition (NFO-CVD). For further controllability, in this study we use nonresonant light to regulate the size of Zn nanoparticles.

First, we deposited Zn nanoparticles by conventional CVD using a propagating light. Gas-phase diethylzinc (DEZ) at a partial pressure of 5 mTorr was used as the gas source. A 500-μW He-Cd laser (λ = 325 nm; its photon energy is higher than the absorption band edge energy of adsorbed DEZn [2] making it resonant to the electronic transition of a DEZn molecule) was used as the light source for the photodissociation of DEZn. The irradiation time was 20 s. An SEM image showed that the grain size ranged from 100-200nm [Fig. 1(a)]. In addition to the He-Cd laser, we deposited Zn with the illumination of 20-μW Ar^+ (λ = 488 nm) and He-Ne (λ = 633 nm) lasers. The irradiation times were 20 s. These are nonresonant light sources, because their photon energies are lower than the absorption band edge energy of DEZn. The respective grain size was less than 50 nm [illuminating λ = 488 nm and 325 nm, Fig. 1(b)] and less than 10 nm [illuminating λ =633 nm and 325 nm, Fig. 1(c)]. The dependency of fabricated size on the wavelength is due to the acceleration of dissociating ethylzinc [3] or the desorption of deposited Zn by the nonresonant light [4], which are originated from the size-dependent resonance in optical absorption.

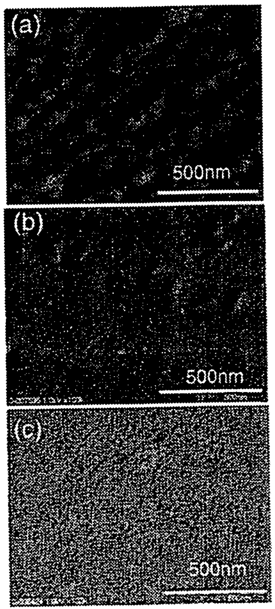

Fig. 1. SEM image of Zn nanoparticles deposited by PCVD: (a) λ = 325, (b) λ = 325 and 488 nm, and (c) λ = 325 and 633 nm.

Second, using this dependence, we performed NFO-CVD. Figure 2 shows the experimental setup. We used a bare UV fiber probe with an apex diameter of 30 nm (see the inset of Fig. 2). The separation between the fiber probe and sapphire substrate was controlled to within a few nanometers using a shear-force technique.

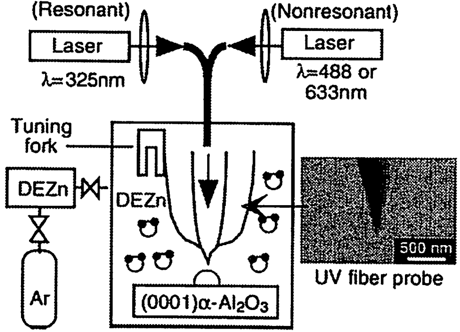

Fig. 2. The experimental setup for near-field optical deposition

Figures 3(a), 3(b), and 3(c) show topographical images of Zn deposited by NFO-CVD with illumination of λ = 325 nm (1 μW), λ = 325 (1 μW) and 488 nm (1 μW), and λ = 325 (1 μW) and 633 nm (1 μW), respectively. The irradiation times were 60 s. During deposition, the partial pressure of DEZn was 100 mTorr. In Fig. 3(d), curves A, B, and C are the respective cross-sectional profiles through Zn dots deposited with illumination of 325 nm, 325 and 488 nm, and 325 and 633 nm. Their full widths at half maximum are 60 nm (curve A), 30 nm (curve B), 15 nm (curve C), respectively, which is consistent with the results in Fig. 1. This experiment confirmed the high controllabirily of the size. In addition, position control is guaranteed by controlling the probe position. Since high-quality ZnO nanocrystallites can be obtained by oxidizing Zn, this method could be used to fabricate position-controlled ZnO nanocrystallites in a highly controlled manner. Since this method is used for a variety of nanomaterials, it is a promising tool for nanophotonics.

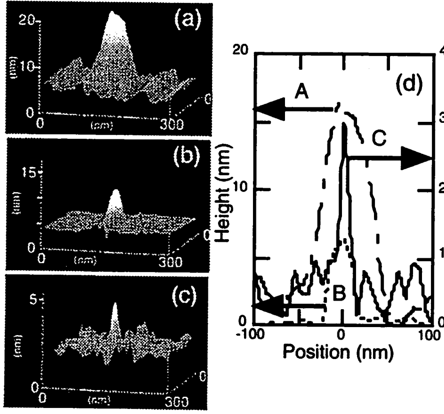

Fig. 3. Bird's-eye views of a shear-force topographical image of Zn deposited by NFO-CVD: (a) λ = 325 nm, (b) λ = 325 and 488 nm, and (c) λ = 325 and 633 nm. (d) Curves A (λ = 325 nm), B (λ = 325 and 488 nm), and C (λ = 325 and 633 nm) show cross-sectional profiles through the deposited Zn dots.

References

1. M. Ohtsu, K. Kobayashi, T. Kawazoe, S. Sangu, and T. Yatsui, "Nanophotonics: design, fabrication, and operation of nanometric devices using optical near fields," IEEE Journal of Selected Topics in Quantum Electronics **8**, 839-862 (2002).
2. T. Yatsui, T. Kawazoe, M. Ueda, Y. Yamamoto, M. Kourogi, and M. Ohtsu, "Fabrication of nanometric single zinc and zinc oxide dots by the selective photodissociation of adsorption-phase diethylzinc using a nonresonant optical near field," Appl Phys. Lett. **81**, 3651-3653 (2002).
3. P. J. Young, R. K. Gosavi, J. Connor, O. P. Strausz, and H. E. Gunning, "Ultraviolet absorption spectra of $CdCh_3$, $ZnCh_3$, and $TeCH_3$," Journal of Chem. Phys. **58**, 5280-5283 (1973).
4. K. F. MacDonald V. A. Fedotov, S. Pochon, K. J. Ross, G. C. Stevens, N. I. Zheludev, W. S. Brpcklesby, and V. I. Emeliyanov, "Optical control of gallium nanoparticles growth," Appl. Phys. Lett. **80**, 1643-1645 (2002).

Speech 7

Physics and Applications of Nanophotonics

Motoichi Ohtsu

Tokyo Institute of Technology

Abstract

This talk reviews recent progress in nanophotonics which was proposed by myself several years ago. Nanophotonics is defined as a technology that utilizes local electromagnetic interactions between a few nanometric element and an optical near field. The primary advantage of nanophotonics is its capacity to realize novel functions based on local electromagnetic interaction. It should be noted that some of the conventional concepts of wave-optics, such as interference, are no longer essential in nanophotonics. Novel nanophotonic devices and their integration are proposed and experimental/theoretical studies on their functions are reviewed. Chemical vapor deposition by optical near field is also demonstrated to deposit a variety of nanometric materials on a substrate.

Notes

23D-15-KL2

Operation and Fabrication of Nanophotonic Devices

Motoichi OHTSU*
Interdisciplinary Graduate School of Science and Technology, Tokyo Institute of Technology
4259 Nagatsuta-cho, Midori-ku, Yokohama, Kanagawa 2265-8502, Japan
E-mail: ohtsu@ae.titech.ac.jp

This talk reviews recent progress in nanophotonics which was proposed by myself several years ago in order to open a new field of optical science and technology beyond the diffraction limit of light. Nanophotonics is defined as a technology that utilizes local electromagnetic interactions between a few nanometric element and an optical near field. Since an optical near field is free from the diffraction of light due to its size-dependent localization and size-dependent resonance features, nanophotonics enables fabrication, operation, and integration of nanometric devices. Thus, this technology can solve the technical problems that are faced by

the future optical industry. They are (1) increased integration of photonic devices if the data transmission rates of optical fiber transmission systems are to reach as high as 10Tb/s by the year 2015, (2) sub-100nm width pattern fabrication by photo-lithography for increasing the DRAM capacity by the year 2010, and (3) recording and readout of 25 nm pit pattern for realizing 1 Tb/in^2 recording density of the optical memory systems by the year 2010.

The primary advantage of nanophotonics is its capacity to realize novel functions based on local electromagnetic interaction. It should be noted that some of the conventional concepts of wave-optics, such as interference, are no longer essential in nanophotonics. Instead, concepts of surface elementary excitation and nano-fabrication technology are essential.

Novel nanophotonic devices and their integration are proposed and theoretical/experimental studies on their functions are reviewed. Chemical vapor deposition by optical near field is also demonstrated to deposit a variety of nanometric materials on a substrate. A prototype of a high density, high speed optical near field memory system is demonstrated.

(*) also with ERATO Localized Photon Project, Japan Science and Technology Corporation, 687-1 Tsuruma, Machida-shi, Tokyo 194-0004, Japan

Optical near-field phenomena and their applications I: *Nanophotonics*

M. Ohtsu[1,2]
1) Interdisciplinary Graduate School of Science and Technology, Tokyo Institute of Technology
4259 Nagatsuta-cho, Midori-ku, Yokohama, Kanagawa 2265-8502, Japan
Phone: +81-45-924-5455, Fax: +81-45-924-5599, E-mail: ohtsu@ae.titech.ac.jp, http://uuu.ae.titech.ac.jp
2) Ohtsu"Localized Photon" Project, ERATO, Japan Science and Technology Corp.
687-1 Tsuruma, Machida-shi, Tokyo 194-0004, Japan
Phone: +81-42-788-6030, Fax: +81-42-788-6031, E-mail: ohtsu@ae.titech.ac.jp

This short presentation briefly introduces the motivation and technical trend of nanophotonics which was proposed by myself several years ago in order to open a new field of optical science and technology beyond the diffraction limit of light[1-4].

Nanophotonics is defined as a technology that utilizes local electromagnetic interactions between a few nanometric element and an optical near field. Since an optical near field is free from the diffraction of light due to its size-dependent localization and size-dependent resonance features, nanophotonics enables fabrication, operation, and integration of nanometric devices. Thus, this technology can solve the technical problems that are faced by the future optical industry. They are (1) increased integration of photonic devices if the data transmission rates of optical fiber transmission systems are to reach as high as 10Tb/s by the year 2015, (2) sub-100nm width pattern fabrication by photo-lithography for increasing the DRAM capacity by the year 2010, and (3) recording and readout of 25 nm pit pattern for realizing 1 Tb/in^2 recording density of the optical memory systems by the year 2010. The primary advantage of nanophotonics is its capacity to realize novel functions based on local electromagnetic interaction. It should be noted that some of the conventional concepts of wave-optics, such as interference, are no longer essential in nanophotonics. Instead, concepts of surface elementary excitation and nano-fabrication technology are essential.

Novel nanophotonic devices and their integration are proposed and theoretical/experimental studies on their functions arestudied. Chemical vapor deposition by optical near field is also demonstrated to deposit a variety of nanometric materials on a substrate. These details are reported by the succeeding presentations entitled, "Optical near-field phenomena and their applications II" and "III", by T. Yatsui, and T. Kawazoe, respectively.

References

1) M. Ohtsu, *Near-Field Nano/Atom Optics and Technology*, Springer-Verlag, Berlin, 1998
2) M. Ohtsu and H. Hori, *Near-Field Nano-Optics*, Kluwar Academic, New York, 1999
3) M. Ohtsu, "Nanophotonics: Design, Fabrication, and Operation of Nanometric Devices Using Optical Near Fields", IEEE J. Selected Topics in Quantum Electron., vol.8, July/August (2002) pp.839-862
4) M. Ohtsu(ed.), *Progress in Nano-Electro-Optics I*, Springer-Verlag, Berlin, 2002

Optical near-field phenomena and their applications II:
Near-field chemical vapor deposition and an optical far-/near-field conversion device

Takashi Yatsui
Ohtsu Localized Photon Project, ERATO, Japan Science and Technology Corporation
687-1 Tsuruma, Machida, Tokyo, Japan 194-0004
+81 42-788-6040, +81 42-788-6031, yatsui@ohtsu.jst.go.jp

We have proposed a nanophotonic integrated circuit (IC) to realize the ultrahigh integration of photonic switching arrays for future optical transmission systems [1]. It is composed of sub-100 nm scale dots and wires, which must be fabricated with nanometer-scale controllability in size and position. This is necessary so that the optical near-field energy can be transferred from one dot to another.

To achieve this level of controllability, we demonstrated the feasibility of nanometer-scale chemical vapor deposition (CVD) using optical near-field techniques [2], and have demonstrated the deposition of 60-nm Zn dots with high controllability [3]. To fabricate smaller size dots, we demonstrated a deposition of nanometer-scale Zn dots using the selective photodissociation of adsorbed diethylzinc (DEZn) molecules, where the photon energy is lower than that of the absorption edge of gas-phase DEZn. We achieved nanometeric prenucleation by dissociating DEZn molecules adsorbed on a substrate. Subsequent deposition was performed by dissociating the adsorbed molecules on the prenucleated Zn. The topographic image of the deposited Zn dot had a full width at half maximum of 25 nm [4]. For further controllability in size, we report that an illumination of nonresonant optical near field, which does not dissociate the DEZn molecules, can dramatically influence and regulate the growth of Zn nanoparticles during near-field CVD. In this deposition the dependency of fabricated size on the wavelength is due to the size-dependent resonance in optical absorption. We will also discuss possibilities of applying this to self-assembly fabrication for mass production of nanophotonic IC at the session. Since these methods can be used for a variety of nanomaterials, it is a promising tool for nanophotonics.

To couple these devices with a conventional diffraction-limited photonic devices, it is required to convert from far-field light to optical near field. As a converter, a plasmon waveguide has been proposed by introducing a metal-coated silicon wedge structure [5]. Guiding characteristics of the plasmon waveguide fabricated by Si anisotropic etching process were evaluated to be the 150-nm beam width and propagation length over several microns.

References

1. M. Ohtsu, K. Kobayashi, T. Kawazoe, S. Sangu, and T. Yatsui, IEEE Journal of Selected Topics in Quantum Electronics **8**, 839 (2002).
2. V. V. Polonski, Y. Yamamoto, M. Kourogi, H. Fukuda, and M. Ohtsu, J. Microsc. **194**, 545 (1999).
3. Y. Yamamoto, M. Kourogi, M. Ohtsu, V. Polonski, and G. H. Lee, Appl. Phys. Lett. **76**, 2173 (2000).
4. T. Yatsui, T. Kawazoe, M. Ueda, Y. Yamamoto, M. Kourogi, and M. Ohtsu, Appl. Phys. Lett **81**, 3651 (2002).
5. T. Yatsui, M. Kourogi, and M. Ohtsu, Appl. Phys. Lett. **79**, 4583 (2001).

Optical near-field phenomena and their applications III:
Non-resonant photo-dissociation and dipole forbidden energy transfer by optical near field

Tadashi Kawazoe
Exploratory Research for Advanced Technology (ERATO), Japan Science and
Technology Corporation (JST), 687-1 Tsuruma, Machida, Tokyo 194-0004, Japan
Tel:+81-42-788-6039, Fax:+81-42-788-6031, e-mail: kawazoe@ohtsu.jst.go.jp

Optical near-fields have been applied to high-resolution optical microscopy, high-density optical memory, atom manipulation, and so on [1]. Its spatial locality also brings novel physical phenomena such as optically forbidden energy transfer [2] and giant second harmonic generation [3]. It is understood that these phenomena occur because it is not necessary for the optical near field to satisfy some of the physical principle that the optical far field has to satisfy. Such novel properties of optical near field cause novel phenomena such as "***the dipole forbidden energy transfer*** between quantum dots" and "***Non-resonant photo-dissociation*** with non-resonant photochemical reaction". We introduce experimental result of such interested phenomena.

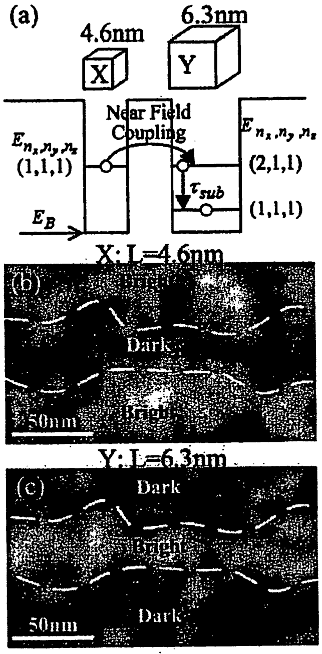

Fig.1. Dipole forbidden energy transfer between QCs.

Figure 1 (a) shows schematic explanation of the dipole forbidden energy transfer between closely located CuCl quantum cubes (QCs) X and Y with the effective side lengths of 4.6nm and 6.3nm, respectively. The quantized exciton energy levels of (1,1,1) in QC X and (2,1,1) in QC Y resonate with each other [4]. In such a resonant condition, the optical near field couples X and Y, and the energy transfer occurs between QCs via the optical near field. The energy transfer time is estimated at 40 ps, assuming that the separation between two QCs is equal to 10nm [5]. This energy transfer time is much shorter than the exciton lifetime and is longer than the inter-sub-level transition time τ_{sub}. Therefore, most of the exciton in a 4.6nm CuCl QC transfers to the neighboring 6.3nm QC. Here, we note that this energy transfer is ***optically forbidden*** due to optically inactive features of the energy level (2,1,1), but becomes allowed with the optical near field due to steep spatial gradient of its field intensity.

Figures 1 (b) and (c) show the 2D images of the luminescence from QCs with the side length of 4.6nm and 6.3nm, respectively at a same area. These images clearly establish anti-correlation features in their intensity distributions, as manifested by the dark and bright regions surrounded by broken curves. This anti-correlation feature can be understood by the energy transfer from X cubes to Y cubes. Namely, a 4.6nm QC located close to a 6.3nm QC cannot emit light, but instead transfers the energy to the 6.3nm QC. As a result, the luminescence intensity from 4.6nm QCs is low while it from 6.3nm QCs is high. In the presentation, we also review the experiment to measure the energy transfer time, which well agrees with the theoretical estimated value.

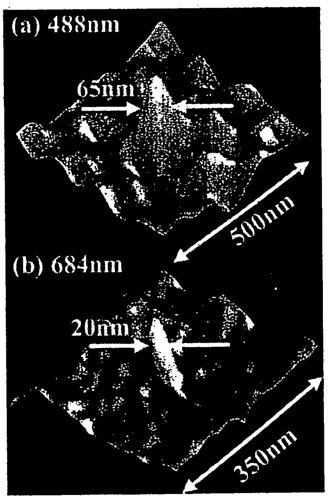

Fig.2. Non-resonant photo-dissociation of Zn dots

The application of near-field optical chemical vapor deposition (NFO-CVD) to nanostructure fabrication has the potential to realize high-density nanometric integrated photonic devices. Previously, we utilized the high spatial resolution capability of the optical near field to deposit Zn nanowires and Zn and Al nanodots [6]. Optical CVD utilizes a two-step process: photodissociation and adsorption. For photodissociation, the far-field light must resonate the reacting molecular gasses in order to excite molecules from the ground state to the excited electronic state. The ***Frank-Condon principle*** claims that this resonance is essential for excitation. The usual metal-organic gas source for optical CVD has the excited electron state in the ultraviolet wavelength region. For NFO-CVD, however, photodissociation can take place in non-resonant conditions, i.e., for visible light, due to the inherent properties of the optical near field [7]. Figure 2 shows shear-force topographic images after NFO-CVD using DEZn gas source on a sapphire substrate with light sources of λ = 488 (a), and 684 (b) nm. Namely, even for the non-resonant light, photodissociation and deposition occurs by using optical near field. We also discuss the physical mechanisms of this phenomenon by using wavelength and intensity dependence. These phenomena will develop the road to new optical device fabrication [8].

References

1. M. Ohtsu, *Near-Field Nano/Atom Optics and Technology* (Springer, New York, 1998).
2. T. Kawazoe, et al., Phys. Rev. Lett. **88**, 6, 067404 (2002).
3. T. Kawazoe, Optics Letters. **26**, p1687 (2001).
4. N. Sakakura et al., Phys. Rev. B **56**, 4051 (1997)
5. K. Kobayashi, et. al, Phys. Rev. A **63**, 013806 (2000).
6. Y. Yamamoto, et. al, Appl. Phys. Lett. **76**, 2173 (2000).
7. T. Kawazoe, et al., Appl. Phys. Lett. **79**, 1184, (2001).
8. M. Ohtsu, et al., IEEE J. Sel. Top. Quant. Electron **8**, 839 (2002).

Characteristic dynamics inherent in a near-field coupled quantum dot System

K. Kobayashi [1), S. Sangu [1), A. Shojiguchi [1), T. Kawazoe [1), and M. Ohtsu [1), 2)

1) ERATO Localized Photon Project, Japan Science and Technology,
687-1 Tsuruma, Machida, Tokyo 194-0004, Japan, email: kkoba@ohtsu.jst.go.jp
2) Interdisciplinary Graduate School of Science and Engineering,
Tokyo Institute of Technology, 4259 Nagatsuta-cho, Midori-ku, Yokohama, Kanagawa 226-8502, Japan

A new way to nano- and atom-photonics will be opened up if spatially localized optical near fields can control carriers transferred between nanoscale material systems. We have been investigating such possibilities using a quantum dot system both theoretically and experimentally [1].

In this report, we discuss interdot energy transfer dynamics driven by optical near fields using the density operator formalism in order to understand physics behind such a nano-device. Numerical results of the time evolution of exciton populations show an oscillatory behavior, as well as slower electron-hole recombination time than that in a single quantum dot, both of which are consistent with recent experimental photoluminescence data using near-field spectroscopy [2]. It indicates the importance of quantum coherence between quantum dots.

A two-quantum dot system consisting of QD 1 (two-level) and QD 2 (three-level) is considered, as schematically shown in Fig. 1. Resonant exciton states (E_2 -level) are coupled via optical near-field interaction of $\hbar U$. Exciton populations dynamics are quantum mechanically obtained [3-4] under the following initial condition: an exciton is created in each quantum dot by a weak cw-excitation and reaches a steady state. Then E_1 -level of QD 1 is resonantly excited by a pulse laser photon. Figure 2 shows the theoretical time evolution of the exciton population in QD 1 depicted by the solid curve and experimental data obtained with CuCl quantum dots marked by the circles. It follows from the result that a characteristic oscillation occurs due to the exciton nutation in E_2 -level as a result of E_1 -level filling, and that electron-hole recombination lifetime is 4.2 ns as twice as that in a single quantum dot. Note that this result cannot be obtained by using the rate equation.

In conclusion, a signal transfer and control in such a quantum dot system is confirmed, and we expect that this is a promising technique for future nano-photonic devices.

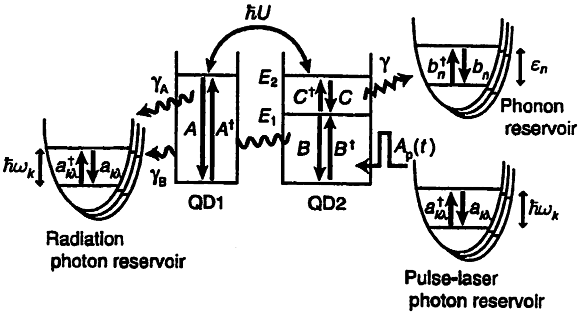

Fig. 1. Schematic drawing of the model

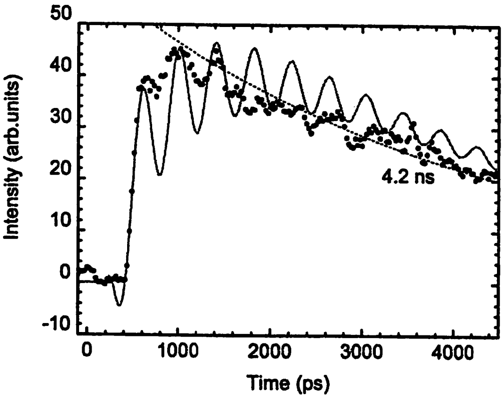

Fig. 2 Time evolution of exciton population and experimental luminescence••

References

1. M. Ohtsu, K. Kobayashi, T. Kawazoe, S. Sangu, and T. Yatsui, IEEE J. Select. Topics in Quant. Electron. 8, 839-862 (2002).
2. T. Kawazoe, private communication.
3. K. Kobayashi, S. Sangu, A. Shojiguchi, T. Kawazoe, K. Kitahara, and M. Ohtsu, J. Microsc. 209 (2003) in press.
4. S. Sangu, K. Kobayashi, A. Shojiguchi, T. Kawazoe, and M. Ohtsu, J. Appl. Phys. 93 (2003) in press.

Dipole-ordered state controlled by localized photons and superradiant multiple pulse generation

K. Kobayashi 1), A. Shojiguchi 1), S. Sangu 1), K. Kitahara 2), and M. Ohtsu 1), 3)

1) ERATO Localized Photon Project, Japan Science and Technology,
687-1 Tsuruma, Machida, Tokyo 194-0004, Japan, email: kkoba@ohtsu.jst.go.jp
2) Division of Natural Sciences, International Christian University,
10-2 Osawa 3-chome, Mitaka-shi, Tokyo 181-8585, Japan
3) Interdisciplinary Graduate School of Science and Engineering,
Tokyo Institute of Technology, 4259 Nagatsuta-cho, Midori-ku, Yokohama, Kanagawa 226-8502, Japan

Much attention has been paid to atom and nanophotonics, and one expects that the inherent phenomena of optical near fields should be applicable to fabrication and devices on a nanometer scale [1]. We have recently proposed a localized photon model to predict a collective dipole oscillation of an N two-level quantum dot (QD) system after local manipulation of the initial quantum states [2]. However, the origin and features of this dipole-ordered state have not been fully explored. In this paper we report an interesting phenomenon of multiple pulse generation superradiantly emitted from the dipole-ordered state, on the basis of the localized photon model in cooperation with a dissipative quantum master equation. We discuss the mechanism, features, and a possible nanophotonic application.

We consider the model discussed in Ref. [2], which consists of an N two-level QD system interacting with localized photons, and add a radiation field weakly interacting with the QDs in the system as a reservoir that does not affect the dynamics, but makes the system a dissipative one. Deriving a dissipative quantum master equation, we examine the emission profiles of the system semi-classically without taking account of quantum correlations. This method has an advantage over the quantum method that one can easily handle a relatively large number N system. We consider a case that is initially non-radiative and subsequently dipole-ordered where the alternating dipole coherences are initially set by a local probe, and at the same time the sign of the population difference in each QD is set opposite to that of the corresponding dipole coherence. The result shows that multiple pulses can be superradiantly emitted from the system.

In order to investigate the origin and mechanism of the multiple pulse generation as well as quantum effects, quantum correlations are considered, while the same initial conditions are set as before. Figure 1 shows one of such results that superradiant multiple pulses are emitted in our case, while the Dicke model shows no superradiance. The difference arises from whether a collective dipole oscillation manifests itself in the system or not, and it is qualitatively predicted in the semi-classical approach though there are quantitative differences. As the exciton-localized photon coupling becomes stronger, the frequency of the total dipole originating in the nonlinearity of the equation increases, which results in collective multiple pulse generation. One expects this kind of phenomenon can be applied to a component of nanophotonics such as a nanometric photonic source of the order of the total QD number [1].

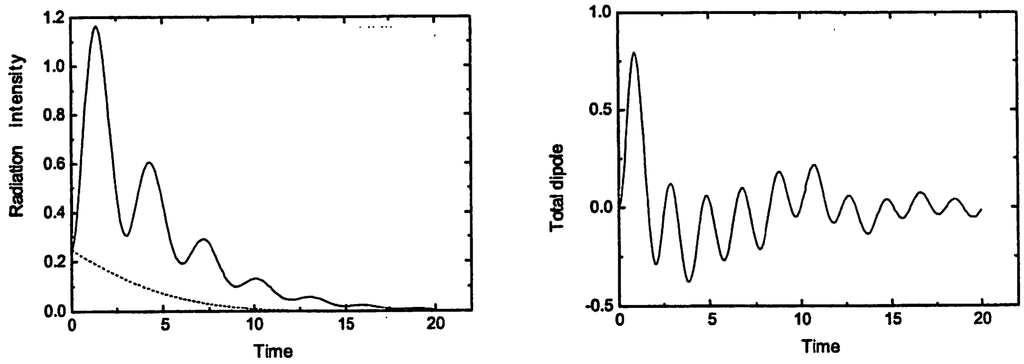

Fig. 1. Time evolution of the radiation intensity (left) and the total dipole of the system (right) obtained with quantum correlations. The solid curves denote the results for the localized photon model while the dotted curves represent the results for the Dicke model.

---

1. M. Ohtsu, K. Kobayashi, T. Kawazoe, S. Sangu, and T. Yatsui, IEEE J. Select. Topics in Quant. Electron. 8, 839-862 (2002).
2. A. Shojiguchi, K. Kobayashi, S. Sangu, K. Kitahara, and M. Ohtsu, Nonlinear Opt. (2002) in press.

Nanoophotonic Devices: Their Functions and Fabrications

M. Ohtsu[1,2)]
1) Interdisciplinary Graduate School of Science and Technology, Tokyo Institute of Technology
4259 Nagatsuta-cho, Midori-ku, Yokohama, Kanagawa 2265-8502, Japan
Phone: +81-45-924-5455, Fax: +81-45-924-5599, E-mail: ohtsu@ae.titech.ac.jp,
http://uuu.ae.titech.ac.jp
2) Ohtsu"Localized Photon" Project, ERATO, Japan Science and Technology Corp.
687-1 Tsuruma, Machida-shi, Tokyo 194-0004, Japan
Phone: +81-42-788-6030, Fax: +81-42-788-6031, E-mail: ohtsu@ae.titech.ac.jp

1. Introduction

This talk reviews recent progress in nanophotonics and atom-photonics which were proposed by myself several years ago in order to open a new field of optical science and technology beyond the diffraction limit of light[1-4)].

2.Principle of nanophotonics

Nanophotonics is defined as a technology that utilizes local electromagnetic interactions between a few nanometric element and an optical near field. Since an optical near field is free from the diffraction of light due to its size-dependent localization and size-dependent resonance features, nanophotonics enables fabrication, operation, and integration of nanometric devices(Fig.1). Thus, this technology can solve the technical problems that are faced by the future optical industry. They are (1) increased integration of photonic devices if the data transmission rates of optical fiber transmission systems are to reach as high as 10Tb/s by the year 2015, (2) sub-100nm width pattern fabrication by photo-lithography for increasing the DRAM capacity by the year 2010, and (3) recording and readout of 25 nm pit pattern for realizing 1 Tb/in^2 recording density of the optical memory systems by the year 2010. The primary advantage of nanophotonics is its capacity to realize novel functions based on local electromagnetic interaction. It should be noted that some of the conventional concepts of wave-optics, such as interference, are no longer essential in nanophotonics. Instead, concepts of surface elementary excitation and nano-fabrication technology are essential.

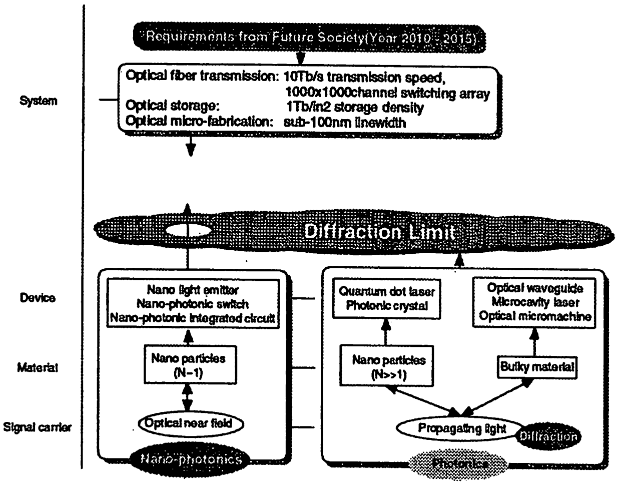

Fig.1
Concepts of nanophotonics.

3.Device operation and fabrication

Novel nanophotonic devices and their integration are proposed and theoretical/experimental studies on their functions are reviewed(Fig.2). Chemical vapor deposition by optical near field is also demonstrated to deposit a variety of nanometric materials on a substrate. A prototype of a high density, high speed optical near field memory system is demonstrated.

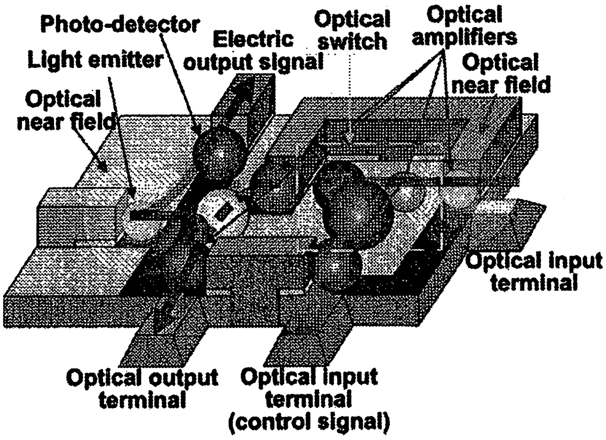

Fig.2
A nanophotonic integrated circuit.

4. Future

Finally, recent progress in our works on atom-photonics, manipulating neutral atoms by optical near field, is reviewed. It can open a new field of atom optics, and can be applied to atomic-scale deposition.

References

1) M. Ohtsu, *Near-Field Nano/Atom Optics and Technology*, Springer-Verlag, Berlin, 1998
2) M. Ohtsu and H. Hori, *Near-Field Nano-Optics*, Kluwar Academic/Plenum Publishers, New York, 1999
3) M. Ohtsu, "Nanophotonics: Design, Fabrication, and Operation of Nanometric Devices Using Optical Near Fields", IEEE J. Selected Topics in Quantum Electron., vol.8, July/August (2002) , in press
4) M. Ohtsu(ed.), *Progress in Nano-Electro-Optics I*, Springer-Verlag, Berlin, 2002

Oct. 20
Plenary (P-3)

Nanophotonics: Design, Fabrication, And Operation of Nanophotonic Devices

M. Ohtsu
Interdisciplinary Graduate School of Science and Technology, Tokyo Institute of Technology, Yokohama, Kanagawa 2265-8502, Japan
E-mail: ohtsu@ae.titech.ac.jp

This talk reviews recent progress in nanophotonics which were proposed by myself several years ago in order to open a new field of optical science and technology beyond the diffraction limit of light1). Nano-photonics is defined as a technology that utilizes local electromagnetic interactions between a few nanometric element and an optical near field. Since an optical near field is free from the diffraction of light due to its size-dependent localization and size-dependent resonance features, nanophotonics enables fabrication, operation, and integration of nanometric devices. Thus, this technology can solve the technical problems that are faced by the future optical industry. They are (1) increased integration of photonic devices if the data transmission rates of optical fiber transmission systems are to reach as high as 10Tb/s by the year 2015, (2) sub-100nm width pattern fabrication by photo-lithography for increasing the DRAM capacity by the year 2010, and (3) recording and readout of 25 nm pit pattern for realizing 1 Tb/in^2 recording density of the optical memory systems by the year 2010.

The primary advantage of nanophotonics is its capacity to realize novel functions based on local electromagnetic interaction. It should be noted that some of the conventional concepts of wave-optics, such as interference, are no longer essential in nanophotonics. Instead, concepts of surface elementary excitation and nano-fabrication technology are essential.

Novel nanophotonic devices and their integration are proposed and theoretical/experimental studies on their functions are reviewed. Chemical vapor deposition by optical near field is also demonstrated to deposit a variety of nanometric materials on a substrate.

1) M. Ohtsu, K. Kobayashi, T. Kawazoe, S. Sangu, and T. Yatsui, "Nanophotonics: Design, Fabrication, and Operation of Nanometric Devices Using Optical Near Fields", IEEE J. Selected Topics in Quantum Electron., vol.8, no.4, July/August issue, 2002, in press

FB1 (Invited)
10:30 – 11:00

Development of nano-photonic devices and their integration by optical near field

T. Yatsui* **and M. Ohtsu*,****

* *Ohtsu Project, ERATO, Japan Science and Technology Corporation*
687-1 Tsuruma, Machida, Tokyo, Japan 194-0004
yatsui@ohtsu.jst.go.jp
** *Interdisciplinary Graduate School of Science and Engineering, Tokyo Institute of Technology,*
4259 Nagatsuta, Midori-ku, Yokohama, Japan 226-8502

Ultrahigh integration of photonic switching arrays is necessary to increase data transmission rates and capacity of future optical transmission system. To accomplish this, the size of all switching devices must be reduced beyond the diffraction limit of light. We have already proposed a nano-photonic integrated circuit (IC) that is composed of nanometer-scale dots and wires (Fig. 1). In this circuit, the optical near field acts as a carrier to transfer signals [1].

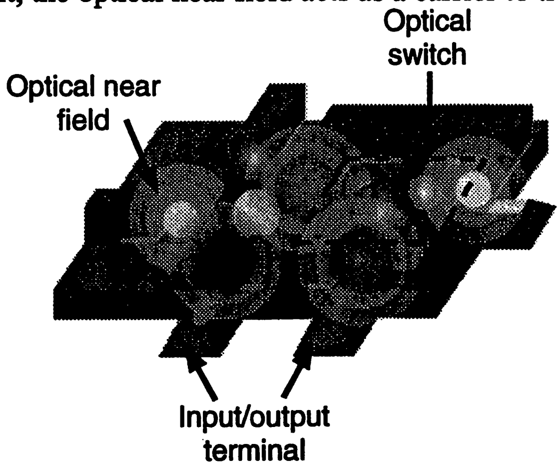

Fig. 1 Nano-photonic IC.

For the works of nano-photonics, a key device is a probe for generating/detecting optical near field with high efficiency and high resolution. To meet this requirement, we realized the successful fabrication of an optical near-field probe with extremely high throughput and small spot size, produced by introducing a pyramidal silicon structure and localized surface plasmon resonance at the metallized probe tip [2].

To fabricate nano-photonic IC, nanometer-scale dots must be deposited on a substrate with nanometer-scale controllability in their size and position. This is necessary so that the optical near-field energy ca be transformed from one dot to another. To achieve this level of controllability, we have demonstrated the feasibility of nanometer-scale chemical vapor deposition (CVD) with high controllability using optical near-field techniques, and have demonstrated the deposition of nanometric Zn, Al, and ZnO [Fig. 2(a) and (b)] [3]. To demonstrate the capability of using ZnO as a light emitter of the nano-photonic IC, we evaluated the quantum size effect of individual ZnO nanocrystallites using optical near field method [Fig. 2(c)] [4]. Furthermore, we observed the near-field optical energy transfer among resonant energy states of CuCl quantum dots [5], which are utilized in the operation of nanometer-scale photonic switches.

0-7803-7595-5/02/$17.00 ©2002 IEEE

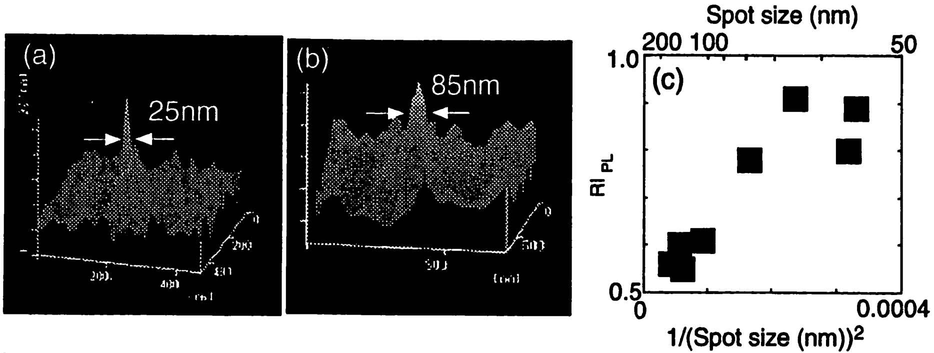

Fig. 2 (a) Zn dot fabricated by near-field optical CVD. (b) Photoluminescence image of single ZnO dot. (c) Size-dependent features of photoluminescence in individual ZnO nanocrystallites.

To couple these devices with a conventional diffraction-limited photonic devices, a plasmon waveguide have been proposed by introducing a metal-coated silicon wedge structure [Fig. 3(a)] [6]. Guiding characteristics of the plasmon waveguide fabricated by Si anisotropic etching process were evaluated to be the 150-nm beam width and propagation length over several microns [Fig. 3(b)].

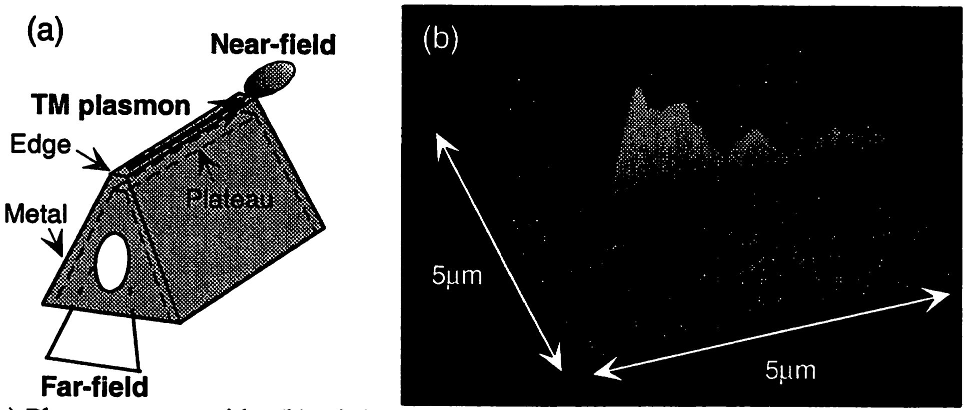

Fig. 3 (a) Plasmon waveguide. (b) Bird's-eye view of electric field distribution along the plateau.

We will also discuss possibilities of applying optical MEMS technique to nano-photonic devices and high-density near-field optical storage at the session.

Refereneces

1. M. Ohtsu, Proc. SPIE **3749**, 478 (1999).
2. T. Yatsui, K. Itsumi, M. Kourogi, and M. Ohtsu, Appl. Phys. Lett. **80**, 2257 (2002).
3. Y. Yamamoto, M. Kourogi, M. Ohtsu, V. Polonski, and G. H. Lee, Appl. Phys. Lett. **76**, 2173 (2000).
4. T. Yatsui, T. Kawazoe, M. Ueda, T. Shimizu, Y. Yamamoto, M. Kourogi, M. Ohtsu, and G. H. Lee, Appl. Phys. Lett. **80**, 1444 (2002).
5. T. Kawazoe, K. Kobayashi, J. S. Lim, Y. Narita, and M. Ohtsu, Phys. Rev. Lett. **88**, 067404 (2002).
6. T. Yatsui, M. Kourogi, and M. Ohtsu, Appl. Phys. Lett. **79**, 4583 (2001).

Fabrication of 25-nm Zn Dot with Selective Photodissociation of Adsorption-phase Dietylzinc by Optical Near Field

T. Yatsui,[a] M. Ueda,[b] Y. Yamamoto,[b] T. Kawazoe,[a] M. Kourogi,[a), b)] and M. Ohtsu[a), b)]
a) ERATO, Japan Science and Technology Corporation, Machida, Tokyo, 194-0004, Japan.
b) Interdisciplinary Graduate School of Science and Engineering, Tokyo Institute of Technology, Yokohama, Kanagawa, 226-8502, Japan.

For realizing nanometer-scale photonic devices and their integration, it is required that nanometer-scale structures are fabricated with nanometric precision. To meet this requirement, we have realized fabrication of 60-nm scale Zn dots with photodissociated gas-phase diethylzinc (DEZn) by optical near field [1]. However, the migration of dissociated Zn limits the lateral size. To overcome this difficulty, we report here successful fabrication of nanometer-scale Zn dot by two-step process; nanometer-scale nucleation and selective deposition on prenucleated Zn with photodissociation of adsorption-phase DEZn by optical near field.

The fiber probe used for photodissociation by optical near field was a sharpened UV fiber probe with an apex diameter of 30 nm. For selective photodissociation of adsorption-phase DEZn, we used He-Cd laser (325 nm) as a light source, because gas-phase DEZn is absorbed hardly at $\lambda > 300$ nm and the absorption spectrum of adsorption-phase DEZn is red-shifted with respect to that of gas-phase [2]. Furthermore, since the extent of molecular adsorption on Zn is larger than that on a substrate [3], the selective growth of adsorption-phase DEZn on prenucleated Zn is expected. As a comparison, the second harmonic of Ar^+ laser ($\lambda = 244$ nm) was used as a light source that resonates the absorption band of gas-phase DEZn. The separation between fiber probe and sapphire substrate was kept within several nanometers by shear-force feedback technique. During deposition, the partial pressure of DEZn was 10 mTorr.

Figures 1(a) and 1(b) show the topographical images of deposited Zn using $\lambda = 325$ and 244 nm, respectively. In Fig. 1(c), the solid and dashed curves are the respective cross sectional profiles through the Zn dots deposited at $\lambda = 325$ and 244 nm. The dashed curve has tails both sides of the peak. These tails correspond to the Zn deposited by photodissociation of gas-phase DEZn. However, the solid curve has no tails and its full width and half maximum and height are 25 and 16 nm, respectively; thus it is clear that the 325 nm propagating light leaked from the probe did not dissociate the gas-phase DEZn. These results indicate that the nanometer-scale nucleation was occurred by optical near field for a 325 nm light. Furthermore, the deposition is grown by molecules adsorbed on prenucleated Zn. Since high-quality ZnO is fabricated by oxidizing Zn, such a nanometric precision of the deposition mechanism could be used to fabricate size- and position-controlled nanometer-scale opto-electronic devices.

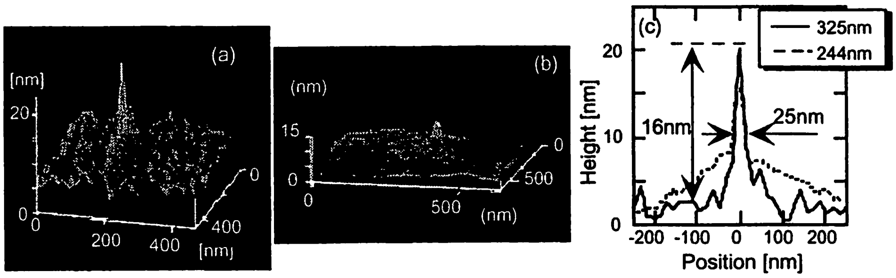

Figure 1: Bird's eye views of shear-force topographical image of Zn deposited by using (a) $\lambda = 325$ nm and (b) $\lambda = 244$ nm. (c) Cross sectional profiles through the deposited Zn dots in (a) and (b).

References

[1] Y. Yamamoto, M. Kourogi, M. Ohtsu, V. V. Polonski, and G. H. Lee, *Appl. Phys. Lett.* 76, 2173 (2000).
[2] Y. Fujita, S. Fujii, and T. Iuchi, *J. Vac. Sci. Technol.* B7, 273 (1989).
[3] D. J. Ehrlich, R. M. Osgood, Jr., And T. F. Deutsch, *J. Vac. Sci. Technol.* 21, 23 (1982).

Fabrication of a temperature-controllable B-doped Si probe for optical near-field photochemical vapor deposition

T-W. Kim, T. Yatsui, M. Kourogi, M. Ohtsu*, Japan science and Technology Coporation, 687-1*
Tsuruma, Machida, Tokyo, Japan 194-0004
** Also at: Interdisciplinary Graduate School of Science and Engineering, Tokyo Institute of Technology,*
4259, Nagatsuta, Midori-ku, Yokohama, Kanagawa, Japan 226-8502

Recently, optical near-field photochemical vapor deposition (NFO-PCVD) attracts much attention as a useful technique to realize nanopotonic near field optical devices. NFO-PCVD method has been successfully used in the fabrication of such nanometric matter as Al, Zn, and ZnO [1]. Because the aperture size directly affects the throughput of optical near field and the resultant size of nanometric matter deposited, it is required to maintain the same aperture size of the fiber probe throughout the integration of near field optical devices. Material deposition occurred at the aperture of fiber probe, caused by the dissociation of adsorbed metal-organic molecules, is thought as one of the reasons to change the aperture size and/or the throughput of optical near field during the process of NFO-PCVD. From this viewpoint, control of the adsorption of metal-organic molecules onto the probe aperture becomes important.

We have developed a temperature-controllable B-doped Si probe in order to prevent the deposition of the adsorbed source molecules onto the aperture of fiber probe. The idea is based on the facts that increasing substrate temperature above 80 °C reduces the adsorption of Diethylzinc molecules on the substrate surface [2] and heavily B-doped Si layer plays as a good current-induced heater [3]. The probes are fabricated using anisotropic etching of n-type silicon on insulator (SOI) and thermal diffusion of boron. Figure 1 illustrates the schematic diagram of cross-sectional view and the scanning electronic microscopy (SEM) image of the fabricated B-doped Si probe. The fabricated B-doped Si probe has the aperture size of about 80 nm and the height of 1.8 □m. By inducing electric power of 1 Watt, temperature of B-doped Si probe can be raised above 80 °C. In this paper, we describe the fabrication method of a temperature-controllable B-doped Si probe and discuss the applicability of the probe for NFO-PCVD.

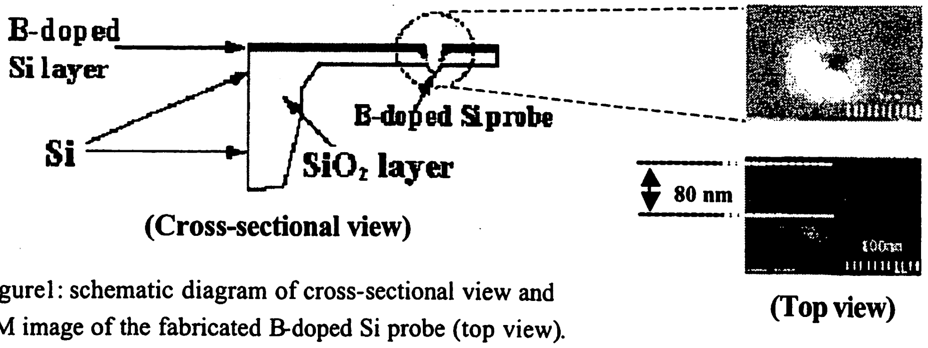

Figure1: schematic diagram of cross-sectional view and SEM image of the fabricated B-doped Si probe (top view).

References

[1] Y. Yamamoto, et al, Appl. Phys. Lett. **76**, 2173 (2000). [2] R. Krchnavek, et al, J. Vac. Sci. Tech. **5**, 20 (1987). [3] H. Yuasa, et al, T. IEE Japan, **117-E**, 275 (1997)

Manifestation of an electric dipole order induced by optical near fields

A. Shojiguchi, K. Kobayashi[A]*, K. Kitahara, S. Sangu*[A]*, M. Ohtsu*[A, B]*,*
International Christian University, 10-2-3, Mitaka, Tokyo 181-8585, Japan,
A) ERATO/JST, 687-1 Tsuruma, Machida, Tokyo 194-0004, Japan,
B) Tokyo Institute of Technology, 4259 Nagatuta, Midori-ku, Yokohama, Kanagawa 226-8502, Japan.

Owing to the recent progress in fine processing technology it becomes possible to investigate the interaction via optical near fields among materials in nano meter scale [1]. Since one of the remarkable characters of optical near fields is non-propagating property, it is more suitable to use localized functions as a basis set than to use plane waves to describe optical near fields. We present a phenomenological model of a near field photon-matter system using such a localized function to describe optical near fields. We suppose quantum dots chain as a matter system and model it as one-dimensional N two-level system (in other words, excitons) with a periodic boundary condition. A localized photon is described as a harmonic oscillator localized in each site, and only allowed to hop to the nearest neighbor sites. As a result of the interaction, quantum dots emit and absorb localized photons. A Hamiltonian of the system consists of three parts as follows:

$$H = (H_a + H_b) + H_{\mathrm{int}}$$

Here H_a describes localized photons, H_b describes excitons, and H_{int} represents the localized photon-exciton interaction. Each Hamiltonian can be expressed as

$$H_a = \varepsilon \sum_{n=1}^{N} a_n^{+} a_n + V \sum_{n=1}^{N} (a_{n+1}^{+} a_n + a_n^{+} a_{n+1}),$$

$$H_b = E \sum_{n=1}^{N} b_n^{+} b_n ,$$

$$H_{\mathrm{int}} = U \sum_{n=1}^{N} (a_n^{+} b_n + b_n^{+} a_n),$$

where n indicates the site number, and a_n (a_n^{+}) and b_n (b_n^{+}) represent annihilation (creation) operators of a localized photon and an exciton, respectively.

We investigate dynamical properties of the system driven by the Hamiltonian. As shown in Fig. 1, we predict a coherent oscillation of dipoles of the whole system started from an initial condition, and show that we can classify each dipole oscillation of the system into four groups depending on the parameters of the Hamiltonian.

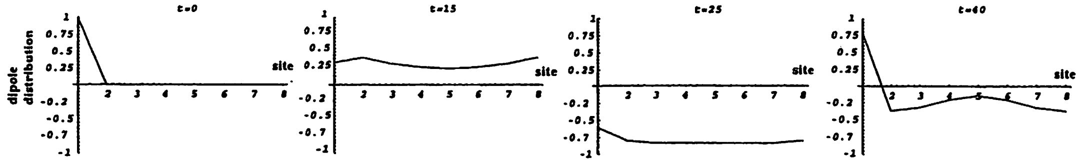

Figure 1: Time evolution of the dipole moment distribution. The vertical and horizontal axes represent the dipole moment and the site number of quantum dots.

Figure 2: Time evolution of the radiation amplitude. The super-radiatiant state has the value of 20 as the radiation amplitude.

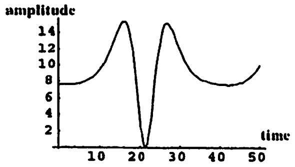

Moreover radiation probability of each state is examined in Fig. 2. It indicates that the state with the coherent oscillation is close to the Dicke's superradiant state. We will discuss the ordering mechanism in detail.

Reference

[1] M. Ohtsu, K. Kobayashi, H. Ito, and G. H. Lee, *Proc. IEEE* **88**, 1499(2000).

Plasmon Condenser with a Microscatter for Optical Far/Near field Conversion

T. Yatsui[a)] *T. Abe*[b)] *M. Kourogi*[a), b)] *and M. Ohtsu*[a), b)]
a) ERATO, Japan Science and Technology Corporation, Machida, Tokyo, 194-0004, Japan.
b) Interdisciplinary Graduate School of Science and Engineering, Tokyo Institute of Technology, Yokohama, Kanagawa, 226-8502, Japan.

To realize nanometer-scale photonic devices and their integration [1], coupling them with external conventional diffraction-limited photonic devices is required by using a nanometer-scale optical waveguide for far/near -field conversion. To meet this requirement, we have reported plasmon waveguide using a metallized silicon wedge structure that converts far-field light to optical near field via one-dimensional (1D) plasmon mode [2]. To couple with 1D plasmon mode efficiently, we propose here a plasmon condenser with a microscatter that focus two-dimensional (2D) surface plasmon (SP) and converts to 1D plasmon mode efficiently.

As a plasmon condenser, carbon columns were aligned by focused ion beam. They were positioned on a circumference of a radius R in order to compensate for phase-matching of the scattered plasmon waves at the focal point. The angular position of the nth column is given by the expression $kR\text{-}kR\cos(\alpha_n)=2\pi n$ [see Fig. 1(a)]. Furthermore, to enhance the efficiency of light scattering a microscatter was deposited at focal point of the plasmon condenser. To excite 2D SP mode and increase the near-field optical energy at the microscatter, 50-nm-thickness gold film was coated. In order to investigate the plasmon enhancement due to the microscatter, we compared the spatial distributions of palsmon condenser without and with the microscatter. The spatial distributions of optical near-field energy were observed by the collection mode near-field optical microscope taken at λ = 785 nm and arrangement for 2D SP excitation in Kretschmann configration.

Figures 1(b) and 1(c) show respective topographical and the near-field optical images of the plasmon condenser without the microscatter. Figures 1(d) and 1(e) are for the plasmon condenser with the microscatter. In Fig. 1(f), curves A, B, and C show the cross sectional profiles along dashed white lines A-A', B-B' [in Fig. 1(c)], and C-C' [in Fig. 1(e)], respectively, where the pick-up intensity were normalized by the incident power of 2D SP in front of the plasmon condenser. Note that the peak intensity of curves B and C are twice and 7 times that of curve A, respectively, and full width at half maximum of curve C is 350 nm. These results confirm that plasmon condenser focuses 2D SP and the microscatter enhances the light scattering. By using these structures in the far/near -field conversion device, higher conversion efficiency from 2D SP to 1D plasmon mode is expected.

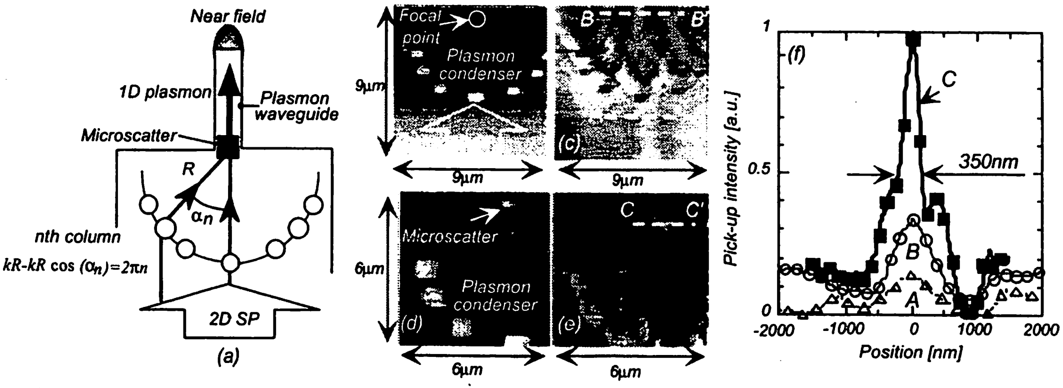

Figure 1: (a) Modeling of plasmon condenser with a microscatter. (b) Topographical image of plasmon condenser. (c) Near-field optical image on (b). (d) Topographical image of plasmon condenser with a microscatter. (e) Near-field optical image on (d). (f) Curves A, B, and C show the cross sectional profiles along the dashed white lines of A-A', B-B', and C-C', respectively.

References

[1] M. Ohtsu, *Proc. of SPIE* 3749, 478 (1999).
[2] T. Yatsui, M. Kourogi, and M. Ohtsu, *Appl. Phys. Lett.* 79, 4583 (2001).

Near-field Pump-probe Luminescence Spectroscopy of CuCl quantum cubes in ultraviolet region

T. Kawazoe, K. Kobayashi, S. Sangu,
Japan Science and Technology Corporation (JST), 687-1 Tsuruma, Machida, Tokyo 194-0004, Japan
M. Ohtsu,
Japan Science and Technology Corporation (JST), and also
Tokyo Institute of Technology, 4259 Nagatsuta, Midori-ku, Yokohama 226-8502, Japan

The coupled quantum-dots system exhibits more unique properties in contrast with the single quantum-dot system. The optical near-field interaction [1] is interesting, as it can govern the coupling strength among quantum dots. Recently, we observed optically forbidden energy transfer between CuCl quantum cubes (QCs) via optical near-field interaction [2]. We consider that a nanometric optical switch based on a new operation principle can be realized by controlling this energy transfer.

The quantized exciton energy levels of (1,1,1) in a 4.6 nm CuCl QC and (2,1,1) in a 6.3 nm QC resonate with each other, as shown in Fig.1 (a) [3]. For this type of resonant condition, the energy transfer between QC via the optical near-field occurs for less than 100 ps, assuming that the separation between two QCs is equal to 10 nm. This energy transfer time is much shorter than the exciton lifetime and is longer than the inter-sub-level transition time. Therefore, most of the exciton in a 4.6-nm CuCl QC transfers to the neighboring 6.3-nm QC. Thus, a 4.6-nm QC, located close to a 6.3-nm QC cannot emit light. However, when (1,1,1) level in a 6.3-nm QC is pumped by a laser, the energy transfer form a 4.6-nm QC to a 6.3-nm QC is obstructed due to the state filling effect of 6.3-nm QC.

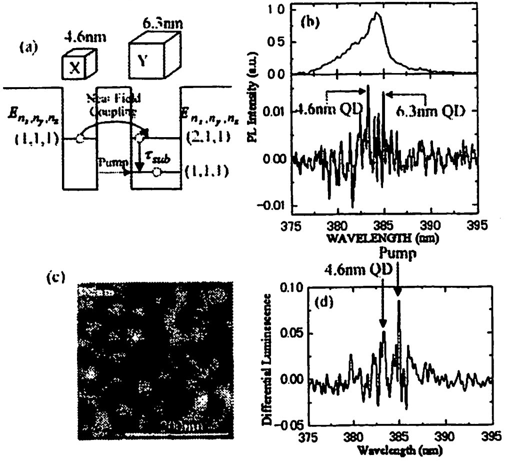

Figure 1: (a) Schematic drawings of closely located CuCl QCs with the effective side lengths of 4.6 nm and 6.3 nm. (b) Far- and near- field luminescence spectra of CuCl QCs embedded in a NaCl matrix. (c) Spatial distributions of the near-field luminescence intensity. (d) Differential luminescence spectrum.

The luminescence from a 4.6 nm and 6.3 nm QCs are shown in the near-field luminescence spectrum in the lower part in Fig.1 (b). For the experiment of the near-field pump-probe luminescence spectroscopy, SH of Ti-sapphire laser (385nm) and He-Cd laser (325nm) are used as pump and probe light source, respectively. The experimental result, observed at the position indicated broken circle in Fig. 1 (c), is shown in Fig. 1 (d) as a differential luminescence spectrum. The luminescence from a 4.6 nm QC increased by the pump of 6.3 nm QC (wavelength of 385 nm), as shown by an allow in Fig. 1 (d). This is the first demonstration of the control of the energy transfer between QCs.

References

[1] K. Kobayashi, S. Sangu, H. Ito, and M. Ohtsu, Phys. Rev. A **63**, 013806 (2000).
[2] T. Kawazoe, K. Kobayashi, J. Lim, Y. Narita and M. Ohtsu, Phys. Rev. Lett. **88**, 6, 067404 (2002).
[3] N. Sakakura and Y. Masumoto, Phys. Rev. B **56**, 4051 (1997).

Localized Photon Picture vs. Effective Interaction Picture: Towards a Nanometric Photonic Device

K. Kobayashi, S. Sangu, T. Kawazoe, ERATO Localized Photon Project, Japan Science and Technology,
687-1 Tsuruma, Machida, Tokyo 194-0004, Japan
A. Shojiguchi, K. Kitahara, Division of Natural Sciences, International Christian University,
10-2 Osawa 3-chome, Mitaka-shi, Tokyo 181-8585, Japan
M. Ohtsu, Japan Science and Technology, and also
Interdisciplinary Graduate School of Science and Engineering,
Tokyo Institute of Technology, 4259 Nagatsuta-cho, Midori-ku, Yokohama, Kanagawa 226-8502, Japan

In near-field optical microscopy and spectroscopy, localization and tunneling of photons have played essential roles, and are now realized as key issues for nanometric photonic devices. For example, the principles of operation of our proposed device [1] are based on excitation energy transfer induced by localized optical near fields between nanometric quantum dots (QDs) [2], and irreversible signal transmissions are guaranteed by the exciton-phonon coupling. Here we report on two alternative approaches: localized photon picture and effective interaction picture to discuss physics behind the devices.

When we explicitly include localized photonic degrees of freedom, we can describe dynamics of a relevant system that are governed by localized photons. The theory predicts, for example, a coherent dipole oscillation of a linear chain of two-level QDs, after local manipulation of initial states of some of the QDs [3]. We find that this kind of phenomenon originates in the fermionic nature and nonlinear effects of excitons. In order to understand such phenomenon more deeply, we use an effective interaction picture [4]. Taking the trace with respect to localized photonic degrees of freedom, we can derive an effective optical near-field interaction between QDs as $\hat{H}_{\text{eff}} = -\sum_{<i,j>} J_{ij}\hat{\vec{P}}(i)\cdot\hat{\vec{P}}(j)$, where $\hat{\vec{P}}(i)$ and J_{ij} are the dipole operator of the i-th QD and the coupling strength between the nearest neighbor QDs, respectively. It follows from this Hamiltonian that the dipole moments of the system tend to align parallel or antiparallel, depending on the sign of the coupling J_{ij}.

The above approaches can be extended to include exciton-phonon coupling in addition to the optical near-field coupling. Using the density operator method, we obtain equations of motion for such a system, and estimate a time scale of exciton population tunneling as a few to 100 picoseconds for CuCl QDs, depending on the sizes and the separation distances of the QDs. This time scale ideally corresponds to the switching speed of our proposed nano-switch.

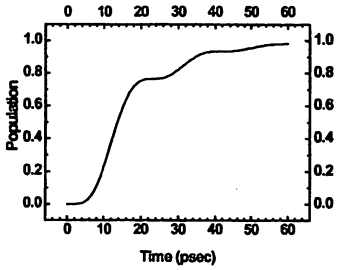

Figure 1: Typical switching behavior obtained for 3-QD system as a model of a nanometric photonic switch.

References

[1] M. Ohtsu, K. Kobayashi, T. Kawazoe, S. Sangu, and T. Yatsui, *to be published in IEEE J.*
[2] T. Kawazoe, K. Kobayashi, J. Lim, Y. Narita, and M. Ohtsu, *Phys. Rev. Lett.* **88**, 067404 (2002).
[3] A. Shojiguchi, K. Kobayashi, K. Kitahara, S. Sangu, and M. Ohtsu, *Proc. 3rd Asia Pacific Workshop on Near Field Optics*, 82 (2001).
[4] K. Kobayashi, S. Sangu, H. Ito, and M. Ohtsu, *Phys. Rev. A* **63**, 013806 (2001).

[I-3] REVIEW PAPERS

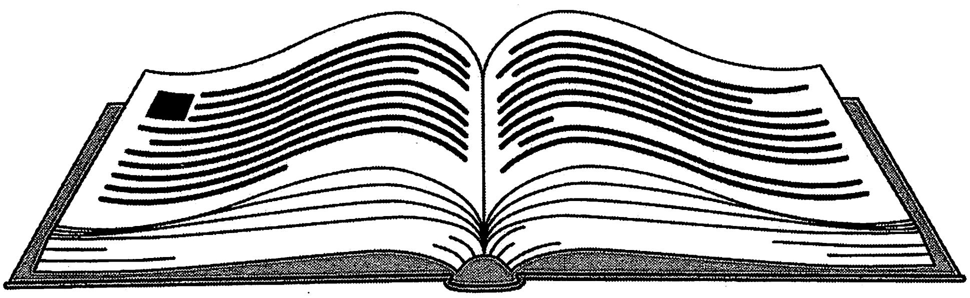

2002年光学界の進展

「光学界の進展」は，過去1年間の光学の研究活動状況ならびに進歩発展について解説したものです．本解説における検索範囲は，応用物理学会を中心として，他に関連する学会・研究会・国際会議等における発表(口頭および論文)で，本文中での検索雑誌・学会等の名称は下表のごとく略記法を用いています．

表　「光学界の進展」引用学会等の省略記号

◆ 学会誌関係	記号	◆ 講演会関係	記号
光学　第30巻第12号	a-0	第49回春季応用物理学関係連合講演会	1
第31巻第n号	a-n	第63回秋季応用物理学会学術講演会	2
Opt. Rev.　Vol. 8, No. 6	b-0	Optics Japan 2002	3
Vol. 9, No. n	b-n	第27回光学シンポジウム	4
応用物理　第70巻第12号	c-0	カラーフォーラム JAPAN 2002	5
第71巻第n号	c-n	第35回光学五学会関西支部連合講演会	6
Jpn. J. Appl. Phys. (1)　Vol. 40, No. 12	d-0	ODF 2002	7
Vol. 41, No. n	d-n	International Conference on “X-Ray Microscopy” 2002	8
Jpn. J. Appl. Phys. (2)　Vol. 40, No. 12	e-0	第15回日本放射光学会年会	9
Vol. 41, No. n	e-n	日本物理学会第57回年次大会	10
Jpn. J. Appl. Phys. Suppl.　Vol. 40, No. 12	f-0	日本物理学会 2002年秋季大会	11
Vol. 41, No. n	f-n	ECOC 2002	12
J. Opt. Soc. Am. (A)　Vol. 18, No. 12	g-0	OECC 2002	13
Vol. 19, No. n	g-n	OFC 2002	14
J. Opt. Soc. Am. (B)　Vol. 18, No. 12	h-0	LEOS 2002	15
Vol. 19, No. n	h-n	2002 OSA Annual Meeting	16
Appl. Opt.　Vol. 40, No. 34	i-01	NFO-AP3	17
Vol. 40, No. 35	i-02	NFO-7	18
Vol. 40, No. 36	i-03	近接場光学研究グループ第11回研究討論会	19
Vol. 41, No. n	i-n	CLEO/QELS 2002	20
Opt. Lett.　Vol. 26, No. 23	j-02	第30回光波センシング技術研究会	21
Vol. 26, No. 24	j-03	量子エレクトロニクス研究会	22
Vol. 27, No. n	j-n	FST 2002	23
Opt. Commun.	k-m-n	ICO 19	24
J. Light Wave Technol.　Vol. 19, No. 12	l-0	OAA 2002	25
Vol. 20, No. n	l-n	ISOM/ODS 2002	26
放射光　第15巻　第n号	m-n	第85回微小光学研究会	27
日本物理学会会誌　第57巻　第n号	n-n	光ディスク懇談会 2002	28
IEEE J. Quantum Electron.　Vol. 38, No. n	o-n	第26回光設計研究グループ研究会	29
レーザー研究　第30巻　第n号	p-n	日本視覚学会 2002年冬季大会	30
分光研究　第51巻　第n号	q-n	Second Asian Conference on Vision	31
IEEE Photon. Technol. Lett.　Vol. 14, No. n	r-n	第35回照明学会全国大会	32
Nature　Vol. m, No. n	s-m-n	BOPM 2002	33
Science　Vol. m, No. n	t-m-n		
Phys. Rev. Lett.　Vol. m, No. n	u-m-n		
Phys. Rev. A.　Vol. m, No. n	v-m-n		
Vision　Vol. 14, No. n	w-n		
照明学会誌　Vol. 86, No. n	x-n		
Phys. Med. Biol.　Vol. 47, No. n	y-n		

による光回路としての機能のみならず，光強度に依存した光スイッチ，リミッター，光ダイオードなどが提案されており，今後さらに新しい非線形光学が展開するはずである[h-9]．

6.8.2　超高速非線形光学

フェムト秒レーザーがさらに汎用性を増し，非線形光学においてもさまざまな報告がなされている．再生増幅器は，パラメトリック増幅器を用いる方法が多く報告されるようになり，高速点火核融合用ドライバーにおいても採用されている[1]．高強度フェムト秒レーザーを用いた高次高調波発生では，波長73.6～42.6 nm帯で10 mJの出力が得られた[j-21]．

再生増幅出力レベルでは，波形整形による多光子励起過程を通じての励起ダイナミクスの制御が活発に研究されている．たとえば，CARS (coherent anti Stokes Raman scattering) 過程を用いた振動準位間の励起分布制御，電子励起準位からの分子間エネルギー移乗の制御などである．興味深いのは，この波形制御技術により，フェムト秒パルスを用いてもCARS分光の波長分解能を劣化せずに計測できる手法が報告されたことである[v-65-5A]．

6.8.3　フォトニックファイバー光学

白色光発生自体は，ラマン効果と自己急峻効果によって理論的にもかなり高い精度で説明できるようになり，フェムト秒レーザーのキャリヤーエンベロープの計測，光シンセサイザー等に応用されている．白色光出力も平均出力2 Wがスペクトル幅310 nmで得られている[j-02]．短波長においてゼロ分散が可能であることから，800 nm帯でのソリトン伝播を用いたスクイーズド光の発生実験[j-8]，ファイバーOPO[j-19]の実験などが特筆に値する．

6.9　展　　望

量子光学は，単一光子源をはじめ非古典光のラインアップも充実し，暗号通信以外のさまざまな光学実験が可能になってきた．スピン，超電導量子磁束による量子計算機が実現するまでの線形光学系での量子ゲート実験も重要であり，2モードスクイージング光によるもつれあい光学の実験同様に，原理実証実験による量子光学の解釈は，もつれた紐がほどけていくような面白さがある．

7.　近接場光学

科学技術振興事業団　小林　潔

12月にアジア太平洋会議[17]，3月にシンポジウム[1]，8月に国際会議[18]が開かれ，日本から新しい流れを感じさせる研究成果が発表された1年であった．応用分野ごとにこの1年の進展を振り返る．

7.1　光近接場プローブと装置

赤外から紫外域にわたり高効率かつ高分解能なプローブを目指してダイヤモンドをコア材とした突起型プローブが開発された[1]．さらにプローブにFeをコート[1]，あるいはスリット[2]を設けることにより局所的な偏光を制御しようという試みもなされ，FDTD (finite-difference time-domain) 計算も行われた．応用特化型プローブとして光CVD (chemical vapor deposition) 用にBドープ型温度制御プローブ[1]とFコートプローブ[2]が提案された．AFM (atomic force microscope) 型プローブの振動モード解析も報告された[2]．

7.2　原子分光と原子の運動制御

原子スピン制御の第一歩として，微小球とファイバープローブを用い，局所円偏光の遠方散乱成分が観測された[1]．またCMモード (Carniglia and Mandel mode) を用いて表面の効果を考慮することにより原子スピン偏極を30%向上させることができるとの指摘があった[18,19]．光近接場ファネルによる冷却Rb原子ビーム形成，スリット型原子偏向器による冷却Rb原子の偏向実験を目指した研究に関しても二重磁気光学トラップ装置の開発とドーナツビームの影響検討など確実な進展がみられた[1,2]．Cs原子の超微細構造スペクトルがFM雑音分光法により観測され[2]，別のグループからは双極子禁制遷移において基板による影響が無視できないという実験データが示された[11]．理論的には非局所応答理論に基づき，半導体微粒子に働く力と原子に働く力の対応が示された[11]．

7.3　微小粒子による局所電場増強と分子分光

伝搬光と巨視的な物質系の相互作用の延長として，金微粒子・半導体粒子の分光，水中の金微粒子操作による顕微鏡，非線形物質を用いた双安定状態の計算などの発表があった[1,2]．さらに局所的な電場増強効果を使って，DNA塩基・カーボンナノチューブのラマン分光が報告された[1,2]．自由電子レーザーを用いた赤外分光，多色蛍光分光，応力分布測定，吸着分子解析が行われた[1,2]．また単一分子蛍光測定の分解能10 nmがFDTD計算では2倍以上になるという結果が報告された[1]．

7.4　量子ドット分光とナノ光デバイス

光近接場相互作用による量子ドット間のエネルギー移動とパルス光による占有状態のオンオフに基づくナノ光スイッチの動作速度が量子マスター方程式により予測され，それに並行してCuCl量子箱を用いた時間空間分解分光実験が行われスイッチ動作が初めて検証された[1,2,18,20]．そのスイッチ時間が理論予測に合致した約60 psであることも示された[2,17,18]．さらに発光スペクトルに振動成分が見出さ

れ，単一CuCl量子箱の電子-正孔再結合寿命に比べ，近接場光により結合した場合は約2倍寿命が長くなることが報告され，理論解析からその起源が初めて明らかになった[2,19]．また近接場測定の分解能を追求した結果，単一GaAs量子ドットのポンププローブ分光によりドット内励起子波動関数の空間積分の可視化に初めて成功したことが報告された[1,18,19,20]．理論的には局在光子の自由度を陽に取り入れたモデルにより近接場特有の新しいダイナミクスが報告された[1,2,10,11,18,20]．これら一連の実験・理論解析はこの分野に新しい方向性を与える特筆すべき成果であろう．近接場光を用い位置制御されたナノドットを作製する技術も大きな進展を遂げた．吸着分子を解離し25 nmのZnドット，さらにエキシマーレーザーによる酸化処理でZnOドットが作られた[1]．材料のガス分子の電子励起エネルギーよりも低い可視のレーザー光照射によりZnドットが解離堆積されることが以前報告されていたが，そのメカニズムを解明するためにあらたに堆積レートの光強度依存性が提出された[2,19]．また材料分子に適切な2波長の近接場光を照射することが作製ドットのサイズを制御するために有効であることが示された[2]．

7.5　近接場光一伝搬光変換素子と産業分野への応用

近接場光と伝搬光の変換を効率よく行うことが産業応用には大きなポイントになるが，三次元から二次元，二次元から一次元への変換素子の報告はこれに糸口を与えている[2]．陽極酸化法による素子形成のその場観察の報告も同様であろう[2]．光記録装置への応用としてSIL (solid immersion lens)搭載型シリコンヘッドによる高速トラッキング，平面型ヘッドによる信号再生の予備実験が報告された[1]．近接場露光ではg線を用いて100 nm，さらに50 nmのパターン形成が可能であることが示された[1,2]．

7.6　展　　望

実験結果と数値計算の比較が行われるなど，この分野に成熟さを感じたが，今後は計算が立脚する理論の適用範囲を明確にする必要があろう．また分野の広がりと同時に，今一度原点に戻った本質的な基礎概念・理論や今年築かれた新しい流れがいっそう発展することを期待したい．

8.　光応用計測

産総研　美濃島薫

時間・空間・周波数などの極限をめざすのは，計測技術の普遍的テーマであろう．時間軸においては，チタンサファイアレーザーが市販され，誰でもフェムト秒パルスが利用できるようになってからすでに10年がたつ．近年では，アト秒領域の研究も伝えられるようになってきた．その間，超短パルスレーザーは多次元・高強度・局在・精密性を生かした応用技術としてのポテンシャルの高さが指摘されてきたが，実際はそれを十分利用できているとはいえなかった．しかし，ここ数年の超短パルスレーザー技術の進歩は著しく，急速に制御技術が進むことで，高精度，高安定なツールとなってきた．さらに，小型化，可搬化，波長領域の拡大や広帯域性も進み，応用範囲が広がっている．特に，フォトニック結晶ファイバーの進展により，従来，光通信帯以外では大掛かりなレーザー増幅器によってしか利用できなかったスーパーコンティニュウム光が，レーザー共振器直接出力光で利用できるようになり，高輝度で高品質な広帯域光源として利用が広がっている．さらに，超短パルスとして時間軸での極限性を利用するのみならず，そのフーリエ領域での周波数軸における精密計測ツールとしての有用性が示され，直交しているかに思われた2つの異分野の極限を追求すると，その先には融合が待っているという事実が如実に示され，ある種のカルチャーショックをもって迎えられた．その結果，光の絶対位相制御の夢が現実のものとなってきており，応用計測技術としても，光の強度のみならず，従来の干渉計などの相対位相制御法によらない絶対位相を精密に制御した光計測が目の前に開けてきている．国内動向としても，応用物理学会の計測光学分類にフェムト秒計測のキーワードが設けられた[2]．「超短光パルスが拓く新たな光技術」[21]，「超精密光計測；光の位相の絶対制御」[22]，「光イメージングの極限に挑む～空間，時間，波長，偏光情報への展開～」[2]が，研究会やシンポジウムのテーマとなり，極短時間領域の計測・制御と応用が特集号で取り上げられた[c-2]．

8.1　距離・形状・位置等の計測

干渉計測以外に限定すると，距離計測が盛んに研究されている．光検出器の二光子吸収を用いた距離計測システムが開発され，直交偏光の強度相関による干渉ノイズの低減，素子の温度依存性の影響が報告された[2,3]．フェムト秒光周波数コムを用いたマイクロメートル分解能の数百m距離測定と，環境変動自動補正が報告された[1,2,21]．周波数シフト帰還型レーザーを利用して広範囲に絶対値を決定する距離計が報告された[20]．反射型モアレによりディスプレイなどの表面形状測定法が報告された[3]．

8.2　速度計測等

半導体レーザーとファイバーを用いた自己混合型レーザードップラー速度計が報告された[1,2]．周波数変調された半導体レーザーによる光波コヒーレンス関数の合成法を用いて，位置と速度を分離測定する手法が報告された[1]．Lambert-Beer則をレーザードップラー速度法に応用し微

チャレンジロード

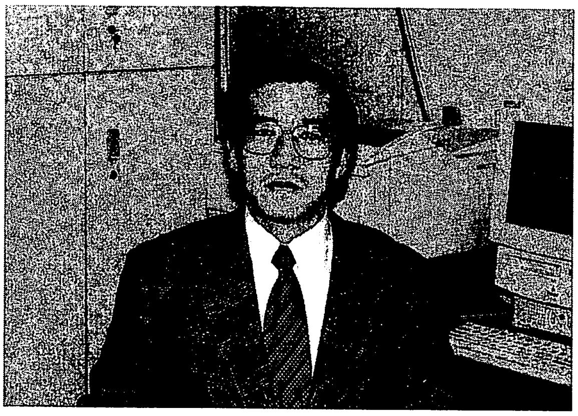
独自の発想で「光のナノ寸法化」を
実現させた大津元一先生

第25回

ナノフォトニクス事始め

大津 元一 Motoichi Ohtsu

東京工業大学 大学院総合理工学研究科 教授

1950年生まれ。1973年東京工業大学工学部電子工学科卒。1978年東京工業大学大学院電子物理工学専攻博士後期課程修了。工学博士。東京工業大学助手、助教授を経て、1991年より現職。この間、1986〜1987年東京工業大学を休職し米国AT＆Tベル研究所研究員。現在、科学技術振興事業団ERATO大津「局在フォトン」プロジェクト総括責任者を兼任。専門はナノフォトニクス。

1. ナノフォトニクスって何？

「ナノフォトニクス」とは私の造語で、「ナノメートル」(100万分の1 mm)と「フォトニクス」(光加工、光デバイス、光システムを実現するための光工学)との合成語である。すなわちナノテクノロジーの光版と思っていただいてもよい。ナノテクノロジーでは一般にボトムアップ型の戦略(「材料→デバイス→システム」といった小→大の構築の考え方)が採用されている。しかし重要なことは同時に「社会の要求→システム→デバイス→材料」という大→小の考え方、すなわちトップダウン型の戦略も配備することである。農耕民族である日本人は古来より稲を育て、収穫した米粒を手のひらに載せて観察し、品種改良を繰り返して来た。これにならって現代の日本人も材料、デバイスのように手のひらに載るものを作ることは得意である。しかし、抽象的なトップダウン戦略は不得意であり、それが1980年代以降、追いつけ追い越せ型の日本の光技術が米国にリードを許した原因である。これに対しナノフォトニクスではボトムアップ、トップダウン両型の戦略を採って世界をリードする。

光の周波数、パワー、偏光、パルス幅などを制御して使うのが従来の光工学である。それらの基本的概念の多くは欧米発であるが、私がナノフォトニクスを着想した1980年代当時、未着手の概念が1つあった。それは「光を小さくする」ことである。光の波は回折と呼ばれる性質をもつ。すなわち光が板に開けられた小さな穴を通り抜けると、その後は広がる。この性質のために凸レンズで光を集めても焦点面上での光のスポットは点にはならず、有限の寸法の「ピンぼけ」となる。その寸法は光の波長(数100nm)程度である。これは光のエネルギーが波

長以下の微小な空間には集中しないことを意味し、顕微鏡の倍率や光メモリの記録密度の上限、さらにはレーザなどの装置寸法の下限を決める。これは回折限界と呼ばれている。

従来の光科学技術は回折限界との戦いであった。たとえば光メモリの高密度化のために短波長光源（紫外線半導体レーザなど）の開発が進んだ。しかし回折限界の枠組みの中での開発は終末に近づいている。一方、21世紀の社会は波長よりずっと小さな寸法の光科学技術を実現するためのブレークスルーを必要としている。そのためには材料をナノ寸法化しただけでは不可能であり、同時に光もナノ寸法化することが唯一の解を与える。これがナノフォトニクスである。私はこの発想のもとに「光を小さくする」研究を開始した。

2. なんて変なことをやっているのだ

光のナノ寸法化は「近接場光」と呼ばれる光を発生させ使うことにより実現する。近接場光を発生させるには従来の光科学技術の延長上にはない概念・方法が必要である。たとえば図１(a)のようにガラス製の光ファイバの先端を尖らしたものを使う。ファイバの後ろから光を入れると、この光はファイバ先端から出射せず、ファイバ先端表面にまつわりついた膜のような光のみが発生する。これが近接場光であり、その膜の厚みはファイバ先端の寸法程度である。これを小さな光源として使うと顕微鏡の倍率、光メモリの記録密度はファイバ先端の寸法によって決まることになる。すなわち光の波長には依存しないので、ファイバ先端を小さくしておけば回折限界の制約から解放される。

1980年代初期はファイバを先鋭化する技術がなく、したがって実際には誰も近接場光を発生させることができなかった。私はこの時点でファイバを高い再現性で先鋭化する方法を開発することが重要と判断し、それに着手した。フッ酸によるエッチングにより溶かし出すことが有利と考えたが、なかなかうまくいかなかった。その証拠に、図２に示すように私の研究ノートの1982年2月のページに「エッチングで先まで尖らず！　テーマとして不可！　自分でやる」という記述がみられる。これは「先鋭化がうまくいかないので卒論の研究テーマとして学生に与えるのは残酷。自分だけで実験を進めよう」という意味である。この当時はファイバの性能がよくなかったこと、観察用の電子顕微鏡の倍率が低かったことに困難さの原因があったと回顧される。

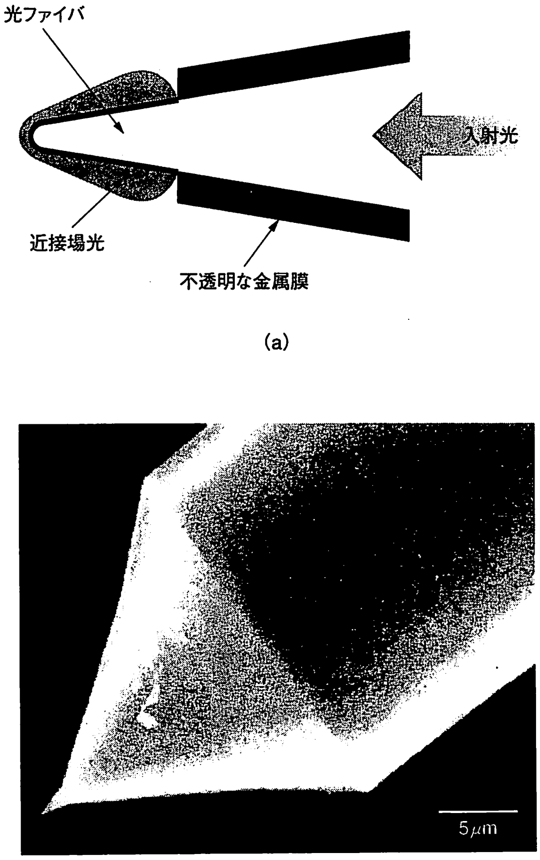

(a)

(b)

図１　(a)近接場光とその発生法、(b)尖ったファイバ

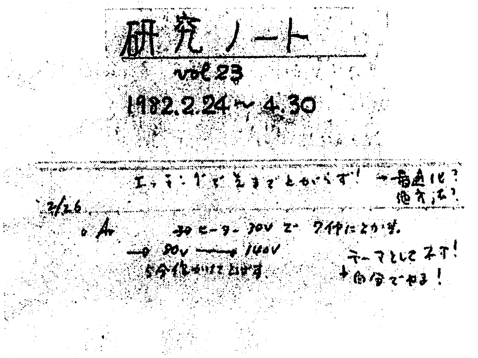

研究ノート

vol 23

1982.2.24〜4.30

エッチングで先まで尖らず！ → 最適化？
他方法？

2/26

○A　30ヒーター 70V で 7件にとかす.

→ 80V ——→ 140V
5分位かけておとす.

テーマとして不可！
↓自分でやる！

図２　1982年2月26日の筆者の研究ノート

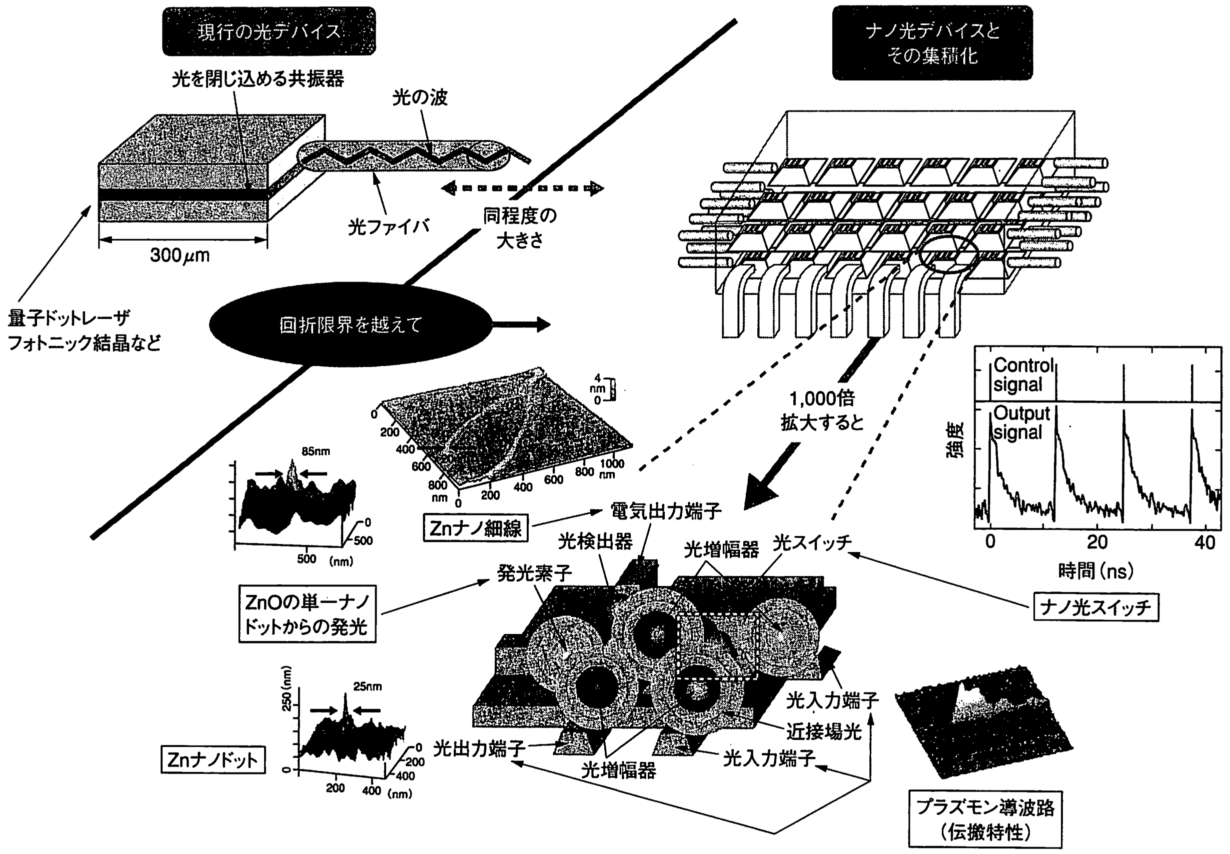

図3　ナノ光デバイスとその集積化の現状

私は1986〜1987年に光ファイバ通信研究の中心である米国AT&Tベル研究所に研究員として勤務する機会を得た。その際の研究テーマの1つとして私はファイバ先鋭化を提案したが却下された。彼らの経験では「米国製のファイバをエッチングで加工しても尖らない」というのが却下の理由であった。これには納得できなかったので、帰国後に日本製のファイバを用いて引き続き試行錯誤を繰り返した。すると尖る条件が見つかったので、再現性よくさらに尖らせるために特別なファイバ素材を試作して使ってみると、図1(b)に示すように先端の寸法が数nmまたはそれ以下まで小さくなった。この時点でナノフォトニクスの研究への展開可能性が見えてきた。その後よく調べてみると、日本ではVAD法と呼ばれる独自の製作法を採用していることが先鋭化の原因であることがわかった。偶然にも日本のファイバの技術力の高さに助けられた。1990年代に入るとこのようにして発明された先鋭化ファイバを用いた顕微鏡でDNAの単一分子などを従来の光学顕微鏡の約100倍高い倍率(電子顕微鏡と同等)で観測できるようになった。この世界記録はいまだに破られていない。

フッ酸を使ってファイバを尖らす技術は今では当たり前のように思われるかもしれない。しかし私が開発するまではこの技術そのものがなく、したがって近接場光を発生させることが難しかったため、これらに汗を流そうとする人はいなかった。その当時は(依然として現在でも)本節表題のように「何て変なことをやっているのだ。そんなことは欧米ではやっていないぞ」というコメントも届いた。

しかしその後の私の研究の進展として、顕微鏡だけではなく試料の構造を調べる分光分析機が実用化している。さらには図3に示すように近接場光を用いた微細加工、光デバイス構成などの技術、すなわちナノフォトニクスが始動している。また昨年は高密度の光メモリを実用化する大型の国家プロジェクトが産業界で開始され

た。実はこれらの進展に関しても多くの苦労話があるが、それは次の機会に譲ろう。

3.　社会の役に立つ時が来た

私がナノフォトニクスの研究を始めたのは当時流行のテーマであったからではなく、また理論家が結論したことであったからではない。将来の光科学技術にとって必要であり、かつこの分野が欠落していると判断したからである。いわば、多くの人たちとはまったく別の方向に向かって、独断と偏見をもって着手した研究であり、無謀にも研究費、実験装置、マンパワーがほぼ０の状態から始めたものである。したがって、世に出して発表して恥ずかしくない成果が得られ始めたのは1980年代終わり頃といってよい。しかしその間、1980年代中頃には欧米でも類似の研究成果が発表され始めたこともあり、この独断と偏見が決して的はずれでないことを知って勇気づけられた。写真はその中の１人であるスイスの研究者と久しぶりに再会したときのスナップである。

さらに最近、私の研究グループは従来の光では実現できなかった新規な光スイッチ機能、光加工を近接場光によって実現し、これがナノフォトニクスの本質であることを示すことができた。図３の集積回路はこの原理に基づくナノ光デバイスから構成されている。このようにファイバ先鋭化法の発明がきっかけとなり、最近では当初の期待以上の方向へと発展している。これらは挑戦者のみが獲得しうる喜びである。他人の（とくに欧米の）研究の後追いや人まねをせず、自分の頭で基本的概念（改良技術ではない）の発見のきっかけをつかみ、執念深く研究を続けると、このような喜びが味わえるようだ。

写真　近接場光研究の旧友との再会（1998年）
右が筆者、中央はIBMチューリッヒ研究所のD.Pohl博士、左は山梨大学の堀裕和教授。

いよいよボトムアップと同時にトップダウン型の戦略を維持しつつ、ナノフォトニクスの概念に基づいてシステムを構築し、21世紀の社会の役に立つ段階が到来した。さて、そろそろ別の変なことを見つけて挑戦してみようかな……。

引用・参考文献）

1）大津元一, 小林潔：近接場光の基礎, オーム社 (2003).

2）大津元一：光の小さな粒, 裳華房 (2001).

3）大津元一：ナノ・フォトニクス, 米田出版 (1999).

特集 4・2

4. ナノオプトロニクス

ナノフォトニクス

大津　元一

大津元一　正員　東京工業大学大学院総合理工学研究科
E-mail　ohtsu@ae.titech.ac.jp

Nano-Photonics. By Motoichi OHTSU, Member (Interdisciplinary Graduate School of Science and Engineering, Tokyo Institute of Technology, Yokohama-shi, 226-8502, Japan).

ABSTRACT

ナノフォトニクスの原理と現状について概説し，将来の社会からの要求にこたえるトップダウン型の研究開発戦略の必要性について述べる．更に，既存の光技術で用いられている伝搬光を使った場合には実現不可能な固有の現象と機能とを実現して使うのがナノフォトニクスの本質であることを指摘する．ナノ寸法を実現することは副産物にすぎない．今後の技術開発の展望についても触れる．

キーワード：近接場光，スイッチ，量子ドット，化学気相たい積

1. まえがき

ナノフォトニクスとは数年前に筆者が命名した光技術であり，まだ国内外の諸学会などで正式に使われている名称ではない(注1)．命名当時は将来技術との認識も多かったが，ナノテクノロジーのブームが始まった後はこの名前を他所でも散見することが多くなった．

図1に示すように西暦2010～2015年の高度情報化・高度福祉化社会の要求にこたえるためには光情報通信システムや光情報記録システムの大容量化・高速化が必要であるが，それには関連する光デバイスの小型化・高度集積化が不可欠である(1),(2)．しかし既存の光技術では光の回折(用語)のために光波長以下に小型化することはできない．ナノテクノロジー技術によりナノ寸法物質を多数作り，量子ドットレーザ，フォトニック結晶などの既存の概念で動作する光デバイスを作成しても，情報のキャリヤとして伝搬光を使う限り上記の回折限界(用語)を超えることは不可能である．

回折限界を超えるためには光デバイス構築の概念のパラダイムシフトが必要となる．すなわち情報のキャリヤとしての光をナノ寸法化するために伝搬光ではなく近接場光を使い，これを少数個のナノ寸法物質間で伝送する．この新概念に立脚した技術がナノフォトニクスと呼ばれている．この技術では波動光学の概念はもはや基本的ではなくなり，レーザ，共振器などの概念は主役の座を降りる．その代り必須なのは表面素励起，局所的電磁相互作用など，従来着目されていなかった概念である．更に，ナノフォトニクスは社会の要求にこたえるためのシステム→デバイス→材料というトップダウン的な戦略に基づく技術であることを指摘しておく．

2. ナノ寸法であることが重要か

近接場光とは振動する電気双極子から発生する光の近接場成分である(3)．その電界の電気力線は電気双極子に局在し，非伝搬である．一方，遠隔場成分の電気力線は電気双極子から分離し，閉曲線となって遠方に伝搬する．従来の光技術ではこの伝搬光を使っており，これは回折する．

ナノフォトニクスでは基板等の巨視的寸法の物質系に囲まれるナノ寸法物質を扱うが，これに光を照射すると物質中の多数の原子に電気双極子が誘起され，各々が図2(a)に示すように近接場光と伝搬光とを発生する．この物質中のすべての電気双極子から発生する近接場光のエネルギーの総和の値はナノ寸法物質表面から遠ざかるにつれて急激に減衰する．ナノ寸法物質の大きさを a，その表面からの距離を r とすると，エネルギーの空間分布の r 方向依存性は $\exp(-r/a)/r$ なる湯川関数で表される(4)．すなわち非伝搬の近接場光はナノ寸法物質表面を膜のように覆うが，その膜の厚みは入射光の波長にはよらずナノ寸法物質の大きさ a 程度である．

図2(b)のように第一のナノ寸法物質表面に近接場光を発生させ，それを微小光源として用いて第二のナノ寸

(注1)　例えば(財)光産業技術振興協会では筆者の提案により1995年に「ナノフォトニクス懇談会」が発足し，研究開発動向の調査活動を行い現在に至っている．

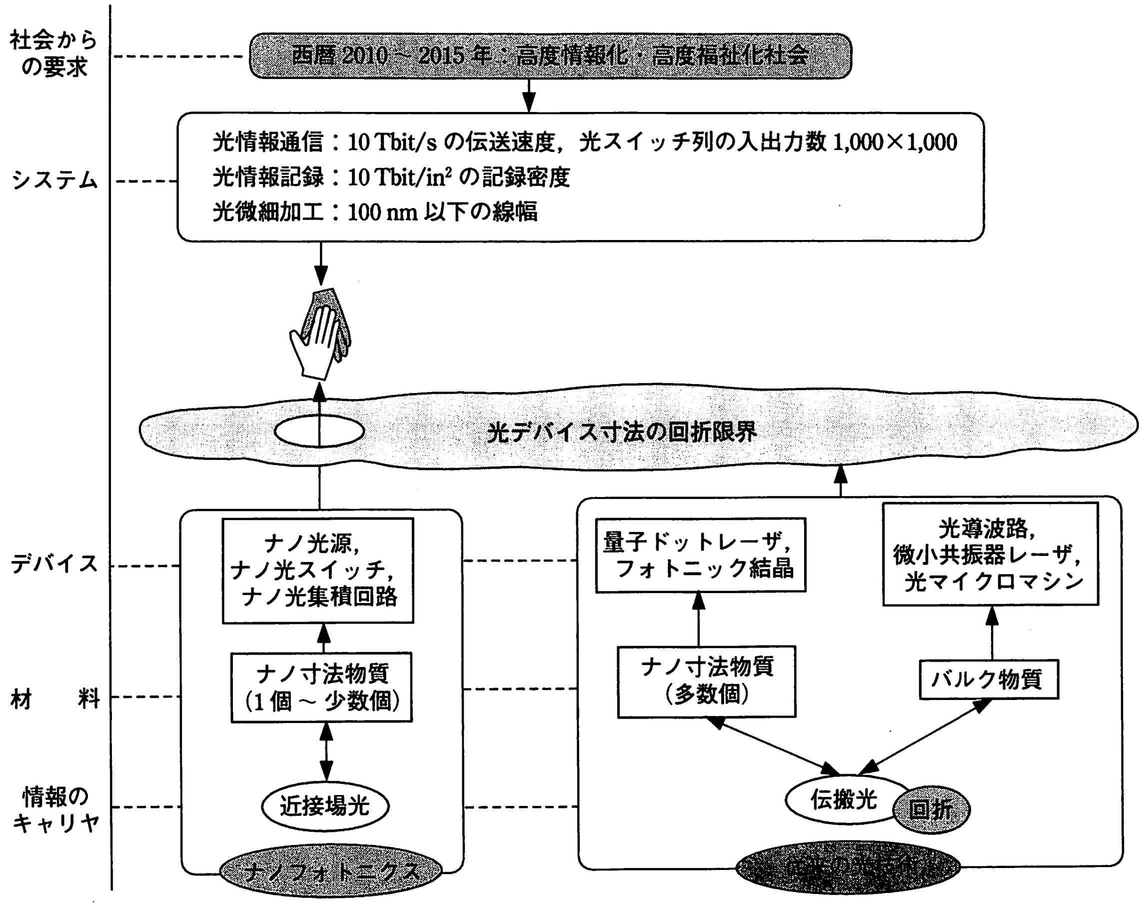

図1　将来の社会からの要求にこたえるナノフォトニクス　情報のキャリヤとして近接場光を使い，回折限界を超えて光デバイスをナノ寸法化する．

法物質に近づけて照明し，それを加工したり，あるいは近接場光のエネルギーを伝送することにより回折限界を超えた微小な光技術，すなわちナノフォトニクスが可能となる．この図は第二のナノ寸法物質に近づけると近接場光の電気力線がその表面に向かって伸び，第二のナノ寸法物質中に電気双極子を励振する様子を示しているが，ここで重要なのは次の二点である．(a)二つのナノ寸法物質が近接場光を媒介として局所的電磁相互作用を行い，相互に結合した状態になっている．〔したがって物質の屈折率などの物理量の値が結合状態に依存して変化する．更に，入射光の波長程度の空間寸法にわたる物理量の平均化近似が有効でなくなる．〕(b)このように結合した微小な系（ナノ系と呼ばれている）が，それよりずっと寸法の大きな巨視系（ナノ寸法物質用の基板，入射光，光検出器等）に囲まれている．〔したがって伝搬光を使う場合には見られないエネルギーの移動（非共鳴エネルギー移動と呼ばれている）が二物質間で起る⑷．すなわちナノ系のみに注目するとエネルギー保存則からのずれが生じる．ただしそのエネルギーの過不足分は上記の巨視系から補てんされるのでナノ系と巨視系とを合わせた全体ではエネルギー保存則は成り立つ．〕

用　語　解　説

回折　既存の光技術では光を波として扱うが，光波は微小な穴を通り抜けた後に発散する．光波を絞って光ファイバの中を伝送させても出射後は発散する．この発散性は回折と呼ばれている．

回折限界　回折のために凸レンズで集光しても焦点面上では光の波長程度の寸法のスポット径までしか絞れない．このピントのぼけのために光を使った計測，加工，デバイス動作は光波長程度以下の寸法を扱うことができない．これは回折限界と呼ばれている．

ナノフォトニクスの本質は上記の二点に注目し，特に〔　〕内に指摘した特徴を生かすことにより，従来の伝搬光を用いた光技術では原理的に実現不可能な現象や機能等を実現して使うことである．その系の寸法がナノメートル程度に小さくなることは副次的な成果にすぎない．

3.　ナノ光デバイスを実現し，それを集積化する

光ファイバ通信の技術ロードマップによると 2015 年には高度情報化社会を支えるために 10Tbit/s のデータ転送速度が必要で，そのためには光交換機用の光スイッチ配列中の入出力端子数は各々 1,000 またはそれ以上必

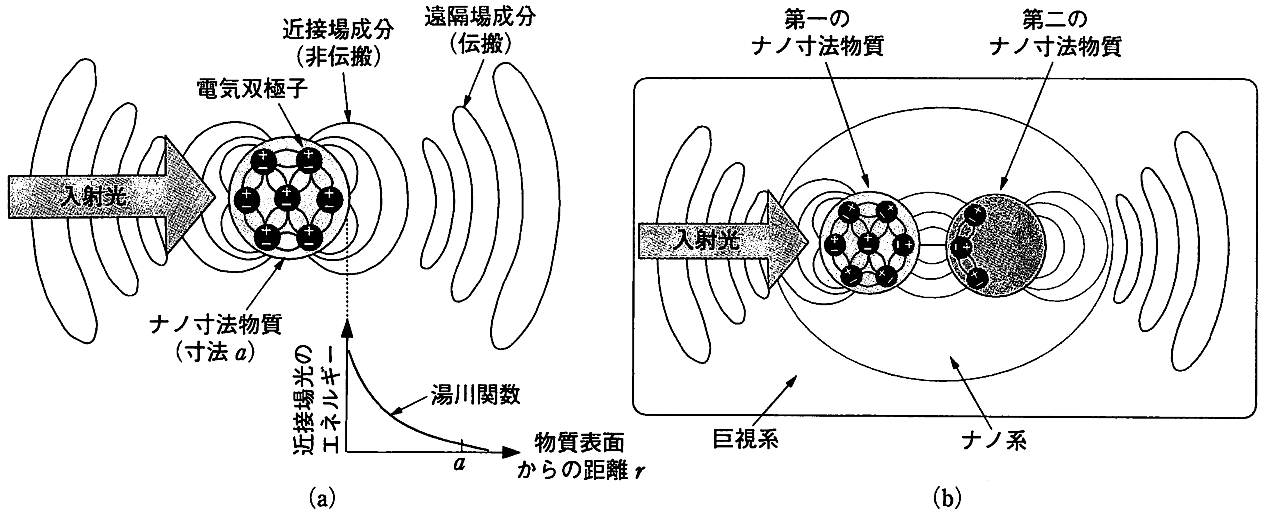

図 2　巨視系に囲まれたナノ系としての近接場光とナノ寸法物質　（a）近接場光の発生の様子とそのエネルギーの空間分布，（b）巨視系（基板，入射光等）に囲まれたナノ系の中で，ナノ寸法物質が近接場光を媒介として局所的電磁相互作用をする様子.

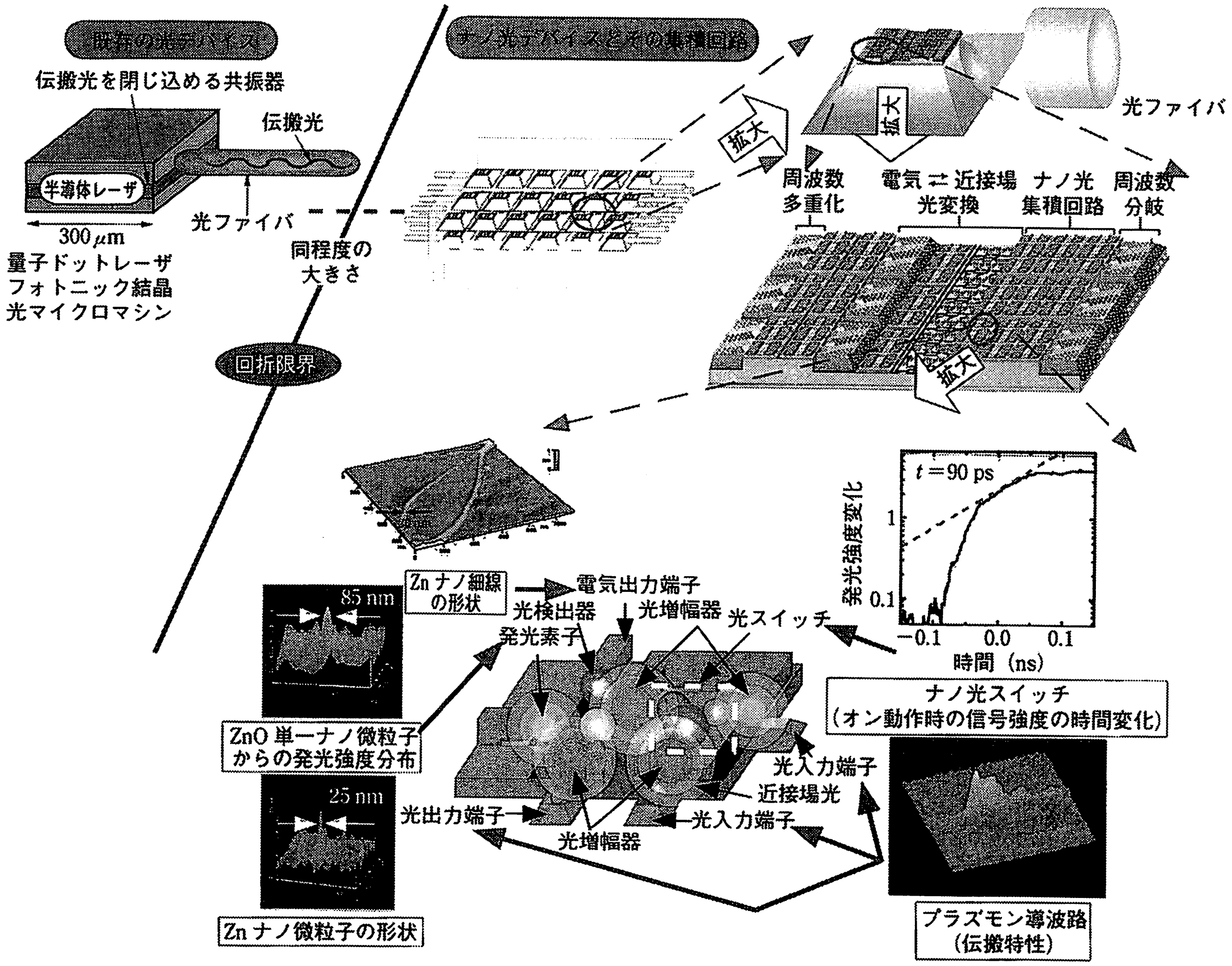

図 3　ナノ光デバイスとその集積回路　寸法比較のために既存の光デバイスの例も示す．ナノ光デバイスの構成要素は少数個のナノ寸法物質であり，情報のキャリヤとして近接場光を用いる．既存の光技術で作られた外部の大寸法の光デバイスと接続するためのインタコネクション（光入力端子，光出力端子）はプラズモン導波路が担う．現在までに図下部に示すように金属細線，微粒子，発光体，プラズモン導波路などが作られている．これらの形状，発光強度の空間分布，プラズモン導波路の伝搬特性，更には図 4 のナノ光スイッチの動作時間（CuCl 量子ドットの場合，90ps）の測定結果を示している.

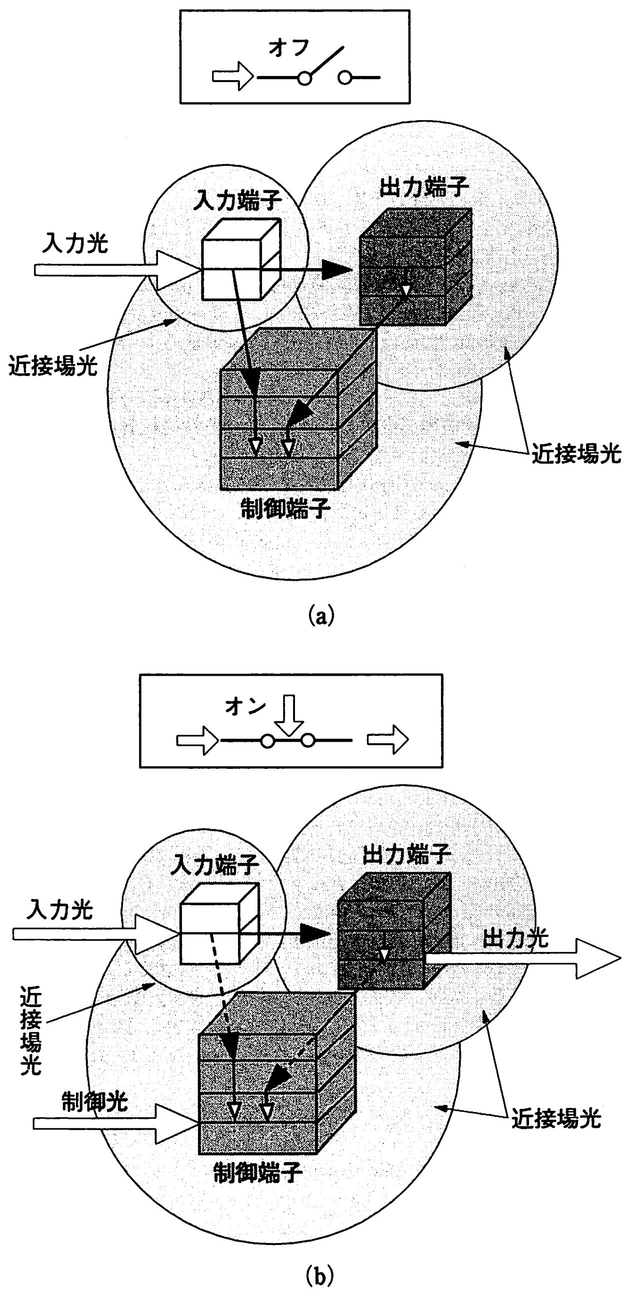

図4　ナノ光スイッチの動作原理　ナノ寸法物質としては寸法比 $1:\sqrt{2}:2$ の三つの半導体量子ドットを各々入力，出力，制御端子として用いる．量子ドット間の近接場光エネルギー移動，各量子ドット内のエネルギー緩和を利用してスイッチング動作を実現する．(a)，(b)は各々光スイッチがオン，オフの状態を表す．

要と推定されている(5)．これらの要求を満たし，更に次世代のシステムへの発展を目指すには光スイッチ配列中の各光デバイスの寸法を回折限界を超えて微小化しなければならない．これは既存の光デバイスやマイクロマシン技術によるデバイスでは困難で，光デバイス構築の概念のパラダイムシフトが必要である．そのためには近接場光を用いたナノ光デバイスとその集積化が唯一の解を与える(6)．この新概念に基づく集積回路の構成の代表例を図3に示す(7)．これは近接場光を媒介とするナノ寸法物質間の局所的電磁相互作用を利用し，個々のナノ寸法物質に近接場光の発生，スイッチング，検出などの機能を発現させ，情報のキャリヤとしての近接場光をナノ寸法物質間で伝送するものである．社会の要求にこたえるためにこのシステムは次の特徴を持つ．

（1）　光スイッチング動作には図4に示すように特定の寸法比の関係を有する三つの量子ドット間の局所的電磁相互作用（2. 末尾の(a)で指摘）による近接場光エネルギー移動と各量子ドット内のエネルギー緩和とを利用している．伝搬光ではこれらの量子ドット間の光エネルギー移動のための光学遷移は禁制されているが，近接場光ではエネルギーがナノ寸法領域に局在するのでこの禁制が解ける(8)．すなわちエネルギーの移動は近接場光の場合にのみ可能であり，これは光デバイス構築の概念のパラダイムシフトの典型である．

（2）　既存の光技術で作られた外部の大寸法の光デバイス（例えば光ファイバなど）と接続して光システムを構築するためのインタコネクションを配備している．これは図3の光デバイス中の近接場光を伝搬光に変換して外部に伝送すること，またはその逆の働きをする．半導体と金属細線から構成されたプラズモン導波路がこの機能を担っている(9)．

図3の集積回路を実現するために，既にZnOナノ微粒子の青色発光やCuClの三つの量子ドットを組み合わせた光スイッチング機能等の実験及び理論的研究が行われている(8)．特に光スイッチングデバイスについては，社会の要求にこたえるために必要な性能を表す性能指数 F が定義され既存の光技術による光スイッチングデバイスと比較されている．すなわちスイッチング時間 t_{sw}，集積度（言い換えるとスイッチングデバイス体積 V），オンオフ時の出力信号強度比（コントラスト）C，動作に必要な電力（言い換えると動作光子数 n_p）を用いて $F = C/t_{\mathrm{sw}}Vn_p$ により定義すると，本素子及び既存の光スイッチングデバイスの性能指数 F_n，F_c の比は $F_n/F_c = 10^2 \sim 10^3$ となり，本デバイスの性能の優位性が理解できる．一般にナノテクノロジー関連のデバイスを評価するときに重要なのはシステム内でのこのような性能の高さである．単に微小であったり，高速であるだけでは不十分である．

4.　ナノ光デバイス用の物質を作る

図3の集積回路を作るには作製対象のナノ寸法物質の寸法，位置，間隔に関する精度が高い加工技術が必要である．この精度はナノ寸法物質間で近接場光を伝送するために不可欠である．更に共通基板の上に多様な物質をたい積できることも重要である．なお，ナノ光デバイスは少数個のナノ寸法物質から構成されるので，大面積に

わたる一括加工などの高速性に対する要求は副次的となる．既存の加工技術では高速性には優れるもののこれらの要求を満たさない．例えば自己組織化などの微小物質たい積法は熱平衡と化学反応とを利用した集団的方法なので，基板面内での個々のナノ寸法物質の寸法，位置，間隔の制御性は高くない．したがって加工技術に関するパラダイムシフトが必要である．

そのためには近接場光を使った化学気相たい積法が有望である．これまでにZn,Alなどの金属，ZnOなどの酸化物の微小パターンなどが形成されている(10)．特に半導体のエネルギー構造を有するZnOの単一ナノ寸法微粒子からの青色発光(11)，その量子サイズ効果(12)などが確認されている．このほかGaAs,GaNなどの化合物半導体のたい積も可能である．

一例として気相の$Zn(C_2H_5)_2$分子を解離してZnをたい積する場合，伝搬光で分子中の電子を励起・解離するには紫外線が必要であったが，近接場光の場合は光子エネルギーの低い青色光や赤色光，すなわち気相の$Zn(C_2H_5)_2$分子に対して非共鳴の光を用いても可能であることが確認されている．これは2.の(a)，(b)に起因し，図4の光スイッチング動作と同じくナノフォトニクス技術による微細加工の概念のパラダイムシフトである(13)．この現象は近接場光を用いれば伝搬光による化学気相たい積に用いられていた光源と分子種との組み合わせの制限から解放されて，新しい物質をたい積できるという技術的ブレークスルーをもたらすことを意味している．

5. まとめと展望

図3に示したナノ光デバイスと集積回路の実現に向けた研究開発が進められており，4.で述べた微細加工技術によって現在までに図3下部に示すような要素が試作されている(14)．一方，光情報記録システム用の1Tbit/in^{2}級高密度光メモリも2010年の社会から要求されることが推定されているが，これをナノフォトニクスの技術によって実現する試みが進んでいる(1)．ここで重要なことは高い信頼性を確保するため，ナノテクノロジーの代表的装置である走査トンネル顕微鏡で採用されているプローブは排除し，記録再生ヘッドには平面型のスライダが採用されている点である．ただし記録再生のためには可動部としてのヘッドは排除されていない．

ナノテクノロジーにおいて可動部のあるシステムは不利であり，将来は図3のような平面埋込み型のナノ光集積回路を新形態の光メモリ用デバイスとして利用することも検討すべきであろう．すなわち，ナノフォトニクスではナノテクノロジーに用いられている走査トンネル顕微鏡のプローブ走査，及び試料と接近させる点接触の二つの概念を排除するべきである．

文　献

(1) 大津元一，“ナノフォトニクスとその展望，” 信学誌，vol.84, no.1, pp.26-32, Jan. 2001.

(2) 大津元一，ナノ・フォトニクス，米田出版，千葉，pp.12-26, 1999.

(3) 大津元一，光の小さな粒，裳華房，東京，pp.19-35, 2001.

(4) K. Kobayashi and M. Ohtsu, “Quantum theoretical approach to a near-field optical system,” J. Microsc., vol.194, no.2, pp.249-254, Feb. 1999.

(5) 光テクノロジーロードマップ報告書(情報通信分野)，(財)光産業技術振興協会（編），(財)光産業技術振興協会，東京，1998.

(6) M.Ohtsu, Near-Field Nano/Atom Optics and Technology, Springer-Verlag, Berlin, pp.31-69, 1998.

(7) M.Ohtsu, “Near-field nano-optics toward nano/atom deposition,” Technical Digest of the 18th Congress of the International Commission for Optics, SPIE Press, New York, pp.478-479 , 1999.

(8) T.Kawazoe, K. Kobayashi, J. Lim, Y. Narita, and M. Ohtsu, “Direct observation of optically-forbidden energy transfer between CuCl quantum cubes by optical near-field spectroscopy,” Phys. Rev. Lett., vol.88, no.6, pp.067404 (1)-(4), Feb. 2002.

(9) T.Yatsui, M.Kourogi, and M.Ohtsu, “Plasmon waveguide for optical far/near-field conversion,” Appl. Phys. Lett., vol.79, no.27, pp.4583-4585, Dec. 2001.

(10) M. Ohtsu, K. Kobayashi, H. Ito, and G.-H. Lee, “Nanofabrication and atom manipulation by optical near-field and relevant puantum optical theory,” Proc. IEEE, vol.88, no.9, pp.1499-1518, Sept. 2000.

(11) 上田　稔，八井　崇，李　謹炯，興梠元伸，大津元一，“近接場光CVDによるZnOナノドットの作製，” 第49回応物春季予稿集，応用物理学会，東京，vol.3, p.1016, March 2002.

(12) T. Yatsui, T. Kawazoe, T. Shimizu, Y. Yamamoto, M. Ueda, M. Kourogi, M. Ohtsu, and G.H. Lee, “Observation of size-dependent features in the photoluminescence of zinc oxide nanocrystallites by near-field ultraviolet spectroscopy,” Appl. Phys. Lett., vol.80, no.8, pp.1444-1446, Feb. 2002.

(13) T.Kawazoe, Y.Yamamoto, and M.Ohtsu, “Fabrication of nanometric Zn dots by nonresonant near-field optical chemical vapor deposition,” Appl. Phys. Lett., vol.79, no.8, pp.1184-1186 , Aug. 2001.

(14) M. Ohtsu, K. Kobayashi, T. Kawazoe, S. Sangu, and T. Yatsui, “Nano-photonics : Design, Fabrication, and Operation of Nanometric Devices using Optical Near Fields,” IEEE J. Sel. Top. Quantum Electron., vol.8, no.4, July/Aug. 2002, 出版予定

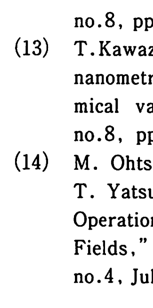

おおつ　もといち
大津　元一　(正員)

昭48東工大・工・電子卒．昭53同大学院博士課程了．同年東工大助手．以来，光エレクトロニクス，近接場光学の研究に従事．現在，同大学教授．工博．昭63日本IBM科学賞，平10井上学術賞，平14表面技術協会論文賞各受賞．平10～現在，科学技術振興事業団創造科学技術推進事業，「局在フォトン」プロジェクト総括責任者兼任．

特集

ナノフォトニクスの新展開

総論：ナノフォトニクスとは何か？ その目指す方向は？

東京工業大学
大津元一

1 なぜ今ナノフォトニクス？

ナノフォトニクスとは筆者が約8年前に命名したもので，光によるナノテクノロジーと理解していただければよい(注)。最近になって各所でこの名前を目にする機会が増えてきたが，この技術を可能にするには

(1) 使用する材料がナノ寸法であること，
(2) 光がナノ寸法であること，

の2点が必要である。

社会は光のナノテクノロジーを必要としているのであろうか？　この疑問に対しては光産業のロードマップが回答を与える。すなわち光情報通信，光情報記録の技術

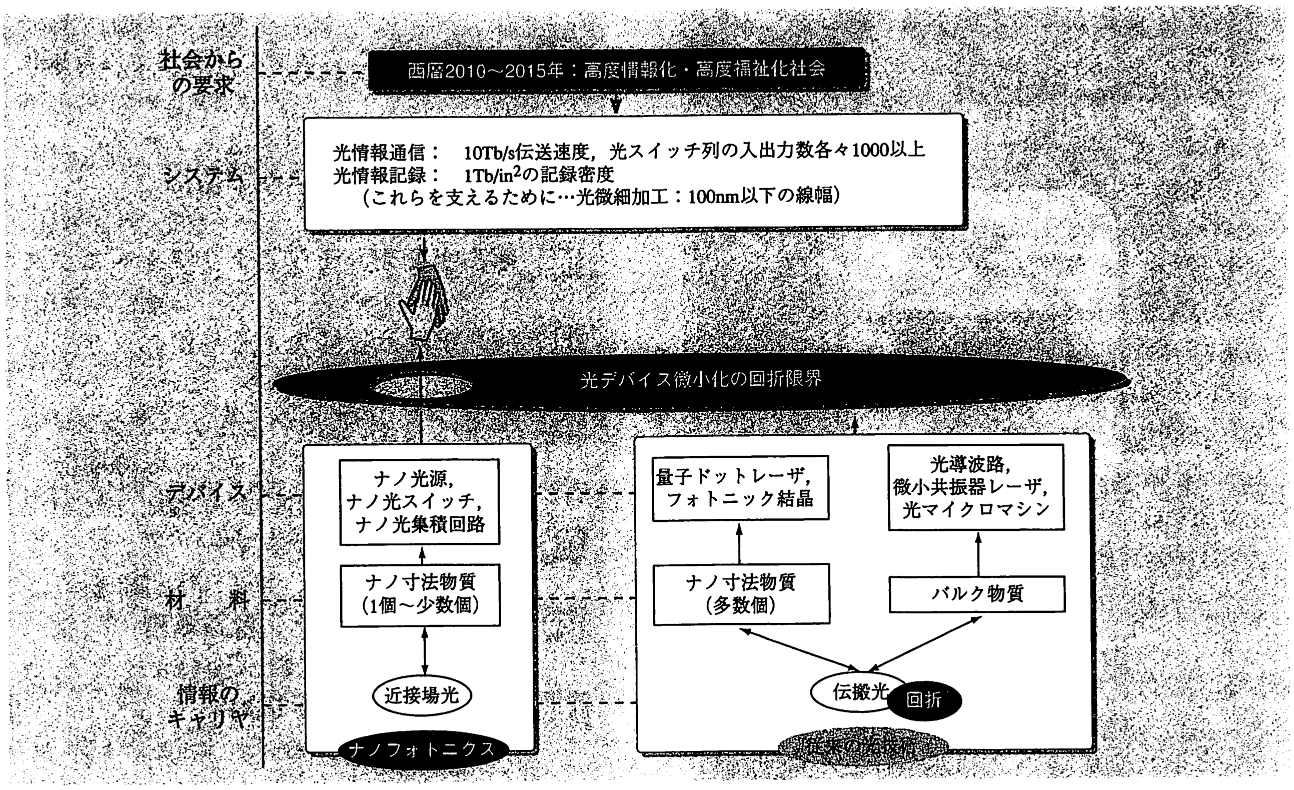

図1　ナノフォトニクスとその必要性

ロードマップによると[1,2]，西暦2010～2015年の高度情報化社会，高度福祉社会は伝送速度10Tb/sに達する超高速光ファイバ通信網，記録密度1Th/in^{2}に達する超高密度光メモリなどを要求している。これを実現するためには各々100nm以下の寸法の光スイッチによる入出力数各々1000以上の光スイッチ列，数10nm寸法のピットの光記録再生などの実現が不可欠である。

ところで光情報通信用の光デバイスとして多数個のナノ寸法材料を用いた最近量子ドットレーザ，フォトニック結晶などが提案されている。これらのデバイス用材料である量子ドットなどの寸法は数ナノメートルに達するので上記の（1）を満たす。しかし使う光は従来どおりの伝搬光なので，その光の広がろうとする性質（回折）のために上記の（2）は満たさない。従ってこれらのデバイスの寸法は光波長以下にならず，上記のような100nm以下の寸法には達しない。この値を実現するには光もナノ寸法化すること，すなわちナノフォトニクスが必要である[3-9]。以上の状況を図1に示す。

2　ナノフォトニクスの本質は何か？

前節中の（2）に記した光のナノ寸法化は近接場光によって実現する。本節ではナノフォトニクスの本質について説明するために，まず近接場光の説明から始める。近接場光の発生，検出の過程を直感的に把握するための最も単純なモデルは単一の電気双極子を用いるものである[10]。真空中で時間的に振動する電気双極子モーメントpから発生する電磁場の電気力線は図2のようになる。この図の中心部の電気力線が近接場光に対応する。これはpから発してpに終端しているので非伝搬光であることを表している。一方その外側にある閉曲線状の電気力線は遠隔場領域へと回折しながら伝搬する光を表している。従来の光技術で使っているのはこの光である。

ナノフォトニクスでは基板その他の巨視的寸法の物質系に囲まれるナノ寸法物質を扱う。特にこの物質の寸法が波長にくらべずっと小さい場合を扱うが，この物質の寸法は，それを量子論で記述したときの状態関数の広がりの程度を表すドブロイ波長よりは大きいものとする。これに光を照射すると物質中の多数の原子に電気双極子が誘起され，各々が図3(a)に示すように近接場光と伝搬光とを発生する。この物質中のすべての電気双極子から発生する近接場光の総和は次の2つの性質を持つ。

(1) 非伝搬である。いいかえると物質表面に局在している。

(2) エネルギーは物質表面から遠ざかるにつれ減少する。その減少の度合いを表す「しみ出しの厚み」は物質の寸法程度である。

図3(b)のように第一のナノ寸法物質表面に近接場光を発生させ，それを微小光源として用いて第二のナノ寸法物質に近づけて照明すると，第二のナノ寸法物質を加工したり，あるいは近接場光のエネルギーを伝送することにより回折限界を超えた微小な光技術が可能となる。これがナノフォトニクスである。この図は第二のナノ寸法物質に近づけると近接場光の電気力線がその表面に向かって伸び，第二のナノ寸法物質中に電気双極子を励振する様子を示しているが，ここで重要なのは次の二点である。

(a) 二つのナノ寸法物質が近接場光を媒介として局所的電磁相互作用を行い，相互に結合した状態になっている。【従って物質の屈折率など，従来の光技術で

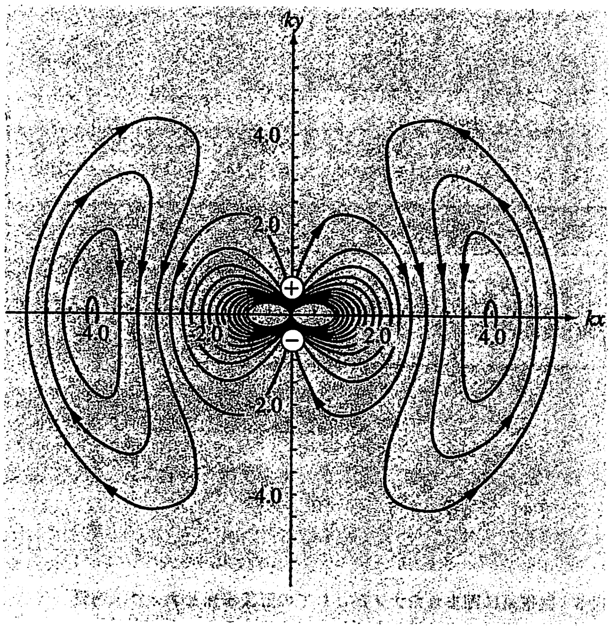

図2　電気双極子モーメントpがその周囲の空間に作る電場の電気力線。横軸，縦軸は各々kx，kyで示している。kは波数

は物質固有と考えられていた物理量の値が結合状態に依存して変化する。さらに，伝搬光との相互作用を考えるときに採用されていた，入射光の波長程度の空間寸法にわたる物理量の平均化近似が有効でなくなる。】

(b) このように結合した微小な系（ナノ系と呼ばれている）が，それよりずっと寸法の大きな巨視系（ナノ寸法物質用の基板，入射光，光検出器等から成る）に囲まれている。【従って伝搬光を使う場合には見られないエネルギーの移動（非共鳴エネルギー移動と呼ばれている）が二物質間で起こる。すなわちナノ系のみに注目するとエネルギー保存則からのずれが生じる。ただしそのエネルギーの過不足分は上記の巨視系から補填されるのでナノ系と巨視系とを合わせた全体ではエネルギー保存則は成り立つ。この他，運動量，角運動量の保存についても同様のことがいえる。】

ナノフォトニクスの本質は上記の (a)，(b) に注目し，特に【　】内に指摘した特徴を生かすことにより，従来の伝搬光を用いた光技術では原理的に実現不可能な現象や機能等を実現して使うことである。その系の寸法がナノメートル程度に小さくなることは副次的な成果にすぎない。すなわちナノフォトニクスとは少数個のナノ寸法物質と近接場光との間の固有の局所的電磁相互作用を用

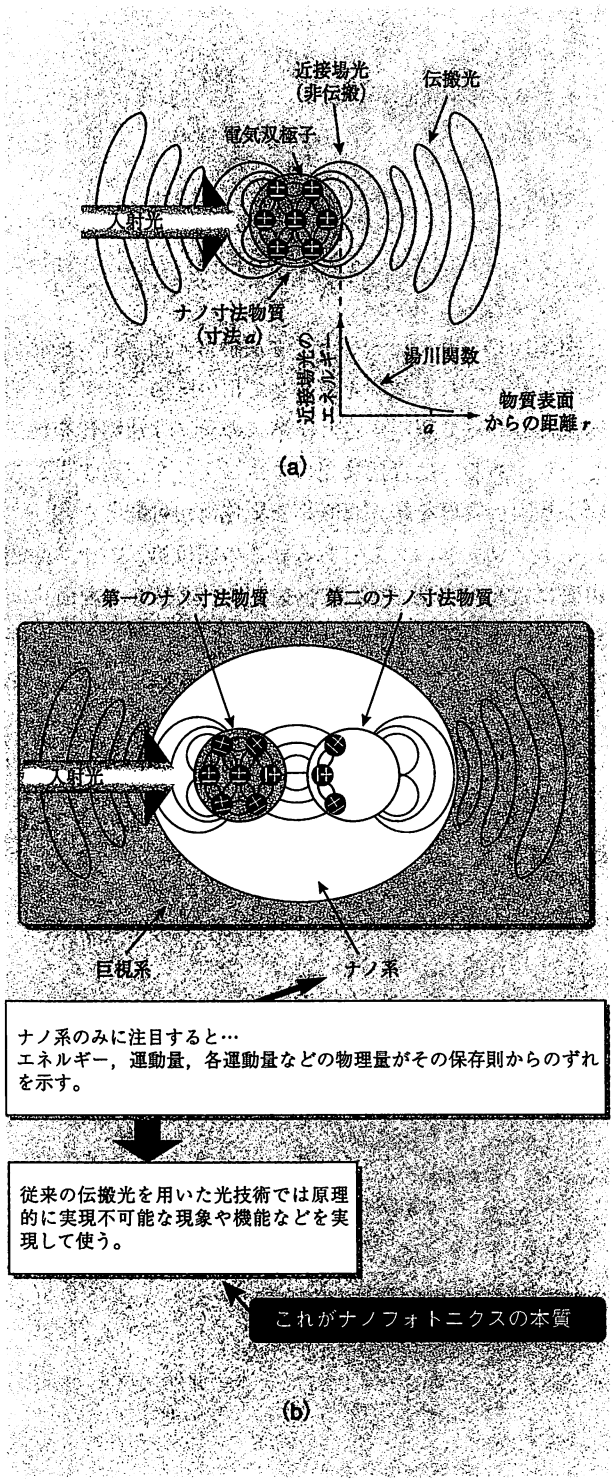

図3　巨視系に囲まれたナノ系としての近接場光とナノ寸法物質
(a) 近接場光の発生の様子とそのエネルギーの空間分布
(b) 巨視系（基板，入射光等）に囲まれたナノ系の中で，ナノ寸法物質が近接場光を媒介として局所的電磁相互作用をする様子

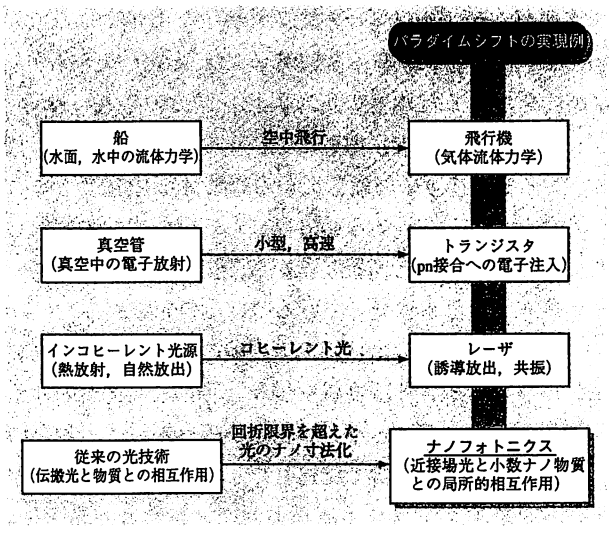

図4　技術のパラダイムシフトの実現例

いた新しい光技術であり，ここでは波動光学の代表的な現象である干渉や，従来の基本デバイスであるレーザなどの概念は主役の座を降りる。すなわち光技術のパラダイムシフトといえる。過去の技術のパラダイムシフトの例は図4にあるように船→飛行機，真空管→トランジスタ，熱光源→レーザなどがあるが，従来の光技術→ナノフォトニクスはこれに匹敵する。

3 ナノフォトニクスの目指す方向

ナノフォトニクスはナノ寸法の近接場光を使う光技術なので，原理的には従来の光技術の大部分を取って代えることが出来る。その代表的な展開の方向として本特集号はナノ寸法光デバイス，超高密度光メモリ，ナノ光加工の技術開発の現状と将来，それらに対するシステム側からの要求，さらにはこれらを支える計測技術などについてトップランナーの研究者技術者による解説記事を掲載する。繰り返しになるがその中で重要なのは，前節の特徴（a)，(b）に基づき，従来の伝搬光を用いた光技術では原理的に実現不可能な現象や機能等を実現して使うことである。たとえばナノ光デバイスの動作原理，化学気相堆積の素過程にそのような際だった特徴が見られるので該当する個所をご一読いただきたい。

同時に重要なことは注目するナノ寸法の物質系と周囲の巨視的な系との間の光信号の授受である。これは一般ユーザーが使えるシステムを構成するために不可欠である。たとえばナノ光デバイスに関しては，外部の巨視的寸法の光デバイスとの光信号の授受のためのインターコネクション用デバイスが必要である。このようなデバイスについても本特集号の中の記事で取り扱われる。

参考文献

1）(財)光産業技術振興協会編，光テクノロジーロードマップ報告書（情報通信分野)，(財)光産業技術振興協会，(1998)
2）(財)光産業技術振興協会編，光テクノロジーロードマップ報告書（情報記録分野)，(財)光産業技術振興協会，(1998)
3）大津元一，ナノ・フォトニクス，米田出版（1999)
4）大津元一，近接場光の基礎，オーム社（2002)
5）M. Ohtsu, *Near-Field Nano/Atom Opticds and Technology*, Springer-Verlag (1998)
6）M. Ohtsu and H. Hori, *Near-Field Nano-Optics*, Kluwar Academic/Plenum Publishers (1999)
7）大津元一，光の小さな粒，裳華房（2001)
8）M. Ohtsu, K. Kobayashi, H. Ito, and G.H. Lee, Proc. IEEE, vol.88, no.9, pp.1499～1518 (2000)
9）M. Ohtsu, K. Kobayashi, T. Kawazoe, S. Sangu, and T. Yatsui, IEEE J. Selected Topics in Quantum Electronics, vol.8, no.4, July/August 2002, 印刷中
10）大津元一，光学，第31巻，第2号，pp.120-127 (2002)

■An introduction: What are nanophotonics and its future?

■Motoichi Ohtsu

■Interdisciplinary Graduate School of Science and Engineering, Tokyo Institute of Technology, Also with Ohtsu's Localized Photon Project, ERATO, Japan Science and Technology Corp.,

■As an introduction to the special issue on nanophotonics, this article reviews the present and future of nanophotonics based on requirements from the future optical transmission and optical storage systems. In order to describe the principle of nanophotonics, interaction between nanometric matters and optical near field are also reviewed.

オオツ　モトイチ
所属：東京工業大学大学院　総合理工学研究科教授，科学技術振興事業団　創造科学技術推進事業大津局在フォトンプロジェクト
連絡先：〒226-8502　横浜市緑区長津田町4259
Tel. 045-924-5455　Fax. 045-924-5599
E-mail：ohtsu@ae.titech.ac.jp

経歴：昭53同東工大大学院博士課程修了。現在，同大学教授。工学博士。ナノおよびアトム・フォトニクスの研究に従事。昭63日本IBM科学賞，平10井上学術賞など受賞。著書「ナノ・フォトニクス」など。

（注）(財)光産業技術振興協会では筆者の提案により1995年に「ナノフォトニクス懇談会」が発足し，現在に至っている。

特集

ナノフォトニクスの新展開

ナノフォトニクスデバイスとその集積化

科学技術振興事業団
川添　忠

1　はじめに

近年の情報通信分野の発展は目覚しいものがある。特に光ファイバー通信など光を用いた通信技術は情報通信の主翼を担い，通信の高速大容量化とともにますます重要性が高まると考えられる。情報通信の高速大容量化に対応するためには，光情報を制御するための光デバイスも高性能化する必要があると同時に微細化も必要となる。例えば，10年後に必要とされる1000×1000の光マトリックス交換機を既存の光デバイス（1mm×1mm）で実現すると極めて巨大になり，現実的ではない。また，電子デバイスがそうであったように，光デバイスの微細・高集積化は光デバイスを高性能・高機能化していくと考えられ，その応用は単なる光交換機に留まらず，光コンピュータなどより高機能な光集積デバイス実現に広がっていくと考えられる。

光デバイスにおける微細化の最大の障害は光の回折限界である。光の回折のため，レンズなど光の波動性を利用した既存の光技術では波長程度の大きさ（1μm程度）にしか集光させることが出来ず，光デバイスの微細化の限界点となる。我々はこのような既存の光技術の限界を超えるため，光の回折限界を越えたナノメートル領域にエネルギーが集中する光，すなわち近接場光を作り，その実体を研究し，応用することを目標に研究を行っている。近接場光を用いたナノフォトニクスデバイス実現は我々の最終目標の一つである。図1に我々の提案している近接場光を用いたナノ光集積回路[1-3]の概念図を示す。光信号は集積回路チップに光ファイバー等で入力され，近接場光に変換された後，周波数分離され，それぞれナノフォトニクスデバイスへ導かれる。1個のデバイスは光近接場で結合した複数の量子ドットで構成されており，1つのデバイスサイズは100nm以下である。信号の入出力および、デバイス間の信号伝送はプラズモン導波を利用したナノプラズモン導波路で接続される。本稿で

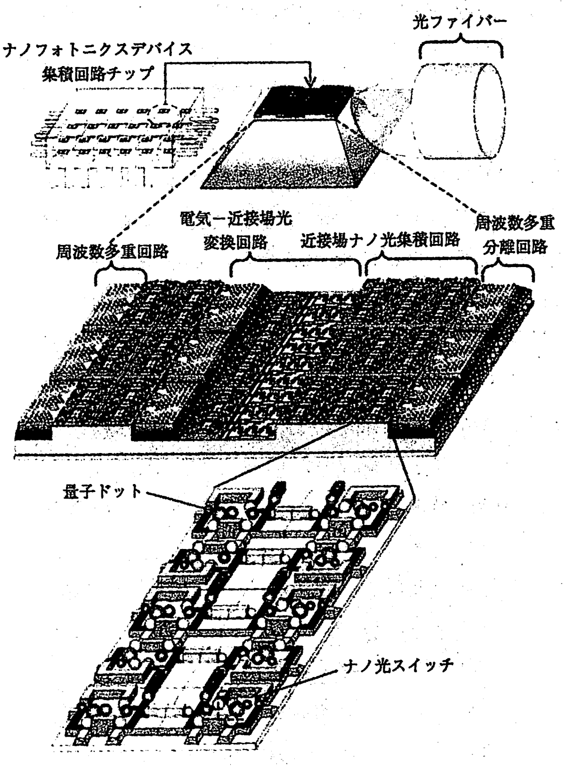

図1　光近接場によるエネルギー移動を利用したナノ光集積回路

はまずナノフォトニクスデバイスの代表例として近接場光を用いたナノ光スイッチの動作原理および検証実験について述べ，続いてナノプラズモン導波路に関する実験結果を示す。

2　近接場光を用いたナノ光スイッチ

図2に我々が提案する近接場光を用いたナノ光スイッチデバイスを構成する3個の量子ドットとそれらのエネルギーレベルを表した図を示す。量子ドットの形状が立方体（量子箱）である場合，1辺Lの量子箱に閉じ込められた光励起担体は量子化され，

$$E_{n_x,n_y,n_z} = E_B + \frac{\hbar^2\pi^2}{2ML^2}\left(n_x^2+n_y^2+n_z^2\right) \qquad (1)$$

で示されるようなエネルギー準位をとる。ここでE_Bはバルク結晶における担体のエネルギー，Mは担体の有効質量，n_x, n_y, n_z （=1,2,3…） は主量子数である。(1)式から，量子箱サイズがL ,$\sqrt{2}L$ $2L$, の量子閉じ込め準位を考えると，量子箱Cube1中の励起子閉じ込め準位$E_{1,1,1}$と量子箱Cube2中の$E_{2,1,1}$が共鳴し，同様に量子箱Cube3中の$E_{2,2,2}$とも共鳴する。このような共鳴状態の量子ドットは光近接場により強く結合し，小林らの近接場相互作用の理論によると共鳴する量子ドット間に働く相互作用は，

$$V(r) = A\frac{\exp(-\mu\cdot r)}{r} \qquad (2)$$

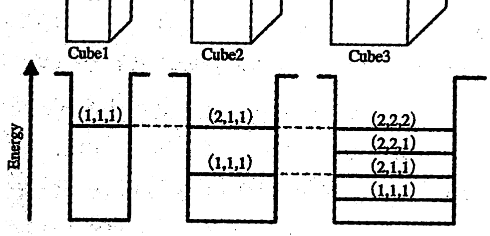

図2　立方体形状をした量子ドット（量子箱）と量子準位

のような湯川関数であらわされる[4)]。ここでrは量子箱間の距離である。A及びμは実験により求める係数であるが，注目するエネルギーレベルの振動子強度等からおよその値が計算でき10nm離れた量子箱間においては100ピコ秒以下でのエネルギー移動が可能であることが求められる。この値は量子ドットを構成する半導体の担体の寿命数ナノ秒に比べ十分早く，また数ピコ秒以下の量子ドット中のサブレベル間緩和よりも十分遅いため，光近接場が支配的となる領域に図2に示すように量子箱が隣接している場合，量子箱Cube1に作られた光励起担体は光近接場を介して隣接する量子箱Cube2へ移動することが予想される。そして最終的には最もエネルギーレベルの低い量子箱Cube3へ励起が移動する。

これら3個の量子箱をそれぞれ入力，出力，コントロール端子と見なし，図3にスイッチのオフ動作状態，オン動作状態の概略図を示す。図中のコントロールドットの準位が空いている場合，入力ドットへ入力された励起エネルギーの一部は出力ドットに移動するが，そこに留まって発光することはできず，コントロールドットまで緩和する。よって，出力ドットから発光できずスイッチの出力が0となりオフ動作が実現される。オン動作はコントロールドットを外部からの制御光で励起することでコントロールドットの準位を埋め，コントロールドットへのエネルギー移動を制限し，入力ドットに存在する励起エネルギーを光近接場によって隣接する出力ドットへ移動させ，そこで発光させることで実現する。

このスイッチ動作の過程で最も重要な物理現象が量子ドット間のエネルギー移動である。光近接場相互作用によるエネルギー移動を観測するため近接場顕微分光を行

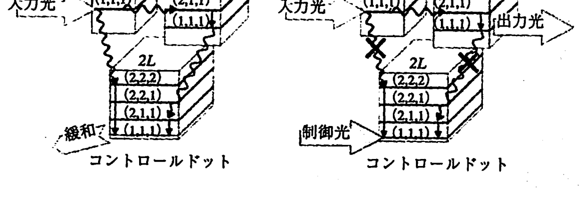

図3　サイズの異なる3つの量子箱を利用したナノ光スイッチのオン動作とオフ動作

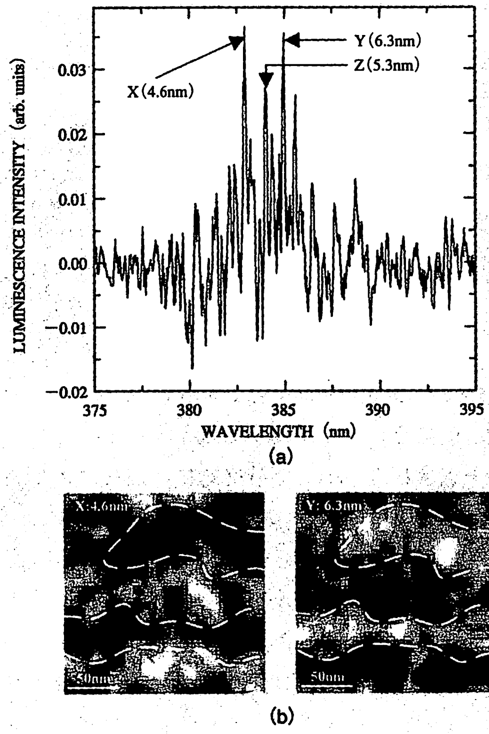

図4
(a) NaCl結晶中に分散成長させたCuCl量子箱の光近接場発光スペクトル
(b) サイズ4.6nmの量子箱からサイズ6.3nmの量子箱へのエネルギー移動を示す発光強度分布

った[5)]。実験には厚さ約100μmのNaCl結晶中に成長させたCuCl量子箱を用いた[6)]。吸収スペクトルから求めたCuCl量子箱の平均サイズは4.3nmであった。測定の直前に劈開した試料を用いたので，シアフォースによる近接場プローブの位置制御のためには十分な試料面の平滑さが得られた。励起子のサブレベルを分離するため15 Kにて測定を行った。図4に集光モードにおける近接場光学顕微鏡による発光スペクトルの測定結果を示す。励起光源にはHe-Cdレーザ（λ=325nm）を用いた。発光スペクトルはCuCl量子箱のサイズ不均一による広がりをもち，エネルギーを選択することで，そのエネルギーに対応するサイズの量子箱からの発光が選択可能となる。サイズの異なるCuClは発光波長が異なり，図中X，Yのピークはそれぞれ4.6nm，6.3nmのCuCl量子箱からの発光に対応し，光近接場を介した共鳴エネルギー移動が観測される条件を満たしている。すなわち，4.6nmのCuCl量子箱の励起子レベル$E_{1,1,1}$と6.3nmの量子箱の励起子レベル$E_{2,1,1}$は共鳴している。

図4(b)にX，Y各々の発光ピークの空間強度分布を測定した結果を示す。図中破線で囲まれた領域に注目すると発光強度分布が反転しているように見える。この発光強度分布の反転は次のように説明できる。用いた試料の量子箱の平均サイズが4.3nmであり，4.6nmのサイズの量子箱は6.3nmの量子箱に比べ圧倒的に多数存在し，測定された全領域にほぼ均一に存在する。しかし，光近接場相互作用が十分に強く働く領域に6.3nmの量子箱を持つ4.6nmの量子箱は発光できずにエネルギーを6.3nmの量子箱へ受け渡す結果，発光スペクトルとして観測されず暗い領域となる。そして，その領域では6.3nmの発光が強くなっていると考えられる。つまり，この発光強度分布の反相関はサイズ4.6nmの量子箱中の$E_{1,1,1}$レベルから6.3nmの量子箱中の$E_{2,1,1}$レベルへの共鳴エネルギー移動が起きたことを示している。このような強度分の相関は共鳴関係を満たさないサイズの量子箱からの発光強度分布では見られなかったこともこの共鳴エネルギー移動現象観測の証拠となった。エネルギー移動が起こった$E_{2,1,1}$レベルは光学禁制レベルであり，光学禁制レベルが光近接場により活性化したという意味で物理的にも大変興味深い現象である。言い換えるとこれは本特集号の「総論」で指摘されているように従来の伝搬光を用いた光技術では原理的に実現不可能な現象である。

用意したCuCl量子箱試料でスイッチ動作を検証するためには図3に示すような量子箱3個の組を試料中にランダムに分散した無数の量子箱から探し出して実験を行うことになる。図5に実際のオン・オフ動作の実験結果を示す。実験を行った3つの量子箱のサイズはそれぞれ，3.5nm，4.6nm，6.3nmであり，励起子のボーア半径を考慮すると（デットレーヤ効果）サイズ比はほぼ$1:\sqrt{2}:2$になっており図3に示したスイッチ動作の条件を満たしていると思われる。図5(a)はオフ動作時のスペクトルで6.3nmの量子箱からの発光のみが観測されている。一方(b)に示すように6.3nmの量子箱に共鳴する光，即ち制御光を入力することで4.6nmの量子箱からの信号が得られた。4.6nmの量子箱からの発光をスイッチ信号の出力と見なせばオン・オフ動作が実現したと見なせる。また，スイッチ信号の得られる領域の大きさを測定したところ

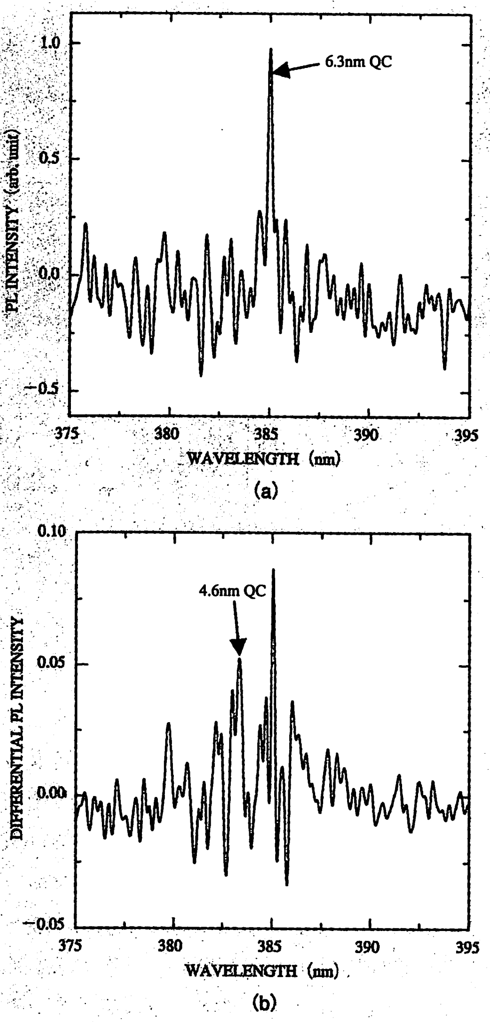

図5　近接場光を用いたナノ光スイッチの動作実験結果
(a) オフ状態　(b) オン状態

そのサイズは30nm以下であることが分かった。このサイズはデバイスサイズに相当する。さらに，信号強度から，この光スイッチの内部量子効率は1に近く高効率で動作することも分かった2)。以上の結果は我々が提案している近接場光を用いたナノ光スイッチの動作メカニズムが将来のナノ光スイッチとして有望であることを示している。

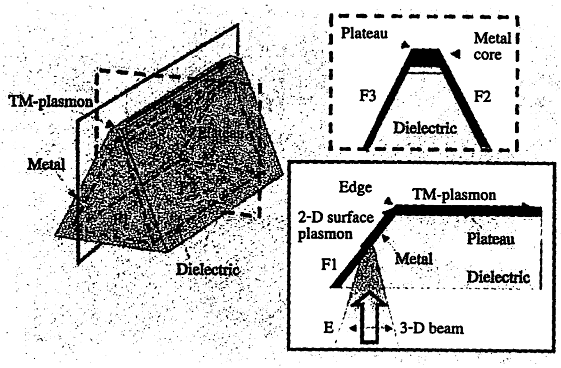

図6　ナノプラズモン導波路構造

3　ナノプラズモン導波路

ナノサイズで動作する光集積回路を外部の光デバイスにより動作させるためには，外部の光デバイスに用いられる伝搬光をナノサイズ集積回路が駆動可能な近接場光に変換する為のナノサイズの光導波路が必要となる。この導波路として要求される性能は下記である。

A.伝搬光から近接場光への変換効率が高いこと。

B.ナノサイズの光デバイス（100nm以下）に対し個別照射を可能とする為に，ビーム径が100nm以下であること。

C.励起光である伝搬光と直接結合することを防ぐ為に，伝搬距離が波長以上であること。

以上の性能を満たす伝搬光／近接場光変換用導波路として，金属コートシリコンウェッジを提案し試作した。図6に示す構造において，伝搬光がF1面において2次元の表面プラズモンに変換され，これがF1面とウェッジ先端面（プラトー）の境界であるエッジによって散乱し，この散乱光によってプラトーの金属部に1次元のTMプラズモンモードが励起されると考えられる。これは，金属をコートする際，プローブ上方から金属を蒸着することにより，プラトー部が他の面（F1，F2，F3）よりも金属膜厚が厚くなり，このプラトー部を金属コア導波路としてみなせる為である。この導波路の特徴として

a. F1とプラトーの境界面であるエッジにおける散乱結合により2次元プラズモンモードと1次元TMプラズモンモードの結合効率が高い。これは前述の要求Aを満たす。

b. TMプラズモンモードはカットオフ径が存在しないために，ビーム径を1nmまで細くすることが可能である。これは前述の要求Bを満たす。

c. TMプラズモンモードの伝搬距離は前述の要求Cを満

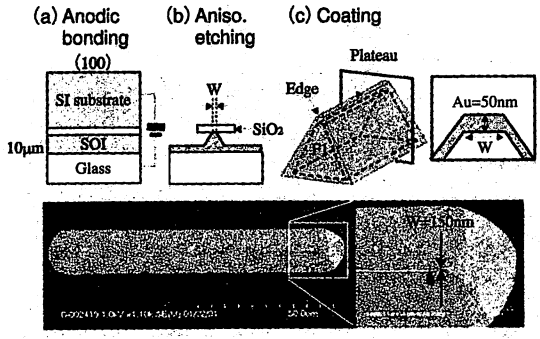

図7　ナノプラズモン導波路の作成法と作製された導波路の電子顕微鏡写真

たす程充分に長い。計算例として，コア径40nmの金属コア導波路（コア：金，波長：830nm）を伝搬するTMプラズモンモードの伝搬長は2.5μmである。

上記プラズモン導波路の作製方法を図7に示す。このような導波路を実現するために必要となる仕様として，表面プラズモンを高効率に励起させる平坦面なF1と均一な幅を有するプラトー，さらには散乱結合を高効率に誘起するための鋭利なエッジが挙げられる。この為，ウェッジ形状のパターニング時に，矩形のマスクをシリコンの結晶方位である〈110〉より30°傾斜して位置合わせを行った。これにより，異方性エッチング時のマスク角部におけるシリコンのオーバーエッチを抑制し，上記要求仕様を満たす形状のシリコンウェッジ（プラトー幅：150nm，プラトー長：80μm）を作製した。

作製したプラズモン導波路について，モード伝搬特性を評価した。測定には，開口径60nmのファイバプローブを用いた。このプラズモン導波路のF1面に波長830nmの光を対物レンズ（NA:0.2）により集光して入射し，プラトーに伝搬する導波モードの観測を行った。実験結果を図8に示す。(a)，(b) はそれぞれTM偏光時（入射偏光がプラトー方向に対して平行）のプラトー幅1μm・150nmに対する電界分布を示している。図 (c)，(d) はそれぞれTE偏光時（入射偏光がプラトー方向に対して垂直）の結果であり，(e)，(f) は (a)（A-A'，a-a'），(b)（B-B'，b-b'）における断面図である。ここで，透過効率（Transmission）はファイバによる検出強度を入射強度で規格化した値である。これらの結果は，TM偏光時のみプラトーに伝搬モードが観測されることを示している。図8 (e) において，白丸にフィッティングした破線より，プラトー幅150nmにおけるモードの伝搬距離は2.5μmであった。この値は，コア径40 nmの金とした円柱導波路における，波長830nmでのTMプラズモンモードの伝搬距離と一致している。また，プラトー幅1.0μmの伝搬距離は4.0μmとウェッジ幅150nmのそれよりも長かった。これは，プラトー幅が広くなることにより，等価屈折率が金と空気との界面に存在する表面プラズモンモードのそれに漸近するためである。これらの結果より，観測されたモードがTMプラズモンモードであることを示している。

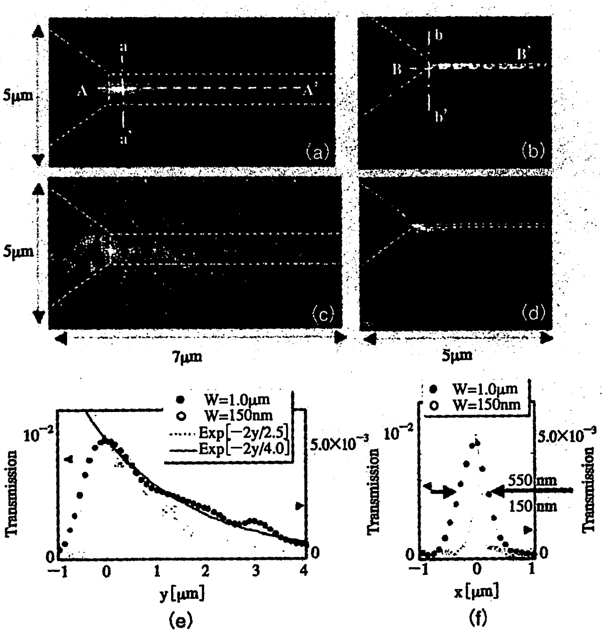

図8　プラズモン導波路の導波実験結果

図8 (f) が示すように，プラトー幅1.0μm・150nmに導波するビームの半値幅は550nm・150nmであった。プラトー幅をさらに細くすることにより，変換デバイスとして要求される性能Bを満たす。さらに，プラトー幅150nmの導波路の透過効率は5.0×10^{-3}と見積もられる。これは，150nmの開口径を持つファイバプローブと比較して一桁高い値であり[8]，この高効率な励起は，F1とプラトーとの境界であるエッジでの散乱結合によるものであろう。この高い透過効率は性能要求のAを満たす。最後に，入射波長よりも長いと見積もられる伝搬長は性

能要求のCを満たし，作製したプラズモン導波路が伝搬光／近接場光変換･伝送デバイスとして充分な性能を満たしていることが分かった[9]。

4　まとめ

本稿では近接場光を用いたナノフォトニクスデバイス実現に向けて我々が取り組んでいる研究の一端を紹介した。ここに紹介したように現在までにサイズ30nmの近接場光を用いたナノ光スイッチの動作原理検証実験に成功し，150nmのナノプラズモン導波路作製を行うなどの成果を上げている。このような波長以下の光デバイスの実現は光の波動性に基づく現状の光技術では難しい。我々は近接場光を光デバイスに積極的に応用することでナノフォトニクスデバイスの実現を目指している。そこには技術的な発明や発見があるだけでなく，新しい物理現象が現れることもあり，注意深く研究を進めて行きたいと考えている。なお，これらのナノフォトニクスデバイスの作製とその集積化のために近接場光を用いたナノ光加工法が開発されている。これについては本特集号の八井氏の記事を参照されたい。

参考文献

1）M. Ohtsu, K. Kobayashi, T. Kawazoe, S. Sangu, and T. Yatsui, IEEE J. Sel. Top. Quant. Electron, 8 （2002） to be published.
2）T. Kawazoe, K. Kobayashi, S. Sangu, and M.Ohtsu,J. Microscopy, （2002） to be published.
3）S. Sangu, K. Kobayashi, A. Shojiguchi, T. Kawazoe, and M. Ohtsu, J. Appl. Phys. submitted for publication.
4）K. Kobayashi, S. Sangu, H. Ito, and M. Ohtsu, Phys. Rev. A, 63, 013806-1-9 （2001）.
5）T. Kawazoe, K. Kobayashi, J. Lim, Y. Narita, and M. Ohtsu, Phys. Rev. Lett., 88, 067404-1-4 （2002）.
6）N. Sakakura and Y. Masumoto, Phys. Rev. B 56, 4051 （1997）.
7）J. Takahara, S. Yamagishi, H. Taki, A. Morimoto, and T. Kobayashi, Opt. Lett., 22, 475 （1997）.
8）T. Yatsui, M. Kourogi, and M. Ohtsu, Appl. Phys. Lett., 73, 2090 （1998）.
9）T. Yatsui, M. Kourogi, and M. Ohtsu, Appl. Phys. Lett., 79, 4583, （2001）.

■ **Nano-photonic device and Integration**

■ Tadashi Kawazoe
■ ERATO, Localized Photon Project, Japan Science and Technology Corporation

■ This paper reviews progress in nano-photonics, a novel optical nano-technology, utilizing local electromagnetic interactions between a few nanometric elements and an optical near field. A prototype of a nano-photonic integrated circuit is presented, in which the optical near field is used as a carrier to transmit a signal from one nanometric dot to another. A key device, the nano-photonic switch, is proposed and demonstrated based on optical near-field energy transfer between quantum dots. To connect the nano-photonic IC to external photonic devices, a nanometer-scale waveguide was developed using a metal-coated silicon wedge structure.

カワゾエ　タダシ
所属：科学技術振興事業団　大津局在フォトンプロジェクト研究員
連絡先：〒194-0004　東京都町田市鶴間687-1
天幸ビル17　4階
Tel. 042-788-6039　Fax. 042-788-6031
E-mail：kawazoe@ohtsu.jst.go.jp
経歴：1996年筑波大学物理学研究科修了。1996～2000年山形大学工学部助手。2000年～現在科学技術振興事業団大津局在フォトンプロジェクト研究員。博士（理学）。近接場光を用いた光デバイスの研究に従事。

特集

ナノフォトニクスの新展開

近接場光による ナノ構造堆積

科学技術振興事業団
八井　崇

1　はじめに

近年，半導体における微細加工技術・薄膜成長技術の発展により，量子効果が顕著となるサイズでの微細な構造を作り出すことが可能になっている。すなわち，電子を低次元構造に閉じ込めることにより，量子効果が発現する構造を人工的に作製することが可能となった。特に零次元構造である量子ドットは，レーザー素子として用いた場合，発光スペクトル線幅の狭窄化や，発振の低閾値化などの特長があり，注目を集めている。さらには，ナノフォトニクスデバイスとその集積化を目指して量子ドットの離散的な準位間の近接場光エネルギー移動を利用したナノ光スイッチ（図1）への応用も提案されており，光デバイスの高速化・高集積化が期待される[1,2]（本特集号の川添氏の記事も参照されたい）。

量子ドットの作製には様々な方法が開発されているが，その方法を大きく分けると，露光装置とエッチングを用いる加工法（トップダウン）と原子・分子を積み上げる加工法（ボトムアップ）が挙げられる。トップダウンは，近年X線や電子線を用いたリソグラフィにより20nm以下の精度の加工が可能であるが，「削る」ことによる加工が主となるため損傷が問題となる。

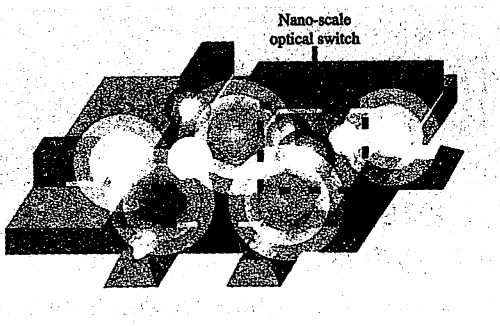

図1　ナノフォトニクスデバイスの中枢部分

これに対してボトムアップは「積み上げる」加工のため損傷は回避できる。近年，量子ドットレーザーなど，量子ドットが高密度に形成されたデバイスに向けて自己組織化を利用した作製法が広く用いられている。これは材料原子・分子が基板との相互作用によって自己整合的に量子構造を作製する手法である。しかし，この方法では各ドットを任意の位置に配置することや，異類ドットを隣接して配置することは困難である。

これに対して，原料分子を光により解離し，堆積させる光化学気相堆積法（光CVD法）は，様々な材料を任意の場所に高精度に堆積することが可能である。通常，光は回折限界により波長サイズ以下に絞ることはできないため，光CVD法における加工精度は光の波長程度であるが，近接場光学の技術を用いることで光の波長より遥かに小さなサイズの微細加工が可能である。この近接場光CVD法を用いれば，単一ドットを高精度に配置し，任意の大きさ・異種のドットを組み合わせて堆積することが可能である。

本稿ではこの近接場光CVD法を用いた微小ドットの堆積について報告する。また，従来の光CVD法では起こり得ない近接場光特有の堆積機構についても紹介する。

2 近接場光CVD法

将来の情報通信の発展を鑑みて，光デバイスに求められるサイズは波長以下になると予想されている[3]。さらには，この要求を満たすナノ光スイッチ[1]を作製するためには10nm程度の量子ドットを10nm程度の位置精度で作製する必要がある。近接場光CVDはこの要求を満たす有効な手段である。図2に近接場光CVDの原理及び実験配置を示す。これは，先鋭化プローブ先端に発生する近接場光により有機金属などの原料ガスを光化学反応で解離し堆積させる方法である。図3に原料ガスとして$Zn(C_2H_5)_2$(DEZn）および，$Al(CH_3)_3$を用いてZn，Alのドットを堆積した結果を示す。この手法により50nm以下の金属微粒子の作製が50nm以下の間隔で可能となっており（図3(a)）[4]，異種ドットの堆積（図3(b)）[5]も実現している。

ここで問題となるのが，気相中で解離された金属原子の拡散である。これは，解離された金属分子が堆積する基板上で吸着し核となるまでに基板上を拡散してしまうため，堆積されるドットのサイズがプローブ先端に発生する近接場光分布よりも大きくなってしまう。この問題を解決する為，我々は吸着分子の吸収スペクトルが気体分子のそれに対して長波長側にシフトする性質[6]を利用し，吸着分子を選択的に解離し堆積することで微小ドットの堆積に成功した。実験は，原料ガスであるDEZnの気相分子の吸収スペクトル端（～λ＝270nm）よりも僅かに長い波長325nmの光源を用いて行った。この結果，ガス分子に対して強い吸収を有する波長244nmでの堆積物（図4(a)）と比較して，堆積したドット近傍での堆積が大幅に抑制され，幅25nm・高さ16nmの高アスペクト比を有するZnドットの堆積（図4(b)）に成功した[7]。

さらに，上記堆積物がZnであることを確認する為，堆積したドットの酸化を行った。酸化はレーザアニーリング法により行い[8]，ドット堆積後に酸素雰囲気中でエキシマレーザ（波長193nm）を照射することにより行った。照射・集光モード近接場顕微鏡を用いて得られた酸化したドットの発光（λ＞360nm）像を示す（図5）[7]。この結果が示すように，100nm以下で堆積した単一ZnOドットの励起子からの発光が確認された。今回作製されたZnOはナノ光スイッチを構成する量子ドットとして利用されるだけでなく，大気中及び室温中で化学的・熱的

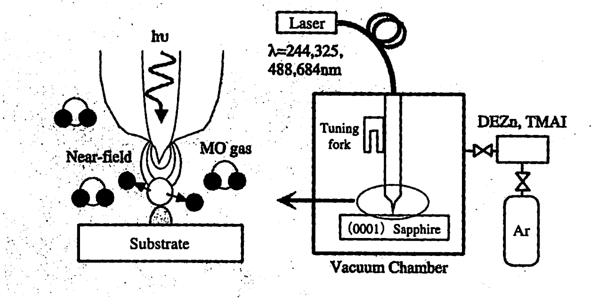

図2　近接場光CVD法及び実験配置

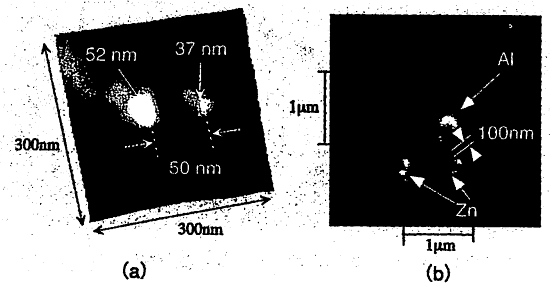

(a)　(b)

図3　近接場光CVD堆積結果
(a) Znドット　(b) 隣接して堆積されたZn・Alドット

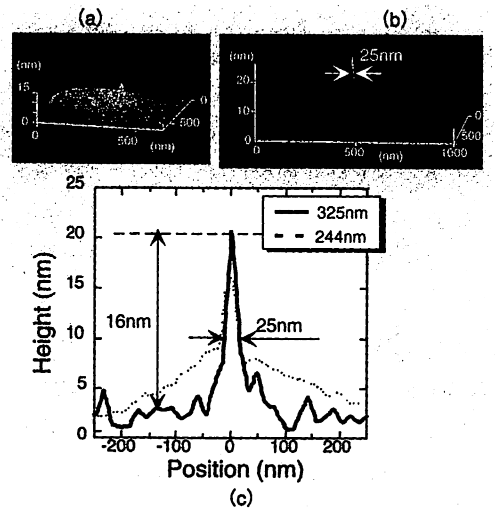

図4　波長
(a) 244nm，(b) 325nmにより堆積されたZnドット
(c) (a)及び(b)の断面図

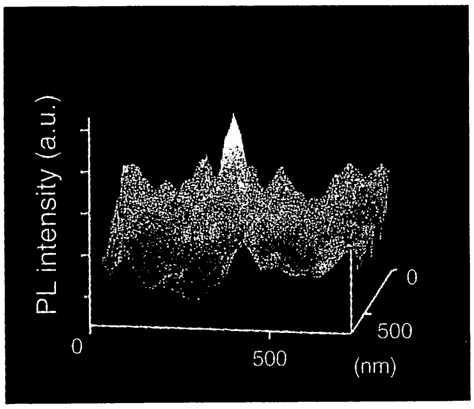

図5　単一に堆積されたZnOドットからの発光像

に安定な性質であるために，室温で動作する紫外発光光源としても期待される。

3　非共鳴近接場光CVD法

通常の光CVD法では堆積に用いる有機金属分子の吸収帯に共鳴した波長の光を利用し，分子を光化学反応により分解し堆積している。上述の実施例では近接場光を狭い空間に局在する小さな光源として利用しているに過ぎない。近接場光は局在しているというだけでなく，双極子禁制な準位への励起や波数保存則の緩和などの特長を持つ。我々は，この近接場光の持つ特徴を利用するために，原料ガスに吸収帯を持たない非共鳴光を利用した近接場光CVD法による堆積を行った[9]。

光源にはガス分子に対して非共鳴である（強い吸収を持たない）波長325・488・684nmの各レーザーを用いて堆積率の波長及び強度依存性を測定した。堆積率は堆積に用いたプローブにより堆積後に測定した形状像から求めた。堆積には無コート先鋭化ファイバプローブを使用した。

図6に堆積率の波長及び光強度依存性を示す[10]。この図から488nmにおいては低パワー領域で1次または2次の依存性であり，強パワー領域で3次の依存性を示している。また，684nmにおいては2次または3次の依存性のみであった。さらに，325nmでは堆積率が1次のみに依存することが明らかとなった。

このように，非共鳴光によって堆積が起きたことは，反応ガスの解離過程に仮想準位を介した多光子過程が発生していると考えられる。ここで，プローブ先端付近の光強度は10kW /cm^{2}以下であると見積もられるため，通常の仮想準位を介した高次の光吸収過程が起きる可能性は小さく，伝搬光では起こることのない近接場光特有の解離過程が働いていることが考えられる。これは伝搬光では，空間的に電場強度が一様であるため，光の振動に原子核が追従できず電子系のみが追従するいわゆる断熱近似が成り立ち，光励起には電子のみが関与する。一方，近接場光は電場強度の局在性からプローブと基板間では核間距離が場所に依存し断熱近似が成り立たない。よって，上記の強度依存性の結果は，断熱近似が破綻したことにより分子振動準位への直接遷移とその分子振動準位を介した多段階遷移による解離過程であると考えられる。

非共鳴光による堆積のうち，先ず488nmによる堆積では光強度が弱い領域で一次の依存性が確認される。これは，波長488nmの光子エネルギーがDEZnの解離エネルギーよりも大きいため，分子振動モードへの直接遷移により解離していると考えられる（図7(a)①）。これに対して光強度が強い場合，2次及び3次の強度依存性が確認されたことは，分子振動準位を介した多段階励起過程

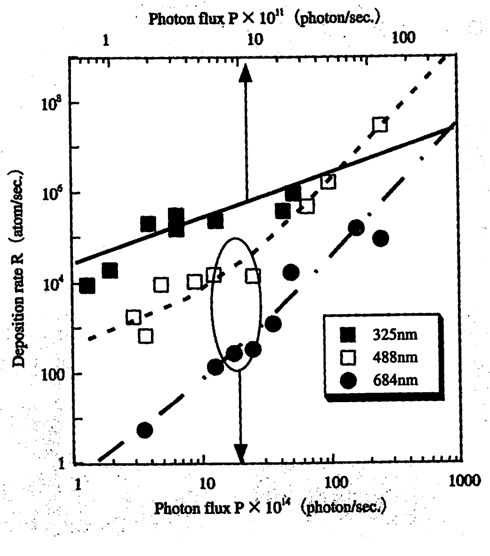

図6　近接場光CVDによる堆積率の波長・強度依存性
実線（$R = A_{325} \times P$），波線（$R = A_{488} \times P + B_{488} \times P^2 + C_{488} \times P^3$），一点波線（$R = B_{684} \times P^2 + C_{684} \times P^3$），P：フォトンフラックス，R：堆積率

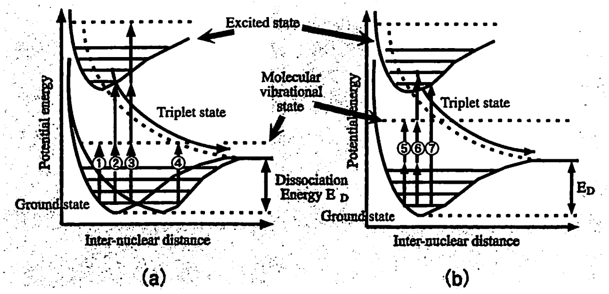

図7　DEZn分子軌道における電子のポテンシャル
(a) 488nm　(b) 684nm (⑤及び⑥), 325nm (⑦)

により解離が起きると考えられる（図7(a)②及び③）。さらに，3次の依存性が顕著に現れていることは，近接場光特有の局所的な電場成分の変動から，核間距離が変動し，三重項状態への直接遷移が可能となった為であろう（図7(a)④）。

一方，684nmの光子エネルギーはDEZnの解離エネルギーより低いため1光子過程は起こり得ない。しかし，488nmの結果同様2次及び3次の強度依存性が確認されたことは，分子振動準位を介した多段階励起過程により解離によるものと考えられる（図7(b)⑤及び⑥）。

これに対して，325nmの解離過程では1次の強度依存性を示したことから，1段階での振動準位への直接励起が発生していることが分かる（図7(b)⑦）。このように，吸収端波長よりも長波長の光源で直接励起が観測されたことは，吸着分子の吸収スペクトルが長波長側にシフトしたため$^{6)}$と考えられる。

4　おわりに

本稿では光デバイスの高集積化を目指して我々が取り組んでいる近接場光CVD法について紹介した。本方法は，光化学反応を利用したものであるため，他の発光素子（GaN，GaAs等）の作製にも応用可能である。さらには，非共鳴光CVD法を用いることで，従来光CVDとしては用いられなかった原料ガスを用いることが可能になるなど様々な応用が期待される。これは本特集号の総論の中で指摘されたように，従来の伝搬光を用いた光技術では原理的に実現不可能な現象を実現して使うことに他ならない。

参考文献

1) M. Ohtsu *et al.*, IEEE Journal of Selected Topics in Quantum Electronics, **8** (2002), in press.
2) T. Kawazoe *et al.*, Phys. Rev. Lett. **88**, 067404 (2002).
3) (財)光産業技術振興協会　光技術ロードマップ (2000).
4) Y. Yamamoto *et al.*, Appl. Phys. Lett. **76**, 2173 (2000).
5) Y. Yamamoto *et al.*, Tech. Digest of the 4th Pacific Rim Conf. on Lasers and Electro-Optics, pp. I520 - I521 (2001).
6) C. J. Chen *et al.*, Chem. Phys. Lett. **98**, 363 (1983).
7) T. Yatsui *et al.*, Tech. Digest of the 7th Int. Conf. On Near-field Optics and Related Tech., 117 (2002).
8) T. Aoki *et al.*, Appl. Phys. Lett. **76**, 3275 (2000).
9) T. Kawazoe *et al.*, Appl. Phys. Lett. **79**, 1184 (2001).
10) 田窪　暁等，近接場光学研究グループ第11回研究討論会予稿集，pp.64-68 (2002).

■ **Deposition of nano-structure using optical near field**

■ Takashi Yatsui
■ Ohtsu Localized Photon Project, ERATO, Japan Science and Technology Corporation

■ For future optical transmission systems, ultrahigh integration of a photonic switching arrays is necessary to increase data transmission rates and capacity. To accomplish this, fabrication process of nanometer-scale structure using optical near field was developed. In this article, a deposition of nanometer-scale Zn and Al dots using photodissociation of metalorganic vapor with optical near field is demonstrated. A novel deposition scheme under nonresonat conditions is also demonstrated and its origin is discussed.

ヤツイ　タカシ
所属：科学技術振興事業団　創造科学推進事業
大津局在フォトンプロジェクト　研究員
連絡先：〒194-0004　東京都町田市鶴間687-1
天幸ビル17　4階
Tel. 042-788-6040　Fax. 042-788-6031
E-mail：yatsui@ohtsu.jst.go.jp

経歴：1995年慶応義塾大学電気工学科卒，2000年東京工業大学総合理工学研究科博士課程修了。2000年より科学技術振興事業団 創造科学推進事業 大津局在フォトンプロジェクト 研究員。ナノフォトニクスデバイスの研究に従事。趣味：サッカー、スキー。

光近接場による原子の偏向と検出

伊藤　治彦*,***・戸塚　弘毅**・大津　元一*,**

Atom Deflection and Detection with Optical Near Fields

Haruhiko ITO*,***, Kouki TOTSUKA** and Motoichi OHTSU*,**

A slit-type deflector can be used for precise control of atomic motion by optical near field. The deflected atoms are observed with a slit-type detector supported by two-color optical near fields with a spatial resolution of 100 nm. Two-step photoionization and two-step resonant excitation followed by blue fluorescence are available for detection. Cold atoms are guided through a blue-detuned hollow light beam from a magneto-optical trap to the slit-type deflector. ^{87}Rb atoms with a mean velocity of 6 m/s can be deflected with a large angle of 0.36 degree and detected with a high efficiency of 38%.

Key words: atom deflection, atom detection, atom guide, optical near field, dipole force

1. 原子偏向器

光との相互作用を利用して原子を制御する，原子光学手法によって微小構造物を作ることが期待されているが，回折限界のために伝搬光では三次元的にナノスケールのものを作るのは原理的に困難である．実際，定在波による線状パターンの作製が行われているが1)，任意形状の作製についての報告はこれまでなされていない．原子光学的手法でドット形状のナノ構造物を作製するためには光近接場を用いるのが有効である2-6)．そのひとつとして，光近接場が及ぼす双極子力によって原子の運動方向を制御する原子偏向器の開発を行っている7)．

図1に示すように，シリコン-オン-インシュレーター基板をフォトリソグラフィーと化学エッチングで加工して作製した幅100 nm，長さ100 μmのスリットの片方のエッジ部に，原子の共鳴周波数よりわずかに周波数を高くした正離調レーザー光を結合させて光近接場を誘起する．光近接場領域に進入してきた原子は斥力の双極子力を受けて，運動方向が変化する．この偏向器ではエッジ部の角度およびアルミニウムの金属コーティングの厚さを調整することによって，光近接場の発生領域がスリット幅とほぼ等しくなるように制御している．光近接場領域に入らない原子はV溝部でブロックされる．

2. 原子検出器

前述の原子偏向器では，基底状態にある原子が偏向される．中性原子の検出にはマイクロチャネルプレートや二次電子増幅法が用いられているが8)，準安定状態の原子の検出には有効であるものの，基底状態の原子に対しては効率が悪い．また，空間分解能もたかだか1 μmと低く，光近接場を用いた高精度な原子制御には不十分である．

スリット幅100 nmの原子偏向器では後方1 cmの距離で10 μm程度の入射方向からの変位を得ることができる．この偏向原子を1%以上の確度で位置検出するために，幅100 nm以下のスリットを有する原子検出器を作製した9-12)．図2に示すように，V溝側から2波長のレーザー光を照射し，スリット部に2色の光近接場を誘起する．V溝構造のため偏向をスリットに垂直になるように選べば，高スループットで光近接場を励起することができる．

光近接場領域に進入してきた原子を2色の光近接場による2段階光イオン化10)または2段階共鳴励起で生じる蛍光の観測12)によって検出する．ルビジウム(Rb)原子の場合，2段階光イオン化では波長780 nmの半導体レーザー光によって$5S_{1/2}$基底状態から$5P_{3/2}$状態へ励起し，次いで波長476.5 nmの高出力アルゴン・イオンレーザー光によってイオン化レベルへ励起する．陽イオン化したRb原子を－3

---

*東京工業大学大学院総合理工学研究科（〒226-8502 横浜市緑区長津田町 4259）　***E-mail: ito@ae.titech.ac.jp
**科学技術振興事業団 ERATO「局在フォトン」プロジェクト（〒194-0004 町田市鶴間 687-1 天幸ビル4階）

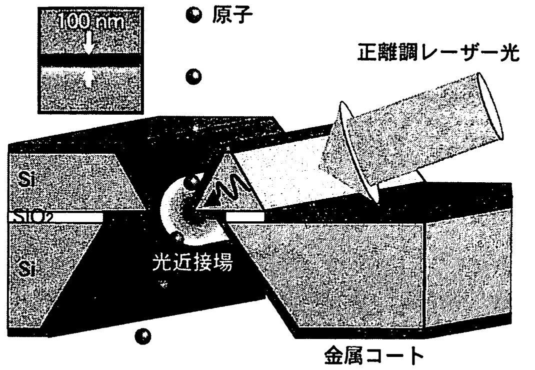

図1　スリット型原子偏向器．正離調レーザー光照射によってスリットのエッジ部に誘起した光近接場から斥力の双極子力を受けて原子の運動方向が変化する．シリコンオンインシュレーター基板を加工して，幅 100 nm，長さ 100 μm のスリットを作製している（左上の走査電子顕微鏡写真を参照）．

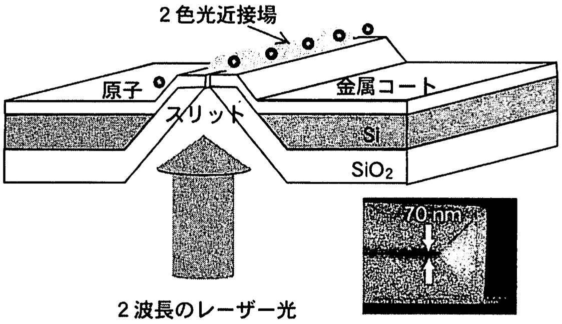

図2　スリット型原子検出器．2波長のレーザー光をV溝側から入射してスリット部に2色の光近接場を誘起し，進入してきた原子を2段階光イオン化もしくは2段階共鳴励起する．前者ではチャネル電子増倍管でイオン計数を行って，後者では原子が緩和する際に発する青い蛍光を分光して検出する．幅 70 nm，長さ 100 μm のスリットを作製している（右下の走査電子顕微鏡写真を参照）．

kV の負バイアスを印可したチャネル電子増倍管によって計数計測する．冷却原子の場合，20%以上の効率で検出することができる[10]．

2段階共鳴励起では，波長 780 nm と 775 nm の2つの半導体レーザー光を用いて $5P_{3/2}$ 状態を介して $5S_{1/2}$ 基底状態から $5D_{5/2}$ 状態へ励起する．その後，Rb 原子は緩和して $6P_{3/2}$ 状態から $5S_{1/2}$ 状態へ遷移するときに波長 420 nm の青い蛍光を発する．この蛍光を光ファイバーで集光し干渉フィルターをつけた分光器に入れて計測する．原子が十分に冷却されていれば3%以上の効率で検出することが可能である[11]．本方法は2段階光イオン化と比べると検出効率の点で劣るが，測定系が簡単なほか，強いレーザー光を使用しなくてもよい利点がある．

3.　冷却原子の誘導と偏向角の評価

作製したスリット型原子偏向器および検出器では 100 nm 以下の寸法の光近接場を用いるため，それとの相互作用を起こすためには速度の遅い冷却された原子が必要である．図3のように，磁気光学トラップ（MOT）および偏光勾配冷却[13]によって平均温度 10 μK の原子集団をつくったのちトラップを切って自由落下させ，正離調した中空の光ビームによって偏向器のスリット部まで誘導する．ここで原子は斥力の双極子力によって中空部分に閉じ込められる．ガウシアンフィルターに通してつくったパワー 600 mW，正離調＋1 GHz の中空光ビームを 26 cm 下方で中空径 500 μm に集光し，直径 2 cm の MOT から ^{87}Rb 原子のロードを繰り返すことによって，速度 6 m/s±0.6 m/s，フラックス 0.9×10^{13} atom/cm^2・s の冷却原子ビームを得ている．原子の誘導効率は80%で，偏向を行ううえで十分なフラックスとなっている．偏向の実証実験は現在進行中である．

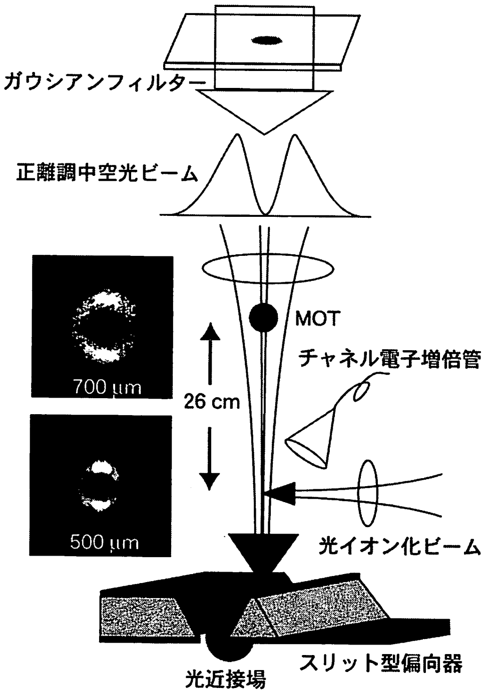

図3　冷却原子の誘導．ガウシアンフィルターによって中空光ビームをつくり，正離調下で MOT から落下する冷却原子を中空領域に閉じ込めスリット型偏向器に送り込む．26 cm 下方で光イオン化によって誘導原子の速度分布とフラックスを計測する．中空径は MOT の位置で 700 μm，計測位置で 500 μm である．

図4に速度 6 m/s でスリット型偏向器に入射した場合の ^{87}Rb 原子の偏向角をスリット端からの距離の関数として計算した一例を示す（近接場光強度を 10 W/cm^2，正離調を＋1 GHz としている）．ファンデルワールス引力による斥力ポテンシャルの減少を考慮に入れると，最大偏向角は 0.36 度となる．作製したスリット型検出器で近接場光イオン化を行えば，100 nm の空間分解能で偏向原子の 38%を検出できることになる．

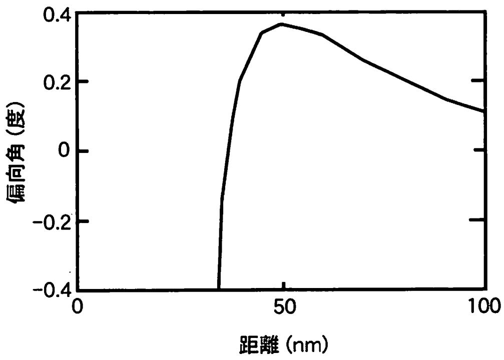

図4　スリット端からの距離の関数としてプロットした偏向角．速度 6 m/s の ^{87}Rb 原子に対しての計算例を示す．スリット端に近い領域ではファンデルワールス引力が強くなり反対方向に曲げられる．

4. 原子偏向技術の応用

偏向に用いる双極子力ポテンシャルの大きさは光強度と周波数離調に依存するため，これらによって偏向角を制御することができる．前述したような速度分布の小さな冷却原子ビームを用いれば，特定の種類の原子のみを基板上の狙った位置まで送り込むことが可能である．

光近接場の応用範囲はさらに広がりをみせているが，光近接場そのものの測定は一般にプローブなどを用いて破壊的に行われ絶対評価が難しいのが現状である．原子偏向法では原子の大きさが光近接場のそれより小さいため，原子をプローブとすることによって非破壊的に光近接場を調べることができる．未解明の光近接場-原子相互作用の詳細な研究やナノ領域での共振器量子電気力学効果の解明などにも威力を発揮するであろう．

文　献

1) R. W. McGowan, D. M. Giltner and S. A. Lee: "Light force cooling, focusing, and nanometer-scale deposition of aluminum atoms," Opt. Lett., **20** (1995) 2535-2537.

2) H. Ito and M. Ohtsu: "Near-field optical atom manipulation: Toward atom photonics," *Near-Field Nano/Atom Optics and Technology*, ed. M. Ohtsu (Springer-Verlag, Tokyo, 1998) pp. 217-266.

3) 伊藤治彦，大津元一："光近接場を用いた原子の制御"，光学，**28** (1999) 610-615.

4) H. Ito, A. Takamizawa, H. Tanioka and M. Ohtsu: "Precise control of atoms with optical near fields: Deflection and trap," Proc. SPIE, **3791** (1999) 2-9.

5) M. Ohtsu, K. Kobayashi, H. Ito and G.-H. Lee: "Nanofabrication and atom manipulation by optical near-field and relevant quantum optical theory," Proc. IEEE, **88** (2000) 1499-1518.

6) H. Ito, A. Takamizawa, H. Tanioka, K. Totsuka and M. Ohtsu: "Toward near-field optical manipulation of atoms using a nanometric fiber probe," *2000 International Quantum Electronics Conference* (IEEE, Nice, 2000) p. 106.

7) K. Totsuka, K. Yamada, H. Ito and M. Ohtsu: "Atom deflector with optical near fields," *Technical Digest of 2002 Quantum Electronics and Laser Science Conference* (OSA, Long Beach, 2002) p. 66.

8) Ch. Kurtsiefer and J. Mlynek: "A 2-dimensional detector with high spatial and temporal resolution for metastable rare gas atoms," Appl. Phys. B, **64** (1997) 85-92.

9) H. Ito, K. Totsuka, T. Kawamura, T. Yatsui and M. Ohtsu: "Near-field optical detection of atoms with high sensitivity and high spatial resolution," *Technical Digest of CLEO/Pacific Rim 2001*, 1 (IEEE, Chiba, 2001) pp. 514-515.

10) K. Totsuka, H. Ito, T. Kawamura and M. Ohtsu: "High spatial resolution atom detector with two-color optical near fields," Jpn. J. Appl. Phys., **41** (2002) 1566-1571.

11) K. Totsuka, H. Ito and M. Ohtsu: "Fluorescence spectroscopy of Rb atoms with two-color optical near fields for a high-resolution slit-type detector," IEICE Trans. Electron. (2002) in press.

12) K. Totsuka, T. Kawamura, T. Yatsui, H. Ito and M. Ohtsu: "A slit-type near-field optical detector for neutral atoms with high sensitivity and nanometric resolution," *Technical Digest of 2001 Quantum Electronics and Laser Science Conference* (OSA, Baltimore, 2001) p. 110.

13) H. J. Metcalf and P. van der Straten: *Laser Cooling and Trapping* (Springer, New York, 1999).

(2002年6月1日受理)

ナノフォトニクス

—ナノ寸法の光デバイスの動作と加工—

大津元一

1. まえがき

今から約10年後の高度情報化社会の要求に応えるためには光情報通信システムや光情報記録システムの大容量化・高速化が必要であり，それには関連する光デバイスの小型化・高度集積化が不可欠である[1,2]．しかし既存の光技術では光の回折（光の波が発散しようとする性質）のために光波長以下に小型化することはできない．ナノテクノロジー技術によりナノ寸法物質を多数作り，量子ドットレーザ，フォトニック結晶などの既存の概念で動作する光デバイスを作成しても，情報のキャリヤとして伝搬光を使う限り上記の回折による限界を超えることは不可能である．

回折限界を超えるためには光デバイス構築の概念のパラダイムシフトが必要となる．すなわち情報のキャリヤとしての光をナノ寸法化するために伝搬光ではなく近接場光を使い，これを少数個のナノ寸法物質間で伝送する．この新概念に立脚した技術がナノフォトニクスと呼ばれている(*)．この技術では波動光学の概念はもはや基本的ではなくなり，レーザ，共振器などの概念は主役の座を降りる．その代わり必須なのは局所的電磁相互作用など，従来着目されていなかった概念である．さらにナノフォトニクスは社会の要求に応えるためのシステム→デバイス→材料というトップダウン的な戦略にもとづく技術であることを指摘しておく．

2. ナノフォトニクスの本質

近接場光とは振動する電気双極子から発生する光の近接場成分である[3]．その電場の電気力線は電気双極子に局在し，非伝搬である．一方，遠隔場成分の電気力線は電気双極子から分離し，閉曲線となって遠方に伝搬する．従来の光技術ではこの伝搬光を使っており，これは回折する．ナノフォトニクスでは基板等の巨視的寸法の物質系に囲まれるナノ寸法物質を扱うが，これに光を照射すると物質中の多数の原子に電気双極子が誘起され，各々が図1(a)に示すように近接場光と伝搬光とを発生する．この物質中のすべての電気双極子から発生する近接場光のエネルギーの総和の値はナノ寸法物質表面から遠ざかるにつ

(*)ナノフォトニクスとは数年前に筆者が命名した光技術である．たとえば㈶光産業技術振興協会では筆者の提案により1995年に「ナノフォトニクス懇談会」が発足し，研究開発動向の調査活動を行い現在に至っている．最近ではこの名前を他所でも散見することが多くなった．

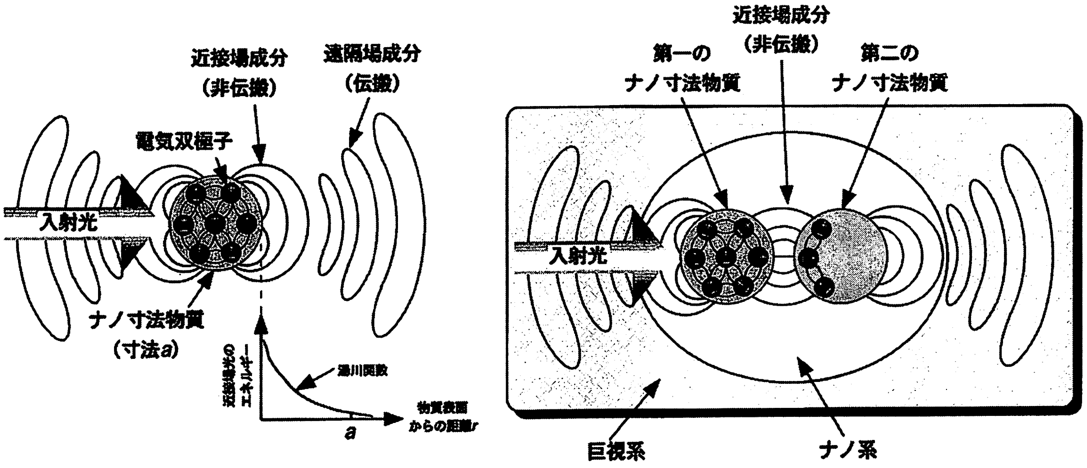

(a) (b)

図1　巨視系に囲まれたナノ系としての近接場光とナノ寸法物質
(a)近接場光の発生の様子とそのエネルギーの空間分布．(b)基板等の巨視系に囲まれたナノ系の中で，近接場光を媒介としてナノ寸法物質が局所的電磁相互作用をする様子．

れて急激に減衰する[4]．非伝搬の近接場光はナノ寸法物質表面を膜のように覆うが，その膜の厚みはナノ寸法物質の大きさ程度であり入射光の波長にはよらない．

図1(b)のように第一のナノ寸法物質表面に近接場光を発生させ，それを微小光源として用いて第二のナノ寸法物質に近づけて照明し，それを加工したり，あるいは近接場光のエネルギーを伝送することにより回折限界を超えたナノフォトニクスが可能となる．ここで重要なのは次の二点である．(a)二つのナノ寸法物質が近接場光を媒介として局所的電磁相互作用を行い，相互に結合した状態になっている．【従って物質の屈折率などの物理量の値が結合状態に依存して変化する．さらに，入射光の波長程度の空間寸法にわたる物理量の平均化近似が有効でなくなる．】(b)このように結合した微小な系（ナノ系と呼ばれている）が，それよりずっと寸法の大きな巨視系（ナノ寸法物質用の基板，入射光，光検出器等）に囲まれている．【従って伝搬光を使う場合には見られないエネルギーの移動（非共鳴エネルギー移動と呼ばれている）が二物質間で起こる[4]．】

ナノフォトニクスの本質は上記の二点に注目し，特に【　】内に指摘した特徴を生かすことにより，従来の伝搬光を用いた光技術では原理的に実現不可能な現象や機能等を実現して使うことである．その系の寸法がナノメートル程度に小さくなることは副次的な成果にすぎない．

3.　ナノ光デバイスとその集積化の試み

2015年には光ファイバ通信システムにおいて10 Tb/sのデータ転送速度が必要で，そのためには光交換機用の光スイッチ配列中の入出力端子数は各々1,000またはそれ以上必要と推定されている．これらの要求を満たし，さらに次世代のシステムへの発展をめざすには光スイッチ配列中の各光デバイスの寸法を回折限界を超えて微小化しなければならない．そのためには近接場光を用いたナノ光デバイスとその集積化が唯一の解を与える．

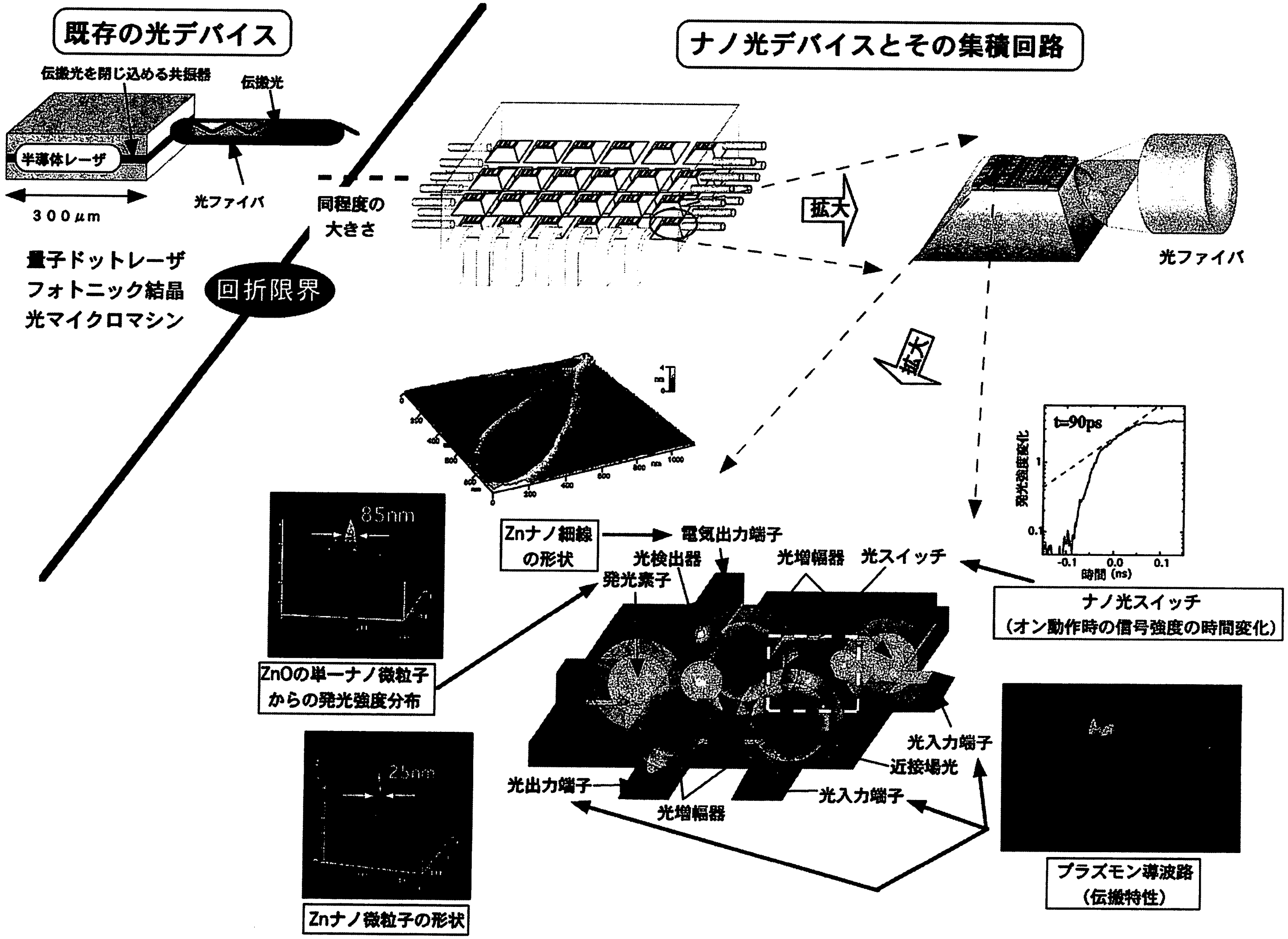

図2 ナノ光デバイスとその集積回路

この新概念にもとづく集積回路の構成の代表例を図2に示す．これは近接場光を媒介とするナノ寸法物質間の局所的電磁相互作用を利用し，個々のナノ寸法物質に近接場光の発生，スイッチング，検出などの機能を発現させ，情報のキャリヤとしての近接場光をナノ寸法物質間で伝送するものである．社会の要求に応えるためにこのシステムは次の特徴を持つ．

(1)光スイッチング動作には特定の寸法比の関係を有する三つの量子ドット間の局所的電磁相互作用（第2節の(a)）による近接場光エネルギー移動を利用している．伝搬光ではこれらの量子ドット間の光エネルギー移動のための光学遷移は禁制されているが，近接場光ではエネルギーがナノ寸法領域に局在するのでこの禁制がとける[5]．即ちエネルギーの移動は近接場光の場合にのみ可能であり，これは光デバイス構築の概念のパラダイムシフトの典型である．

(2)既存の光技術で作られた外部の大寸法の光デバイス（たとえば光ファイバなど）と接続して光システムを構築するためのインターコネクションを配備している．これは図2の光デバイス中の近接場光を伝搬光に変換して外部に伝送すること，またはその逆の働きをする．半導体と金属細線から構成されたプラズモン導波路がこの機能を担っている[6]．

図2の集積回路を実現するために，すでにZnOナノ微粒子の青色発光やCuClの三つの量子ドットを組み合わせた光スイッチング機能等の実験及び理論的研究が行われている[5]．特に光スイッチングデバイスについては，社会の要求に応えるために必要な性能を表す性能指数の値が既存の光技術による光スイッチングデバイスより10^2～10^3倍大きく，その性能の優位性が理解できる．一般にナノテクノロジー関連のデバイスを評価するときに重要なのはシステム内でのこのような性能の高さである．単に微小であったり，高速であるだけでは不十分である．

4. ナノ光デバイスのためのナノ光加工

図2の集積回路を作るには作製対象のナノ寸法物質の寸法，位置，間隔に関する精度が高い加工技術が必要である．この精度はナノ寸法物質間で近接場光を伝送するために不可欠である．さらに共通基板の上に多様な物質を堆積できることも重要である．既存の加工技術では高速性には優れるもののこれらの要求を満たさない．たとえば自己組織化などの微小物質堆積法は熱平衡と化学反応とを利用した集団的方法なので，基板面内での個々のナノ寸法物質の寸法，位置，間隔の制御性は高くない．従って加工技術に関するパラダイムシフトが必要である．

そのためには近接場光を使った化学気相堆積法が有望である．これまでにZn，Alなどの金属，ZnOなどの酸化物の微小パターンなどが形成されている[7]．特に半導体のエネルギー構造を有するZnOの単一ナノ寸法微粒子からの青色発光，その量子サイズ効果[8]などが確認されている．この他GaAs，GaNなどの化合物半導体の堆積も可能である．

一例として気相の$Zn(C_2H_5)_2$分子を解離してZnを堆積する場合，非共鳴の青色光や赤色光を用いても可能であることが確認されている[9]．これは第2節の(a)，(b)に起因し，前節の光スイッチング動作と同じくナノフォトニクス技術による微細加工の概念のパラダイムシフトである．この現象は近接場光を用いれば伝搬光による化学気相堆積に用いられていた光源と分子種との組み合わせの制限から解放されて，新しい物質を堆積できるという技術的ブレークスルーをもたらすことを意味している．

5. まとめ

将来の光情報通信システムを支えるために図2に示したナノ光デバイスと集積回路の実現にむけた研究開発が進められており，第4節で述べた微細加工技術によって現在までに図2下部に示すような要素が試作されている10)．これは新形態の光メモリ用デバイスとして将来の光情報記録システムへ応用される可能性も示している．

▨参考文献▨

1）大津元一，電子情報通信学会誌，**84**（2001）26

2）大津元一，ナノ・フォトニクス（米田出版，1999）

3）大津元一，光の小さな粒（裳華房，2001）

4）K. Kobayashi and M. Ohtsu, J. Microscopy, **194** (1999) 249

5）T. Kawazoe, et al., Phys. Rev. Lett., **88** (2002) 0674041

6）T. Yatsui, et al., Appl. Phys. Lett., **79** (2001) 4583–4585

7）M. Ohtsu, et al., Proc. IEEE, **88** (2000) 1499

8）T. Yatsui, et al., Appl. Phys. Lett., **80** (2002) 1444

9）T. Kawazoe, et al., Appl. Phys. Lett., **79** (2001) 1184

10) M. Ohtsu, et al., J. Selected Topics in Quantum Electronics, **8** (2002) 印刷中

大津 元一（おおつ・もといち）
東京工業大学大学院総合理工学研究科 教授